High-Order Direct Numerical Simulation of Finite Span Wings

Joseph-Raffael Rinaldi

A Thesis

in

The Department

of

Mechanical, Industrial and Aerospace Engineering

Presented in Partial Fulfillment of the Requirements

for the Degree of

Master of Applied Science (Mechanical Engineering) at

Concordia University

Montréal, Québec, Canada

January 2026

CONCORDIA UNIVERSITY

School of Graduate Studies

This is to certify that the thesis prepared

By: **Joseph-Raffael Rinaldi**

Entitled: **High-Order Direct Numerical Simulation of Finite Span Wings**

and submitted in partial fulfillment of the requirements for the degree of

Master of Applied Science (Mechanical Engineering)

complies with the regulations of this University and meets the accepted standards with respect to originality and quality.

Signed by the Final Examining Committee:

_____ Chair
Dr. Name of the Chair

_____ External Examiner
Dr. Name of External Examiner

_____ Examiner
Dr. Name of Examiner One

_____ Supervisor
Dr. Name of Supervisor

Approved by _____
Dr. Muthukumaran Packirisamy, Chair
Department of Mechanical, Industrial and Aerospace Engineering

_____ 2026

_____
Dr. Mourad Debbabi, Dean
Faculty of Engineering and Computer Science

Abstract

High-Order Direct Numerical Simulation of Finite Span Wings

Joseph-Raffael Rinaldi

A wide range of modern aerodynamics applications, such as unmanned aerial vehicles (UAV) and electric vertical takeoff and landing (eVTOL) aircraft, require accurate aerodynamic predictions in transitional Reynolds number regimes. However, current industry-standard computational fluid dynamics (CFD) methodologies, specifically the Reynolds-averaged Navier Stokes (RANS) approach, fail to yield accurate results in this flow regime. To address this limitation, we are proposing the use of direct numerical simulation (DNS) in lieu of RANS for these applications. These DNS simulations will serve as a foundation for validating future studies on transitional Reynolds number regimes in the vicinity of Re = 10,000. In this presentation, we will showcase a series of high-order DNS simulations using the flux reconstruction method to analyze transitional and turbulent flow over finite-span NACA 0018 wings. The study examines angles of attack from 0° to 20° and span-to-chord ratios ranging from 1 to 4, simulated over 100 non dimensional time units. A structured mesh was generated with appropriate y^+ values to ensure the resolution of the viscous sub-layer. The mesh extends 10 chord lengths in all directions from the airfoil's side view and 2 chord lengths from the wing tips, enabling accurate capture of wingtip vortices and downstream turbulent structures. Particular focus will be placed on analyzing turbulent transition, resulting in turbulent flow structures, first and second-order turbulent statistics, aerodynamic forces, and surface flow characteristics. Several key physical phenomena in this flow regime will be examined in contrast to conventional aerodynamic configurations, including the generation of negative lift at low angles of attack, a non-linear lift coefficient behavior, and the delayed onset of stall with increasing span-to-chord ratios.

Acknowledgments

I am sincerely thankful to my colleagues in the Computational Aerodynamics Laboratory for their support, collaboration, and willingness to share their knowledge. The many discussions we shared greatly enriched both my research and personal growth. I would like to give special thanks to Carlos, who generously continued to guide me through the lab systems even after his graduation, as well as to Marie-Pier, Amar, and Mohammad, whose patience and dedication in explaining concepts and engaging in discussions were invaluable throughout my graduate studies.

I owe my deepest gratitude to my supervisor, Dr. Brian Vermeire, for his exceptional mentorship and unwavering support. His guidance, expertise, and countless hours of discussion profoundly shaped my understanding of complex topics in computational aerodynamics and have had a lasting impact on my academic development. I am truly grateful for the opportunity to learn under his supervision.

I would also like to acknowledge Concordia University for providing an excellent academic environment and supporting my research endeavors. I am thankful to Compute Canada for granting generous computational resources, without which this work would not have been possible. I also gratefully acknowledge the Natural Sciences and Engineering Research Council of Canada (NSERC) for their financial support, which played a crucial role in enabling this research.

Finally, I wish to thank my family and friends for their constant encouragement, patience, and support throughout this journey. Their presence and companionship made this experience both rewarding and memorable.

Contents

List of Figures

List of Tables

List of Acronyms

Notation	Description
ACM	Artificial Compressibility Method
AOA	Angle of Attack
AR	Aspect Ratio
BR2	Second Bassi–Rebay Riemann Solver
CFD	Computational Fluid Dynamics
CFL	Courant–Friedrichs–Lewy
DG	Discontinuous Galerkin
DNS	Direct Numerical Simulation
EDAC	Entropically Damped Artificial Compressibility
eVTOL	Electric Vertical Takeoff and Landing
FEM	Finite Element Method
FR	Flux Reconstruction
HORUS	High-Order Unstructured Solver
ILES	Implicit Large Eddy Simulation
LES	Large Eddy Simulation
MAVs	Micro-Aerial Vehicles
NASA	National Aeronautics and Space Administration
P-ERK	Paired Explicit Runge-Kutta
PPE	Pressure Poisson Equation

Notation	Description
PSD	Power Spectral Density
RANS	Reynolds-averaged Navier Stokes
RK	Runge-Kutta
RK_{33}	Three-stage Third Order Runge–Kutta Scheme
RK_{44}	Four-stage Fourth Order Runge–Kutta Scheme
SD	Spectral Difference
SG	Staggered Grid
SGS	Subgrid-Scale
SV	Spectral Volume
TKE	Turbulent Kinetic Energy
UAV	Unmanned Aerial Vehicle
WMLES	Wall-Modeled Large Eddy Simulation

Nomenclature

English Letters

a	Characteristic Wave Speed
a_{ij}	Stage Coefficients
b_i	Stage Weights
$\overline{C}_D$	Time-Averaged Three-Dimensional Coefficient of Drag
$\overline{C}_f$	Time-Averaged Coefficient of Friction
$\overline{C}_L$	Time-Averaged Three-Dimensional Coefficient of Lift
$\overline{C}_p$	Time-Averaged Coefficient of Pressure
C	Chord Length
c	Non-Dimensional Chord Length
c_i	Stage Times
C_L	Three-Dimensional Coefficient of Lift
c_s	Speed of Light
$C_{D,i}$	Three-Dimensional Coefficient of Induced Drag
$\overline{D}$	Time-Averaged Three-Dimensional Drag
$\mathbf{D}$	Derivative Matrix
E	Energy
e	Internal Energy
E_k	Kinetic Energy of an Eddy
e_{sf}	Span Efficiency Factor
$\overline{\overline{F_C}}$	Convective Flux Tensor
$\overline{\overline{F}}$	Flux Tensor
$\vec{F}$	Force
$\vec{F}_C$	Convective Flux

$\vec{F}_D$	Diffusive Flux
$\vec{F}_{e,j}$	Euler Flux
$\vec{F}_{inv}$	Inviscid Flux
$\vec{F}_{v,j}$	Viscous Navier-Stokes Flux
$\vec{F}_v$	Viscous Flux
f	Flux
f_i^c	Corrected and Continuous Flux
f_i	Local Polynomial Flux
g_L	Left Interface Correction Function
g_R	Right Interface Correction Function
h_e	Element Width
$\mathbf{I}$	Identity Matrix
k	Thermal Conductivity
$\overline{L}$	Time-Averaged Three-Dimensional Lift
L	Characteristic Length
M	Artificial Mach Number
Ma	Mach Number
$\hat{n}$	Unit Outward Normal
N_e	Number of Non-Overlapping Elements
N_p	Number of Solution Points
N_{DOF}	Number of Degrees of Freedom
p	Pressure
p_∞	Free-Stream Static Pressure
P_P	Legendre Polynomial
p_s	Polynomial Degree of the Solution
$\dot{Q}$	Heat Transfer Rate
$\vec{q}$	Heat Flux
$\vec{R}$	Residual
R_L	Left Radau Polynomial
R_R	Right Radau Polynomial

Re	Reynolds Number
Re_η	Reynolds Number of the Kolmogorov Scale
Re_o	Reynolds Number of the Largest Eddy
S	Control Surface
s	Number of Stages
S_R	Reference Area
T	Temperature
t	Time
t_a	Acoustic Time Scale
t_c	Convective Time Scale
t_f	Final Time
$\vec{u_p}$	Vector of Conserved Variables in Pseudo-Time
$\vec{u}$	Vector of Conserved Variables
u	Velocity
u^*	Friction Velocity
u_η	Velocity of the Kolmogorov Scale
u_∞	Free-Stream Velocity
u_o	Velocity of the Largest Eddy
$\vec{v}$	Velocity Vector
$\dot{W}_p$	Work Rate of the Pressure Forces
$\dot{W}_v$	Work Rate of the Viscous Shear Stresses
$\dot{W}$	Work Rate
$\vec{x}$	Position Vector
x	Cartesian Coordinate Position
x_L	Left Element Interface
x_R	Right Element Interface
y	Cartesian Coordinate Position
y^+	Dimensionless Wall Distance

Greek Letters

α	Advection Speed

δ_{ij} Kronecker Delta

δ_i Correction Term

Δt Time Step Size

Δx Grid Spacing

ε Dissipation Rate

ϕ Nodal Polynomial Basis

η Kolmogorov Scale

μ Dynamic Viscosity

ν Kinematic Viscosity

ρ Density

$\overline{\overline{\sigma}}$ Internal Stress Tensor

$\overline{\overline{\tau}}$ Viscous Shear Stress Tensor

τ Timescale of an Eddy

τ_η Timescale of the Kolmogorov Scale

τ_o Timescale of the Largest Eddy

τ_p Pseudo-Time Variable

τ_w Wall Shear Stress

Ω Control Volume

Ω' Reference Control Volume

ξ Standard Reference Element

ζ Artificial Compressibility Factor

Mathematical Symbols

ℓ Length Scale of an Eddy

ℓ_o Length Scale of the Largest Eddy

ℓ_{DI} Length Scale Limit of an Eddy Before Entering the Dissipation Range

ℓ_{EI} Length Scale Limit of an Eddy Before Entering the Universal Equilibrium Range

$\mathcal{L}$ Flow Scale

Superscripts

$\overline{\square}$ Time-Averaged Term

$\vec{\square}$ Vector Notation

$\square^{\circ}$ Degrees

$\square^{*}$ Common Flux at the Interface

$\square'$ Fluctuating Term

$\square^{c}$ Continuous

$\square^{h}$ Global

$\square^{T}$ Transpose

$\square^{t+1}$ Next Time Step

$\square^{t}$ Current Time Step

Subscripts

$\square_{ij}$ Index

$\square_{init}$ Initial Condition

$\square_{i+1}$ Downwind Index

$\square_{i-1}$ Upwind Index

Operators

$\bigoplus$ Direct Sum

$\cdot$ Dot Product

$\vec{\nabla}$ Gradient

$\int$ Integral

$\prod$ Product

$\oint$ Surface Integral

Σ Sum

$\otimes$ Tensor Product

Chapter 1

Introduction

The primary motivation for this work is to apply accurate and computationally efficient methods for predicting aerodynamic performance in Micro-Aerial Vehicles (MAVs). However, the implications of this work extend beyond MAVs, with broader relevance to multiple sectors within the aerospace industry. These include the design and optimization of next-generation aircraft for civil applications, the development of aerodynamic systems suitable for the thin Martian atmosphere, and performance optimization in motorsports engineering. The study employs a high-fidelity turbulence modeling strategy, alongside high-order numerical methods used to discretize the governing equations. Particular attention is given to the Flux Reconstruction (FR) approach—a high-order spatial discretization well-suited for resolving complex flow structures via DNS. The application of FR for DNS enables accurate capture of small-scale features characteristic of turbulent aerodynamic flows. We begin with a comprehensive grid convergence study to calibrate and validate the computational model and mesh. Subsequently, a comparative analysis is conducted involving four wings of varying spans, benchmarked against an idealized infinite-span wing, to evaluate the influence of spanwise confinement and finite aspect ratio on aerodynamic behavior.

1.1 Motivation

At the heart of innovation lies a deep understanding of fundamental principles. Fluid dynamics is no exception, with a constant influx of new studies being published. Ongoing interest in this

field stems from its critical role across a wide range of industries—from aerospace and biomedical engineering to meteorology and architecture. While fluid dynamics is universally important, the specific flow regimes encountered can vary significantly depending on the application.

These flow regimes are often characterized by the Reynolds number, a dimensionless quantity that describes the relative influence of inertial to viscous forces in a flow. High Reynolds number flows ($Re > 10^6$) are generally well studied, particularly due to their prevalence in traditional aerospace applications [1, 2]. In contrast, low Reynolds number flows have historically received less attention within the aerospace community [3], largely because they occur less frequently in conventional flight conditions.

The Reynolds number is defined as

$$Re = \frac{\rho u L}{\mu}, \tag{1.1}$$

where ρ is the fluid density, u is the fluid velocity, L is the characteristic length and μ is the dynamic viscosity of the fluid. This ratio encapsulates the balance between inertial and viscous forces, and governs the transition between laminar and turbulent flow, among other key flow features.

However, with the rise of small UAVs, low Reynolds number flows have gained increasing significance, prompting renewed research and analysis in this regime [4]. MAVs, in particular, have become increasingly popular due to their lightweight design, enhanced maneuverability, and compact size. Recent advancements in high-precision manufacturing have further enabled the development of even smaller and more efficient MAVs. These systems have proven valuable in various applications, including surveillance, disaster response, and infrastructure inspection [5].

While MAVs currently represent one of the most impactful innovations within the low Reynolds number regime, another critical area of interest is extraterrestrial flight. As mentioned earlier, one of the key parameters influencing the Reynolds number is fluid density. On Mars, for example, the atmospheric density is approximately $\rho \approx 0.017 kg/m^3$, in stark contrast to Earth's average of $\rho \approx 1.225 kg/m^3$ [6, 7]. As a result, a vehicle of similar size and speed would experience significantly lower Reynolds numbers on Mars, drastically affecting aerodynamic performance [8, 9].

This challenge is exemplified by NASA's Ingenuity helicopter, which was specifically designed

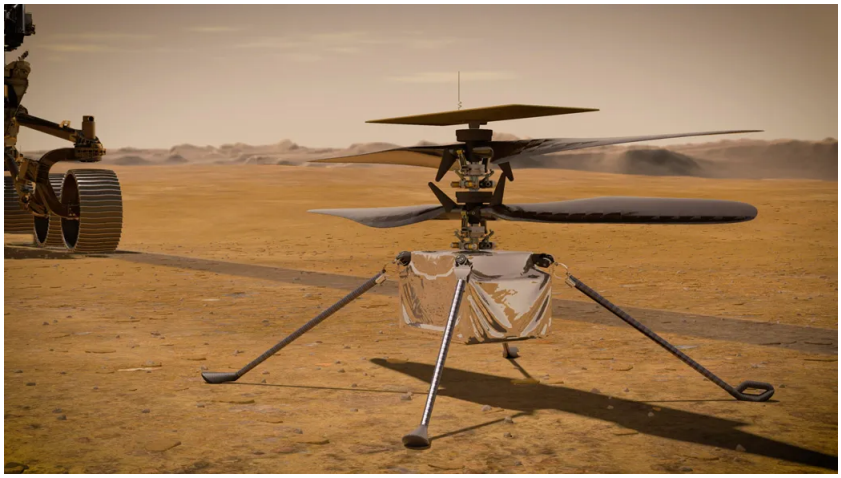

Figure 1.1. Artist's concept of the mars Ingenuity helicopter [10]

to operate in the Martian atmosphere. Ingenuity features an enlarged rotor system operating at higher rotational speeds and an ultra-lightweight structure to generate sufficient lift in the thin atmosphere—design constraints that would not be necessary for terrestrial flight [11]. Such differences underscore the importance of understanding low Reynolds number aerodynamics for both terrestrial and extraterrestrial applications.

Another application where low Reynolds number flows play a significant role is in motorsport aerodynamics, particularly in the design of aerodynamic components such as wings and diffusers. In these scenarios, the wings are relatively small and often operate at lower speeds compared to those seen in conventional aviation, resulting in lower Reynolds numbers [12]. Unlike traditional airfoils, which are designed to generate lift, motorsport wings are inverted and optimized to produce downforce—an aerodynamic force that presses the vehicle onto the track surface, enhancing tire grip and improving handling through corners [13].

At low Reynolds numbers, however, the flow is more susceptible to early separation and transitional behavior, which can compromise aerodynamic efficiency [14]. As a result, motorsport engineers must carefully balance wing geometry, angle of attack, and surface finish to maintain attached flow and maximize downforce while minimizing drag. This highlights the critical need for precise modeling and experimentation in the low Reynolds number regime to extract optimal performance under strict design and regulatory constraints.

The importance of understanding low Reynolds number flows lies in the fact that they inherently challenge the assumptions of classical aerodynamic theory. Fundamental models—such as thin airfoil theory—begin to break down in this regime, as they are predicated on the presence of a high Reynolds number flow, where inertial forces dominate and a thin, turbulent boundary layer develops along the surface [15, 16]. In contrast, low Reynolds number flows are characterized by dominant viscous forces, leading to the formation of thick, laminar boundary layers that are more prone to early separation [9, 17].

These differences fundamentally alter the aerodynamic behavior of airfoils and other surfaces, requiring new analytical approaches and design strategies. By improving our understanding of these nontraditional flow regimes, it becomes possible to design aerodynamic devices tailored specifically for low Reynolds number applications—preserving desirable performance characteristics while enabling innovation in emerging fields such as MAVs, extraterrestrial flight, and motorsport engineering.

1.2 Numerical Analysis

While it is commonly assumed that turbulence is a random process due to its chaotic nature, this is untrue [18]. A truly random motion would not have a deterministic model, such as the Navier-Stokes equations. The existence of these equations imply, in theory, that turbulence can be resolved. However, as turbulence is chaotic and highly complex, an analytical precise solution is almost impossible to obtain [19]. This results in the use of statistical methods to describe turbulent structures, modeling them as a random process while they have coherent structures that proves that there is an underlying structure to the chaos.

These coherent structures are observed as turbulent energy cascades, whereby large turbulent structures break down into smaller structures until the local flow is dominated by viscous forces and the kinetic energy dissipates in the form of heat [1, 19]. This process is referred to as the energy cascade theory. These structures vary widely in length, with some being as large as the physical length scale of the problem of interest, while the smallest can be much smaller. These structures are known as eddies and are characterized by a length scale ℓ. These length scales also have a

characteristic velocity $u(\ell)$ and timescale $\tau(\ell) = \ell/u(\ell)$. The group of eddies with the largest length scales are denoted as ℓ_o and are comparable to the flow scale $\mathcal{L}$. As such, their characteristic velocity and timescales can be denoted as $u_o \equiv u(\ell_o)$ and $\tau_o = \ell_o/u_o$ respectively. These large eddies are unstable, as their Reynolds number $Re_o \equiv u_o\ell_o/\nu$ is large in comparison to the Reynolds number of the flow, and break up into smaller eddies. This process continues until the eddies reach a size where they are stable and have a sufficiently low Reynolds number, whereby the viscous forces can dominate and dissipate the kinetic energy, E_k, of the eddies.

Kolmogorov was capable of advancing the energy cascade theory by using a series of hypotheses. The first of these hypotheses was based on the directionality of the eddies through the cascade. He suggested that while the large scale eddies were anisotropic, their directional biases would be lost in the chaotic process of scale reduction and there would be a transitional length scale, defined by ℓ_{EI}, by which the eddies would become isotropic [19]. The isotropic eddies ($\ell < \ell_{EI}$) would be considered as the small-scale turbulent structures. This provides a clear distinction between large and small-scale structures, as the small structures become directionally independent from the energy dissipation between eddies. This assumption extends further as Kolmogorov argued that if the directionality of the eddies was lost, all geometric information, values determined by the mean flow field and boundary conditions, is also lost. As such, this suggests that the small-scale eddies are now universal as they carry no information about the system that they have been produced from. Thus in this context, these universal small-scale motions would be similar in all turbulent flows, with sufficiently high Reynolds number [19].

In this small-scale range ($\ell < \ell_{EI}$), referred to as the universal equilibrium range, Kolmogorov makes his second hypothesis. He suggests that these universal small-scale structures are uniquely determined by the fluid's kinematic viscosity ν and the dissipation rate ε [19]. This allows the small eddies to quickly adapt to maintain a dynamic equilibrium with the energy transferred by the large eddies. With these two parameters, unique length, velocity and time scales are formed called the Kolmogorov scales

$$\eta \equiv \left(\frac{\nu^3}{\varepsilon}\right)^{\frac{1}{4}}, \tag{1.2}$$

$$u_\eta \equiv (\varepsilon\nu)^{\frac{1}{4}}, \tag{1.3}$$

$$\tau_\eta \equiv \left(\frac{\nu}{\varepsilon}\right)^{\frac{1}{2}}. \tag{1.4}$$

The Kolmogorov scales only characterize the very smallest eddies, as the Reynolds number determined for an eddy of length η is unity,

$$Re_\eta = \frac{\eta u_\eta}{\nu} = 1, \tag{1.5}$$

which is consistent with these eddies proceeding to get smaller until they are small enough for dissipation from the viscous effects to occur. Additionally, by rearranging the Kolmogorov scales, it is possible to express the dissipation rate solely in terms of viscosity and time scale

$$\varepsilon = \frac{\nu}{{\tau_\eta}^2}. \tag{1.6}$$

By comparing the smallest and the largest scales, it is observed that the resulting ratios are a function of Reynolds number

$$\eta/\ell_o \approx Re^{-\frac{3}{4}}, \tag{1.7}$$

$$u_\eta/u_o \approx Re^{-\frac{1}{4}}, \tag{1.8}$$

$$\tau_\eta/\tau_o \approx Re^{-\frac{1}{2}}. \tag{1.9}$$

When following the approximation that the largest eddies have an energy in the order of ${u_0}^2$ and the rate of dissipation can assumed to correspond to $\varepsilon \approx {u_o}^2/\tau_o = {u_o}^3/\ell_o$. The scale ratios have an inversely proportional relationship with the Reynolds number, thus for very small values of η, the Reynolds number is extremely high. This means there are scenarios in which for large enough values of Re, there exists a range of scales ℓ that are small when compared to ℓ_o and large when compared to η. In such a region where $\ell_o \gg \ell \gg \eta$, the Reynolds number would still be sufficiently high for viscous effects to have little affect on the eddies. Thus, Kolmogorov made the third hypothesis, that there exists a region with a universal form uniquely determined by ε, independent of ν [19].

For convenience, a length scale of ℓ_{DI} is introduced. This length scale subdivides the range of the universal equilibrium ($\ell_{EI} > \ell > \eta$) into the inertial range ($\ell_{EI} > \ell > \ell_{DI}$) and the dissipation

range ($\ell_{DI} > \ell > \eta$). As the name suggests, motions in the inertial range are dominated by inertial effects, while the dissipation range experiences the viscous effects and are thus responsible for all of the energy dissipation.

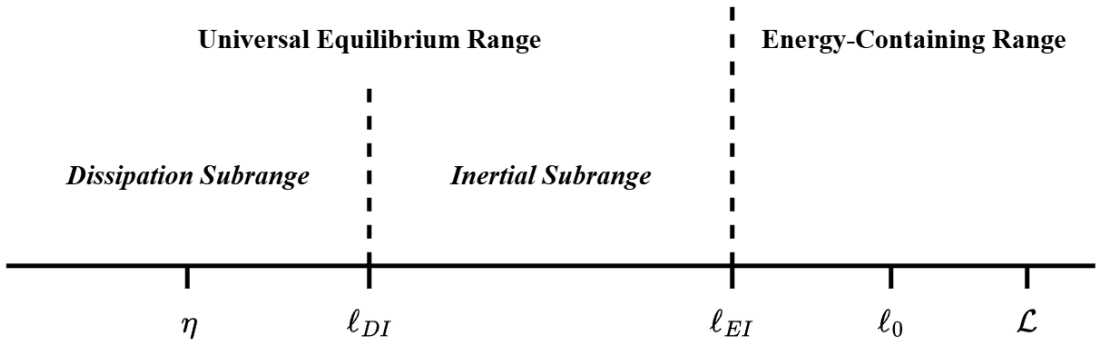

Figure 1.2. Energy cascade of the large to small-scale turbulent structures [19]

Using figure 1.2, turbulence can be understood as a cascade of energy through three distinct ranges: the energy-containing range ($\mathcal{L} > \ell > \ell_{EI}$), the inertial range ($\ell_{EI} > \ell > \ell_{DI}$) and the dissipation range ($\ell_{DI} > \ell > \eta$). In the energy-containing range, the largest eddies form under the influence of the system's geometry and boundary conditions. These structures are typically anisotropic and serve as the source of turbulent energy. As they break down into smaller scales, energy is transferred with minimal loss into the inertial range. Within the inertial range, turbulent motions become increasingly isotropic and universal, governed primarily by inertial interactions. In the inertial range, energy continues to cascade toward smaller scales, again with minimal dissipation. Finally, in the dissipation range, the smallest eddies are dominated by viscous forces. In this regime, kinetic energy is irreversibly converted into heat, marking the end of the energy cascade of the turbulent structures.

Understanding turbulent energy cascades is essential when analyzing the computational demands of numerical methods in fluid dynamics. In turbulent flows, energy is injected at large scales and transferred through a cascade of smaller eddies until it is dissipated as heat at the smallest scales. Accurately capturing this wide range of scales is computationally intensive, especially as the Reynolds number increases, as seen in equation 1.7. Since an increase in the Reynolds number leads to a decrease in the smallest turbulent scales and by consequence the distance between sampling points

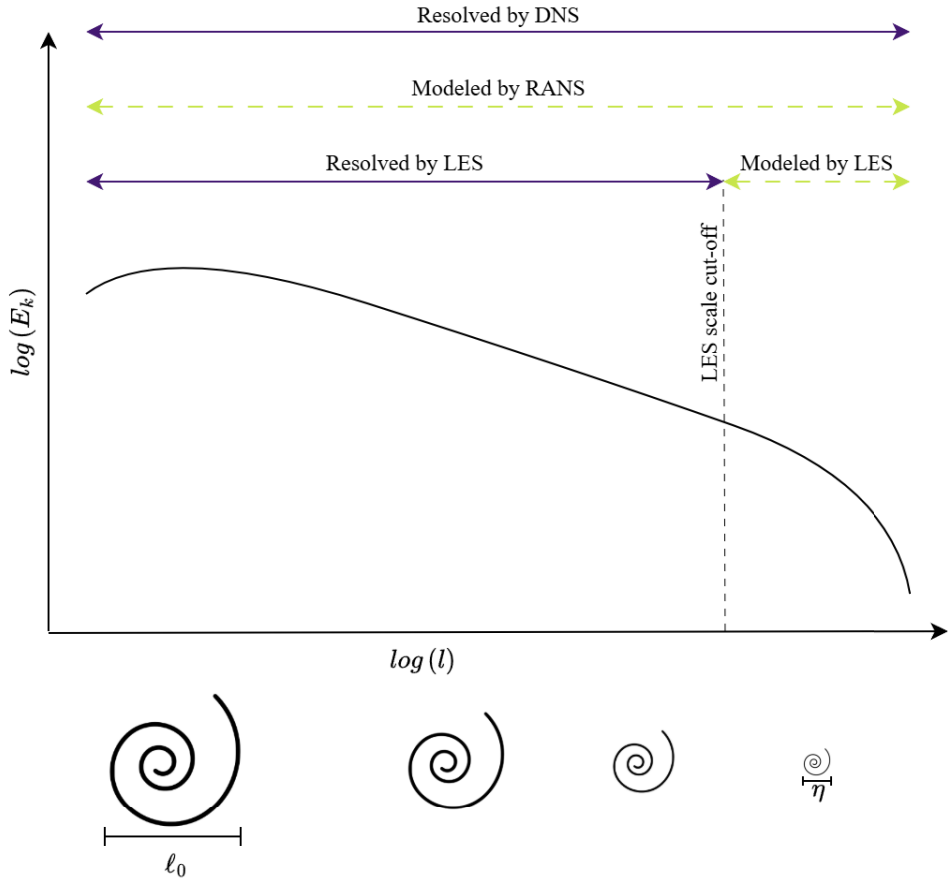

Figure 1.3. Numerical method handling of energy cascades [20, 21]

(Δx). This challenge directly influences the choice of numerical modeling approach, depicted in figure 1.3: DNS resolves all scales of turbulence, offering the highest fidelity at the cost of immense computational resources; Large Eddy Simulation (LES) resolves larger turbulent structures while modeling the smaller ones, reducing computational demands while retaining much of the flow's dynamic behavior; RANS models, the most computationally efficient, statistically represent all turbulent scales through averaged equations and turbulence models [1, 19]. Each method offers a trade-off between accuracy and computational cost, grounded in how they handle the turbulent energy cascade.

1.2.1 Direct Numerical Simulations (DNS)

DNS is the most accurate numerical technique available for simulating turbulent flows, as it fully resolves all relevant spatial and temporal scales of turbulence, down to the smallest dissipative Kolmogorov scales. DNS achieves this by solving the unsteady Navier–Stokes equations without any turbulence modeling or simplifications, provided it is given sufficient numerical resolution in both space and time. As a result, it provides highly detailed insights into the underlying physics of fluid flow [19].

However, the high fidelity of DNS comes with extraordinary computational costs. To accurately capture the entire range of turbulent scales, the computational mesh must be sufficiently fine, with grid spacing on the order of the Kolmogorov length scale. Additionally, time steps must be small enough to resolve the fastest temporal fluctuations. The number of grid points required grows rapidly with Reynolds number, approximately scaling with $Re^{9/4}$ in three-dimensional flows [1]. Therefore, DNS becomes impractical for high Reynolds number flows typical in industrial or aerospace applications.

Due to these limitations, DNS is primarily suited for low Reynolds number flows, canonical flow problems, or fundamental turbulence research, where detailed flow physics can be studied in simplified geometries under controlled conditions [1, 19, 22].

1.2.2 Reynolds Averaged Navier-Stokes (RANS)

The RANS approach is widely used in the aerospace industry due to its ability to provide sufficiently accurate estimates of key engineering performance indicators, such as lift and drag coefficients, at relatively low computational cost [18, 19]. This is achieved by applying averaging operations, such as Reynolds decomposition, which expresses any instantaneous flow property ($u(\vec{x}, t)$), into the sum of the mean and fluctuating components:

$$u(\vec{x}, t) = \overline{u(\vec{x})} + u(\vec{x}, t)', \tag{1.10}$$

where $\overline{u}$ represents the time-averaged term and u' represents the fluctuating term [18]. Through this decomposition, turbulent fluctuations are effectively smoothed out, and the flow equations are transformed into a form that describes the mean behavior of the flow. As a result, the system becomes

steady, and detailed information about the instantaneous dynamics of the turbulence is lost.

However, applying this time-averaging process to the Navier–Stokes equations introduces additional terms, most notably the Reynolds stress tensor, which arises from the averaging of the nonlinear convective terms. These new terms render the system of equations under-determined, as they introduce unknowns that cannot be computed without resolving the fluctuating components of the flow. To close the system, turbulence models are introduced to approximate the Reynolds stresses. A common approach involves invoking the Boussinesq hypothesis, which assumes that the Reynolds stresses are proportional to the mean rate of strain via an eddy viscosity [1, 18]. These models are typically calibrated for specific classes of flows using experimental or high-fidelity simulation data.

While RANS offers a computationally efficient means of simulating aerodynamic systems, it inherently limits the solution to a time-averaged, steady-state representation. The accuracy of this approach strongly depends on the suitability and calibration of the turbulence model for the specific flow conditions, particularly in regions where flow separation, transition, or unsteadiness play a significant role.

1.2.3 Large Eddy Simulation (LES)

LES serves as a middle ground between the high-fidelity but computationally expensive DNS and the more approximate yet efficient RANS approach. LES resolves the larger, energy-containing turbulent structures directly, while modeling only the smaller, more isotropic scales using a subgrid-scale (SGS) model. This makes LES particularly effective in capturing unsteady flow features that significantly influence overall flow behavior, such as vortex shedding, flow separation, and transitional phenomena [1].

LES solves the filtered, unsteady Navier–Stokes equations, where a spatial filtering operation removes the small-scale fluctuations below a certain cutoff defined by the grid size [19]. The resulting subgrid stress tensor, which accounts for the interaction between resolved and unresolved scales, must be modeled—most commonly using eddy-viscosity-based models such as the Smagorinsky model or dynamic SGS models.

Compared to DNS, LES reduces computational cost by avoiding the need to resolve the smallest turbulent scales. However, it still requires relatively fine meshes and small time steps, especially in

regions with high gradients or near solid boundaries. Wall-resolved LES, which attempts to resolve turbulence all the way to the wall, remains computationally expensive. In contrast, wall-modeled LES (WMLES) applies a turbulence model near walls to reduce grid requirements and is often used in practical engineering applications.

LES is well-suited for flows where large-scale unsteadiness plays a critical role and where higher accuracy is needed than what RANS can offer. It is commonly used in aeroacoustics, bluff-body flows, and combustion studies, where capturing the dynamics of large eddies is essential to predicting key performance or safety characteristics [19, 23].

1.3 Previous Works

In the field of aerospace engineering, traditional applications predominantly involve flows with a high Reynolds number. Given the computational efficiency and established reliability of RANS models under such conditions, it is unsurprising that a substantial body of knowledge has been developed for high-Reynolds number regimes. However, many aerodynamic behaviors commonly regarded as fundamental or invariant do not hold in low-Reynolds number flows. This section seeks to shed light on how key aerodynamic characteristics deviate in low-Reynolds-number regimes and to examine the limitations and breakdown of certain classical aerodynamic theorems under these conditions.

1.3.1 Low Reynolds Aerodynamic Characteristics

Traditionally, airfoil behavior is described by thin airfoil theory, which—despite its idealization of the airfoil as an infinitely thin plate—provides a foundational understanding of key aerodynamic principles. One such principle is the linear relationship between lift coefficient and angle of attack (AOA), which is generally valid in high-Reynolds-number flows. However, this linearity deteriorates in low-Reynolds-number regimes, where nonlinearity in the lift response, even at low AOAs, becomes apparent. This deviation is predominantly attributed to flow separation phenomena.

Ohtake et al. [24] identify the onset of flow separation along the upper surface—observed in experimental studies—as a primary contributor to the loss of linearity in lift with respect to angle

of attack. Similarly, researchers such as Winslow et al. [25] have employed RANS-based simulations to replicate this nonlinearity, consistently attributing it to flow separation effects. Although RANS models have demonstrated some success in capturing these trends, their typical steady-state formulation limits their ability to resolve the inherently unsteady dynamics of flow separation and transition. Furthermore, while experimental data provide valuable benchmarks, they often lack the spatial and temporal resolution needed to fully characterize complex flow structures. As such, the precise mechanisms within flow separation that contribute to lift nonlinearity may remain partially obscured—particularly those arising from the chaotic and transitional nature of low-Reynolds-number flows as they evolve toward turbulence.

In certain cases, the nonlinearity of lift in low-Reynolds-number flows extends to the generation of negative lift at low AOAs, as observed in the experimental work of Ohtake et al. [24]. This phenomenon was further investigated by Yonemoto et al. [26], who proposed that the negative lift arises due to flow separation progressing along the upper surface toward the trailing edge, accompanied by a localized flow reversal at the trailing edge. Such behavior reflects a breakdown of the Kutta condition at low Reynolds numbers, as evidenced by the establishment of a counter-circulatory flow around the sharp trailing edge.

The conditions under which negative lift may occur were expanded upon by Tank et al. [27], who suggested that airfoils with smooth surfaces and sufficient thickness are more prone to producing negative lift at small AOAs. Although Winslow et al. [25] successfully reproduced the nonlinear lift behavior observed experimentally, their computational results indicated the generation of a small positive lift under comparable conditions, deviating from the experimental findings. Consequently, Tank et al. [27] advised caution in interpreting their own results, citing significant discrepancies across studies, like those in Winslow et al. [25].

In 2020, Aguilar Cabello et al. [28] provided a physical interpretation of the negative lift mechanism, identifying a counter-clockwise recirculation zone at the trailing edge, and once again reproduced the phenomenon. However, their findings highlighted that a three-dimensional wing with an aspect ratio (AR) of at least 3 was necessary to observe the onset of negative lift. Notably, these investigations were conducted using RANS solvers, which, while useful, impose limitations when modeling the inherently unsteady and chaotic nature of transitional flows.

1.3.2 Structures in DNS

As demonstrated in previous studies, flow separation plays a critical role in determining the aerodynamic performance of a wing. While RANS models often struggle to capture unsteady separation dynamics, DNS offers a more accurate representation of separated flow regions. In the work of Bilbao-Ludena et al. [29], DNS was applied to a wing employing a NACA 0018 airfoil at a Reynolds number of $Re = 10,000$ and an angle of attack of 10°. Their results revealed flow separation initiating near the leading edge; however, the separation did not span the entire wing. Due to the influence of wingtip vortices, flow remained attached near the outboard regions, with the separated region being displaced inboard. Despite this delayed separation at the tips, a recirculation zone persisted near the trailing edge.

Although wingtip vortices may appear to promote flow attachment in localized areas, it is important to recognize that such vortices are also inherently associated with lift loss and increased induced drag. These side effects arise from the pressure equalization across the wing span, which governs the formation of wingtip vortices. While the primary focus of the study was to characterize the inception and evolution of five distinct vortical structures, it also highlighted an early onset of separation without subsequent reattachment in a low-Reynolds-number regime. Notably, the wingtip vortices appeared to suppress separation along the outboard sections, with only a small recirculation bubble forming near the trailing edge at the wingtip. However, it remains uncertain whether the benefits of delayed separation due to vortex-induced attachment outweigh the performance penalties introduced by induced drag and pressure equalization in the edge region.

1.3.3 Periodic Domains

As discussed in Section 1.1, low-Reynolds-number flows inherently involve low Mach numbers, introducing the condition of near-incompressibility to the governing equations. This presents additional challenges in the numerical solution of such flows. While the mathematical implications of incompressibility will be detailed in Chapter 2, the current study adopts the Entropically Damped Artificial Compressibility (EDAC) method as a means of addressing this challenge. The EDAC approach has demonstrated robust performance in simulating low-Reynolds-number flows, particularly

when integrated into high-order numerical frameworks.

In a 2023 study, Vermeire [30] proposed a high-order implicit Large Eddy Simulation (ILES) framework based on the EDAC formulation, combined with a FR method for spatial discretization. This coupling was shown to enhance numerical consistency and stability, particularly in the low-Mach-number regime. The use of EDAC within this high-order context allows for the simulation of incompressible and weakly compressible flows without the need for solving pressure Poisson equations, thereby improving computational efficiency while maintaining accuracy.

Vermeire [30] validated the approach using canonical benchmark cases such as the Taylor-Green vortex and turbulent channel flow, achieving results that closely aligned with DNS reference data. Additionally, the methodology was applied to the flow over a periodically bounded airfoil at low Reynolds numbers. The outcomes of this case study were consistent with available DNS data, demonstrating the capability of the EDAC-FR approach within an ILES framework. However, it is important to note that the simulations were limited to spanwise-periodic configurations, and no finite-span geometries were considered in the study.

1.4 Objectives

The present study seeks to extend the investigations discussed in Section 1.3 by employing the in-house High-Order Unstructured Solver (HORUS), developed by the Computational Aerodynamics Laboratory at Concordia University. Utilizing a FR approach, HORUS will be used to simulate the flow around a NACA 0018 airfoil at a Reynolds number of $Re = 10,000$. These simulations will be conducted across a range of wing spans—from 1 to 4 chord lengths—to systematically capture the influence of wingtip vortices on lift production, particularly their role in promoting flow attachment near the wing tips.

A key objective of this work is to explore the phenomenon of negative lift in a non-steady, turbulence-resolving context, offering an opportunity to more accurately characterize the complex, chaotic flow behaviors—such as unsteady separation and transition to turbulence—that are often oversimplified in traditional RANS models. By leveraging the high-fidelity, unsteady nature of the simulation framework, this study aims to provide enhanced insight into the mechanisms of flow

separation that contribute to lift nonlinearity in low-Reynolds-number regimes.

Beyond these specific goals, the study also aims to address broader knowledge gaps in low-Reynolds-number aerodynamics. Through detailed visualizations and analysis of transitional and turbulent structures, the work will contribute to a clearer understanding of how separation influences aerodynamic performance. Quantitative results will include distributions of lift, drag, pressure, and skin friction coefficients, as well as turbulent kinetic energy and Reynolds stress fields. These outputs will serve not only to elucidate flow physics but also to provide valuable benchmark data for the validation of emerging computational methods.

1.5 Outline

Chapter 1 presents a general introduction to the current study, outlining the motivation for investigating low-Reynolds-number flows in the context of emerging and innovative applications. It includes an overview of various methodologies employed in the simulation of turbulent flows, a review of pertinent literature to establish a foundation for understanding less conventional aerodynamic phenomena, and the objectives that have guided this work.

Chapter 2 derives the governing equations for this work, starting with the Navier-Stokes equations and following their derivation until it arrives to the EDAC equations.

Chapter 3 presents the FR approach, a spatial discretization scheme, and the Paired Explicit Runge-Kutta (P-ERK) scheme, temporal discretization scheme, which is used to advance the solution in time.

Chapter 4 determines appropriate polynomial level needed to properly resolve the flow in this work and provides validation for results obtained.

Chapter 5 presents the results and the observations of this work.

Chapter 6 summarizes conclusions and provides a framework for future works.

Chapter 2

Governing Equations

This chapter begins with the derivation of the compressible Navier–Stokes equations based on the fundamental conservation laws of mass, momentum, and energy. Following this, the inherent limitations of these equations—particularly in the context of low-Mach-number and nearly incompressible flows—are discussed. To address these challenges, various approaches for enforcing incompressibility are introduced, including the use of the pressure Poisson equation for strictly incompressible formulations, as well as the Artificial Compressibility Method (ACM). The chapter concludes with the formulation and discussion of the EDAC method, which forms the basis for the physical modeling in the present study.

2.1 General Form of the Conservation Law

The law of conservation asserts that, for any conserved variable, its quantity variation over time is governed by net change of the conserved variable passing through the volume's surface, a quantity known as flux [31]. By considering the finite control volume Ω, enclosed by the control surface S, the general conservation law can be expressed, in the integral form, as

$$\frac{\partial}{\partial t}\int_{\Omega} \vec{u}\ \mathrm{d}\Omega + \oint_{S} \overline{\overline{F}} \cdot \hat{n}\ \mathrm{d}S = 0, \tag{2.1}$$

where $\vec{u}$ represents the vector of conserved variables, $\overline{\overline{F}}$ is the flux tensor indicating the rate at which $\vec{u}$ is transported through the surface S and $\hat{n}$ denotes the unit outward normal vector on the surface.

By applying Gauss' divergence theorem, which converts a surface integral into a volume integral of the divergence of a vector field

$$\oint_S \overline{\overline{F}} \cdot \hat{n} \ \mathrm{d}S = \int_\Omega \vec{\nabla} \cdot \overline{\overline{F}} \ \mathrm{d}\Omega, \tag{2.2}$$

Equation 2.1 can be rewritten as

$$\frac{\partial}{\partial t} \int_\Omega \vec{u} + \int_\Omega \vec{\nabla} \cdot \overline{\overline{F}} \ \mathrm{d}\Omega = 0. \tag{2.3}$$

Since this equation must hold for any arbitrary control volume, the integrand itself must vanish, yielding the differential form of the conservation law

$$\frac{\partial \vec{u}}{\partial t} + \vec{\nabla} \cdot \overline{\overline{F}} = 0. \tag{2.4}$$

With the general form of the conservation law established and Gauss' theorem applied, the subsequent sections will define the specific conserved quantities—mass, momentum, and energy—and their corresponding fluxes.

2.1.1 The Mass Conservation Equation

The principle of mass conservation states that mass can neither be created nor destroyed within a fluid system [31]. In this context, the conserved variable $\vec{u}$ is the fluid density ρ (specific mass), expressed in $\mathrm{kg/m^3}$. Since mass is transported exclusively by convection and not by diffusion, the flux term consists solely of a convective component, given by $\vec{F_C} = \rho\vec{v}$, where $\vec{v}$ denotes the velocity vector.

Accordingly, in the absence of sources or sinks, the integral form of the mass conservation law is expressed as

$$\frac{\partial}{\partial t} \int_\Omega \rho \ \mathrm{d}\Omega + \oint_S \rho\vec{v} \cdot \hat{n} \ \mathrm{d}S = 0, \tag{2.5}$$

and by applying Gauss' divergence theorem (Equation 2.2), it transforms the surface integral into a volume integral, yielding the differential form

$$\frac{\partial \rho}{\partial t} + \vec{\nabla} \cdot (\rho \vec{v}) = 0. \tag{2.6}$$

This differential form of the mass conservation equation is commonly referred to as the *continuity equation* [31].

2.1.2 The Momentum Conservation Equation

Momentum is defined as the product of mass and velocity. Similar to the treatment in Section 2.1.1, momentum can be expressed in a per-unit-volume form. Thus, the conserved vector quantity $\vec{u}$ in this context is $\rho\vec{v}$. The corresponding convective flux tensor is given by

$$\overline{\overline{F_C}} = \rho \vec{v} \otimes \vec{v}, \tag{2.7}$$

and its contribution through the surface element $\mathrm{d}S$, is expressed as

$$\overline{\overline{F_C}} \cdot \mathrm{d}S = \rho \vec{v} \left(\vec{v} \cdot \mathrm{d}S \right). \tag{2.8}$$

While mass conservation inherently implies no change in mass within a closed system, momentum conservation is governed by Newton's Second Law, which states that the time rate of change of momentum is equal to the sum of the forces acting on the control volume. These forces can be classified as internal or external [31]. In the current context, only internal forces—represented by the stress tensor—are considered.

The internal stress tensor $\overline{\overline{\sigma}}$, consists of isotropic and deviatoric components, defined as

$$\overline{\overline{\sigma}} = -p\mathbf{I} + \overline{\overline{\tau}}. \tag{2.9}$$

where p is the pressure, $\mathbf{I}$ represents the identity matrix and $\overline{\overline{\tau}}$, the viscous shear stress tensor. The

viscous shear stress tensor is defined as

$$\overline{\overline{\tau}} = \mu \left(\nabla \vec{v} + (\nabla \vec{v})^T \right) - \frac{2}{3} \mu \left(\nabla \cdot \vec{v} \right), \tag{2.10}$$

or in index notation

$$\tau_{ij} = \mu \left[\left(\frac{\partial u_j}{\partial x_i} + \frac{\partial u_i}{\partial x_j} \right) - \frac{2}{3} \mu \left(\nabla \cdot \vec{v} \right) \delta_{ij} \right]. \tag{2.11}$$

where μ is the dynamic viscosity and δ_{ij} denotes the Kronecker delta.

The net force acting on the control volume is thus composed of inviscid (pressure) and viscous components:

$$\sum \vec{F} = \vec{F}_{inv} + \vec{F}_v = \oint_S -p\hat{n} \ \mathrm{d}S + \oint_S \tau \cdot \hat{n} \ \mathrm{d}S, \tag{2.12}$$

Accordingly, the integral form of the momentum conservation equation becomes:

$$\frac{\partial}{\partial t} \int_\Omega \rho \vec{v} \ \mathrm{d}\Omega + \oint_S \rho \vec{v} \otimes \vec{v} \cdot \hat{n} \ \mathrm{d}S = \oint_S -p \cdot \hat{n} \ \mathrm{d}S + \oint_S \tau \cdot \hat{n} \ \mathrm{d}S, \tag{2.13}$$

which, by applying Gauss' divergence theorem, transforms into the differential form:

$$\frac{\partial \rho \vec{v}}{\partial t} + \rho \left(\vec{v} \cdot \vec{\nabla} \right) \vec{v} = -\vec{\nabla} p + \vec{\nabla} \cdot \overline{\overline{\tau}}. \tag{2.14}$$

This equation represents the momentum conservation law in its differential form, accounting for both inertial and viscous effects in a compressible fluid, referred to as the *Navier-Stokes equations of motion* [31].

2.1.3 The Energy Conservation Equation

While the mass conservation equation is derived from the principle of zero net mass change and the momentum conservation equation stems from Newton's Second Law, the energy conservation equation is based on the First Law of Thermodynamics [32]. This law states that the time rate of change of the internal energy within a closed system must equal the sum of the heat added to the system and the work done on the system [31]. Mathematically, the First Law of Thermodynamics is

expressed as

$$\frac{\mathrm{d}E}{\mathrm{d}t} = \dot{Q} + \dot{W}, \tag{2.15}$$

where E is the total energy of the system, including both internal energy e and kinetic energy $\vec{v}^2/2$. The terms $\dot{Q}$ and $\dot{W}$ represent the rates of heat transfer and work done, respectively.

In accordance with the formulations used for mass and momentum conservation, the conserved variable $\vec{u}$ for energy is the total energy per unit volume, ρE. The corresponding convective flux is given by

$$\vec{F}_C = \rho \vec{v} E. \tag{2.16}$$

Unlike mass, energy can also be transported by diffusion, specifically through heat conduction. This diffusive flux is described by Fourier's law

$$\vec{F}_D = \vec{q} = -k\vec{\nabla}T, \tag{2.17}$$

where k is the thermal conductivity and T is the temperature. The rate of heat transfer into the system can then be expressed as

$$\dot{Q} = -\oint_S \vec{q} \cdot \hat{n} \ \mathrm{d}S = \oint_S k\vec{\nabla}T \cdot \hat{n} \ \mathrm{d}S. \tag{2.18}$$

The sign convention used here considers heat entering the system from the surroundings as positive.

As discussed in Section 2.1.2, body forces are neglected in this context. Thus, the work done on the system arises solely from surface forces—namely pressure and viscous shear stresses. These contributions are expressed as

$$\dot{W} = \dot{W}_p + \dot{W}_v = \oint_S p\,(\vec{v} \cdot \hat{n}) \ \ \mathrm{d}S - \oint_S (\tau \cdot \vec{v}) \cdot \hat{n} \ \ \mathrm{d}S, \tag{2.19}$$

The integral form is written as

$$\frac{\partial}{\partial t}\int_\Omega \rho E \ \ \mathrm{d}\Omega + \oint_S \rho E\,(\vec{v} \cdot \hat{n}) \ \ \mathrm{d}S = \oint_S k\vec{\nabla}T \cdot \hat{n} \ \ \mathrm{d}S + \oint_S p\,(\vec{v} \cdot \hat{n}) \ \ \mathrm{d}S - \oint_S (\tau \cdot \vec{v}) \cdot \hat{n} \ \ \mathrm{d}S, \tag{2.20}$$

which, by applying Gauss' divergence theorem (Equation 2.2), transforms the integral form into the

differential form

$$\frac{\partial \rho E}{\partial t} + \rho E \left(\vec{\nabla} \cdot \vec{v} \right) = \vec{\nabla} \cdot \left(k \vec{\nabla} T \right) + p \left(\vec{\nabla} \cdot \vec{v} \right) - \vec{\nabla} \cdot \left(\overline{\overline{\tau}} \cdot \vec{v} \right). \tag{2.21}$$

This is the differential form of the energy conservation law, incorporating both convective and diffusive heat transfer as well as the mechanical work due to pressure and viscous effects in a compressible fluid.

2.2 Compressible Navier-Stokes Equations

In Section 2.1 the conservation laws were applied to the three primary conserved quantities that govern the behavior of a fluid system: mass, momentum, and energy [18, 31, 32]. These laws describe how key flow properties—such as density, velocity, pressure, and temperature—evolve in time and space. When applied to a viscous compressible fluid, the resulting set of equations is known as the Navier-Stokes equations.

Using the previously derived formulations, the compact vector form of the compressible Navier-Stokes equations can be written as

$$\frac{\partial \vec{u}}{\partial t} + \nabla \cdot \left(\vec{F}_{inv}(\vec{u}) - \vec{F}_v(\vec{u}, \nabla \vec{u}) \right) = 0, \tag{2.22}$$

where $\vec{w}$ is the vector of conserved variables, and $\vec{F}_{inv}$ and $\vec{F}_v$ represent the inviscid and viscous flux vectors, respectively.

The vector of conserved variables is

$$\vec{u} = \begin{bmatrix} \rho & \rho \vec{v} & \rho E \end{bmatrix}^T. \tag{2.23}$$

The corresponding inviscid flux vector is

$$\vec{F}_{inv} = \begin{bmatrix} \rho \vec{v} & \rho \vec{v} \otimes \vec{v} + p\mathbf{I} & (\rho E + p)\vec{v} \end{bmatrix}^T. \tag{2.24}$$

The viscous flux vector is

$$\vec{F}_v = \begin{bmatrix} 0 & \overline{\overline{\tau}} & \left(\overline{\overline{\tau}} \cdot \vec{v}\right) - k\nabla T \end{bmatrix}^T. \tag{2.25}$$

For a three-dimensional Cartesian coordinate system, the equations can be explicitly expanded as

$$\vec{u} = \begin{bmatrix} \rho \\ \rho u \\ \rho v \\ \rho w \\ \rho E \end{bmatrix}, \quad \vec{F}_{inv} = \begin{bmatrix} \rho v_i \\ \rho u v_i + p\delta_{ix} \\ \rho v v_i + p\delta_{iy} \\ \rho w v_i + p\delta_{iz} \\ v_i(\rho E + p) \end{bmatrix}, \quad \vec{F}_v = \begin{bmatrix} 0 \\ \tau_{ix} \\ \tau_{iy} \\ \tau_{iz} \\ u\tau_{ix} + v\tau_{iy} + w\tau_{iz} - k\frac{\partial T}{\partial x_i} \end{bmatrix}, \tag{2.26}$$

where v_i represents the velocity component in the i^{th} direction (with $i = x, y, z$), and δ_{ij} is the Kronecker delta, which serves to isolate the pressure term in the corresponding momentum equation direction. Since the fluxes are directional, the inviscid and viscous flux vectors in the x-direction, as an example become

$$\vec{F}_{inv_x} = \begin{bmatrix} \rho u \\ \rho u^2 + p \\ \rho u v \\ \rho u w \\ u(\rho E + p) \end{bmatrix}, \quad \vec{F}_{v_x} = \begin{bmatrix} 0 \\ \tau_{xx} \\ \tau_{xy} \\ \tau_{xz} \\ u\tau_{xx} + v\tau_{xy} + w\tau_{xz} - k\frac{\partial T}{\partial x} \end{bmatrix}. \tag{2.27}$$

While the compressible Navier-Stokes equations provide a comprehensive framework for describing fluid flow across all regimes, they exhibit significant challenges as the Mach number approaches zero and becomes incompressible. The Mach number is defined as

$$Ma = \frac{v}{c}, \tag{2.28}$$

where v is the local flow velocity and c_s is the speed of sound of the fluid in the described system.

In low Mach number flows, the time scales governing pressure and density become decoupled. Pressure evolves on the acoustic time scale, given by $t_a = L/c$, while density evolves on the

convective time scale, $t_c = L/v$, where L is a characteristic length scale [33]. Using Equation 2.28, it is evident that as the Mach number tends toward zero, the acoustic time scale becomes much smaller than the convective time scale. As a result, acoustic waves propagate significantly faster than the fluid motion, introducing a stiff system of equations. This stiffness necessitates extremely small time steps to resolve acoustic dynamics accurately, rendering simulations computationally expensive and inefficient [34].

Although preconditioning techniques can be employed to accelerate convergence in this regime, the process often remains prohibitively expensive [35, 36, 37, 38]. To address this, alternate approaches exist that adapt the compressible Navier-Stokes equations to operate more effectively in the incompressible regime. One such method involves enforcing strict incompressibility within the governing equations.

2.3 Incompressible Navier-Stokes Equations

Compressibility is inherently linked to variations in density, as is is the process by which a fluid changes its volume while maintaining a fixed mass. By enforcing incompressibility, the fluid density is held constant, and thus its time rate of change becomes zero [1, 31]. When this condition is applied to the mass conservation equation (Equation 2.6), a new constraint is developed

$$\vec{\nabla} \cdot \vec{v} = 0. \tag{2.29}$$

This condition, stating that the divergence of the velocity field is zero, implies there is no local volumetric expansion or compression within the flow—therefore defining an incompressible system.

With this constraint, both the momentum and energy equations can be simplified.

In the case of the energy equation, enforcing incompressibility effectively decouples it from the mass and momentum equations, as described in Section 2.2, particularly when the system is also isothermal [31]. In an isothermal system, the temperature remains constant, and thus

$$\nabla T = 0. \tag{2.30}$$

Applying both constraints (incompressibility and isothermal conditions) to the energy conservation equation 2.21 significantly simplifies it to

$$\frac{\partial \rho E}{\partial t} = 0. \tag{2.31}$$

In this form, the energy equation becomes trivially satisfied or no longer dynamically relevant to the system.

With the energy equation decoupled and the mass conservation equation reduced to a constraint, the primary governing equation for an incompressible flow becomes the momentum conservation equation. By dividing the momentum equation by the fluid density and applying the incompressibility condition from equation 2.29, the equation simplifies to the incompressible Navier-Stokes form

$$\frac{\partial \vec{v}}{\partial t} + (\vec{v} \cdot \nabla)\, \vec{v} = -\frac{1}{\rho} \nabla p + \nu \nabla^2 \vec{v}, \tag{2.32}$$

where ν is the kinematic viscosity of the fluid. It is important to note that while the mass conservation equation reduces to $\vec{\nabla} \cdot \vec{v} = 0$ in incompressible flows, $(\vec{v} \cdot \nabla)\, \vec{v} = \vec{v} \cdot (\nabla \vec{v}) \neq 0$. This term instead represents the convective derivative, not the divergence of velocity, and captures the nonlinear advection of momentum within the flow [1, 31].

2.3.1 Pressure Poisson Equation

The first method that aims to employ the incompressible Navier-Stokes equations is the Pressure Poisson Equation (PPE). By taking the divergence of Equation 2.32, the following expression is obtained

$$\frac{1}{\rho} \nabla^2 p = -\nabla \cdot (\vec{v} \cdot \nabla)\, \vec{v}, \tag{2.33}$$

which provides a relation that governs the pressure field corresponding to a given velocity field.

This formulation of the incompressible Navier-Stokes equations successfully eliminates the stiffness associated with acoustic waves in the compressible regime. However, it introduces a new challenge: implicit global coupling of the system. Since Equation 2.33 is an elliptic partial differential equation, the pressure at every point in the domain depends on the values at all other points. This

global interdependence requires solving a global linear system at every time step, introducing the need for an additional solver [34].

While the motivation for using incompressible formulations is to reduce computational cost in low Mach number regimes, the PPE introduces complexities that can still be computationally expensive. Although efficient Poisson solvers exist for low-order schemes [39, 40, 41, 42], this study aims to use a high-order numerical method, where computational efficiency is paramount.

Recent work by Fortunato and Townsend [43] have made significant progress toward scalable solvers for high-order discretizations, but the inherent global nature of the PPE still makes it less suited to parallelized, explicit, and locally-solvable methods. For these reasons, alternative approaches to incompressible flow modeling are worth exploring.

2.3.2 The Artificial Compressibility Method

While Poisson's approach enforces incompressibility strictly, Chorin [44] proposed an alternative: that incompressibility could be achieved artificially. This approach led to the ACM, which approximates incompressible flow by approaching the limit of compressibility—rather than working directly in the incompressible regime. Methods built on this idea are called pseudo-compressible methods.

Chorin's [44] insight was to replace the elliptic pressure solution with a hyperbolic formulation, thereby avoiding the global coupling introduced by the PPE. To do so, he assumed the flow is isentropic, meaning there is no variation in entropy. Under this assumption, the mass conservation equation can be reformulated as

$$\frac{\partial p}{\partial t} + \zeta \nabla \cdot \vec{v} = 0, \tag{2.34}$$

where $\zeta = 1/M^2$ is the artificial compressibility factor, and M is the artificial Mach number, independent of the true Mach number. This equation introduces an artificial time scale for pressure evolution that balances with the divergence of velocity.

By setting the artificial Mach number sufficiently low, the method enforces a nearly constant pressure, thereby recovering the divergence-free condition seen in Equation 2.29 and mimicking a truly incompressible fluid. The degree of incompressibility can be tuned by adjusting the artificial

Mach number, making the method flexible and controllable.

To enforce incompressibility at each time step, ACM introduces a pseudo-time stepping process. The governing equations are marched in a pseudo-time variable τ_p until convergence is reached, ensuring that the system satisfies the incompressible condition before advancing the physical time step. This makes ACM particularly well-suited for steady-state simulations, where accurate time evolution is not required.

The conservative form of the artificial compressibility formulation is given by

$$\frac{\partial \vec{u}}{\partial t} + \frac{\partial \vec{u}_p}{\partial \tau_p} + \nabla \cdot \vec{F} = 0, \tag{2.35}$$

where $\vec{u}$ is the vector of conserved variables

$$\vec{u} = \begin{bmatrix} 0 \\ v_i \end{bmatrix}, \tag{2.36}$$

and $\vec{u}_p$ is the pseudo-time vector of conserved variables

$$\vec{u}_p = \begin{bmatrix} p \\ v_i \end{bmatrix}. \tag{2.37}$$

$\vec{F}$ is the total flux, which encapsulates inviscid Euler fluxes $\vec{F}_e$

$$\vec{F}_{e,j}(\vec{v}) = \begin{bmatrix} \zeta v_j \\ v_i v_j + \delta_{ij} p \end{bmatrix}, \tag{2.38}$$

and the viscous Navier–Stokes fluxes $\vec{F}_v$

$$\vec{F}_{v,j}(\vec{v}, \nabla \vec{v}) = -\nu \begin{bmatrix} 0 \\ \frac{\partial v_i}{\partial x_j} \end{bmatrix}. \tag{2.39}$$

Since the artificial compressibility method is entirely local, it is compatible with the same solvers

developed for the compressible Navier–Stokes equations. This compatibility makes ACM an appealing choice, as its implementation often requires minimal modifications to existing solver frameworks. However, despite avoiding the globally coupled pressure solve required by the PPE, ACM introduces a pseudo-time dimension and necessitates inner iterations to enforce incompressibility. These iterations, although local, add computational overhead and increase the time needed to resolve each physical time step.

As a result, while ACM is indeed more suited to explicit, local, and parallelized solvers, making it a computationally attractive alternative for high-order methods, it still falls short in terms of the critical efficiency needed for simulations over large domains. The added cost of pseudo-time convergence limits its scalability, particularly in unsteady flow problems or expansive grids, where performance must be optimized at every level.

2.3.3 The Entropically Damped Artificial Compressibility Method

Building on the concept of artificial incompressibility introduced by the ACM, Clausen [33] proposed a more efficient alternative: the EDAC method. While ACM achieves incompressibility by assuming an isentropic flow—ideal for capturing rapidly propagating acoustic waves—this assumption becomes less effective for slower wave phenomena, such as viscous effects. Recognizing this limitation, Clausen [33] proposed a strategy that actively damps density fluctuations, rather than passively constraining them through isentropic assumptions.

This damping is achieved by introducing controlled entropy generation into the system, which dissipates acoustic modes and thereby stabilizes the flow field. EDAC leverages thermodynamic relationships between pressure, temperature, and density—targeting the pressure fluctuations as a way to indirectly regulate density. This marks a conceptual inversion of the ACM: instead of enforcing isentropy, EDAC introduces entropy to stabilize the solution.

The evolution of pressure under the EDAC formulation is governed by the following equation:

$$\frac{\partial p}{\partial t} + \vec{v} \cdot \nabla p + \frac{1}{M^2} \nabla \cdot \vec{v} = \frac{1}{Re} \nabla^2 p. \tag{2.40}$$

Applying the incompressibility condition from equation 2.29, the expression simplifies to

$$\frac{\partial p}{\partial t} + \vec{v} \cdot \nabla p = \frac{1}{Re} \nabla^2 p. \tag{2.41}$$

This equation is then coupled with the incompressible Navier–Stokes momentum equations to form a complete system. Trojak et al. [34] present the system in a flux-conservative form

$$\frac{\partial \vec{u}}{\partial t} + \nabla \cdot \vec{F} = 0, \tag{2.42}$$

where $\vec{u}$ is the vector of conserved variables

$$\vec{u} = \begin{bmatrix} p \\ v_i \end{bmatrix}, \tag{2.43}$$

where $\vec{F}$ is the total flux, which encapsulates inviscid Euler fluxes $\vec{F}_e$

$$\vec{F}_{e,j}(\vec{v}) = \begin{bmatrix} v_j(p + \zeta) \\ v_i v_j + \delta_{ij} p \end{bmatrix}, \tag{2.44}$$

and the viscous Navier–Stokes fluxes $\vec{F}_v$

$$\vec{F}_{v,j}(\vec{v}, \nabla \vec{v}) = -\nu \begin{bmatrix} \frac{\partial p}{\partial x_j} \\ \frac{\partial v_i}{\partial x_j} \end{bmatrix}. \tag{2.45}$$

This formulation of artificial compressibility avoids the use of elliptic partial differential equations that globally couple the system, as seen in the PPE, and also eliminates the need for a pseudo-time dimension, as required by the ACM. As such, the EDAC method emerges as the most computationally efficient approach among the methods presented. Furthermore, the EDAC method has demonstrated reliable accuracy in low Reynolds number regimes [33, 34, 30]. In these conditions, it effectively suppresses acoustic oscillations, whereas the ACM tends to permit the propagation of such waves—resulting in errors in both pressure and velocity divergence.

The EDAC method has also proven effective when combined with the FR method [30, 34, 45],

which will be introduced in Chapter 3. While it offers the best balance of accuracy and efficiency, its performance depends critically on the careful selection of the artificial compressibility factor. If the factor is set too low, the accuracy of the solution degrades; if it is set too high, the method's computational efficiency diminishes [34].

Given these advantages—computational efficiency, accuracy in low Reynolds number flows, and compatibility with high-order FR schemes—the EDAC method will serve as the governing formulation for the simulations conducted in this study.

Chapter 3

Numerical Methods

In Chapter 2, the governing equations of the system were introduced. However, in order to accurately simulate the case at hand, appropriate numerical methods are required for both the spatial and temporal discretization of these equations. This chapter presents the schemes used for the implementation of the governing equations: FR for spatial discretization and P-ERK methods for temporal discretization. To introduce the spatial discretization, a simplified one-dimensional system is first considered [46] before extending the formulation to multiple dimensions [47, 48].

3.1 Flux Reconstruction Approach to Spatial Discretization

The FR approach was developed by Huynh [46], who introduced the method as a high-order accurate technique for spatially discretizing general conservation laws using polynomial approximations. The FR method replicates the capabilities of other high-order schemes, such as Discontinuous Galerkin (DG), Spectral Volume (SV), Spectral Difference (SD), and Staggered Grid (SG) methods, by employing correction functions that enforce continuity at element interfaces, thereby enabling the solution of conservation laws in their differential form.

3.1.1 One Dimensional Application of Flux Reconstruction

As stated previously, to introduce the FR method, it is beneficial to first consider a one-dimensional linear advection system, governed by the conservation law in differential form

$$\frac{\partial u}{\partial t} + \frac{\partial f}{\partial x} = 0, \tag{3.1}$$

where $u = u(x,t)$ represents the conserved variable, and $f = f(u)$ is the corresponding flux. For linear advection, the flux can be expressed as $f = \alpha u$, where α is a constant advection speed.

The spatial domain Ω is partitioned into a set of N_e non-overlapping elements Ω_i [49]. Within each element, the solution is approximated using N_p solution points, and each element is bounded by local coordinates x_L^i and x_R^i, defining the element limits. Figure 3.1 illustrates this domain decomposition, highlighting the central element Ω_i and the location of its solution points, along with the adjacent upwind element Ω_{i-1} and downwind element Ω_{i+1}.

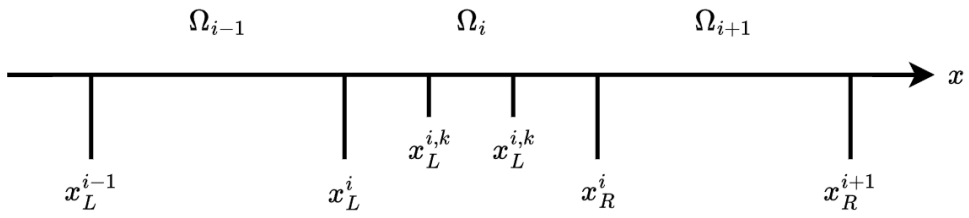

Figure 3.1. Domain division in the FR method [21].

The FR method, being fundamentally a high-order Finite Element Method (FEM), involves mapping each physical element in the domain Ω to a standard reference element $\xi \in [-1, 1]$, thereby normalizing the element size. This transformation is performed within a reference domain Ω', facilitating a uniform formulation of the numerical scheme across all elements. To map the global elements to the reference space and vice versa, a linear transformation function is typically employed

$$\xi(x) = \frac{2}{h_e}\left(x - \frac{x_L + x_R}{2}\right), \tag{3.2}$$

$$x(\xi) = \frac{1}{2}\left(x_L + x_R + h_e\xi\right), \tag{3.3}$$

where h_e is the width of an element. This mapping ensures that computations performed in the reference space can be accurately translated to the physical domain and allows the numerical method to be applied uniformly across all elements. To support differentiation and integration across domains, the Jacobian of the transformation and its inverse are given by

$$\frac{\mathrm{d}\xi}{\mathrm{d}x} = \frac{2}{h_e}, \tag{3.4}$$

$$\frac{\mathrm{d}x}{\mathrm{d}\xi} = \frac{h_e}{2}. \tag{3.5}$$

These metrics are essential for converting derivatives and integrals between the physical and reference frames, preserving accuracy and consistency throughout the domain.

The solution for the conserved variable over the domain can be approximated through a direct sum of the solutions on each element, expressed as

$$u(x,t) \approx u^h(x,t) = \bigoplus_{i=1}^{N_e} u_i^h(x,t), \tag{3.6}$$

where $u^h(x,t)$ denotes the global piecewise-continuous approximation of the conserved variable, and $u_i^h(x,t)$ represents the local solution on the i^{th} element. The accuracy of this local approximation depends on the number of solution points N_p, which defines the polynomial degree of the solution as $p_s = N_p - 1$.

Within each element, the continuous solution is expressed using a nodal polynomial basis ϕ, defined in both the reference space and, via mapping, the physical space [50]

$$u_i^h(\xi,t) = \sum_{k=1}^{N_p} u(\xi_{i,k},t)\phi_k(\xi) \tag{3.7}$$

$$u_i^h(x,t) = \sum_{k=1}^{N_p} u(x_{i,k},t)\phi_{i,k}(x) \tag{3.8}$$

These nodal basis functions are constructed using Lagrange polynomials, where ϕ_k denotes the k^{th} Lagrange basis function. These are first defined in the reference space and then mapped to the

physical space. The general form of the Lagrange basis functions is given by

$$\phi_k(\xi) = \prod_{s=1, s\neq k}^{N_p} \frac{\xi - \xi_s}{\xi_k - \xi_s} \tag{3.9}$$

$$\phi_{i,k}(x) = \prod_{s=1, s\neq k}^{N_p} \frac{x - x_{i,s}}{x_{i,k} - x_{i,s}} \tag{3.10}$$

where ξ_s, ξ_k, $x_{i,s}$ and $x_{i,k}$ are nodal locations in the reference and physical domains, respectively.

As previously discussed, the mapping of physical elements to a standardized reference domain ensures uniform element width throughout the mesh. This allows the nodal basis functions to be computed once in the reference space for a given polynomial degree and then reused across all elements by mapping them back to the physical space. Figure 3.2 illustrates the resulting nodal basis functions constructed using Gauss quadrature nodes for polynomial degrees $p_s = 0 \rightarrow 5$.

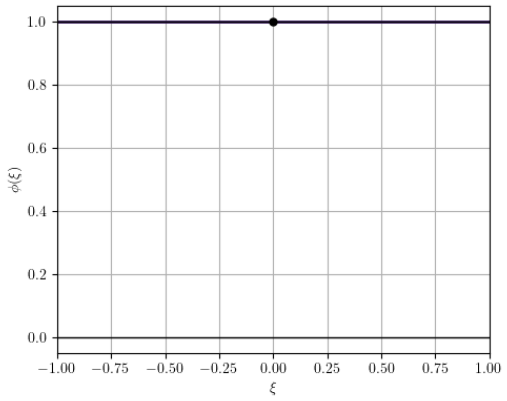

(a) $p_s = 0$

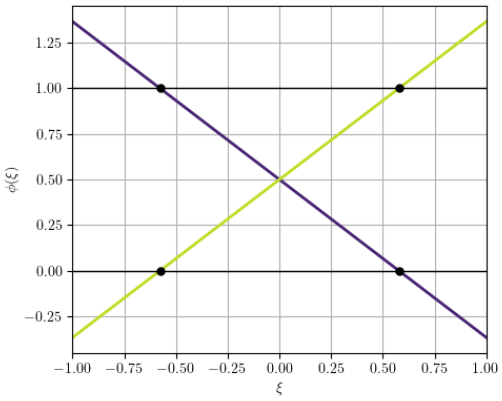

(b) $p_s = 1$

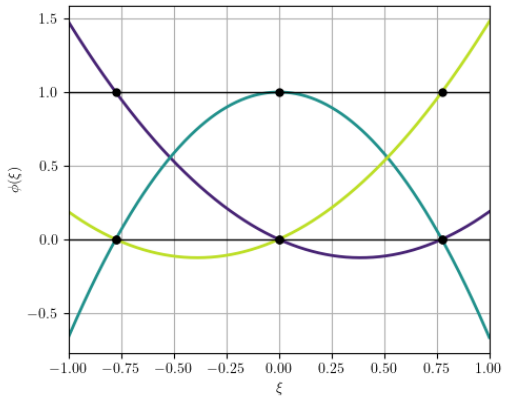

(c) $p_s = 2$

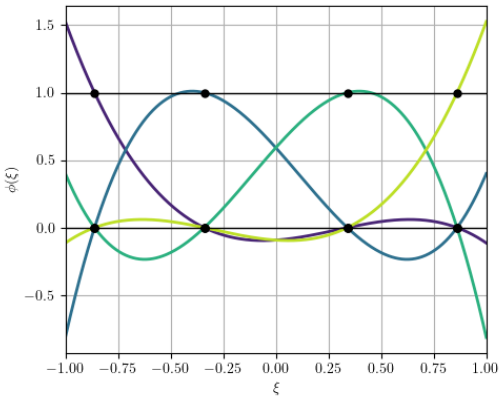

(d) $p_s = 3$

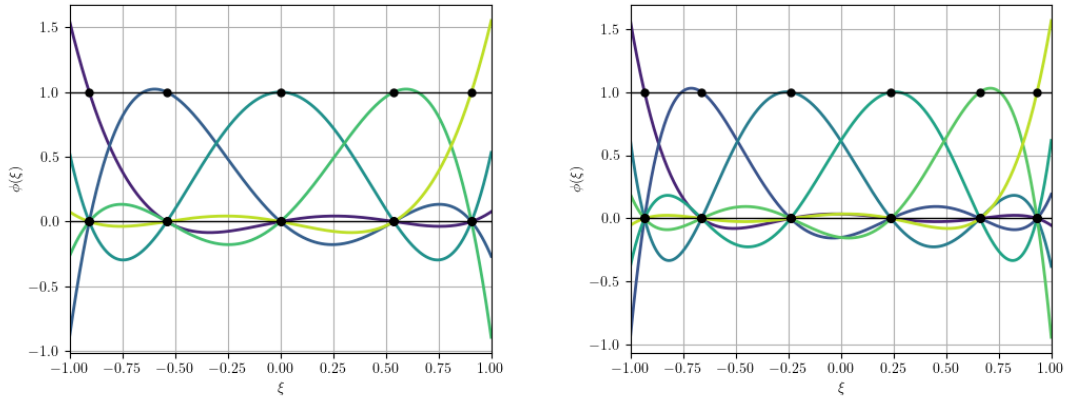

(e) $p_s = 4$ (f) $p_s = 5$

Figure 3.2. Nodal basis functions using Gauss quadrature points.

Just like for the conserved variable, the flux polynomial can also be represented in both the reference and global spaces, through the use of the nodal basis functions

$$f_i^h(\xi, t) = \sum_{k=1}^{N_p} f(\xi_{i,k}, t)\phi_k(x), \tag{3.11}$$

$$f_i^h(x, t) = \sum_{k=1}^{N_p} f(x_{i,k}, t)\phi_{i,k}(x). \tag{3.12}$$

Since each element in the FR method is treated independently, continuity of the solution is not inherently guaranteed at element interfaces. While the conserved variable is represented as a piecewise-continuous function, the flux—which depends on both the variable and its spatial derivatives—is generally discontinuous across element boundaries. This discontinuity becomes problematic, as the flux must be spatially differentiated, and discontinuities at the interfaces can lead to numerical inaccuracies and instabilities due to a lack of inter-element communication [46].

To address this issue, the FR method reconstructs the flux across each element such that it is continuous at the interfaces, as seen in Figure 3.3. This reconstructed, or corrected, flux ensures that the global approximation respects the continuity required for stable and accurate spatial differentiation. Furthermore, in order to preserve consistency between the flux and the conserved quantity, it is essential that both are represented by polynomials of compatible degrees.

In the case of the linear advection equation (Equation 3.1), only the flux term is spatially

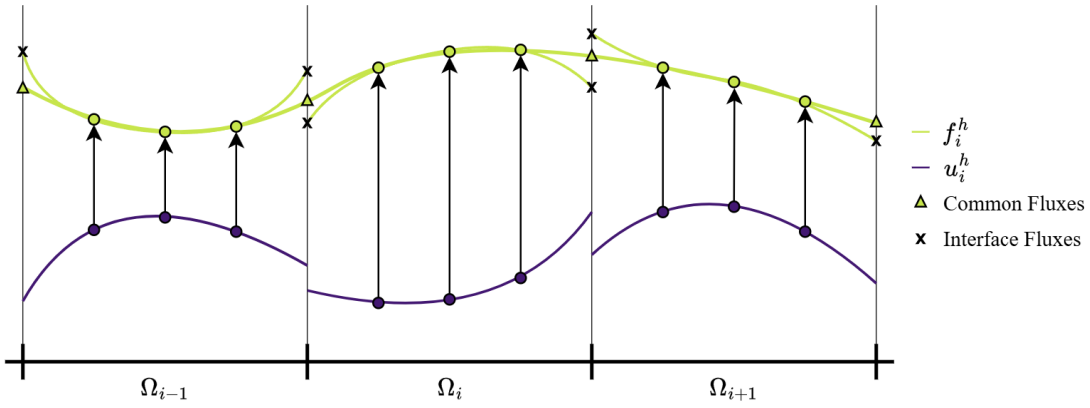

Figure 3.3. Continuous representation of the discontinuous flux across element interfaces [21].

differentiated, which means that an uncorrected polynomial approximation of the flux will be of degree $p_s - 1$. To maintain the formal order of accuracy of the solution, the corrected flux must therefore be constructed using a polynomial of degree $p_s + 1$.

To achieve both continuity and consistency, the FR method introduces a correction to the elemental flux approximation

$$f_i^c = f_i + \delta_i \tag{3.13}$$

where f_i^c is the corrected, continuous flux on element i, f_i is the local polynomial flux approximation, and δ_i is the correction term designed to enforce continuity across element interfaces. The correction term is constructed using correction functions $g_L(\xi)$ and $g_R(\xi)$, which are defined on the reference element for the left and right boundaries, respectively

$$\delta_i = \left[f_{i,L}^* - f_i(-1)\right] g_L(\xi) + \left[f_{i,R}^* - f_i(1)\right] g_R(\xi). \tag{3.14}$$

Here, $f_{i,L}^*$ and $f_{i,R}^*$ denote the common fluxes computed at the left and right interfaces of element i. These common fluxes are obtained via a Riemann solver, which combines information from adjacent elements to produce a physically consistent and stable approximation at the interface.

The choice of Riemann solver influences the numerical properties of the scheme. For instance, the upwind solver—where the flux is biased in the direction of wave propagation—tends to introduce dissipative errors, which enhance numerical stability but may dampen physical features. In contrast, the central solver, which averages left and right fluxes, leads to dispersive errors, preserving oscillatory

features but possibly causing nonphysical artifacts.

To balance these effects, blended Riemann solvers are often employed, combining dissipative and dispersive behaviors to optimize accuracy and stability. In the present work, separate Riemann solvers are employed for the inviscid and viscous fluxes, consistent with the Navier-Stokes equations introduced in Chapter 2. The Rusanov Riemann solver is used for the inviscid (Euler) fluxes due to its robustness and built-in dissipation [34, 30], while the second Bassi–Rebay (BR2) scheme is adopted for handling the viscous fluxes [51, 30].

The correction functions must satisfy the following boundary conditions in the reference space [50]

$$g_L(-1) = 1, \;\; g_L(1) = 0, \;\; g_R(-1) = 0, \;\; g_R(1) = 1,$$

and must be of degree $p_s + 1$ consistent with the flux polynomial, as they will ultimately be differentiated to a degree of p_s. The choice of correction function influences the spatial discretization scheme recovered by the FR method. Different high-order schemes—such as the DG, SV, SD, and SG methods—correspond to unique sets of correction functions. In this work, the FR approach employs correction functions that recover the DG method.

This is achieved through the use of Radau polynomials in constructing the correction functions. Specifically, the left and right correction functions are defined as

$$g_L(\xi) = R_{R,P+1}(\xi) + \frac{(-1)^{P+1}}{2} \left[P_{P+1}(\xi) - P_P(\xi) \right], \tag{3.15}$$

$$g_R(\xi) = R_{L,P+1}(\xi) + \frac{(-1)^{P+1}}{2} \left[P_{P+1}(-\xi) - P_P(-\xi) \right], \tag{3.16}$$

where R_R and R_L denote the right and left Radau polynomials, respectively, and $P_P(\xi)$ are the Legendre polynomials, which form an orthogonal set of modal basis functions. The one-dimensional Legendre and Radau polynomials of varying orders are illustrated in Figure 3.4.

With the discontinuous flux and correction terms defined, the continuous flux derivative can now be evaluated using a derivative matrix $\mathbf{D}$ of size $N \times N$, where $N = p_s + 1$, in the reference space

$$\frac{\partial f_i^c(\xi, t)}{\partial \xi} = \mathbf{D} f_i^c(\xi, t) \tag{3.17}$$

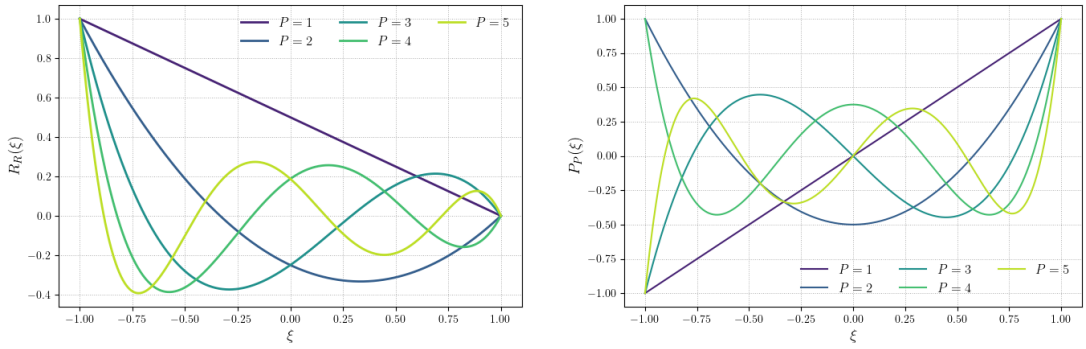

(a) Right Radau polynomials

(b) Legrendre polynomials

Figure 3.4. One-dimensional polynomials of varying degrees from $p_s = 1 - 5$.

which, when expanded using the definition of the corrected, continuous flux, yields [50]

$$\frac{\partial f_i^c(\xi,t)}{\partial \xi} = \frac{\partial f_i(\xi,t)}{\partial \xi} + \left[f_{i,L}^* - f_i(-1)\right] \frac{\partial g_L(\xi)}{\partial \xi} + \left[f_{i,R}^* - f_i(1)\right] \frac{\partial g_R(\xi)}{\partial \xi}. \tag{3.18}$$

Although this formulation is constructed in the reference space, it can be mapped back to the physical space using the Jacobian transformation defined in Equation 3.2, resulting in

$$\frac{\partial u_i^g(x,t)}{\partial t} + \frac{\partial f_i^c(\xi,t)}{\partial \xi} \frac{\partial \xi}{\partial x} = 0. \tag{3.19}$$

With the method established, the FR scheme can now be applied to a one-dimensional linear advection system. The method was tested on a standard benchmark problem in which a sine wave propagates over time in a periodic domain of length 1, starting at the origin. The advection speed was set to $\alpha = 1$, and the initial condition was defined as $u_{init} = sin(2\pi x)$. Under these conditions, the wave completes a full cycle and returns to its original position after one second, so the simulation was run to a final time of $t_f = 1$.

To demonstrate the accuracy of higher-order methods, the domain was discretized into four equally sized elements ($N_e = 4$). The FR scheme used Radau-based correction functions to recover the DG method. Temporal integration for all cases was carried out using a four stage, fourth-order Runge–Kutta scheme, RK_{44}. For simplicity, the Riemann solver employed to compute the common interface fluxes was an upwind scheme, rather than a blended solver.

As shown in Figure 3.5, increasing the polynomial degree improves the agreement between the

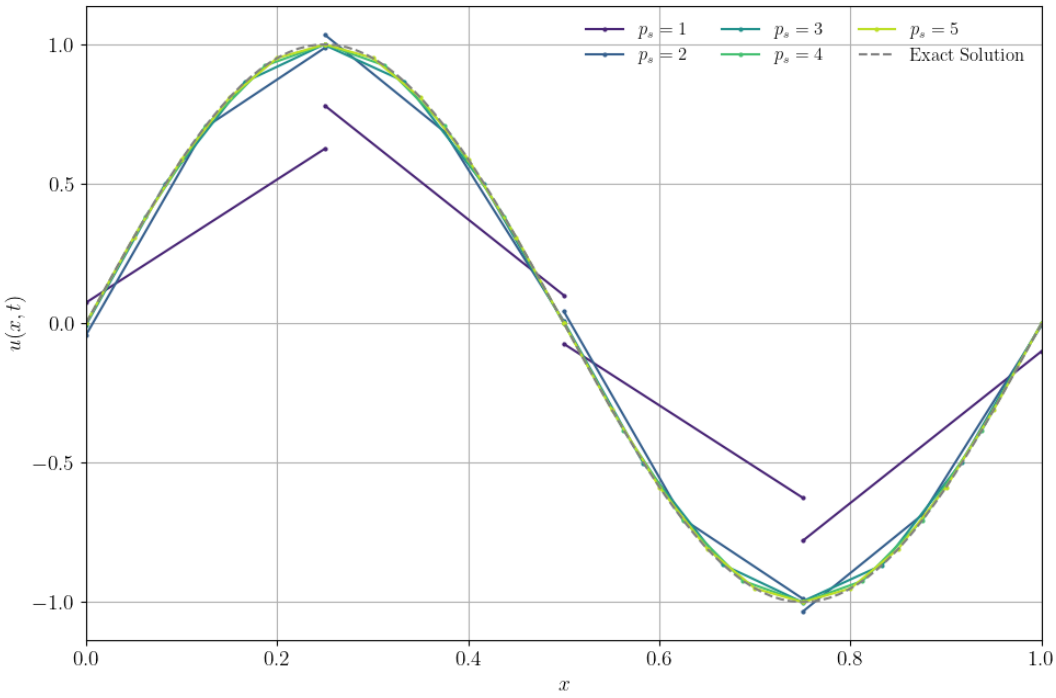

Figure 3.5. Solution of a linear advection system at the time 1 using various polynomial degrees of the FR method.

numerical and exact solutions. This highlights one of the key strengths of high-order methods: even with a coarse mesh, solutions of relatively low error can be obtained.

3.1.2 Multi-dimensional application of Flux Reconstruction

While the previous section demonstrated the application of the FR scheme in a one-dimensional setting, the method can be extended to multidimensional systems with relative ease [52]. Consider the multidimensional conservation law in differential form, as derived in Section 2.2,

$$\frac{\partial \vec{u}}{\partial t} + \nabla \cdot \vec{f} = 0, \tag{3.20}$$

where $\vec{u}$ is the vector of conserved variables and $\vec{f}$ is the flux vector. The domain Ω is again divided into non-overlapping elements, each of which is discretized by a set of solution points. These elements are bounded from left to right over the domain $x \in [x_L, x_R]$.

In the one-dimensional case, the number of solution points was denoted by N_p. For multidimensional domains, this is generalized to the number of degrees of freedom, N_{DOF}, which depends on both the element type and the polynomial degree p_s. The expressions for N_{DOF} for common element types are summarized in Table 3.1.

Table 3.1. Number of degrees of freedom per element type

Element Type	Dimensions	N_{DOF}
Line	1D	$p_s + 1$
Quadrilateral	2D	$(p_s + 1)^2$
Triangle	2D	$(p_s + 1)(p_s + 2)/2$
Hexahedron	3D	$(p_s + 1)^3$
Triangular Prism	3D	$(p_s + 1)^2(p_s + 2)/2$
Tetrahedron	3D	$(p_s + 1)(p_s + 2)(p_s + 3)/6$

As in the one-dimensional case, the solution points are mapped to a reference space Ω', where $\vec{\xi} \in [-1, 1]$ [47]. Following Section 3.1.1, the global solution is constructed as a direct sum of element-wise contributions. Extending Equation 3.6 to vector notation yields

$$\vec{u}(\vec{x}, t) \approx \vec{u}^h(\vec{x}, t) = \bigoplus_{i=1}^{N_e} \vec{u}_i^h(\vec{x}, t), \tag{3.21}$$

where $\vec{u}^h(\vec{x}, t)$ denotes the global, piecewise-continuous approximation, and $\vec{u}_i^h(\vec{x}, t)$ represents the local solution on the i^{th} element.

Using the nodal basis functions ϕ_k, the local solution and fluxes can be interpolated in both reference and physical spaces

$$\vec{u}_i^h(\vec{\xi}, t) = \sum_{k=1}^{N_{DOF}} \vec{u}(\vec{\xi}_{i,k}, t)\phi_k(\vec{\xi}), \tag{3.22}$$

$$\vec{u}_i^h(\vec{x}, t) = \sum_{k=1}^{N_{DOF}} \vec{u}(\vec{x}_{i,k}, t)\phi_k(\vec{x}), \tag{3.23}$$

$$\vec{f}_i^h(\vec{\xi}, t) = \sum_{k=1}^{N_{DOF}} \vec{f}(\vec{\xi}_{i,k}, t)\phi_k(\vec{\xi}), \tag{3.24}$$

$$\vec{f}_i^h(\vec{x},t) = \sum_{k=1}^{N_{DOF}} \vec{f}(\vec{x}_{i,k},t)\phi_k(\vec{x}). \tag{3.25}$$

Here, ϕ_k represents the nodal basis functions k^{th} degree. A visualization of these functions in two dimensions is provided in Figure 3.6.

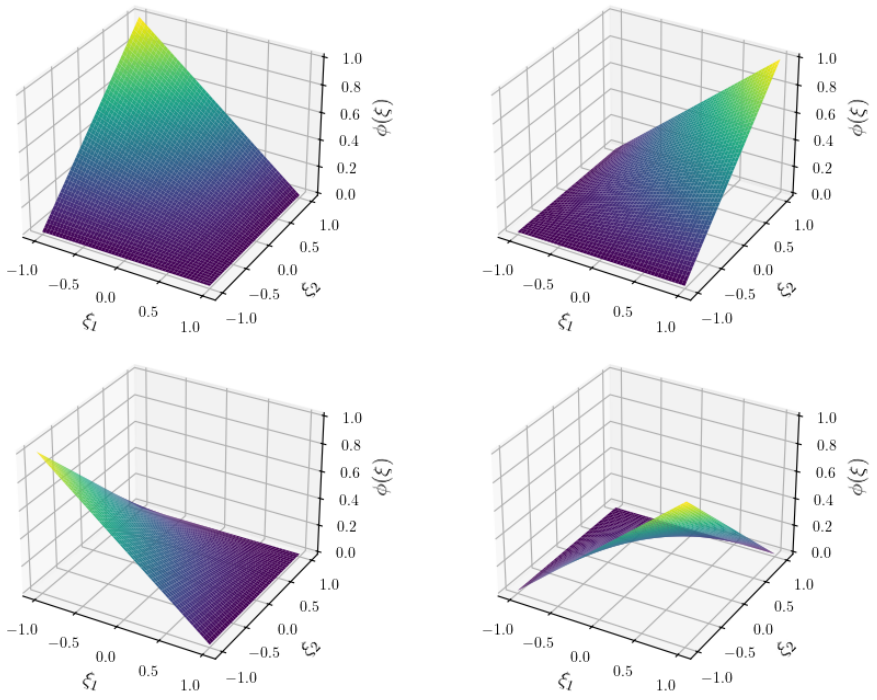

Figure 3.6. First degree two-dimensional nodal basis functions.

With both the solution and flux fields represented in a discontinuous form, a continuous flux can be reconstructed using the same correction procedure as described in Section 3.1.1. The conservation law, incorporating a correction field $\vec{\delta}_i$, can be written in vector form as [52, 48]

$$\frac{\partial \vec{u}_i^h}{\partial t} + \nabla \cdot \vec{f}_i^h + \vec{\delta}_i = 0. \tag{3.26}$$

Expanding this for each solution point $k = 1, 2, ..., N_{DOF}$ yields

$$\frac{\partial \vec{u}_{i,k}^h}{\partial t} + \left(\nabla \cdot \vec{f}_i^h\right)\Big|_{\vec{x}_{i,k}} + \vec{\delta}_{i,k} = 0. \tag{3.27}$$

This formulation evaluates the flux divergence and correction field at each solution point in the

element. For the present work, the correction functions are chosen such that the scheme recovers the multidimensional DG method [52].

3.2 Runge Kutta Approach to Temporal Discretization

Returning to Section 2.2, the differential form of the conservation equation (Equation 2.4) is given as:

$$\frac{\partial \vec{u}}{\partial t} + \nabla \cdot \vec{F} = 0, \tag{3.28}$$

where $\frac{\partial \vec{u}}{\partial t}$ governs the temporal evolution of the system, and $\nabla \cdot \vec{F}$ governs its spatial behavior. While Section 3.1 derived the method used to discretize the spatial component of the system, this section focuses on the discretization of the temporal component.

Temporal discretization methods are broadly classified into explicit and implicit schemes, based on the information used to advance the solution in time. Explicit schemes compute the solution at the next time step using only known information from the current or previous time levels. In contrast, implicit schemes involve information from future time steps, which is not yet known, and typically require solving a nonlinear system at each iteration [18].

Each approach has its own strengths and limitations. Implicit methods are generally unconditionally stable, allowing for larger time steps without violating stability constraints. However, this comes at the cost of increased computational complexity due to the need for iterative solvers. Explicit methods, on the other hand, are easier to implement and computationally less expensive per time step, since they do not require solving a system of equations. Their primary drawback is that they are conditionally stable, meaning the maximum allowable time step is constrained by the Courant–Friedrichs–Lewy (CFL) condition, given by:

$$\text{CFL} = \frac{a\Delta t}{\Delta x}, \tag{3.29}$$

where a is the characteristic wave speed, Δt is the time step size, and Δx is the grid spacing. To maintain stability, the CFL number typically must remain below a critical threshold, often less than 1 [18].

For the present study, an explicit time integration scheme is employed. This choice is motivated by its relative simplicity and efficiency, especially in the context of high-order spatial discretizations, where the per-time-step overhead of implicit methods becomes prohibitive.

3.2.1 Traditional Runge Kutta

One of the most commonly used explicit time-stepping approaches is the family of classical RK methods [53]. These methods employ a multi-stage approach in which a residual is evaluated at each intermediate stage to advance the solution in time.

Starting from the conservation equation (Equation 2.4), it can be rearranged into a residual form

$$\frac{\partial \vec{u}}{\partial t} = \vec{R}(\vec{u}), \tag{3.30}$$

where $\vec{u}$ is the vector of conserved variables, and $\vec{R}(\vec{u})$ represents the residual arising from the spatial discretization.

Using a finite difference approximation, the time derivative can be expressed as:

$$\frac{\partial \vec{u}}{\partial t} = \frac{\vec{u}^{t+1} - \vec{u}^{t}}{\Delta t}, \tag{3.31}$$

which can be rearranged to yield the Forward Euler method, a single-stage explicit scheme

$$\vec{u}^{t+1} = \vec{u}^{t} + \vec{R}(\vec{u}^{t})\Delta t, \tag{3.32}$$

where $\vec{u}^{t+1}$ is the vector of the conserved variables at the following time step and $\vec{u}^{t}$ is the vector of the conserved variables at the current time step [18, 53].

While Equation 3.32 represents a first-order accurate method, RK methods generalize this approach by introducing intermediate stages to increase temporal accuracy. These intermediate solutions are computed as

$$\vec{u}_i = \vec{u}^{t} + \sum_{j=1}^{s} a_{ij}\vec{R}(\vec{u}_j)\Delta t, \tag{3.33}$$

where $\vec{u}_i$ is the solution at the i^{th} stage, s is the total number of stages, and a_{ij} are the stage

coefficients. The final solution at the next time step is then computed as

$$\vec{u}^{t+1} = \vec{u}^t + \sum_{i=1}^{s} b_i \vec{R}(\vec{u}_i)\Delta t, \tag{3.34}$$

where b_i are the weights for each stage.

The coefficients a_{ij}, b_i, and the stage times

$$c_i = \sum_{j=1}^{s} a_{ij}, \tag{3.35}$$

are typically organized into a Butcher tableau [54]

$$\begin{array}{c|c} \vec{c} & \mathbf{A} \\ \hline & \vec{b} \end{array} = \begin{array}{c|ccc} c_1 & a_{11} & \dots & a_{si} \\ \vdots & \vdots & \ddots & \vdots \\ c_s & a_{s1} & \dots & a_{ss} \\ \hline & b_1 & \dots & b_s \end{array} . \tag{3.36}$$

A scheme is explicit if all $a_{ij} = 0$ for $i \leq j$, making the matrix $\mathbf{A}$ strictly lower triangular. This ensures that each stage depends only on known quantities from previous stages.

As an example, a three-stage, third order Runge–Kutta scheme, denoted as RK_{33}

$$\begin{array}{c|c} \vec{c} & \mathbf{A} \\ \hline & \vec{b} \end{array} = \begin{array}{c|ccc} 0 & & & \\ 1/2 & 1/2 & & \\ 1 & -1 & 2 & \\ \hline & 1/6 & 2/3 & 1/6 \end{array} . \tag{3.37}$$

The stages of the RK_{33} method are computed as follows

$$\begin{array}{ccc} \text{Stage 1} & \text{Stage 2} & \text{Stage 3} \\ \vec{u}_1 = \vec{u}^t & \vec{u}_2 = \vec{u}^t + \frac{\Delta t}{2}\vec{R}_1 & \vec{u}_3 = \vec{u}^t - \Delta t\vec{R}_1 + 2\Delta t\vec{R}_2 \\ \vec{R}_1 = \vec{R}(\vec{u}_1) & \vec{R}_2 = \vec{R}(\vec{u}_2) & \vec{R}_3 = \vec{R}(\vec{u}_3) \end{array} .$$

The final solution is then given by

$$\vec{u}^{t+1} = \vec{u}^{t} + \Delta t \left(\frac{1}{6}\vec{R}_1 + \frac{2}{3}\vec{R}_2 + \frac{1}{6}\vec{R}_3 \right). \tag{3.38}$$

3.2.2 Paired-Explicit Runge Kutta

While classical explicit RK methods are compatible with the EDAC formulation and are relatively straightforward to implement, they impose a strict stability constraint on the maximum allowable time step. This limitation becomes especially restrictive in regions with numerical stiffness, such as boundary layers. To overcome this issue in the present work, the second-order P-ERK scheme is employed for time integration.

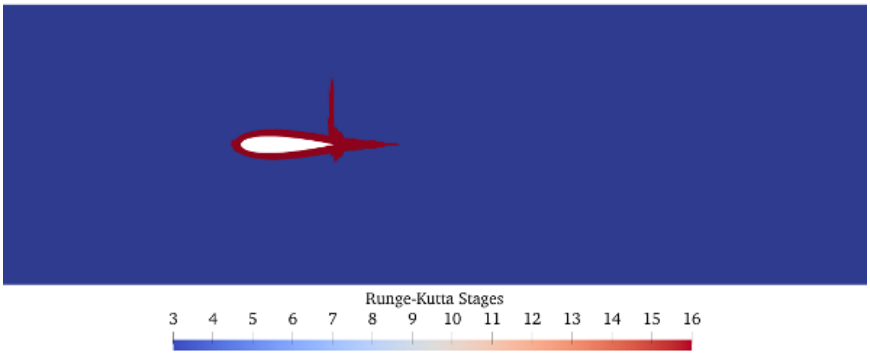

Figure 3.7. Distribution of the internal stages of the RK method within the domain.

P-ERK is a type of partitioned Runge–Kutta method that enables the use of RK schemes with varying numbers of active internal stages in different regions of the computational domain [55, 56, 57]. This flexibility allows for increased efficiency: schemes with more stages are applied in stiff regions, such as boundary layers, to enhance stability, while fewer-stage schemes are used in non-stiff regions like the farfield, thereby reducing computational cost, an example of which can be seen in Figure 3.7.

A key advantage of P-ERK schemes is that they allow for this localized variation in stage count without compromising conservation properties or the global order of accuracy. The Butcher tableaus used for the schemes in this study are taken from the supplementary material of Vermeire [55].

Chapter 4

Numerical Method Validation and Grid Convergence

This chapter presents the foundational elements of the current study. It begins with a detailed description of the computational domain, outlining its geometric configuration, boundary conditions, and physical relevance to the problem under consideration. Following this, a grid convergence study is performed to evaluate the sensitivity of the numerical solution to mesh resolution, thereby ensuring the reliability and accuracy of the discretized system. Finally, a series of validation simulations are conducted, in which the employed numerical methods are benchmarked against analytical solutions or experimental data to confirm their correctness and suitability for the targeted application.

The present work sets out to extend and continue on the findings of the studies presented in Section 1.3 by simulating a finite wing with varying spans in low-Reynolds-number flow. The wing features a NACA 0018 airfoil cross-section and is placed in a quiescent ambient environment. The flow is characterized by a Reynolds number of $Re = 10,000$, where

$$Re = \frac{u_\infty c}{\nu}, \tag{4.1}$$

u_∞ is the free-stream velocity, c is the airfoil chord length, and ν is the kinematic viscosity of the fluid. Additionally, the solver uses an incompressibility factor $M = 0.2$, ensuring the incompressibility assumption remains valid.

4.1 Computational Domain

The computational domain was kept consistent across all polynomial degrees, when running the grid convergence study. It extended $10c$ upstream, $11c$ downstream (in the wake region), and $10c$ above and below the airfoil's chord line, where c is the chord length. The domain thickness in the spanwise direction was set to $0.4c$, with the airfoil extending across the entire spanwise length of the domain to approximate an infinite-span wing.

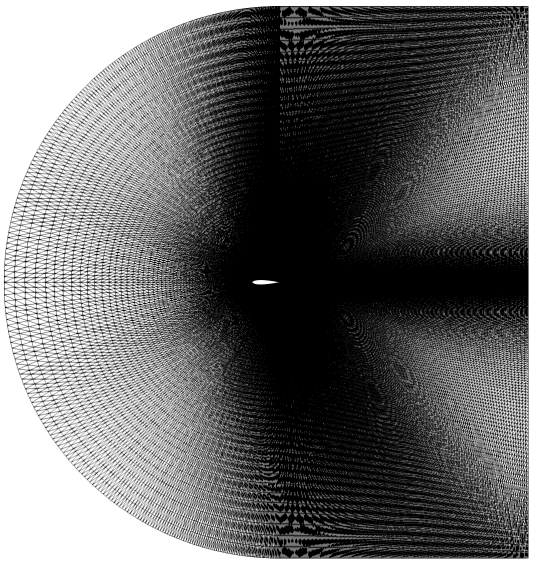

Figure 4.1. C-type mesh.

A structured mesh was employed, with refinement concentrated in the boundary layer region around the airfoil and in the wake to adequately resolve key flow features. The spanwise extent of the domain was evenly divided into five elements, resulting in a total of 103,984 prismatic elements.

Boundary conditions were assigned as follows: a Riemann invariant condition was applied on the outer boundaries, a no-slip condition was enforced on the airfoil surface, and periodic boundary conditions were imposed on the spanwise boundaries. The periodicity allowed for the simulation of a nominally infinite-span wing, minimizing spanwise end effects.

For the finite-span simulations, the streamwise and vertical extents of the domain were retained, but the spanwise length was increased to reflect the wing's finite geometry. In these cases, the domain extended an additional $2c$ beyond the wing tip to allow for the development of wingtip

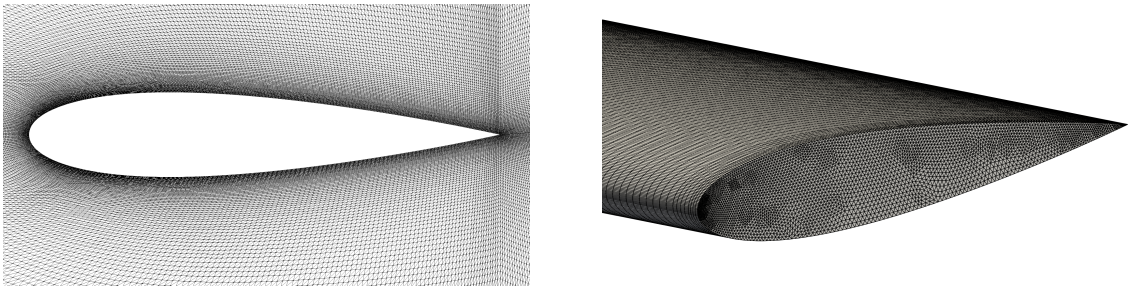

(a) Zoomed Mesh (b) Surface Mesh

Figure 4.2. Mesh details.

vortices without influence from the domain boundaries. The mesh was significantly refined in the wingtip region to capture the small-scale structures that emerge there, while the coarsest spanwise element width in the mid-span region remained consistent with that of the infinite-span simulations, approximately $0.04c$. Table 4.1, shows the number of elements in the domain for each simulated span length.

Table 4.1. Domain elements for each span length

Span	Elements
Periodic	66,000
1	621,847
2	786,355
3	950,983
4	1,115,551

The boundary conditions for the finite-span cases remained the same. Additionally, the entire domain was simulated without imposing a symmetry boundary, enabling the natural development of asymmetric turbulent structures.

Each simulation was run for 100 convective time units, defined by:

$$t_c = \frac{c}{u_\infty} \tag{4.2}$$

where u_∞ is the free-stream velocity. Statistical quantities were computed using data from the final $60t_c$ ensuring that the derived statistics reflect the fully developed state of the flow around the airfoil.

4.2 Grid Convergence Study

To determine the appropriate polynomial degree for the large-scale simulations, a grid convergence study was conducted for the angle of attack of 8°. This preliminary study aimed to identify the polynomial degree that provides sufficient accuracy while maintaining manageable computational cost. The following section compares the aerodynamic characteristics obtained using the first four polynomial degrees and selects the most suitable degree for use in the large-scale simulations.

Figure 4.3 presents iso-surfaces of the Q-criterion for each polynomial degree, colored by velocity magnitude. For the lowest degree, $p_s = 1$, the vortical structures appear large and underdeveloped, indicating that the flow remains predominantly laminar and does not transition to turbulence. While the $p_s = 2$ simulation exhibits flow transition, it lacks the finer details observed in the $p_s = 3$ and $p_s = 4$ cases and under-predicts the velocity magnitudes within the turbulent structures. Although the $p_s = 3$ and $p_s = 4$ results are qualitatively similar, the $p_s = 4$ simulation exhibits more coherent and well-defined vortical structures, whereas the $p_s = 3$ case shows more chaotic and less organized features.

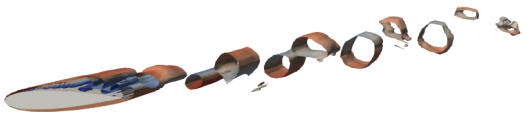

(a) $p_s = 1$

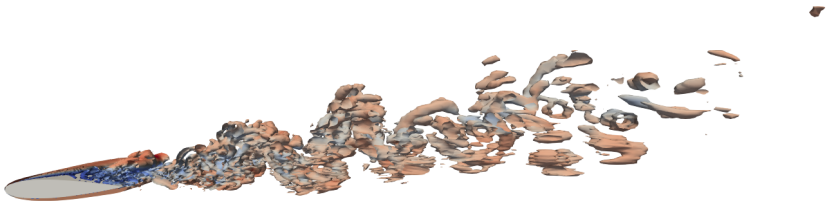

(b) $p_s = 2$

(c) $p_s = 3$

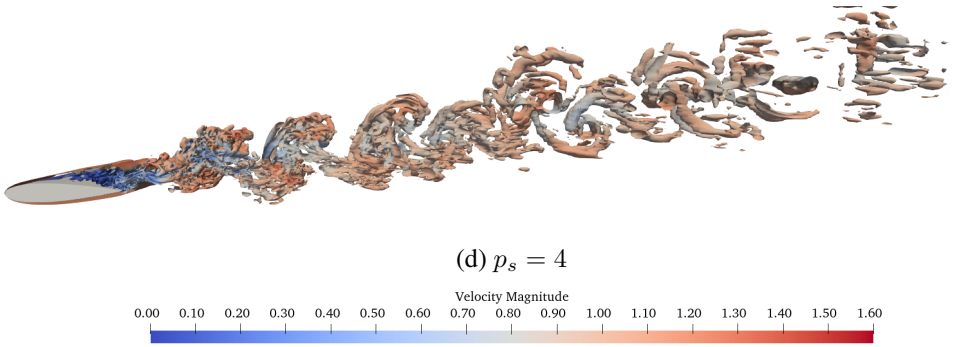

(d) $p_s = 4$

Figure 4.3. Isosurfaces of Q-criteria coloured by velocity magnitude for the infinite span cases.

Figure 4.4 presents the time-averaged pressure coefficient distribution, defined as

$$\overline{C}_p = \frac{\overline{p} - p_\infty}{\frac{1}{2}\rho_\infty {u_\infty}^2}, \tag{4.3}$$

where $\overline{p}$ is the time-averaged pressure at the surface node. The case with polynomial degree $p_s = 1$ significantly over-predicts the suction on the upper surface, particularly near the leading and trailing edges, compared to the higher-degree simulations. A similar trend is observed on the pressure side, though to a lesser extent. With $p_s = 2$, the pressure distribution improves, though a slight over-prediction remains near the stagnation point on the pressure side. Overall, however, it shows much closer agreement with the higher-order cases. For $p_s = 3$ and $p_s = 4$, the pressure coefficient distributions are nearly indistinguishable, suggesting convergence in solution accuracy at these polynomial degrees.

Following the trends observed in the time-averaged pressure coefficient, Figure 4.5 shows the time-averaged coefficient of friction, defined as

$$\overline{C}_f = \frac{\overline{\tau}_w}{\frac{1}{2}\rho_\infty {u_\infty}^2}, \tag{4.4}$$

where $\overline{\tau}_w$ is the time-averaged wall shear stress. As with the pressure distribution, the simulation with polynomial degree $p_s = 1$ significantly under-predicts the coefficient of friction, reflecting the absence of turbulent transition. This case also indicates a delayed flow separation compared to the higher-order simulations. The $p_s = 2$ simulation shows greater discrepancies in the coefficients of friction plot than in the coefficient of pressure plot, particularly around the transition and separation

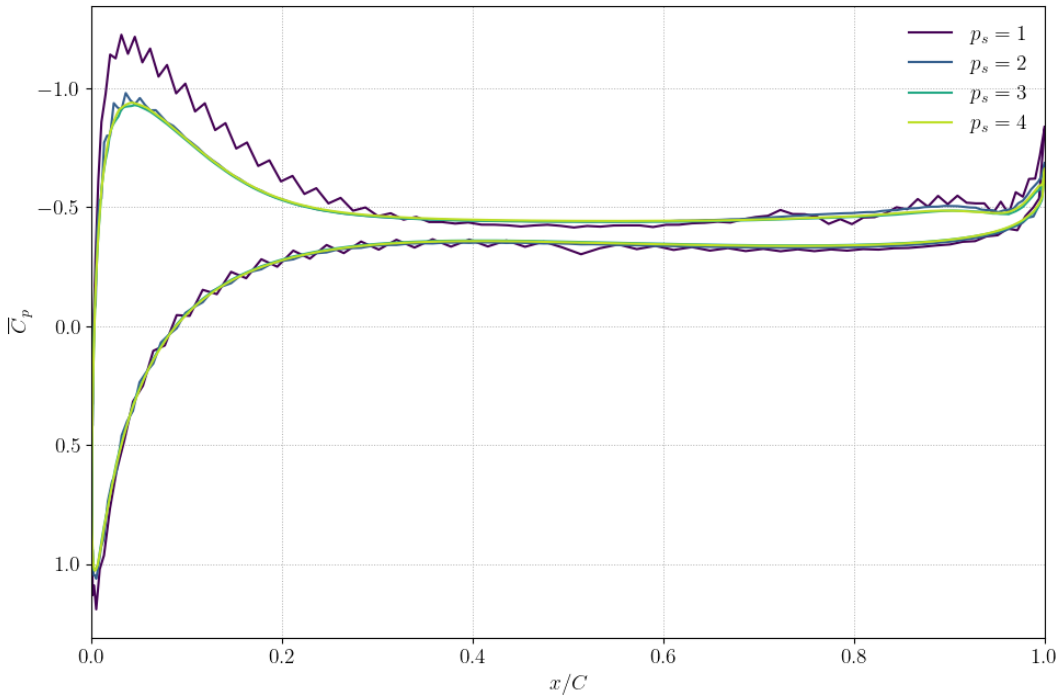

Figure 4.4. Time-averaged pressure coefficient distributions for the infinite span cases.

regions. However, its overall behavior is still qualitatively similar to the $p_s = 3$ and $p_s = 4$ cases. The $p_s = 3$ and $p_s = 4$ results are again nearly indistinguishable, suggesting convergence. The largest variations between the polynomial degrees appear near the location where a counter-clockwise vortex is shed from the lower surface, highlighting the sensitivity of wall shear stress predictions in regions of strong unsteadiness.

The time-averaged force coefficients and y^+ values for each polynomial degree are summarized in Table 4.2. The time-averaged coefficient of lift is defined as

$$\overline{C}_L = \frac{\overline{L}}{\frac{1}{2}\rho_\infty {u_\infty}^2 S_R}, \tag{4.5}$$

and the time-averaged coefficient of drag as

$$\overline{C}_D = \frac{\overline{D}}{\frac{1}{2}\rho_\infty {u_\infty}^2 S_R}, \tag{4.6}$$

where $\overline{L}$ and $\overline{D}$ are the time-averaged lift and drag forces, respectively, and S_R is the reference area.

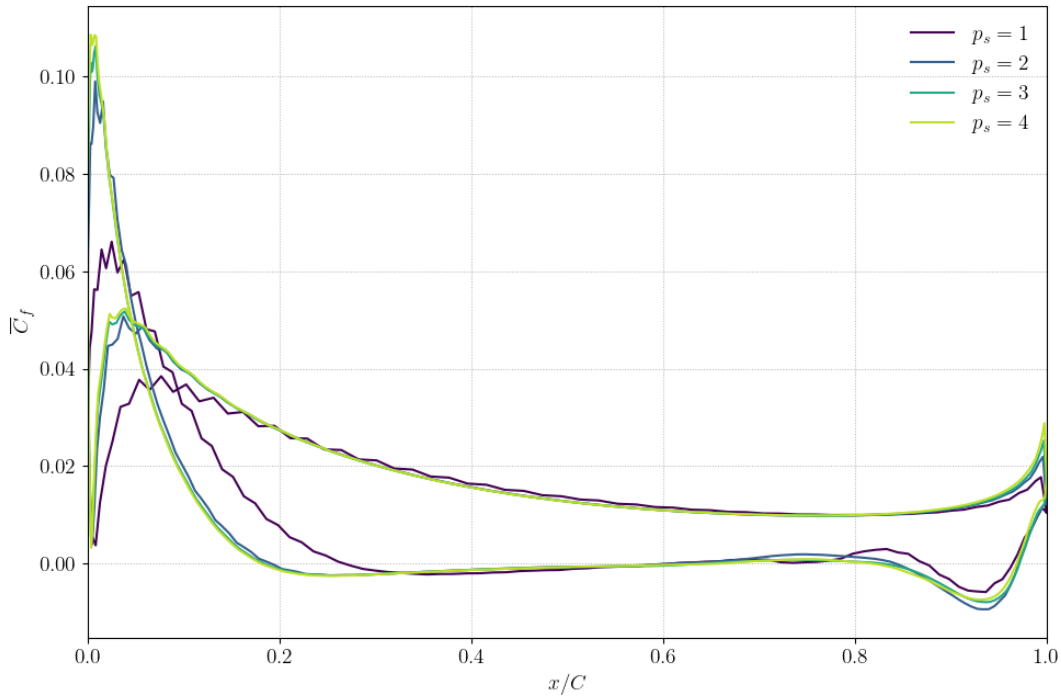

Figure 4.5. Time-averaged friction coefficient distributions for the infinite span cases.

As seen in previous results, all four polynomial degrees produce similar force coefficients, though the $p_s = 1$ case slightly overestimates both lift and drag. The $p_s = 2$, $p_s = 3$ and $p_s = 4$ simulations yield nearly identical results, indicating convergence in the force predictions.

Table 4.2. Lift and drag coefficients for the infinite span cases

p_s	$\overline{C}_L$	$\overline{C}_D$	Mean y^+	Max y^+
1	0.29	0.14	0.54	1.33
2	0.25	0.13	0.31	0.89
3	0.23	0.12	0.18	0.56
4	0.24	0.12	0.12	0.37

These similarities are partly attributed to the mesh resolution in the boundary layer. Although the same mesh is used across all simulations, the position of the first solution point relative to the wall, quantified by the dimensionless wall distance y^+, varies with polynomial degree. The y^+ value is defined as

$$y^+ = \frac{yu^*}{\nu}, \tag{4.7}$$

where y is the distance from the wall to the first solution point, ν is the kinematic viscosity of the

fluid and u^* is the friction velocity, given by

$$u^* = \sqrt{\frac{\tau_w}{\rho}}. \tag{4.8}$$

Despite using identical mesh geometries, higher polynomial degrees provide increased resolution within each element, thereby affecting the distribution of solution points and the resulting y^+ values. This, in turn, influences the accuracy of boundary layer predictions and the computed force coefficients.

To ensure that simulations qualify as DNS, the maximum y^+ value should generally remain below 1. This criterion guarantees sufficient resolution of the near-wall region, capturing the smallest turbulent scales—further discussed in Section 1.2. Although y^+ can vary with the angle of attack, maintaining sufficiently low y^+ values ensures DNS-level resolution across a range of flow conditions.

For the grid convergence study, it was observed that the case with $p_s = 1$ exceeded the $y^+ = 1$ threshold, indicating that it does not meet the resolution requirements for DNS. In contrast, all higher-order cases ($p_s = 2$, $p_s = 3$, and $p_s = 4$) satisfied the DNS criterion, with adequately resolved wall regions. These observations are consistent with earlier results, wherein simulations using higher polynomial degrees yielded nearly identical and physically reliable outcomes, while the lowest-order case ($p_s = 1$) consistently exhibited significant deviations from the more accurate higher-order solutions.

In Figure 4.6, the power spectral density (PSD) is presented at four distinct locations within the fluid domain, revealing similar overall trends among the polynomial degrees. The simulation with $p_s = 1$ displays pronounced cyclic peaks throughout the spectrum, which is indicative of non-turbulent, periodic vortex shedding. This observation is consistent with the previously discussed Q-criterion visualizations, where the flow remained largely laminar. In contrast, the higher-order simulations ($p_s = 2$, $p_s = 3$, and $p_s = 4$) exhibit more broadband spectral content characteristic of turbulent flow. Despite the differences in spectral distribution, all four cases share a dominant frequency, suggesting a consistent primary shedding mechanism. Notably, the results for $p_s = 3$ and $p_s = 4$ are closely aligned across the entire frequency range, while the $p_s = 2$ case slightly

overestimates the PSD in the post-peak region relative to the higher-order cases.

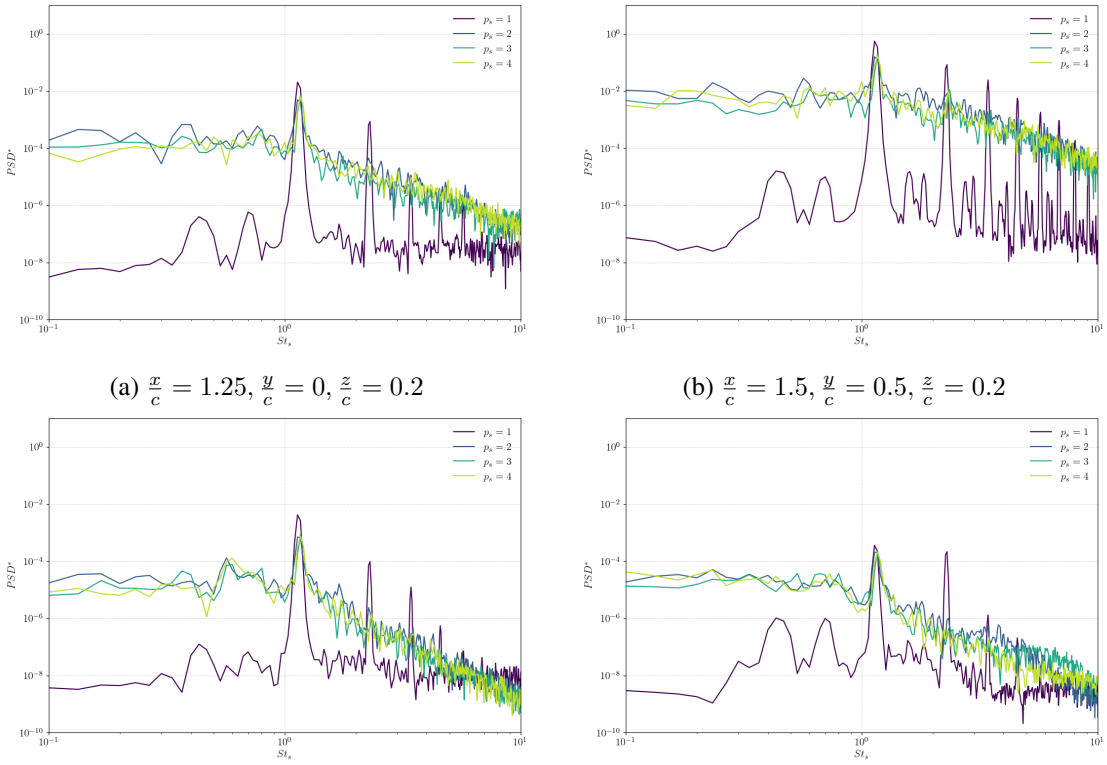

(a) $\frac{x}{c} = 1.25, \frac{y}{c} = 0, \frac{z}{c} = 0.2$

(b) $\frac{x}{c} = 1.5, \frac{y}{c} = 0.5, \frac{z}{c} = 0.2$

(c) $\frac{x}{c} = 2, \frac{y}{c} = 1, \frac{z}{c} = 0.2$

(d) $\frac{x}{c} = 3, \frac{y}{c} = 1, \frac{z}{c} = 0.2$

Figure 4.6. PSD at various sampler points for the infinite span cases.

Figure 4.7 presents the distribution of turbulent kinetic energy (TKE) within the domain, computed using the time-averaged velocity fluctuations

$$\text{TKE} = \frac{1}{2}\left(\overline{u'^2} + \overline{v'^2} + \overline{w'^2}\right), \tag{4.9}$$

where u', v' and w' denote the fluctuating components of velocity in the streamwise, vertical, and spanwise directions, respectively.

The TKE distribution follows trends consistent with previously presented data. The lowest-order case ($p_s = 1$) displays an elevated concentration of kinetic energy being shed from the lower surface of the airfoil and a relatively disorganized region above the upper surface. Moreover, the energy dissipates more slowly in this case, as evidenced by the persistence of high-energy regions far downstream in the wake. This behavior aligns with earlier findings suggesting the absence of a fully

developed turbulent flow for $p_s = 1$.

In contrast, the higher-order simulations ($p_s = 2$, $p_s = 3$, and $p_s = 4$) show more structured and localized TKE distributions. Two distinct regions of elevated energy, one originating from the lower surface and another from the separated shear layer on the upper surface, are clearly visible. These features become more sharply defined with increasing polynomial degree, indicating improved resolution of small-scale turbulence and flow separation structures.

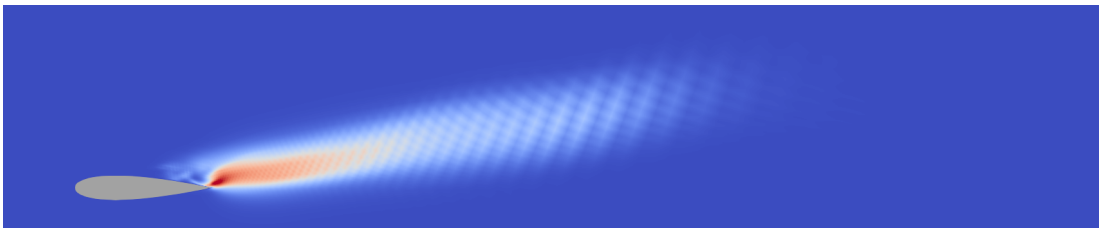

(a) $p_s = 1$

(b) $p_s = 2$

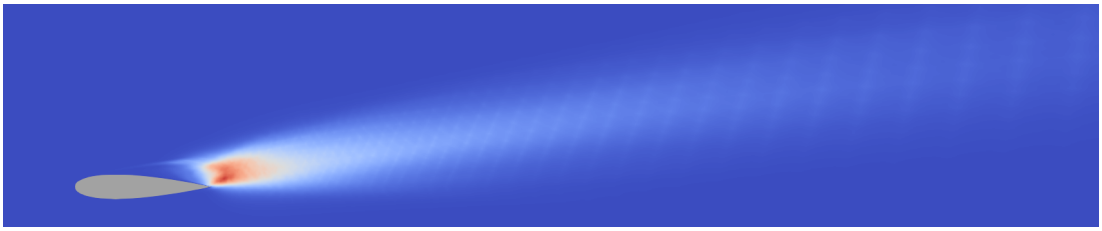

(c) $p_s = 3$

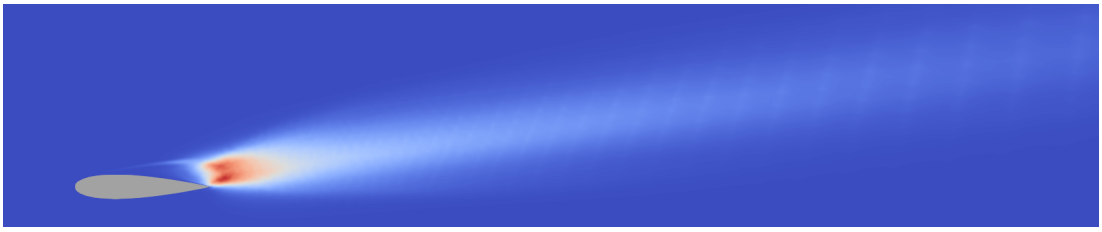

(d) $p_s = 4$

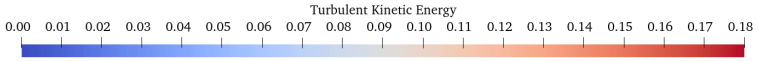

Figure 4.7. TKE for the infinite span cases.

The final aerodynamic quantity assessed in the grid convergence study is the Reynolds stress

distribution within the flow domain. For the case of an infinite-span wing, spanwise components of the Reynolds stress tensor can be neglected, as there is no significant spanwise flow—such as that generated by wingtip vortices—present. Therefore, only the primary in-plane components are considered: the normal Reynolds stresses in the streamwise (RS_{uu}) and vertical (RS_{vv}) directions, along with the shear Reynolds stress in the x–y plane (RS_{uv}). The Reynolds stresses are computed using the expression

$$RS_{ij} = \overline{u_i u_j} - \overline{u_i}\,\overline{u_j} \tag{4.10}$$

where u_i and u_j are the instantaneous velocity components in the i and j directions, and $\overline{u_i}$ and $\overline{u_j}$ represent their respective time-averaged values. These quantities provide insight into the distribution and intensity of turbulence within the domain, and offer a deeper understanding of the differences in turbulence prediction between polynomial degrees. In particular, the comparison of Reynolds stress components allows for further assessment of how well each polynomial degree captures the anisotropic and fluctuating nature of turbulent flows.

(a) $p_s = 1$

(b) $p_s = 2$

(c) $p_s = 3$

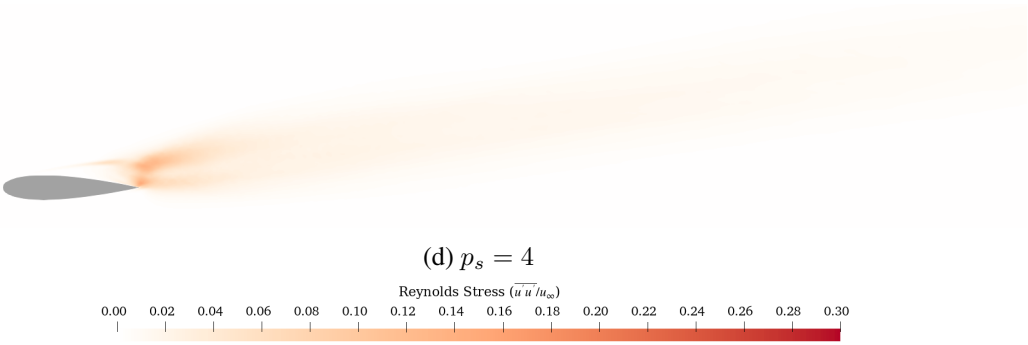

(d) $p_s = 4$

Figure 4.8. Reynolds stress $\left(\overline{u'u'}/u_\infty\right)$ for the NACA 0018 cases.

As with the other aerodynamic characteristics previously discussed, the first-order polynomial case ($p_s = 1$) exhibits notable discrepancies when compared to the higher-order simulations. Specifically, in the context of Reynolds stresses, Figure 4.8 reveals that the $p_s = 1$ case significantly overestimates the normal stress in the streamwise direction near the trailing edge of the airfoil. Additionally, it shows a lack of turbulent dissipation in the wake and a more disordered structure within the recirculation region. These trends are consistent across the other Reynolds stress components as well. Figures 4.9 and 4.10 display similar overestimation and disorganized stress fields on the upper surface for the $p_s = 1$ case.

(a) $p_s = 1$

(b) $p_s = 2$

(c) $p_s = 3$

(d) $p_s = 4$

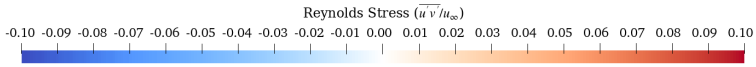

Figure 4.9. Reynolds stress $\left(\overline{u'v'}/u_\infty\right)$ for the NACA 0018 cases.

For the higher-order polynomial cases ($p_s = 2$, $p_s = 3$, and $p_s = 4$), the results are largely consistent and nearly identical across all components of the Reynolds stresses. While the $p_s = 2$ case exhibits some limitations in accurately capturing the flow behavior within the recirculation region, it still performs well in resolving the wake dynamics. In comparison, the $p_s = 3$ and $p_s = 4$ simulations show excellent agreement, producing highly similar results across all Reynolds stress components. This further confirms their ability to resolve the turbulent structures with high fidelity.

(a) $p_s = 1$

(b) $p_s = 2$

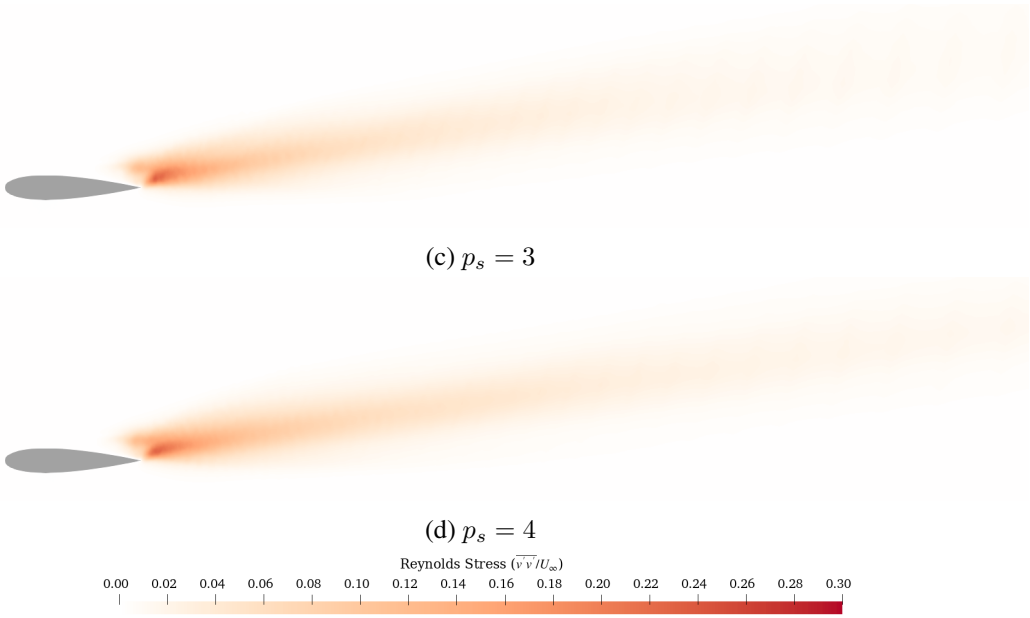

(c) $p_s = 3$

(d) $p_s = 4$

Figure 4.10. Reynolds stress $\left(\overline{v'v'}/u_\infty\right)$ for the NACA 0018 cases.

Based on the results presented, an appropriate polynomial degree can now be selected for simulating the large-scale domains. Table 4.3 summarizes the computational time (in hours) required for each polynomial degree. It is evident that with each increase in polynomial order, the computational time approximately doubles. Although the simulation with $p_s = 1$ was completed rapidly, the results clearly indicated that it failed to accurately resolve the flow physics.

Table 4.3. Execution time for simulating 100 convective time steps of the domain

p_s	Computational Time [h]
1	4.87
2	11.20
3	22.78
4	42.71

While theoretical understanding supports the use of higher-order methods for improved accuracy, as reflected in the greater fidelity observed in the higher-degree simulations, a practical balance must be maintained between accuracy and computational cost. In this study, the results for polynomial degrees $p_s = 3$ and $p_s = 4$ were nearly indistinguishable from an engineering perspective. That is, although small differences exist, they are negligible relative to the precision typically required in industrial applications.

Given that the $p_s = 4$ simulations required nearly an additional full day of computation compared to $p_s = 3$, the latter was selected as the optimal polynomial degree for all subsequent subgrid-scale simulations.

4.3 Validation

In the previous section, it was demonstrated that a polynomial degree of $p_s = 3$ yields results that are nearly indistinguishable from those obtained with a higher-order degree, while significantly reducing computational cost. This confirms that $p_s = 3$ is an appropriate choice for the present study. However, validation against established results is still required to ensure the credibility of the simulation framework.

To complete the validation process, this section compares the results obtained at an angle of attack of 10° with benchmark data reported by Bilbao-Ludena et al. [29] and Zhang et al. [58], as previously introduced in Section 1.3.

Table 4.4. Lift and drag coefficients at 10° for a periodic NACA 0018 airfoil

	$p_s = 3$	Zhang et al.[58]	Percent Difference
$\overline{C}_L$	0.265	0.254	4.21%
$\overline{C}_D$	0.138	0.132	4.44%

As only Zhang et al. [58], reported the lift and drag coefficients for a NACA 0018 airfoil at 10° in a flow of $Re = 10^4$ for a three dimensional infinite span wing, this study's methodology is solely compared to it. As can be seen from Table 4.4, both the lift and drag coefficients are roughly similar, with a percent error of approximately 4%, showing good agreement.

For the coefficients of pressure and friction, the present results are compared with those of Bilbao-Ludena et al. [29] and Zhang et al. [58] Figure 4.11 presents the surface distribution of the pressure coefficient. Overall, the present study shows good agreement with the general shape and trends observed in the reference works, though some discrepancies are evident. One such discrepancy is the slightly delayed pressure recovery after the stagnation point on the pressure side. Although the recovery trend aligns well with the reference data, it occurs approximately $0.02x/C$ later in the present simulation. On the suction side, the current results slightly over-predict both the global

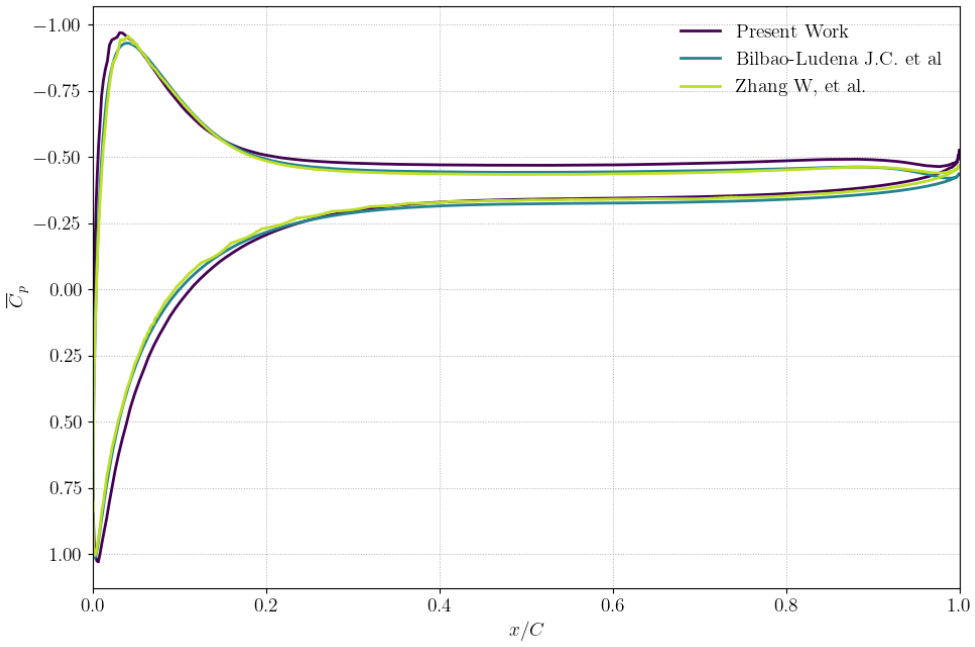

Figure 4.11. Time-averaged pressure coefficients over the airfoil.

minimum and the value at the pressure plateau. This is attributed to a recirculation bubble that follows a flow separation at $x/C = 0.2$.

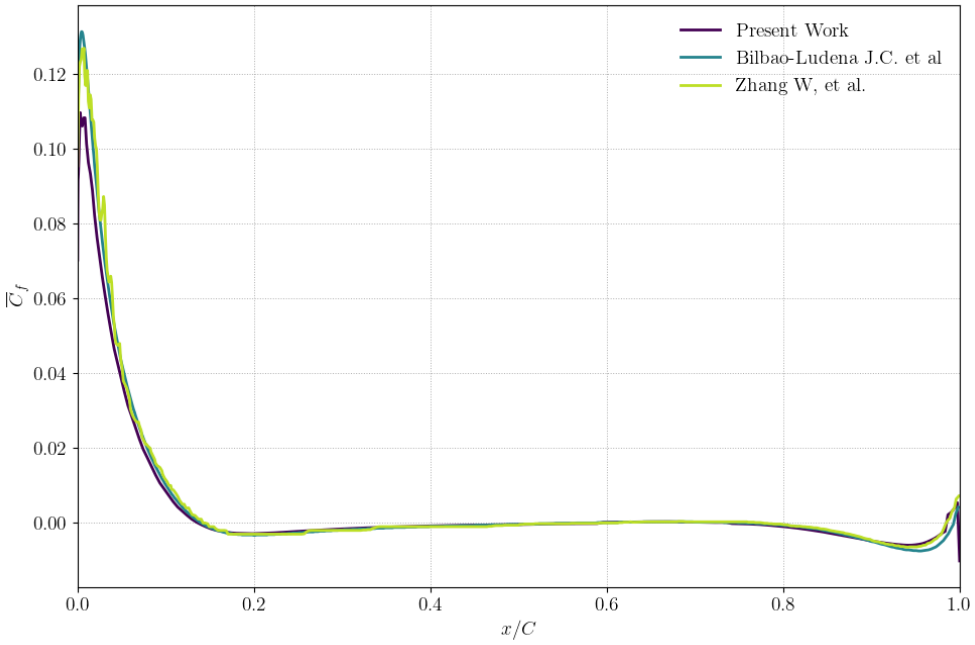

Figure 4.12. Time-averaged friction coefficients over the airfoil.

Figure 4.12 presents the comparison of the coefficient of friction on the suction side of the airfoil. As with the pressure coefficient, the present results show good overall agreement with the reference data. However, a noticeable discrepancy arises near the leading edge, where the present simulation under-predicts the global maximum of the friction coefficient associated with flow acceleration. Despite this, the simulation accurately captures the subsequent decay in friction due to the adverse pressure gradient, as well as the onset and extent of flow separation and the region of recirculation.

Given these differences, it is reasonable to attribute the majority of the observed discrepancies to the method by which incompressibility is enforced. As discussed in Chapter 2, the present work employs the EDAC formulation, whereas both reference studies make use of the fractional step method. This variation in the treatment of compressibility likely contributes to the minor deviations in the reported values. Nevertheless, despite these discrepancies, the overall results demonstrate strong agreement and confirm the validity of the present approach.

Chapter 5

Results

Before presenting the key observations derived from the study, it is important to highlight fundamental differences in the aerodynamic behavior observed within this particular flow regime. In conventional aerodynamic conditions, flow separation typically occurs at high angles of attack and is closely associated with stall. This phenomenon arises because, under higher Reynolds numbers, the flow possesses sufficient kinetic energy to overcome the low to moderate adverse pressure gradients encountered on the upper surface of the airfoil. However, at sufficiently low Reynolds numbers, the flow's kinetic energy is considerably diminished. As a result, even modest adverse pressure gradients become insurmountable, leading to early flow separation. This behavior has been clearly observed in the present study, as illustrated in Figure 5.1.

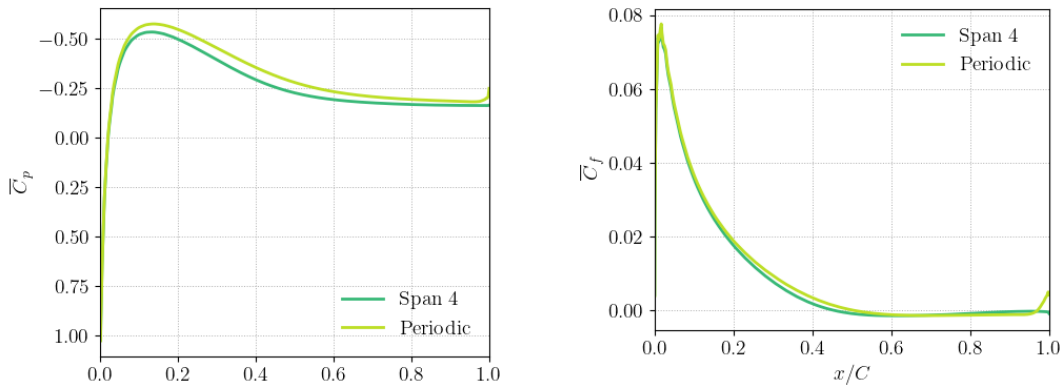

(a) Pressure

(b) Friction

Figure 5.1. Coefficients at the mid-span of the upper surface of the airfoil at the angle of attack of 1°.

The figures clearly demonstrates that, in the current low-Reynolds-number regime, flow separation begins as soon as the airfoil is subjected to a non-zero angle of attack. This is evident from the coefficient of friction, which becomes negative, indicating local flow reversal, and from the coefficient of pressure, which exhibits a plateau beyond the mid-chord region. These two features are characteristic of the formation of a recirculation bubble, wherein the flow detaches from the surface and subsequently reattaches further downstream. While these mechanisms are common in aerodynamics, their occurrence at such low angles of attack is a distinctive feature of low-Reynolds-number flows, in contrast to their manifestation at higher angles in more conventional regimes.

In the following sections, the presented plots will focus on the simulation case of Span 4. While the observations are described in the context of this specific case, it is important to emphasize that the identified trends are representative of all four span configurations. The corresponding plots for each span length are provided in the Appendix. Instances where unique or span-specific observations were made are explicitly noted within the discussion.

5.1 Aerodynamic Effects of Finite Spans and Tip Vortex Dynamics

In Section 1.3, previous studies relevant to the current work were reviewed. One of the key references was the study by Bilbao-Ludena et al. [29], which examined the formation and evolution of wingtip vortices. Although the present study does not directly investigate the internal dynamics of these vortices, Ludena's observations are particularly insightful. He noted that while the finite-span wings tend to exhibit earlier flow separation in this flow regime, the tip vortex can also prevent flow detachment in the outboard regions of the wing. This duality raised an important question regarding whether wingtip vortices might yield net aerodynamic benefits, despite their well-known drawbacks.

It is widely recognized that wingtip vortices induce drag and diminish lift through pressure equalization. However, the potential for improved flow attachment due to vortex-induced suction offered a hypothesis: might the reattachment partially or fully offset the associated performance losses? Notably, for wings with identical chord lengths, the relative area influenced by this reattachment increases as the span decreases. If tip-induced flow reattachment does enhance aerodynamic performance, smaller-span wings—experiencing proportionally greater tip effects—should outperform

longer-span wings.

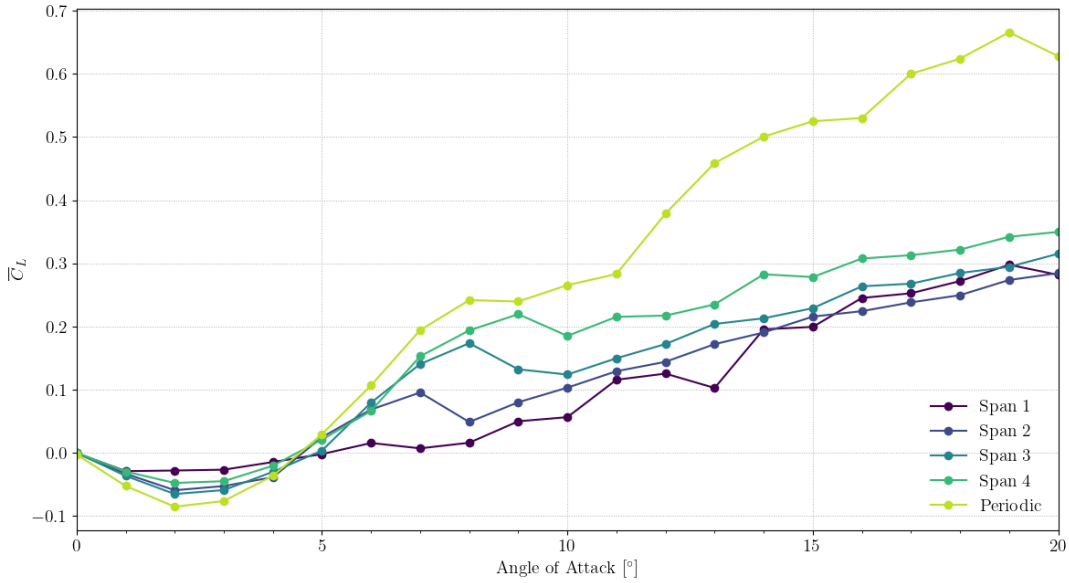

Figure 5.2. Time-averaged coefficient of lift of various wing spans.

However, as shown in Figure 5.2, no significant lift benefit is observed from the wingtip vortices. The infinite-span case consistently generates the highest lift across the range of angles of attack, attributable to the absence of spanwise flow and associated pressure equalization effects. The lift performance of the finite-span wings improves progressively with increasing span, suggesting that the presence of the tip vortex ultimately degrades, rather than enhances, aerodynamic efficiency in this regime—consistent with trends observed in higher Reynolds number flows.

A similar trend is evident in the drag characteristics shown in Figure 5.3. Somewhat counter-intuitively, the infinite-span case exhibits the highest drag values, despite the absence of wingtip vortices—structures traditionally associated with increased drag due to the formation of induced flow circulation. At first glance, this might imply a potential performance benefit stemming from the vortex-induced flow attachment observed in the finite-span wings. However, such an interpretation requires deeper examination and context.

Drag in aerodynamic systems is not only a function of flow separation or tip effects, but is also intrinsically linked to the lift generated. According to classical aerodynamic theory, particularly in the context of lifting-line theory, the induced drag component increases quadratically with lift, as

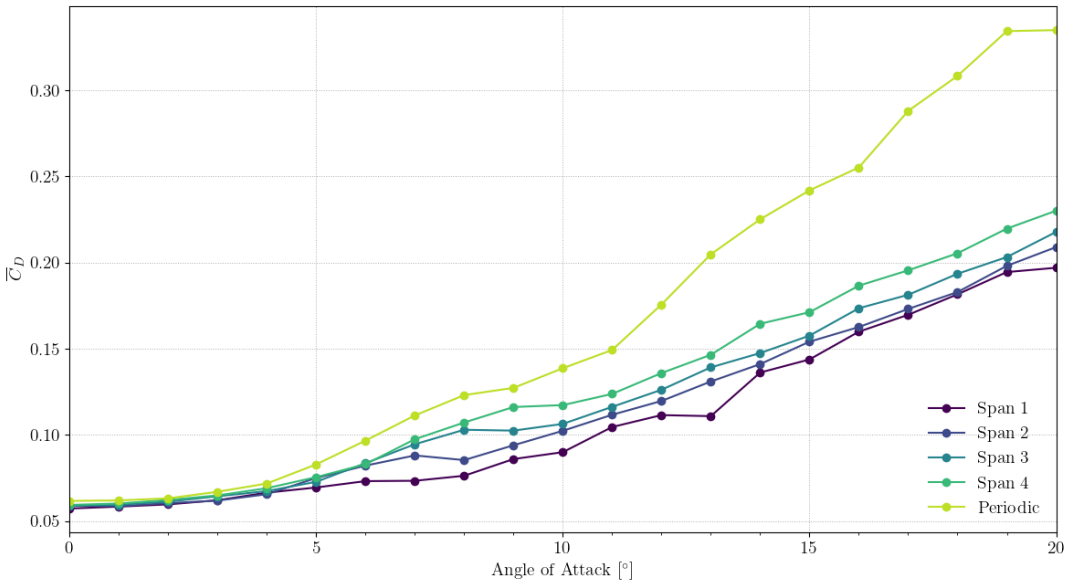

Figure 5.3. Time-averaged coefficient of drag of various wing spans.

expressed in the induced drag formulation

$$C_{D,i} = \frac{C_L^2}{\pi e_{sf} \mathrm{AR}}, \tag{5.1}$$

where e_{sf} is the span efficiency factor and AR is the aspect ratio of the wing. In this formulation, a wing with a larger span and higher lift will inherently experience a greater magnitude of induced drag, even in the absence of tip vortices.

This helps explain the higher drag observed in the infinite-span configuration: it generates more lift across the domain and thus incurs a higher induced drag penalty. Conversely, the shorter-span wings produce less lift and consequently less induced drag, despite the presence of vortices that would otherwise be expected to degrade performance.

Therefore, evaluating drag in isolation may yield misleading conclusions regarding aerodynamic performance. A more informative approach is to consider aerodynamic efficiency, often referred to as wing fitness. This metric captures the net aerodynamic benefit of a configuration, balancing the desirable lift production against the penalty of drag. In this context, the comparison of finite and infinite span wings must account for how effectively each configuration converts energy into useful aerodynamic force.

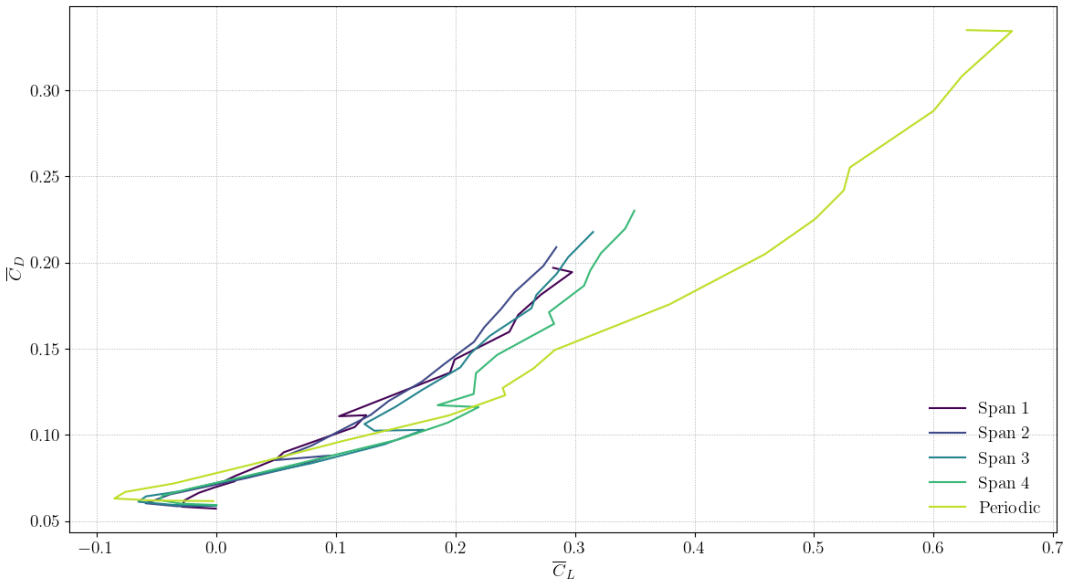

Figure 5.4. Wing efficiency of various wing spans.

Figure 5.4 presents the aerodynamic fitness of each wing configuration, defined as the lift-to-drag ratio. It reveals that for a given lift coefficient, particularly below $\overline{C}_L = 0.2$, the finite-span wings demonstrate comparable efficiency to one another and a superior efficiency relative to the infinite-span case. This suggests that while the wingtip vortex does not enhance lift directly, it may contribute to more favorable flow characteristics—such the partially suppressed separation—that help maintain efficiency under certain conditions.

Notably, the abrupt decline in aerodynamic fitness beyond this threshold correlates with a marked weakening of the wingtip vortex. This observation will be explored in more depth later in the chapter, but it hints at a unique behavior in low Reynolds number flows: the wingtip vortex, while typically viewed as a detriment in classical aerodynamics, may provide localized gains in efficiency that are not present in traditional high Reynolds number scenarios.

5.2 Regions of Aerodynamic Lift

While Section 5.1 focuses on analyzing the influence of wingtip vortices on aerodynamic performance—specifically lift and drag—this section shifts the emphasis toward how these performance metrics compare with those observed in conventional, higher Reynolds number flows. Referring

back to Figure 5.2 from the previous section, it is evident that the lift curve generated in this study does not resemble the typical behavior seen in traditional flow regimes.

In classical aerodynamics, lift curves are generally characterized by two distinct regions: an initial linear growth in lift with increasing angle of attack, followed by a sharp drop in lift—commonly known as stall—that occurs at higher angles. This produces a curve resembling a slanted hook. However, the low Reynolds number regime considered in the present work deviates significantly from this conventional behavior.

The discrepancy arises because the physical mechanisms that shape the lift curve within flows of higher Reynolds numbers do not hold under low Reynolds conditions. In higher Reynolds number flows, it is common to assume that the flow is predominantly inviscid, as the inertial forces vastly outweigh the viscous forces due to the higher flow velocity. Under these assumptions, thin airfoil theory becomes applicable, predicting that the coefficient of lift increases linearly with angle of attack, with a theoretical slope of 2π for an infinitely thin, camberless airfoil.

While thin airfoil theory is an idealization, it often provides an excellent approximation in high Reynolds number flows, where the presence of a thin, turbulent boundary layer helps maintain flow attachment over the airfoil. In contrast, at low Reynolds numbers, the dominance of viscous forces leads to early flow separation and laminar boundary layer behavior, invalidating the assumptions of thin airfoil theory and resulting in the fundamentally different lift characteristics observed in this study.

Figure 5.5 illustrates the four distinct regions into which the lift curve can be divided. These regions are defined as follows: the negative lift region, occurring between 0° and 4.5°; the non-linear lift region, spanning 4.5° to 8.5°; the pseudo-stall region, observed between 8.5° and 10.5°; and the linear lift region, which begins beyond 10.5°. While this figure focuses on the wing with a span of 4, similar trends are consistently observed across all simulated cases shown in Figure 5.2, with the exception of the infinite span case. However, it is notable that the onset of the pseudo-stall region is delayed as the span increases, suggesting a span-dependent shift in aerodynamic behavior.

In addition to the lift curve, the coefficient of drag also exhibits distinct regions that correlate with the phases of the lift development. As shown in Figure 5.6, the drag curve can be divided into three main regions. The quadratic drag growth region spans both the negative and non-linear

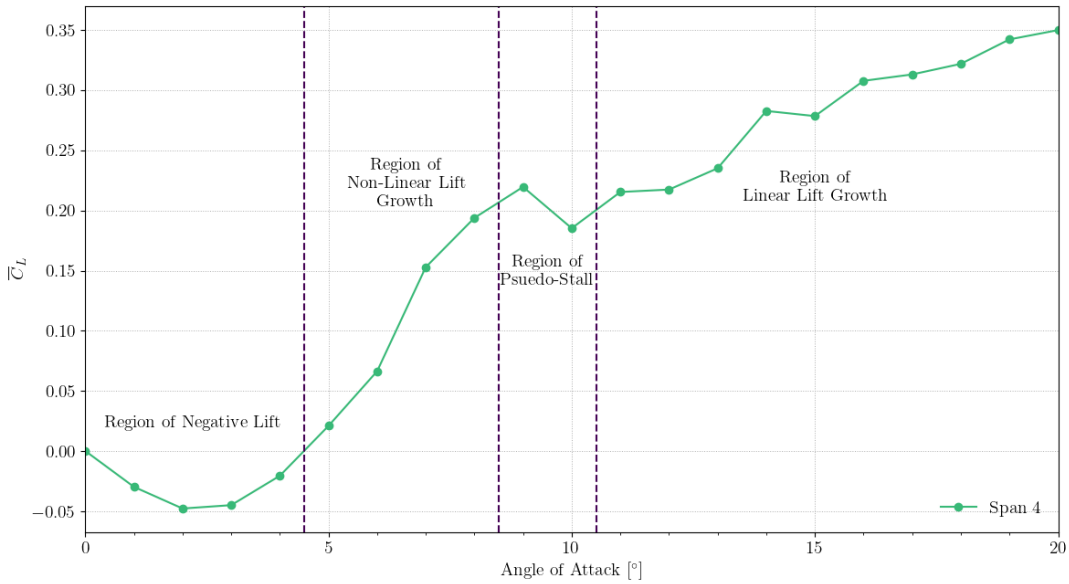

Figure 5.5. Sectioned coefficient of lift curve.

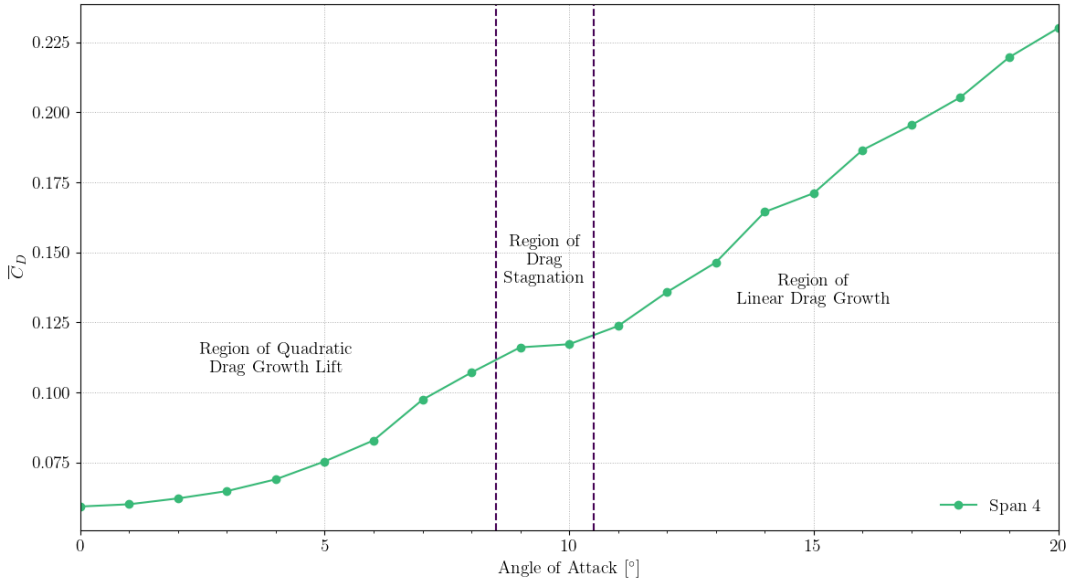

Figure 5.6. Sectioned coefficient of drag curve.

lift regions, characterized by a steep rise in drag. This is followed by the drag stagnation region, which corresponds to the pseudo-stall phase in the lift curve. Finally, the linear drag growth region coincides with the linear lift region, indicating a re-establishment of steady aerodynamic behavior. As with the lift curve, these drag curve regions are consistently observed across all spanwise cases,

with the exception of the infinite span case, with the drag stagnation region always occurring in tandem with the pseudo-stall behavior in the lift response. The following sections will explore each of these regions in more detail, with a focus on identifying the aerodynamic mechanisms driving these transitions and the broader implications for low Reynolds number flight.

5.2.1 Region of Negative Lift

In Section 1.3.1, the occurrence of negative lift at relatively low angles of attack was discussed. This phenomenon, attributed to a recirculating flow structure around the airfoil that disrupts the satisfaction of the Kutta condition, has been previously observed in both wind tunnel experiments and lower-fidelity simulations, such as those using RANS models. However, it is believed that the present study is the first to capture this behavior using a DNS approach. The use of DNS not only validates earlier findings from experimental and RANS studies but also enables the observation of finer-scale turbulent and vortical structures that were previously unresolved. As a result, this work offers a more comprehensive understanding of the mechanisms driving negative lift in low Reynolds number flows and provides new insights into the complex fluid dynamics at play in this regime.

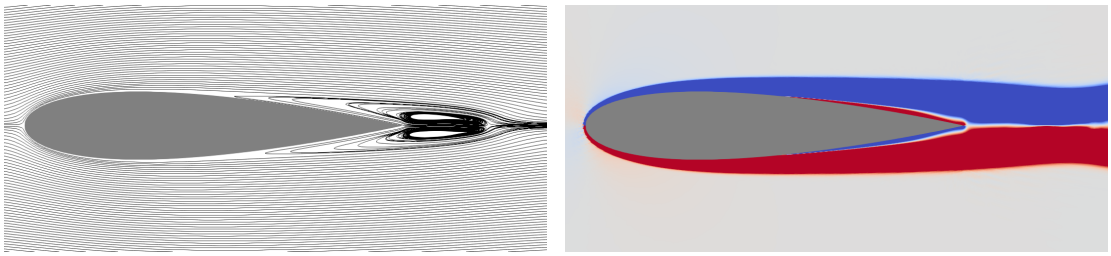

(a) Flow streamlines (b) Vorticity

Figure 5.7. Flow dynamics of a wing of span 4 at 0°.

While none of the simulated cases exhibit significant negative lift at an angle of attack of 0°, the results remain insightful in understanding the flow behavior under these conditions. As shown in Figure 5.7a, the wing behaves more like a bluff body than a streamlined airfoil. In this regime, the flow dynamics resemble those around a cylinder, rather than a typical lifting surface. This is evidenced by the presence of recirculation zones on both the upper and lower surfaces of the airfoil, indicating flow separation on both sides. Such separation implies that the incoming flow lacks sufficient momentum to stay attached, a characteristic commonly seen in low Reynolds number

flows.

Although this behavior is atypical for symmetric airfoils at zero angle of attack in high Reynolds number regimes—where the flow would typically remain attached—it is consistent with prior theoretical and experimental findings discussed in Section 1.3. Despite the bluff body-like appearance, there is no net circulation around the wing, meaning the Kutta condition remains satisfied. Consequently, all cases produce negligible lift at 0° angle of attack, which aligns with theoretical expectations for symmetric airfoils without any angle of attack.

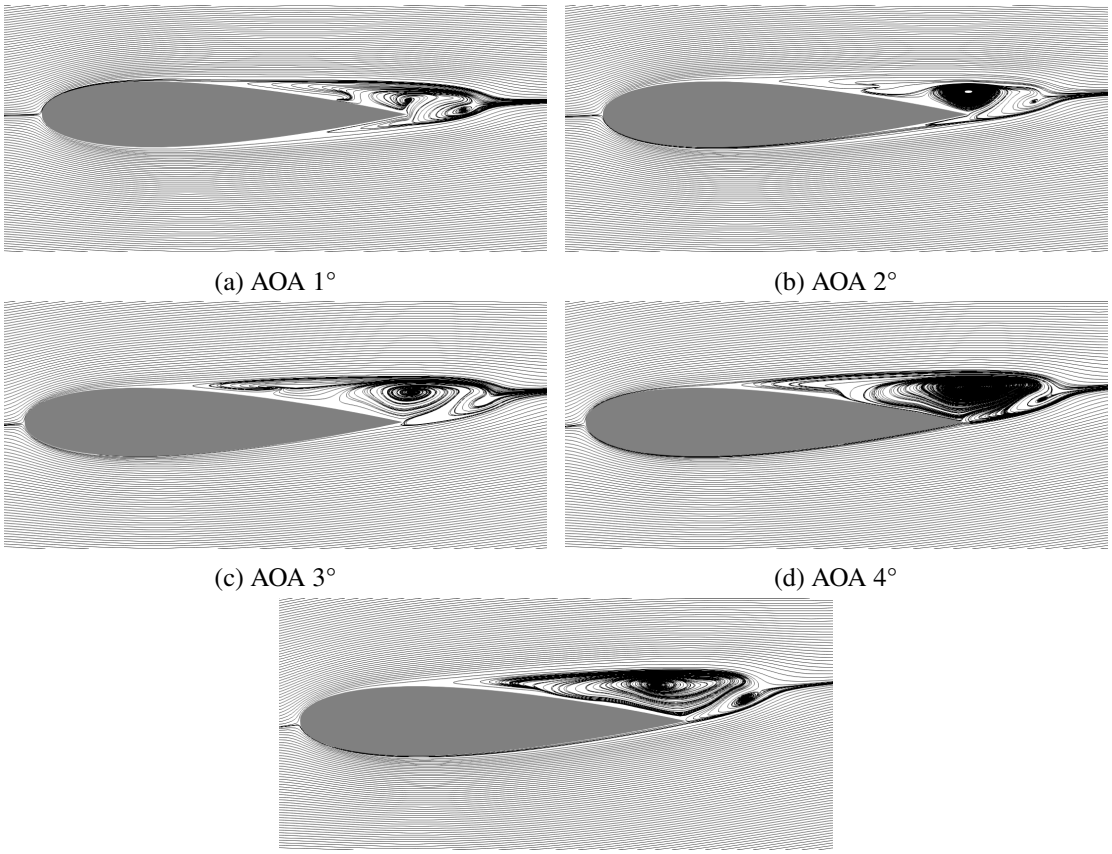

(a) AOA 1°

(b) AOA 2°

(c) AOA 3°

(d) AOA 4°

(e) AOA 5°

Figure 5.8. Flow streamlines around a wing of span 4 at various angles of attack.

Figure 5.9 illustrates the streamlines around the airfoil, for all angles of attack that produce a negative lift coefficient, as well as the first angle at which positive lift is generated (5°). While Figure 5.7a previously showed bluff-body-like flow behavior at 0°, these streamline visualizations reveal how the recirculation zones evolve with increasing angle of attack. Notably, once the airfoil is

subjected to an inclined freestream, the upper surface recirculation bubble begins to dominate.

At 0°, symmetry in both geometry and flow leads to nearly identical separation points and recirculation zones on the upper and lower surfaces. However, introducing an angle of attack alters the pressure distribution: the upper surface experiences a higher adverse pressure gradient due to the increased curvature the flow must follow, prompting earlier flow separation. This earlier separation gives the upper recirculation bubble more time and space to develop, thereby increasing its strength.

In high Reynolds number flows, the more energetic lower surface flow typically remains attached and suppresses the influence of the upper recirculation. However, in low Reynolds number conditions, the flow lacks the inertia necessary to overcome even modest adverse pressure gradients. Consequently, the lower surface flow also begins to separate—albeit more mildly—creating a low-pressure void near the trailing edge on the lower surface.

This void region, which is the most apparent in Figure 5.8a, allows the stronger upper surface recirculation bubble to expand and effectively ”wrap around” the trailing edge. The result is a net circulation in the opposite direction of what would be expected for positive lift generation. This violates the Kutta condition and produces a negative lift coefficient. These findings are consistent with prior observations made in lower-fidelity simulations and wind tunnel tests, such as those discussed by Aguilar Cabello, but the present DNS study provides direct numerical evidence of this mechanism.

Figure 5.9 illustrates the streamline behavior near the trailing edge—specifically the final tenth of the chord—for angles of attack that produce negative lift, as well as the first angle where positive lift is observed. These visualizations provide deeper insight into how flow structures contribute to lift inversion and the eventual transition to positive lift.

In Figure 5.9a, the streamline patterns clearly show a dominant clockwise vortex originating from the upper surface. A portion of this reversed flow penetrates into the region near the lower surface, briefly flowing upstream before being re-entrained into the main freestream. This flow pattern constitutes a clear violation of the Kutta condition and confirms the presence of net circulation around the trailing edge—opposite in direction to what is typically associated with positive lift.

Figure 5.8a further highlights the complex vortex dynamics. In addition to the dominant clockwise vortex, two other vortical structures are evident: (1) a smaller counter-clockwise vortex in the wake,

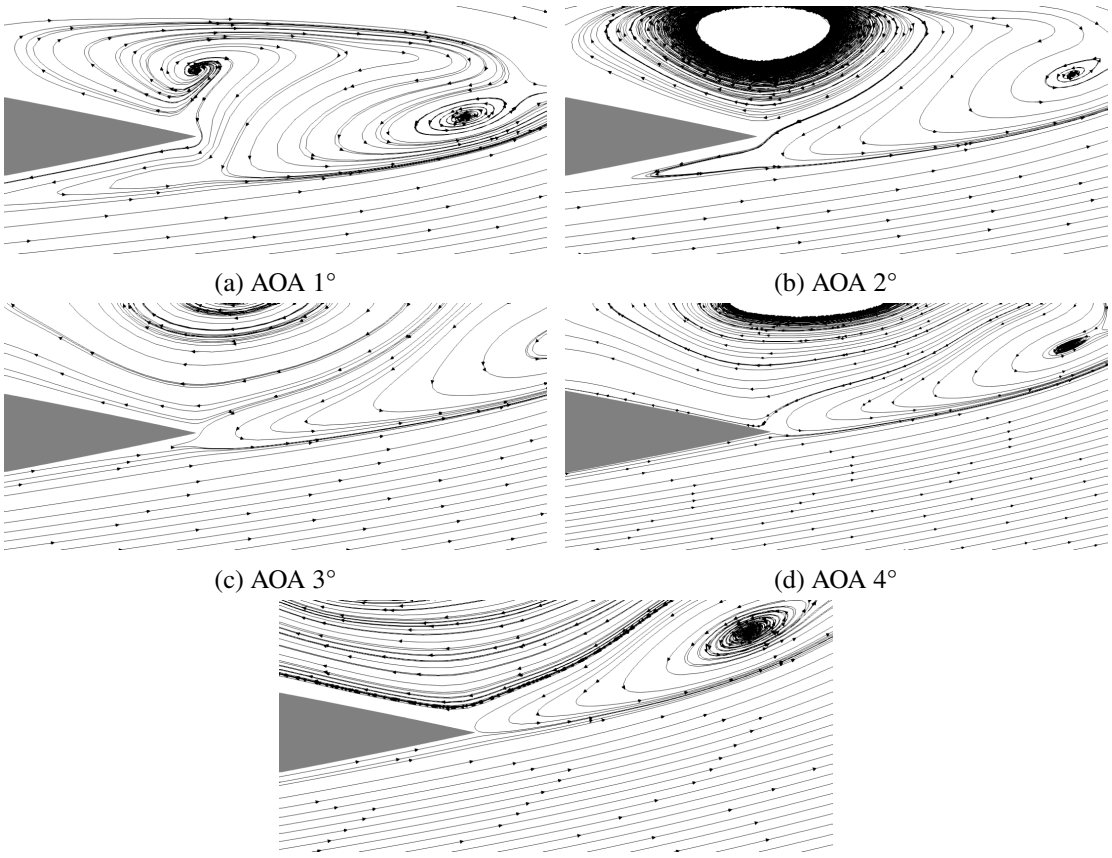

(a) AOA 1°

(b) AOA 2°

(c) AOA 3°

(d) AOA 4°

(e) AOA 5°

Figure 5.9. Flow streamlines around the trailing edge of a wing of span 4 at various angles of attack.

formed where the reversed flow from the upper surface interacts with the freestream exiting the lower surface, and (2) a vortex along the upper surface of the wing, driven by trans-spanwise flow generated by the wingtip vortices, which eventually escapes the main recirculation zone.

These same mechanisms—particularly the void near the trailing edge created by lower surface separation and subsequently filled by the upper surface vortex—can also be observed in Figures 5.9b and 5.9c. However, in these cases, the extent of flow spillover from the upper to the lower surface decreases. Interestingly, although the case at 1° exhibits the most spillover, it does not result in the largest magnitude of negative lift. This suggests that negative lift generation may depend not only on the amount of spillover but also on the strength of the recirculation vortex.

For example, at 1°, the upper vortex appears weaker, which may diminish the lift-reducing effect despite the greater spillover. In contrast, the 2° case demonstrates a stronger upper vortex, which

may more effectively drive negative lift even with limited spillover. This interplay between vortex strength and spillover extent appears to be a critical factor in determining the magnitude of negative lift generation.

At 4°, shown in Figure 5.9d, the spillover mechanism is no longer present. Nevertheless, a small amount of negative lift is still observed. The streamlines reveal that while the flow remains mostly attached, there is a significant deflection near the trailing edge, forming a steep curvature away from the surface. This deflection suggests residual circulation about the trailing edge, albeit weaker, which contributes to the lingering negative lift.

By 5°, as shown in Figure 5.9e, this curvature vanishes, and the flow follows a smooth and attached path around the airfoil. This is also the first angle at which positive lift is produced, indicating the reestablishment of conventional airfoil behavior and restoration of the Kutta condition.

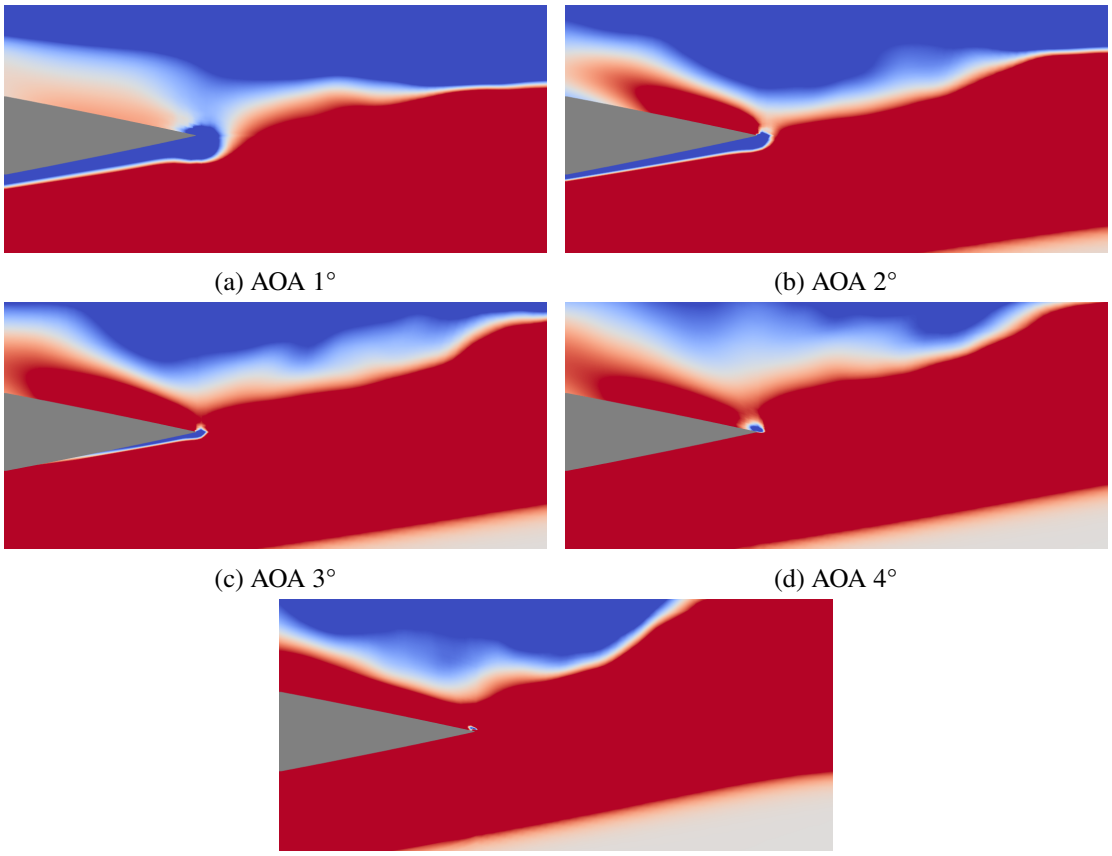

(a) AOA 1°

(b) AOA 2°

(c) AOA 3°

(d) AOA 4°

(e) AOA 5°

Figure 5.10. Vorticity around a wing of span 4 at various angles of attack.

Figure 5.10 displays the vorticity field near the trailing edge of the wing, providing insight into the rotational flow behavior contributing to lift characteristics. Between the angles of 1° and 4°, a region of negative (clockwise) vorticity is consistently observed at the trailing edge. This vorticity gradually weakens with increasing angle of attack and becomes negligible by 5°, corresponding with the restoration of positive lift.

Interestingly, this clockwise vorticity originates on the lower surface of the airfoil but progressively shifts upward, toward the upper surface, before dissipating. This evolution is a key indicator of how the trailing-edge flow structure transitions from an abnormal separated regime into one consistent with conventional attached flow.

In typical high Reynolds number flow over an airfoil at positive angle of attack, one would expect to observe a counter-clockwise vortex being shed from the trailing edge. This occurs because the higher pressure on the lower surface tends to curl into the low-pressure region on the upper surface. However, the freestream momentum generally carries the flow outward, generating a trailing-edge vortex with counter-clockwise rotation—consistent with the generation of positive lift and adherence to the Kutta condition.

In contrast, the simulations presented here reveal the opposite behavior. Due to premature flow separation on the lower surface—caused by the low-energy nature of the low Reynolds number flow—a clockwise vorticity structure is formed instead. This abnormal vortex structure reinforces the circulation reversal around the trailing edge, promoting the flow spillover observed in earlier streamline plots. As a result, the clockwise vorticity at the trailing edge directly correlates with the generation of negative lift in this angle of attack range.

In contrast to the previous works presented in Section 1.3, which investigated a NACA 0012 airfoil at a Reynolds number of $Re = 40,000$, this study utilizes a thicker NACA 0018 airfoil in a significantly lower Reynolds number flow of $Re = 10,000$. Given these fundamental differences, it is difficult to draw direct comparisons between the two cases beyond general trends and shared physical mechanisms.

In the prior studies, the region of negative lift was consistently observed to end by an angle of attack of approximately 2°. However, in the present simulations, negative lift persists up to nearly 4.5°. Although the exact reason for this extended range cannot be definitively stated, it is

hypothesized that the increased airfoil thickness plays a crucial role—particularly from an energy and pressure gradient perspective.

Similarly, the higher Reynolds number in previous works implies a more energetic flow, which is better able to resist separation. As discussed earlier, the onset of separation in low Reynolds flows is closely tied to the presence of moderate adverse pressure gradients. These gradients lead to early flow detachment, allowing the formation of recirculation zones and, subsequently, the circulation and spillover mechanisms that produce negative lift.

A thinner airfoil, such as the NACA 0012, would generate a less severe adverse pressure gradient on the lower surface. This would enable the flow to begin remaining attached at a smaller angle, higher pressure retention on the lower surface. Both effects contribute to earlier re-establishment of the Kutta condition and suppression of the negative lift behavior. Therefore, in higher Reynolds number flows or with thinner airfoils, the region of negative lift is naturally reduced, as the flow is more capable of maintaining attachment and resisting the conditions that lead to reversed circulation.

Additionally, this study examined the influence of span length on the behavior of negative lift within this low Reynolds number regime. While the reasons behind why certain span cases produced more negative lift than others remain unclear, one consistent trend emerged: the overall extent of the negative lift region appears unaffected by span. All simulated cases—including the four finite-span configurations and the infinite-span reference—transitioned to positive lift production at nearly the same angle of attack. This suggests that span length does not significantly influence the range of angles over which negative lift occurs.

This observation contrasts with the behavior of the pseudo-stall region, whose onset and characteristics were found to be sensitive to span length. In that case, increasing span delays the onset of pseudo-stall, highlighting a key distinction in how span affects different aerodynamic metrics at low Reynolds numbers.

5.2.2 Region of Pseudo-Stall

Stall is traditionally defined as the separation of flow along the surface of an airfoil, leading to a sudden loss of lift. In each of the finite-span cases studied here, a similar abrupt drop in lift is observed. However, in low Reynolds number flows, flow separation is prevalent even at low angles

of attack. This makes it difficult to classify the observed behavior as a conventional stall, since one could argue that the wings are already in a stalled condition from the onset of any angle of attack.

Therefore, the term pseudo-stall is used to describe this phenomenon—it resembles classical stall in appearance but is governed by different underlying flow physics. This section aims to investigate the mechanism responsible for the loss of lift in this regime and to explore its connection to the behavior of the wingtip vortices.

An examination of Figure 5.2 reveals that the pseudo-stall region is present in all finite-span wing cases but is notably absent in the infinite-span case. This observation strongly suggests that wingtip vortices play a significant role in the emergence of the pseudo-stall phenomenon. Moreover, while the presence of wingtips appears to be the primary cause of pseudo-stall, the angle at which it begins is influenced by the span length. Specifically, pseudo-stall is observed to initiate at approximately 6° for a span of 1, 7° for a span of 2, 8° for a span of 3, and 9° for a span of 4.

This trend implies an interlinked relationship: the occurrence of pseudo-stall is enabled by wingtip effects, while its onset is governed by the span. Larger spans delay the onset, suggesting a span-dependent sensitivity to the flow structures that trigger pseudo-stall in low Reynolds number regimes.

Figure 5.11 illustrates the spanwise distribution of the coefficient of friction near the wingtip, approximately $\approx 0.12c$ from the edge. While all angles of attack exhibit similar overall trends, there are several key differences that may help explain the onset of pseudo-stall. Notably, with increasing angle of attack, the friction coefficient decays more rapidly after the global maximum—associated with the adverse pressure gradient—indicating earlier boundary layer weakening. Among these cases, the 10° profile decays to the lowest plateau value and shows a delayed recovery compared to the others. Additionally, near the trailing edge ($x/C \approx 0.85$), it exhibits a noticeably steeper decline in surface friction. This reduction points to a significant loss of local boundary layer momentum, likely due to a weakening or breakdown of the downwash generated by the wingtip vortex. Such behavior may signify the onset of vortex shedding, representing a critical transition in the structure of the trailing vortex system and its influence on aerodynamic performance.

Figure 5.12 provides another perspective on the surface friction distribution, now plotted along the airfoil surface with contour lines indicating the sign change of the friction coefficient. These

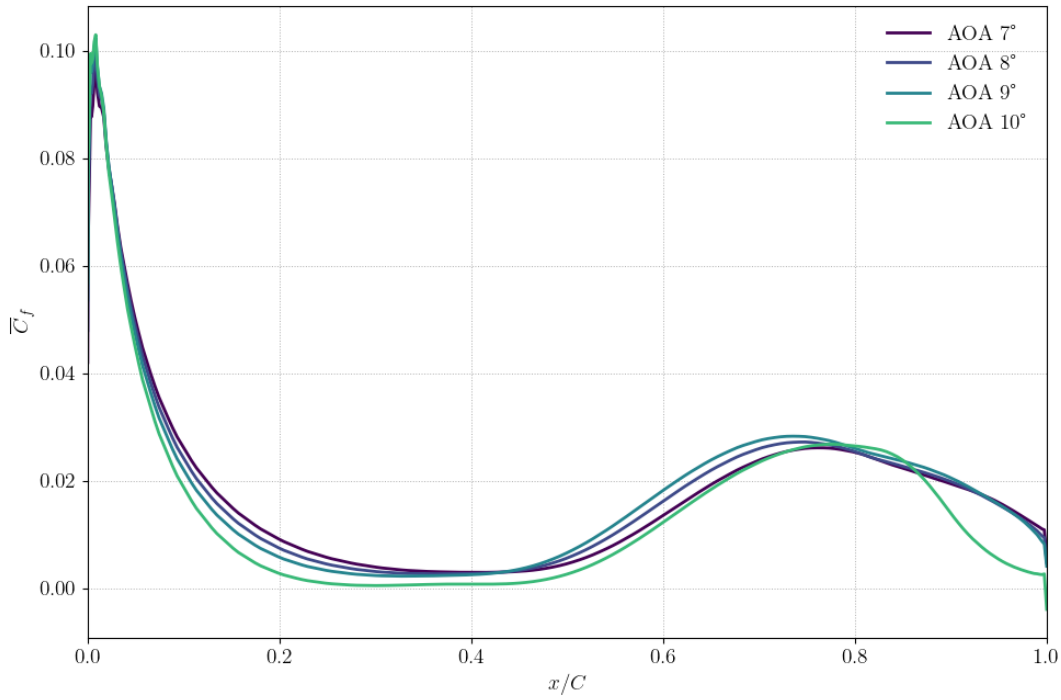

Figure 5.11. Coefficient of friction of the upper surface at $1.8764c$ from the mid-span.

contours serve as visual indicators of flow reversal and thus highlight regions of flow separation. From these visualizations, it is evident that although a large portion of the span experiences separation at higher angles of attack, the wing edges—particularly near the tips—tend to remain largely attached. Each case shows a narrow stream, originating near the leading edge, that enters the flow domain from the wingtips. This stream consistently curls inboard and expands with chordwise progression. This feature results from the downwash generated by the wingtip vortex.

These figures further support the conclusion that pseudo-stall is associated with a weakening of the wingtip vortex. Annotations on each figure denote two critical measurements: the distance from the wing edge to the onset of flow separation, and the lateral width of the curling stream near the trailing edge. Regarding the length to separation, it is expected to decrease with increasing angle of attack due to the stronger adverse pressure gradient, leading to earlier flow separation. This earlier separation provides more opportunity for the separation to expand outward before encountering a fully developed wingtip vortex. While gradual decreases in separation length are observed between 7°–8° $0.024c$ and 8°–9° $0.026c$, a significantly larger reduction of $0.049c$ occurs

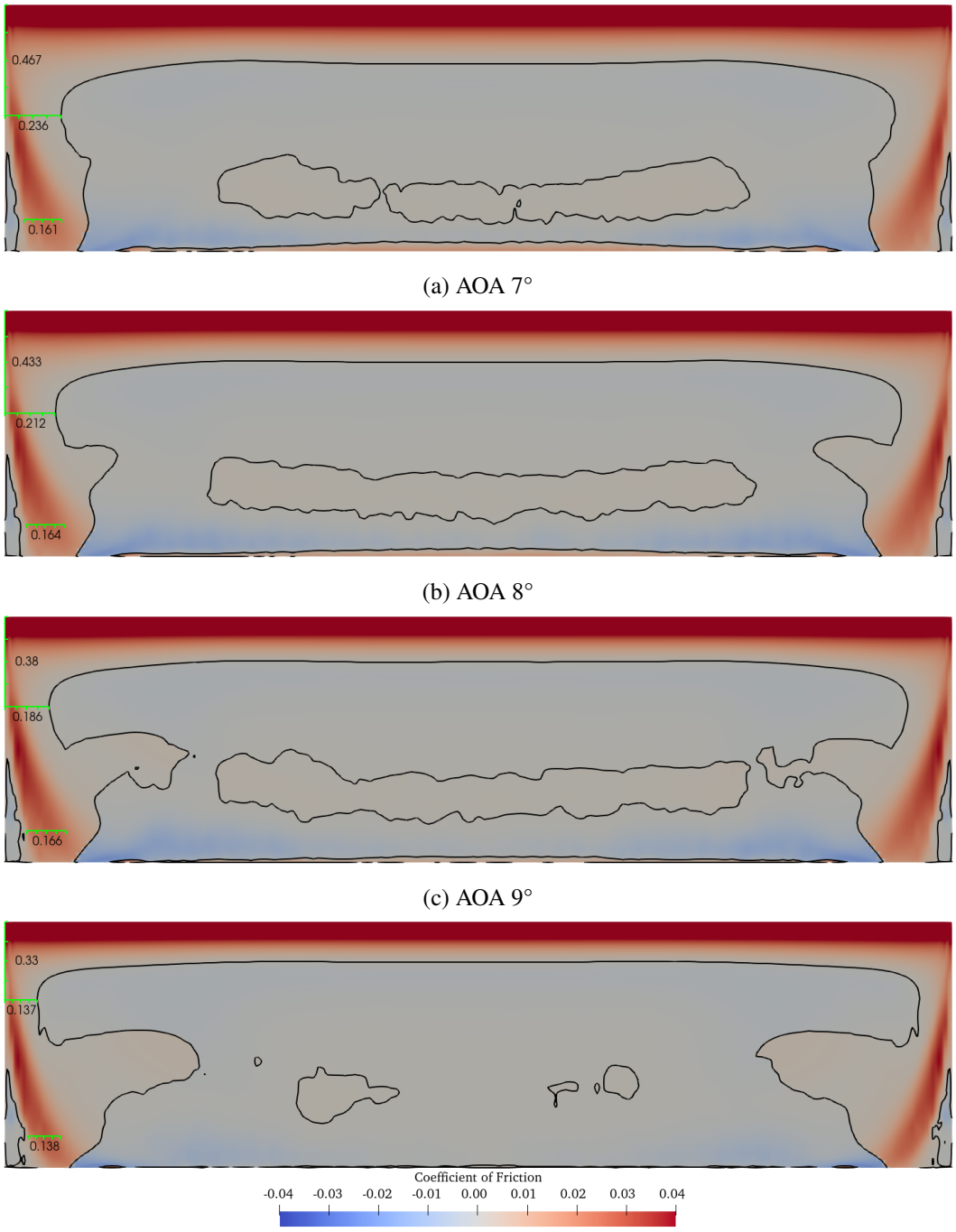

(a) AOA 7°

(b) AOA 8°

(c) AOA 9°

(d) AOA 10°

Figure 5.12. Coefficient of friction over the upper surface of a span 4 wing at various angles of attack.

from 9° to 10°—coinciding with the pseudo-stall region. This sharp drop strongly suggests a notable weakening of the vortex structure.

Conversely, the lateral width of the vortex-induced stream is expected to increase with angle of

attack due to a greater pressure differential between the upper and lower surfaces. Indeed, this trend is observed from 7° to 9°; however, at 10°, there is a pronounced reduction in width. This collapse in spanwise vortex influence reinforces the notion that the downwash generated by the wingtip vortex has diminished substantially. In earlier cases, this downwash played a key role in suppressing outboard expansion of the separated flow. Its reduced influence at 10° allows the separation region to propagate more freely, further reinforcing the link between wingtip vortex strength and the onset of pseudo-stall.

While the occurrence of pseudo-stall has been linked to the weakening of the wingtip vortex influence, the specific angle at which it begins has not yet been discussed in detail. Although the mechanisms behind pseudo-stall are more complex than what this study was designed to fully capture, a clear trend was identified. The following figures present the coefficient of friction distribution on the lower surface of the wing, analogous to the upper surface plots shown previously in Figure 5.12.

As shown in Figure 5.13, symmetric separation bubbles are present on the lower surface prior to the onset of pseudo-stall. These features are clearly visible in Figures 5.13a and 5.13c, but they disappear at angles beyond the pseudo-stall threshold. Although this study was not able to identify a definitive mechanism linking the disappearance of these bubbles to the initiation of pseudo-stall, the observed correlation is noteworthy. It is important to emphasize, however, that this correlation does not necessarily imply that the establishment of fully attached flow on the lower surface directly causes pseudo-stall.

5.2.3 Region of Non Linear Lift

As discussed earlier, a region of non-linear lift growth was observed across all simulated cases. This behavior is atypical in high Reynolds number flows, which generally exhibit linear lift characteristics consistent with the assumptions of thin airfoil theory—namely, inviscid flow and dominance of inertial forces. In contrast, the current study operates within a low Reynolds number regime, where viscous effects become significant and alter the aerodynamic response. This section examines the flow dynamics responsible for the observed non-linearity in lift development and presents key observations regarding the mechanisms driving this deviation from classical theory.

In Figure 5.14, two distinct trends emerge in the pressure distribution over the wing surface. At

(a) Span 3, AOA 8°

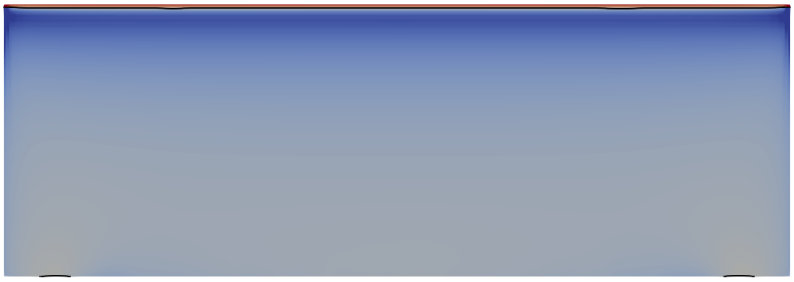

(b) Span 3, AOA 9°

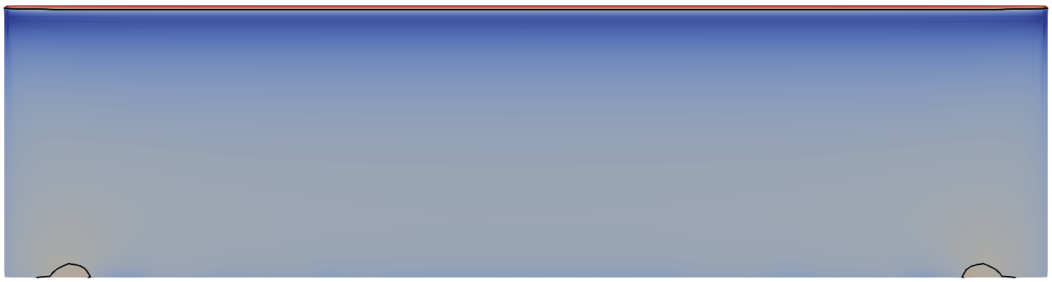

(c) Span 4, AOA 9°

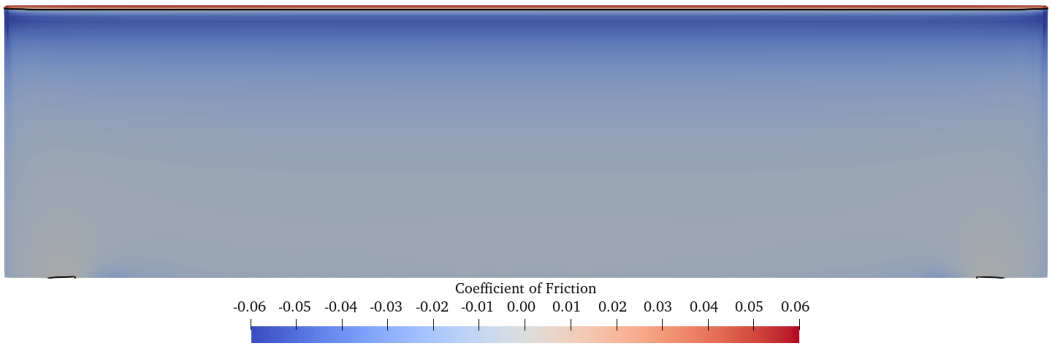

(d) Span 4, AOA 10°

Figure 5.13. Coefficient of friction over the lower surface in the region of pseudo-stall.

lower angles of attack—specifically 5° and 6°—the peak suction on the suction surface is weakest, as expected for the smallest angles in the non-linear lift growth region. Notably, the suction pressure decays and plateaus at a level substantially higher (i.e., less negative) than the pressure on the pressure

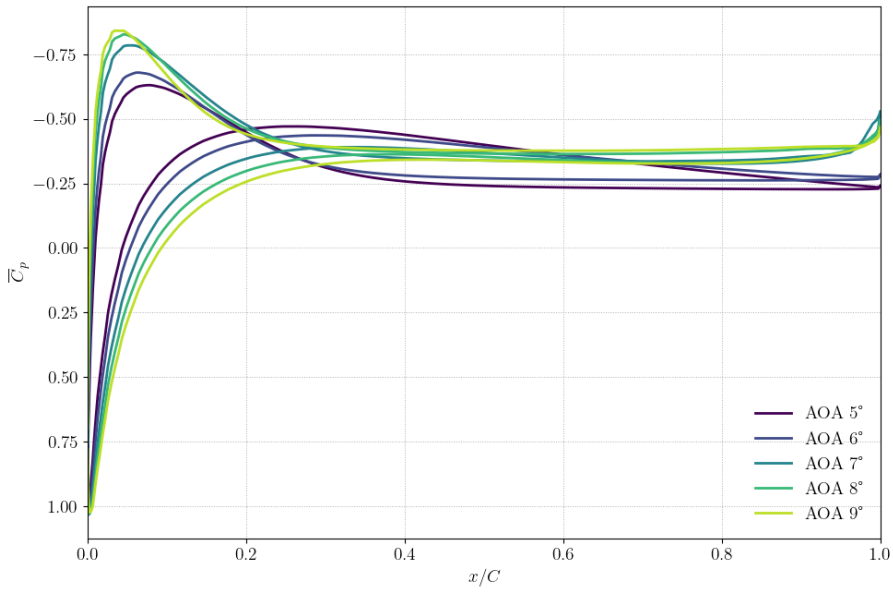

Figure 5.14. Coefficient of pressure at mid-span for a wing of span 4 at various angles of attack in the region of non linear lift.

surface. This results in a net negative pressure differential over the aft portion of the chord, effectively canceling part of the lift generated in the forward region and leading to a reduced overall lift force.

In contrast, for the higher angles of 7°, 8°, and 9°, although the peak suction is stronger, the suction-side pressure decays more rapidly but plateaus at a level roughly equal to that on the pressure side. This convergence yields a minimal pressure differential in the aft section, allowing the lift generated in the leading portion of the chord to be largely preserved.

Thus, at 5° and 6°, a significant portion of the aft chord contributes to a reverse pressure gradient that diminishes lift. For 7° to 9°, the more favorable pressure balance across the aft section enables net positive lift accumulation. This transition in pressure behavior across the chord explains the non-linear lift growth observed in this intermediate angle of attack range.

Figure 5.15 illustrates a flow mechanism that may be responsible for the change in behavior observed in Figure 5.14. Specifically, at an angle of attack of 7°, a new counter-clockwise vortex forms near the trailing edge and remains present at higher angles. This vortex appears to play a key role in stabilizing the pressure distribution on the suction surface, particularly in the aft portion of the airfoil. By promoting a more uniform pressure distribution across the upper and lower surfaces toward the trailing edge, this vortex helps to equalize the aft pressure differential. As a result, it

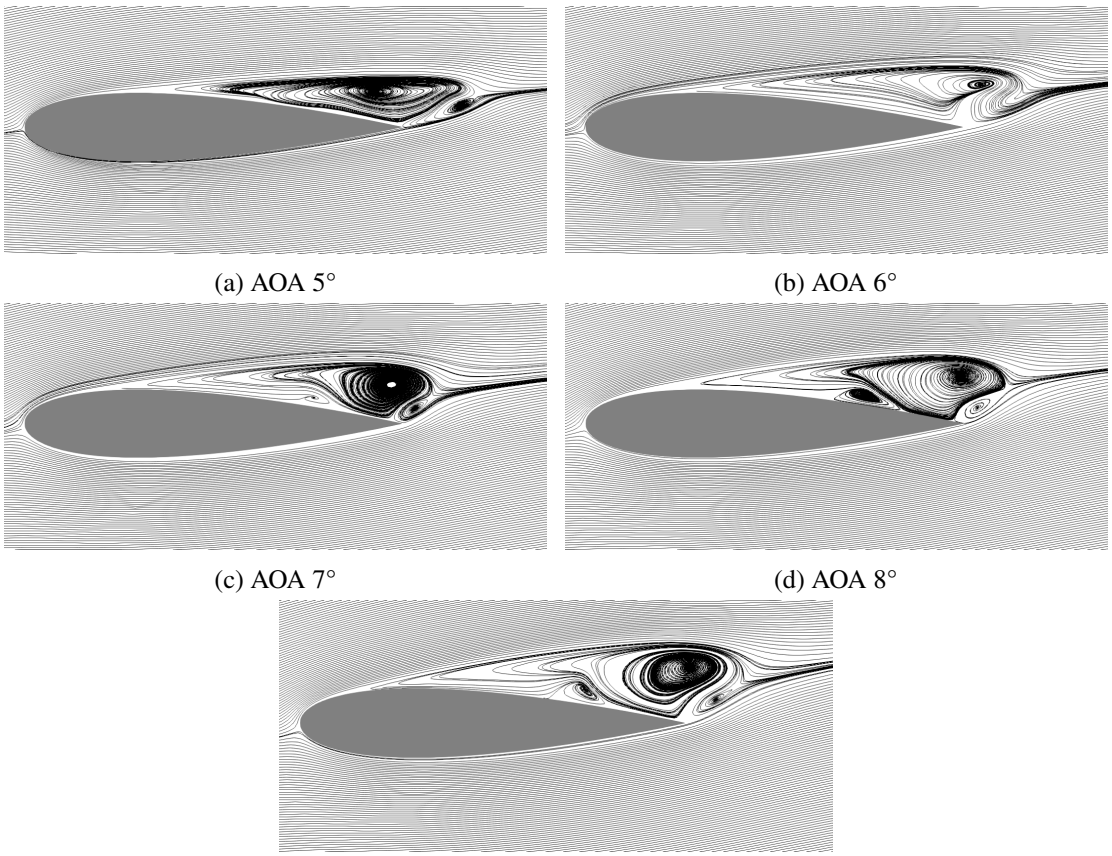

(a) AOA 5°

(b) AOA 6°

(c) AOA 7°

(d) AOA 8°

(e) AOA 9°

Figure 5.15. Flow streamlines around a wing of span 4 at various angles of attack in the non linear lift region.

allows more of the lift generated near the leading edge to be preserved—unlike in earlier cases (e.g., 5° and 6°), where the absence of this vortex led to adverse pressure differences and a reduction in total lift.

5.2.4 Region of Linear Lift

In the previous section, the region of non-linear lift growth was examined. This section now turns to the linear region. While linear lift behavior is typically associated with high Reynolds number flows at small angles of attack—where thin airfoil theory assumptions hold—it is important to note that linear lift growth can also occur in the post-stall region. In this regime, the airfoil no longer functions effectively as an aerodynamic lifting surface. Instead, lift is generated primarily through an increase in the projected surface area exposed to the free stream. Since aerodynamic force is a

function of both pressure and area, increasing the exposed surface area results in greater lift, even though flow over the surface may be largely separated. This geometric mechanism underlies the observed linear lift growth in the post-stall region.

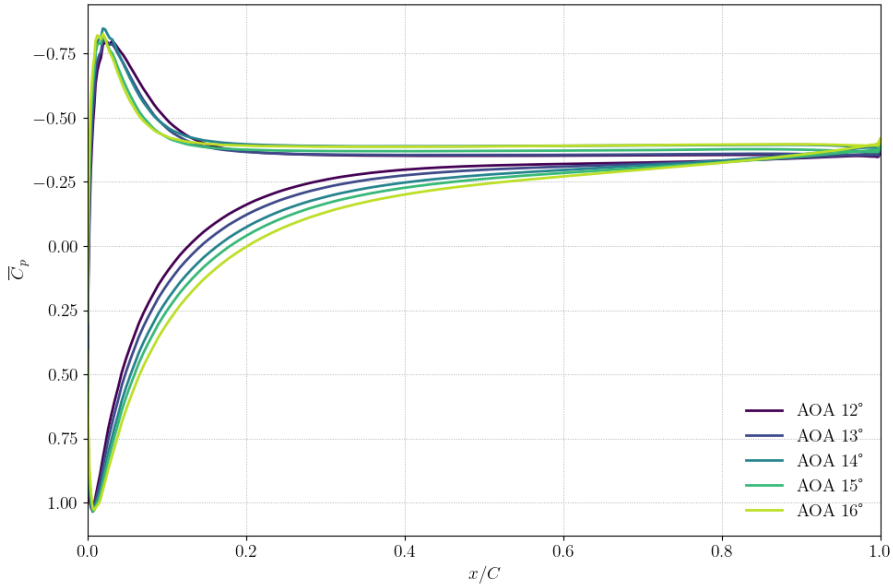

Figure 5.16. Coefficient of pressure at mid-span for a wing of span 4 at various angles of attack in the region of linear lift.

Figure 5.16 demonstrates that the mechanism behind lift growth after pseudo-stall is the same as that observed post-stall. In the figure, all presented angles of attack exhibit nearly identical peak suction forces on the upper surface. While the rate of decay varies slightly among the cases, the suction values eventually plateau at similar levels—those with faster decay tend to plateau slightly higher. This suggests that the suction contribution to lift remains relatively consistent across these angles, and thus any differences in total lift must stem from the pressure side.

On the pressure surface, it is observed that as the angle of attack increases, the pressure force decays more gradually along the chord. This slower decay indicates that more of the surface maintains higher pressure for longer, contributing to greater overall lift. These observations support the conclusion that, in this region, lift is no longer primarily generated by aerodynamic mechanisms such as favorable pressure gradients or attached flow. Instead, it arises from a geometric mechanism, whereby increased effective surface area exposed to the free stream contributes to lift through increased pressure force.

5.3 Development of the Turbulent Flow Structures

While Sections 5.1 and 5.2 present the results from a numerical perspective, the following section provides a visual interpretation of the observed flow behavior. Figure 5.17 shows Q-criterion contours at a value of 0.1 for all 21 simulated angles of attack in the Span 4 case. These contours are taken after 100 convective time-steps, once the flow has reached a fully developed state.

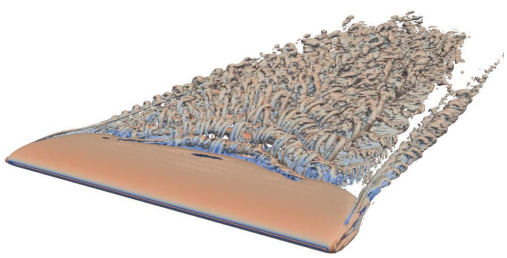

(a) 0°

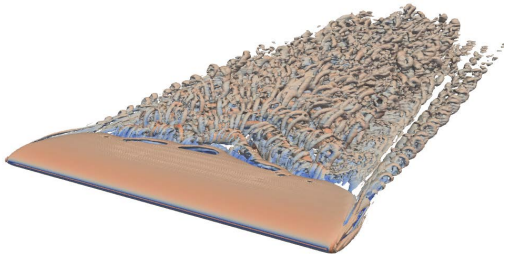

(b) 1°

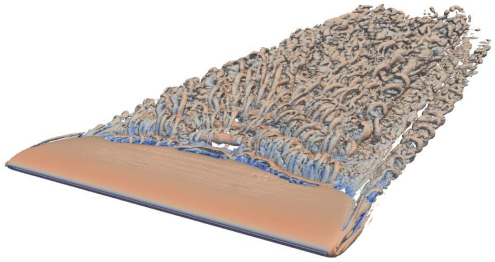

(c) 2°

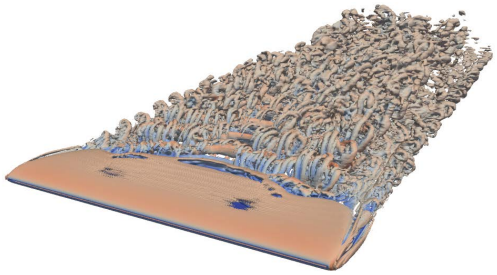

(d) 3°

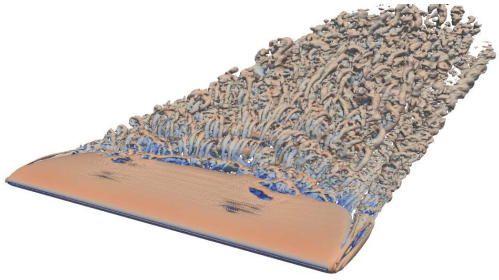

(e) 4°

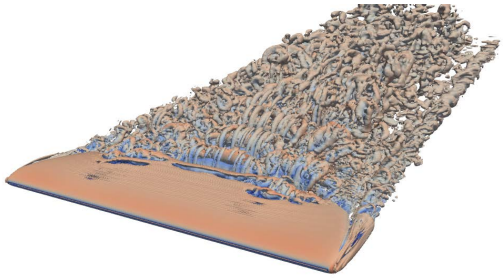

(f) 5°

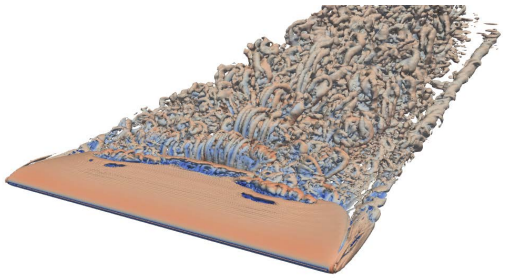

(g) 6°

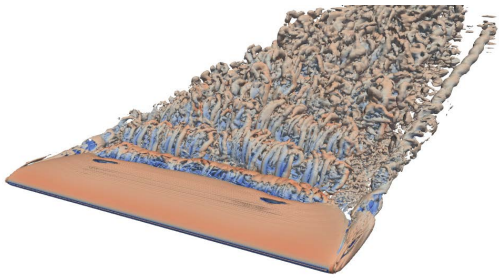

(h) 7°

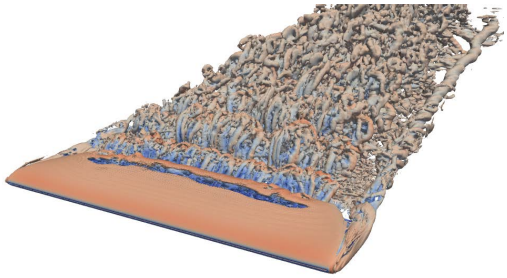

(i) 8°

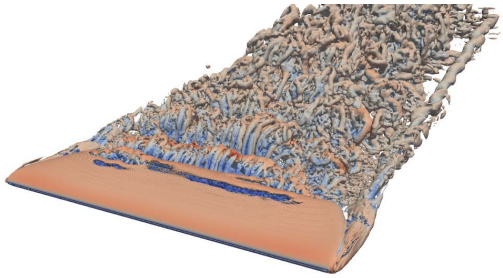

(j) 9°

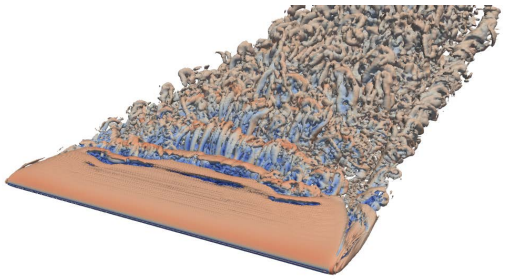

(k) 10°

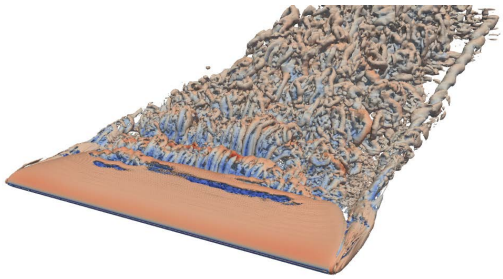

(l) 11°

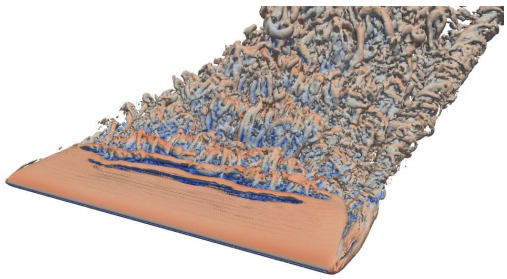

(m) 12°

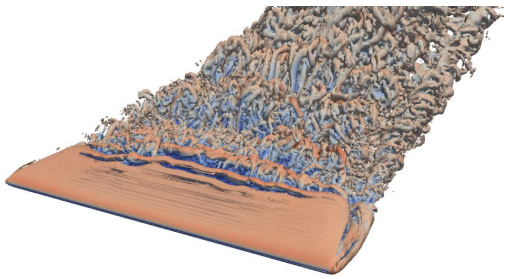

(n) 13°

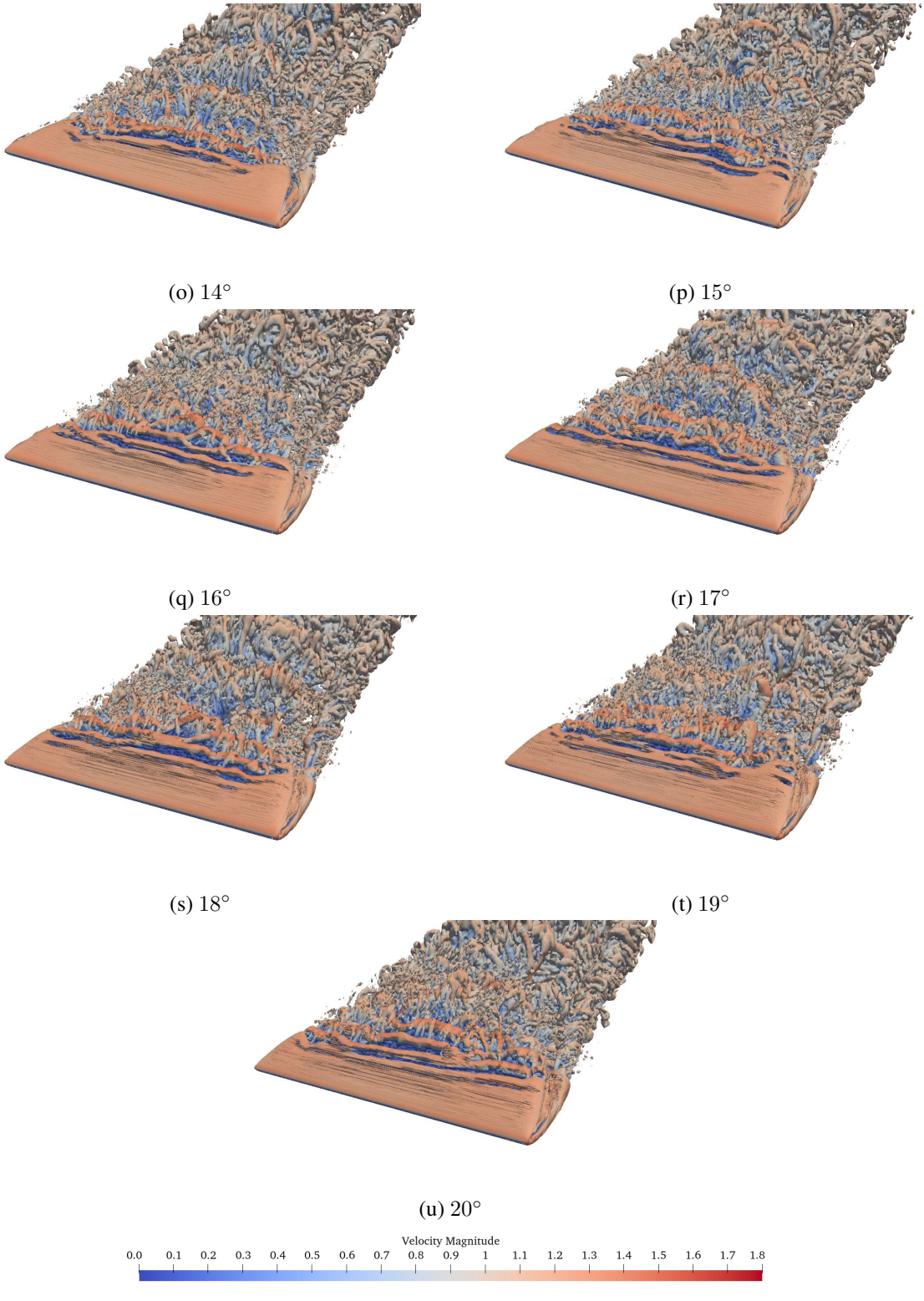

Figure 5.17. Q-criterion contours at each simulated angle of attack for a span 4 wing.

Looking at Figure 5.17a ($0°$) to Figure 5.17e ($4°$), corresponding to the negative lift region, the flow over the wing remains largely smooth until the onset of turbulence near the trailing edge. These contours also show that the wingtip vortex remains well-isolated from the wake turbulence, maintaining a coherent core structure surrounded by an outer spiral. Both features persist downstream until gradual dissipation occurs.

Transitioning to Figures 5.17f ($5°$) through 5.17j ($9°$), which coincide with the non-linear lift region, flow separation begins to develop. At $5°$ and $6°$, separation initiates at the trailing edge in a non-uniform manner. From $7°$, onward, however, the separation becomes more uniform across the span. The separated flow forms a smoother, more coherent structure that reattaches only near the wing tips. In this regime, the wingtip vortex remains isolated from the wake, though the outer spiral structure diminishes, leaving primarily the core structure downstream.

In the post pseudo-stall regime, Figure 5.17k on-wards, the flow undergoes a dramatic transition. Distinct separation occurs earlier along the chord, with coherent vortical structures shed before the wake region. The surface flow becomes increasingly chaotic, and the wingtip vortex is no longer isolated; instead, it convects inward toward mid-span, merging with the wake turbulence. Consequently, the wake itself becomes significantly more disordered compared to the pre–pseudo-stall angles.

5.3.1 Asymmetric Flow

For the case of span 3, the Q-criterion contours exhibit the same overall trends as those discussed in Section 5.3, once aligned with the lift behavior presented in Section 5.2. However, the same level of agreement is not observed for the cases of spans 1 and 2. While these shorter spans show good consistency with the larger-span cases in the post–negative lift region, their behavior at small angles of attack is markedly different: the flow develops asymmetries not present in the higher-span configurations.

Figure 5.18 illustrates the asymmetries observed in the simulations. These asymmetric flow features persist up to an angle of attack of approximately $3°$ to $4°$, although their severity diminishes with increasing angle. While no definitive physical explanation was identified, the overall aerodynamic trends and integrated force coefficients remained consistent with the results from the span 3

and span 4 cases.

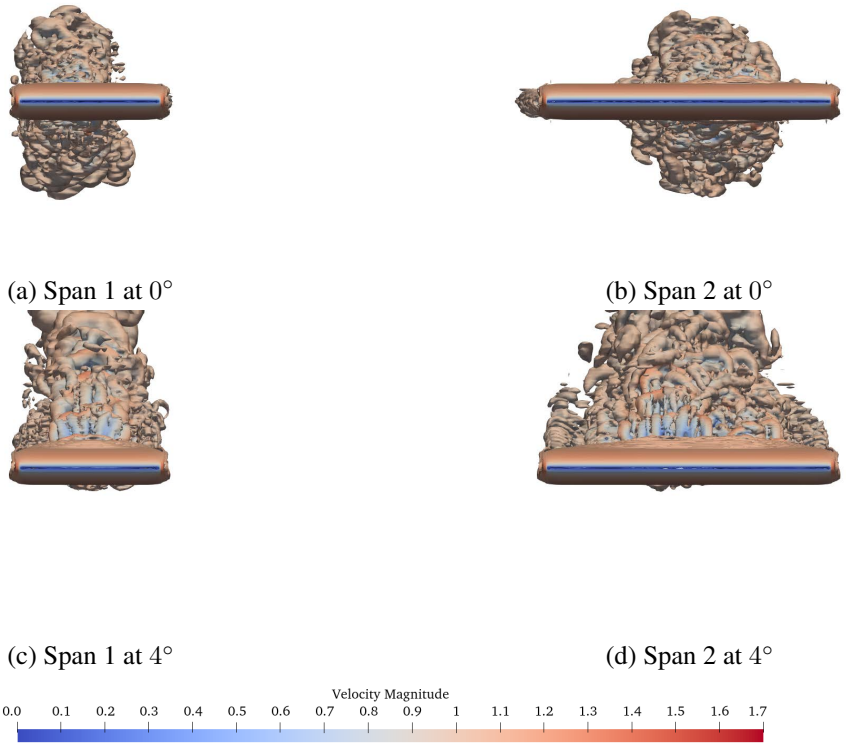

(a) Span 1 at 0°

(b) Span 2 at 0°

(c) Span 1 at 4°

(d) Span 2 at 4°

Figure 5.18. Asymmetric Q-criterion contours.

Although asymmetry is not commonly observed in the flow over geometrically symmetric wings, it has been documented in symmetric bluff-body annular flows [59]. In such annular configurations, when the Reynolds number is sufficiently low, the flow issuing from the annular jet behaves as a bluff body and may exhibit spontaneous asymmetry. Previous studies have shown that these flow asymmetries can be suppressed through the introduction of swirl into the jet. In the context of the present study, it is important to note that the airfoil, as introduced at the beginning of Chapter 5, functions primarily as a bluff body rather than as an aerodynamic lifting surface. Consequently, it is plausible that the underlying mechanism responsible for the observed asymmetries is analogous in both cases.

Chapter 6

Conclusion

This thesis investigated the aerodynamic performance and flow behavior of a NACA 0018 airfoil in low Reynolds number conditions ($Re = 10,000$), with a particular focus on finite-span effects. This led to the identification and analysis of several non-traditional aerodynamic phenomena, including the generation of negative lift at positive angles of attack, the onset of a pseudo-stall behavior, the presence of non-linear lift characteristics driven by unsteady laminar separation, and the emergence of linear lift trends attributed to geometric lift generation in the post-stall regime.

High-fidelity simulations were conducted across a range of angles of attack and spanwise domain extents. By systematically varying the wing span, both infinite and finite-span configurations were analyzed to isolate and understand the impact of three-dimensional effects, particularly those induced by wingtip vortices. While the presence of a negative lift region has been observed in earlier studies, this work uniquely identified a broader range of negative lift angles for the thicker NACA 0018 airfoil. The study attributed this to the compounded effects of airfoil thickness and lower flow energization due to the reduced Reynolds number.

A key focus of this thesis was the identification and characterization of a phenomenon termed "pseudo-stall." Unlike classical stall driven by leading-edge separation and global loss of lift, the occurrence of pseudo-stall was shown to originate from the weakening of the wingtip vortex. Visualizations of surface friction and pressure distribution revealed that pseudo-stall is tied to the breakdown of suction side vortex-induced downwash, and its onset angle increases with span length. Importantly, the range of angles producing negative lift was shown to be unaffected by span, while

the spanwise onset of pseudo-stall was clearly linked to the evolving structure and strength of the wingtip vortex.

This study used the EDAC formulation as the system of governing equation to simulate low Reynolds number incompressible flow regimes. The EDAC method modifies the classical compressible Navier Stokes equations by introducing artificial compressibility in a mathematically consistent and entropy stable manner. This approach enhances numerical stability and robustness in under-resolved laminar and transitional flows, where traditional formulations may suffer from spurious oscillations or convergence issues.

The EDAC equations maintain conservation of mass, momentum, and energy, with viscous stresses modeled using the Newtonian fluid assumption and laminar viscosity. The entropy consistent structure of the EDAC system allows it to support high-order unsteady solvers and provides an ideal foundation for DNS, where accurate resolution of all relevant flow scales is required without turbulence modeling.

For spatial discretization, the FR) method was employed due to its high-order accuracy, low dissipation, and ability to capture complex flow structures on unstructured meshes. Time advancement was performed using a P-ERK scheme, which offers improved temporal stability and accuracy while remaining computationally efficient for unsteady DNS computations.

This thesis has provided new insights into the aerodynamic behavior of finite-span wings operating in the low Reynolds number regime. A key contribution of this work is the characterization of pseudo-stall as a distinct phenomenon, shown to be governed primarily by the behavior and weakening of the wingtip vortex. Unlike conventional stall, pseudo-stall is not driven by full flow separation but rather by the loss of vortex-induced downwash, which alters the spanwise lift distribution.

The analysis presented detailed observations of surface pressure and friction distributions, enabling a clearer understanding of how lift evolves before, during, and after stall. In particular, the emergence of negative lift at positive angles of attack, the non-linear region of lift growth, and the transition into a post-stall linear lift regime have all been linked to unique flow structures such as counter-rotating vortices and early separation bubbles.

Future research is encouraged to further investigate the mechanisms underlying pseudo-stall, including its onset criteria and dependency on span and tip effects. Additionally, the observed

correlation between lower surface flow behavior and pseudo-stall onset warrants further examination. Exploring the influence of airfoil thickness on the negative lift region, as well as evaluating other airfoil geometries, dynamic stall conditions, and active flow control strategies aimed at modifying wingtip vortices, may offer paths to mitigate or exploit these phenomena for improved aerodynamic performance in low Reynolds number applications.

References

[1] P. A. Davidson, Ed., *Turbulence: an introduction for scientists and engineers*, Oxford, UK New York: Oxford University Press, 2010, 657 pp., ISBN: 978-0-19-852948-4.

[2] M. Saldana et al., "The reynolds number: A journey from its origin to modern applications," *Fluids*, vol. 9, no. 12, p. 299, Dec. 16, 2024, ISSN: 2311-5521.

[3] M. Okamoto and A. Azuma, "Experimental study on aerodynamic characteristics of unsteady wings at low reynolds number," *AIAA Journal*, vol. 43, no. 12, pp. 2526–2536, Dec. 2005, ISSN: 0001-1452, 1533-385X.

[4] T. A. Shams, S. I. Ali Shah, and M. A. Ahmad, "Study of low reynolds number aerodynamics for low aspect ratio MAV wing," in *2018 IEEE 21st International Multi-Topic Conference (INMIC)*, Karachi: IEEE, Nov. 2018, pp. 1–8, ISBN: 978-1-5386-7536-6.

[5] S. W. Hameed, N. Imanberdiyev, E. Camci, W.-Y. Yau, and M. Feroskhan, "Bio-inspired classification and evolution of multirotor micro aerial vehicles (MAVs): A comprehensive review," *Robotics and Autonomous Systems*, vol. 182, p. 104 802, Dec. 1, 2024, ISSN: 0921-8890.

[6] L. Caros et al., "Direct numerical simulation of flow over a triangular airfoil under martian conditions," *AIAA Journal*, vol. 60, no. 7, pp. 3961–3972, Jul. 2022, ISSN: 0001-1452, 1533-385X.

[7] M. Lazaridis, *First Principles of Meteorology and Air Pollution* (Environmental Pollution). Dordrecht: Springer Netherlands, 2011, vol. 19, ISBN: 978-94-007-0161-8.

[8] T. Suwa, K. Nose, D. Numata, H. Nagai, and K. Asai, "Compressibility effects on airfoil aerodynamics at low reynolds number," in *30th AIAA Applied Aerodynamics Conference*, New Orleans, Louisiana: American Institute of Aeronautics and Astronautics, Jun. 25, 2012, ISBN: 978-1-62410-185-4.

[9] W. J. F. Koning, W. Johnson, and H. F. Grip, "Improved mars helicopter aerodynamic rotor model for comprehensive analyses," *AIAA Journal*, vol. 57, no. 9, pp. 3969–3979, Sep. 2019, ISSN: 0001-1452, 1533-385X.

[10] "Ingenuity mars helicopter on the martian surface (artist's concept) - NASA. "[Online]. Available: https://www.nasa.gov/image-article/ingenuity-mars-helicopter-martian-surface-artists-concept/.

[11] M. Von Ehrenfried, *Perseverance and the Mars 2020 Mission: Follow the Science to Jezero Crater*. Cham: Springer International Publishing, 2022, ISBN: 978-3-030-92117-0.

[12] M. F. U. Rab, M. J. Alam, A. Akhlaque, and M. Mahrukh, "Comparative analysis of high-lift airfoils for motorsports applications," presented at the AFM18, Ljubljana, Slovenia, Jul. 10, 2018, pp. 173–183.

[13] S. C. Kim and S. Y. Han, "Effect of steady airflow field on drag and downforce," *International Journal of Automotive Technology*, vol. 17, no. 2, pp. 205–211, Apr. 2016, ISSN: 1229-9138, 1976-3832.

[14] T. J. Mueller, "The influence of laminar separation and transition on low reynolds number airfoil hysteresis," *Journal of Aircraft*, vol. 22, no. 9, pp. 763–770, Sep. 1985, ISSN: 0021-8669, 1533-3868.

[15] C. Badrya, B. Govindarajan, and I. Chopra, "Basic understanding of unsteady airfoil aerodynamics at low reynolds numbers," in *2018 AIAA Aerospace Sciences Meeting*, Kissimmee, Florida: American Institute of Aeronautics and Astronautics, Jan. 8, 2018, ISBN: 978-1-62410-524-1.

[16] S. Wang, Y. Zhou, M. M. Alam, and H. Yang, "Turbulent intensity and reynolds number effects on an airfoil at low reynolds numbers," *Physics of Fluids*, vol. 26, no. 11, p. 115 107, Nov. 1, 2014, ISSN: 1070-6631, 1089-7666.

[17] P. M. Munday, K. Taira, T. Suwa, D. Numata, and K. Asai, "Nonlinear lift on a triangular airfoil in low-reynolds-number compressible flow," *Journal of Aircraft*, vol. 52, no. 3, pp. 924–931, May 2015, ISSN: 0021-8669, 1533-3868.

[18] B. C. Vermeire, C. A. Pereira, and H. Karbasian, *Computational Fluid Dynamics: An open-source approach*. Canada: Concordia University, 2020, 215 pp.

[19] S. B. Pope, *Turbulent flows*, 1. publ., 12. print. Cambridge: Cambridge Univ. Press, 2015, 771 pp., ISBN: 978-0-521-59125-6.

[20] C. A. Pereira, "Solution-acceleration strategies for high-order unstructured methods," Ph.D. dissertation, Concordia University, Montréal, Québec, Canada, Jul. 2023, 221 pp.

[21] C. Kolokotronis, "Feature-based polynomial adaptation for high-order methods applied to martian aerodynamics," Ph.D. dissertation, Concordia University, Montréal, Québec, Canada, May 26, 2023, 145 pp. [Online]. Available: `https://spectrum.library.concordia.ca/id/eprint/993020/`.

[22] W. Rodi, "DNS and LES of some engineering flows," *Fluid Dynamics Research*, vol. 38, no. 2, pp. 145–173, Feb. 2006, ISSN: 0169-5983, 1873-7005.

[23] S. Moreau, "The third golden age of aeroacoustics," *Physics of Fluids*, vol. 34, no. 3, p. 031 301, Mar. 1, 2022, ISSN: 1070-6631, 1089-7666.

[24] T. Ohtake, Y. Nakae, and T. Motohashi, "Nonlinearity of the Aerodynamic Characteristics of NACA0012 Aerofoil at Low Reynolds Numbers," *JOURNAL OF THE JAPAN SOCIETY FOR AERONAUTICAL AND SPACE SCIENCES*, vol. 55, no. 644, pp. 439–445, 2007, ISSN: 1344-6460.

[25] J. Winslow, H. Otsuka, B. Govindarajan, and I. Chopra, "Basic understanding of airfoil characteristics at low reynolds numbers (104–105)," *Journal of Aircraft*, vol. 55, no. 3, pp. 1050–1061, May 2018, ISSN: 0021-8669, 1533-3868.

[26] K. Yonemoto, K. Takato, H. Ochi, and S. Fujie, "Kutta condition violation in two-dimensional NACA0012 airfoil at low reynolds number," in *26th AIAA Applied Aerodynamics Conference*, Honolulu, Hawaii: American Institute of Aeronautics and Astronautics, Aug. 18, 2008, ISBN: 978-1-60086-987-7.

[27] J. Tank, L. Smith, and G. R. Spedding, "On the possibility (or lack thereof) of agreement between experiment and computation of flows over wings at moderate reynolds number," *Interface Focus*, vol. 7, no. 1, p. 20 160 076, Feb. 6, 2017, ISSN: 2042-8898, 2042-8901.

[28] J. Aguilar-Cabello, P. Gutierrez-Castillo, L. Parras, C. Del Pino, and E. Sanmiguel-Rojas, "On the onset of negative lift in a symmetric airfoil at very small angles of attack," *Physics of Fluids*, vol. 32, no. 5, p. 055 107, May 1, 2020, ISSN: 1070-6631, 1089-7666.

[29] J. C. Bilbao-Ludena and G. Papadakis, "Structure of vorticity and turbulence fields in a separated flow around a finite wing: Analysis using direct numerical simulation," *Physical Review Fluids*, vol. 8, no. 1, p. 014 704, Jan. 20, 2023, ISSN: 2469-990X.

[30] B. C. Vermeire, "High-order implicit large eddy simulation using entropically damped artificial compressibility," *Computers & Fluids*, vol. 268, p. 106 065, Jan. 2024, ISSN: 00457930.

[31] C. Hirsch, *Numerical computation of internal and external flows: fundamentals of computational fluid dynamics*, 2nd ed. Oxford Burlington, MA: Elsevier/Butterworth-Heinemann, 2007, ISBN: 978-0-7506-6594-0.

[32] J. D. Anderson, *Computational fluid dynamics: the basics with applications* (McGraw-Hill Series in Mechanical Engineering), Internat. ed., [repr.] New York: McGraw-Hill, 1995, 547 pp., ISBN: 978-0-07-001685-9.

[33] J. R. Clausen, "Entropically damped form of artificial compressibility for explicit simulation of incompressible flow," *Physical Review E*, vol. 87, no. 1, p. 013 309, Jan. 28, 2013, ISSN: 1539-3755, 1550-2376.

[34] W. Trojak, N. Vadlamani, J. Tyacke, F. Witherden, and A. Jameson, "Artificial compressibility approaches in flux reconstruction for incompressible viscous flow simulations," *Computers & Fluids*, vol. 247, p. 105 634, Oct. 2022, ISSN: 00457930.

[35] E. Turkel, "Preconditioned methods for solving the incompressible and low speed compressible equations," *Journal of Computational Physics*, vol. 72, no. 2, pp. 277–298, Oct. 1987, ISSN: 00219991.

[36] B. Va, W.-T. Lee, and P. Roe, "Characteristic time-stepping or local preconditioning of the euler equations," in *10th Computational Fluid Dynamics Conference*, Honolulu,HI,U.S.A.: American Institute of Aeronautics and Astronautics, Jun. 24, 1991.

[37] Y.-H. Choi and C. Merkle, "The application of preconditioning in viscous flows," *Journal of Computational Physics*, vol. 105, no. 2, pp. 207–223, Apr. 1993, ISSN: 00219991.

[38] E. Turkel, A. Fiterman, and B. Vanleer, "Preconditioning and the limit to the incompressible flow equations," NAS 1.26:191500, Jul. 1, 1993, NTRS Author Affiliations: NASA Langley Research Center NTRS Document ID: 19940009244 NTRS Research Center: Legacy CDMS (CDMS).

[39] B. L. Buzbee, G. H. Golub, and C. W. Nielson, "On direct methods for solving poisson's equations," *SIAM Journal on Numerical Analysis*, vol. 7, no. 4, pp. 627–656, Dec. 1970, ISSN: 0036-1429, 1095-7170.

[40] A. McKenney, L. Greengard, and A. Mayo, "A fast poisson solver for complex geometries," *Journal of Computational Physics*, vol. 118, no. 2, pp. 348–355, May 1995, ISSN: 00219991.

[41] G. H. Golub, L. C. Huang, H. Simon, and W.-P. Tang, "A fast poisson solver for the finite difference solution of the incompressible navier–stokes equations," *SIAM Journal on Scientific Computing*, vol. 19, no. 5, pp. 1606–1624, Sep. 1998, ISSN: 1064-8275, 1095-7197.

[42] A. Gholami, D. Malhotra, H. Sundar, and G. Biros, "FFT, FMM, or multigrid? a comparative study of state-of-the-art poisson solvers for uniform and nonuniform grids in the unit cube," *SIAM Journal on Scientific Computing*, vol. 38, no. 3, pp. C280–C306, Jan. 2016, ISSN: 1064-8275, 1095-7197.

[43] D. Fortunato and A. Townsend, "Fast poisson solvers for spectral methods," *IMA Journal of Numerical Analysis*, vol. 40, no. 3, pp. 1994–2018, Jul. 17, 2020, ISSN: 0272-4979, 1464-3642.

[44] A. J. Chorin, "A numerical method for solving incompressible viscous flow problems," *Journal of Computational Physics*, vol. 135, no. 2, pp. 118–125, Aug. 1997, ISSN: 00219991.

[45] M.-P. Bolduc, R. Ghoreishi, and B. C. Vermeire, "A high-order entropically-damped artificial compressibility approach on moving and deforming domains," *Computers & Fluids*, vol. 257, p. 105 839, May 2023, ISSN: 00457930.

[46] H. T. Huynh, "A flux reconstruction approach to high-order schemes including discontinuous galerkin methods," in *18th AIAA Computational Fluid Dynamics Conference*, Miami, Florida: American Institute of Aeronautics and Astronautics, Jun. 25, 2007, ISBN: 978-1-62410-129-8.

[47] H. Gao and Z. Wang, "A high-order lifting collocation penalty formulation for the navier-stokes equations on 2-d mixed grids," in *19th AIAA Computational Fluid Dynamics*, San Antonio, Texas: American Institute of Aeronautics and Astronautics, Jun. 22, 2009, ISBN: 978-1-62410-137-3.

[48] T. Haga, H. Gao, and Z. J. Wang, "A high-order unifying discontinuous formulation for the navier-stokes equations on 3d mixed grids," *Mathematical Modelling of Natural Phenomena*, vol. 6, no. 3, pp. 28–56, 2011, ISSN: 0973-5348, 1760-6101.

[49] R. Ghoreishi and B. C. Vermeire, "Vorticity-based polynomial adaptation for moving and deforming domains," *Computers & Fluids*, vol. 231, p. 105 160, Dec. 2021, ISSN: 00457930.

[50] K. Liu, Y. Lu, and C. You, "High-order ALE method for the navier–stokes equations on a moving hybrid unstructured mesh using flux reconstruction method," *International Journal of Computational Fluid Dynamics*, vol. 27, no. 6, pp. 251–267, Jul. 2013, ISSN: 1061-8562, 1029-0257.

[51] F. Bassi and S. Rebay, "A high-order accurate discontinuous finite element method for the numerical solution of the compressible navier–stokes equations," *Journal of Computational Physics*, vol. 131, no. 2, pp. 267–279, Mar. 1997, ISSN: 00219991.

[52] H. T. Huynh, "A reconstruction approach to high-order schemnes including discontinuous galerkin for diffusion," in *47th AIAA Aerospace Sciences Meeting including The New Horizons*

Forum and Aerospace Exposition, Orlando, Florida: American Institute of Aeronautics and Astronautics, Jan. 5, 2009, ISBN: 978-1-60086-973-0.

[53] E. Hairer, S. P. Nørsett, and G. Wanner, *Solving ordinary differential equations I: nonstiff problems* (Springer series in computational mathematics 8), 2nd rev. ed. Heidelberg ; London: Springer, 2009, 528 pp., ISBN: 978-3-540-56670-0.

[54] J. C. Butcher, "Coefficients for the study of runge-kutta integration processes," *Journal of the Australian Mathematical Society*, vol. 3, no. 2, pp. 185–201, May 1963, ISSN: 0004-9735.

[55] B. C. Vermeire, "Paired explicit runge-kutta schemes for stiff systems of equations," *Journal of Computational Physics*, vol. 393, pp. 465–483, Sep. 2019, ISSN: 00219991.

[56] S. Hedayati Nasab and B. C. Vermeire, "Third-order paired explicit runge-kutta schemes for stiff systems of equations," *Journal of Computational Physics*, vol. 468, p. 111 470, Nov. 2022, ISSN: 00219991.

[57] D. Doehring, L. Christmann, M. Schlottke-Lakemper, G. J. Gassner, and M. Torrilhon, *Fourth-order paired-explicit runge-kutta methods*, Version Number: 1, 2024. Accessed: Oct. 21, 2025.

[58] W. Zhang and R. Samtaney, "A direct numerical simulation investigation of the synthetic jet frequency effects on separation control of low-re flow past an airfoil," *Physics of Fluids*, vol. 27, no. 5, p. 055 101, May 1, 2015, ISSN: 1070-6631, 1089-7666.

[59] S. E. Gillani and Y. M. Al-Abdeli, "Insights into the intrinsic asymmetry of bluff-body stabilised swirling and non-swirling annular flows," *Experimental Thermal and Fluid Science*, vol. 150, p. 111 063, Jan. 2024, ISSN: 08941777.

Appendix A

Q-criterion Contour Plots

A.1 Span 1

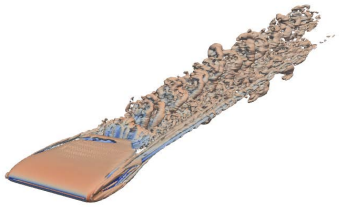

(a) 0°

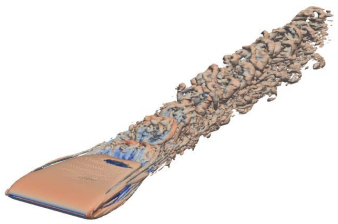

(b) 1°

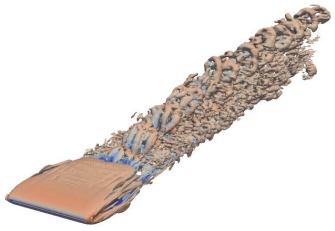

(c) 2°

(d) 3°

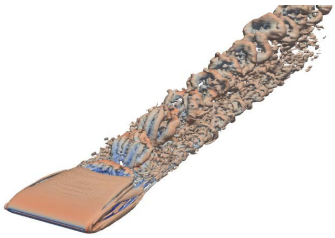

(e) 4°

(f) 5°

(g) 6°

(h) 7°

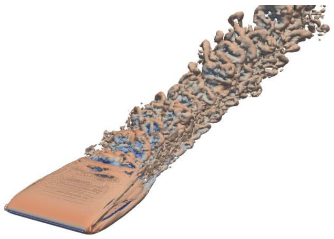

(i) 8°

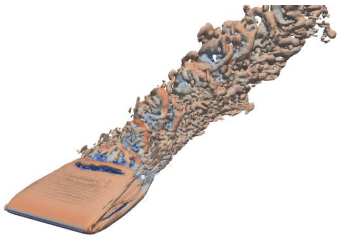

(j) 9°

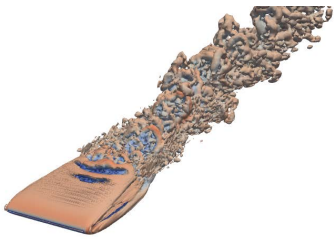

(k) 10°

(l) 11°

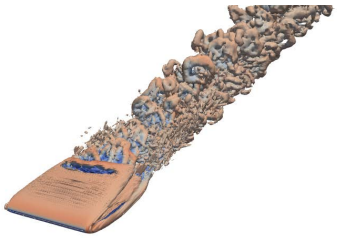

(m) 12°

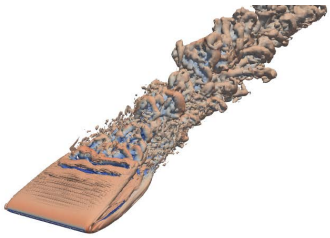

(n) 13°

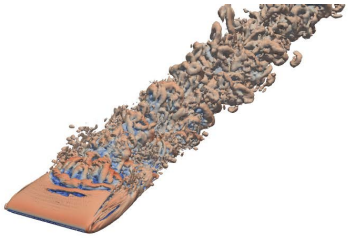

(o) 14°

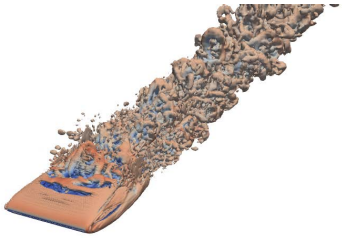

(p) 15°

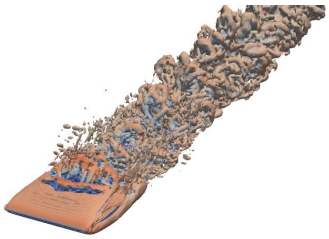

(q) 16°

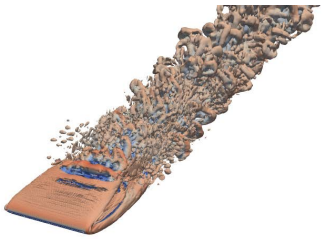

(r) 17°

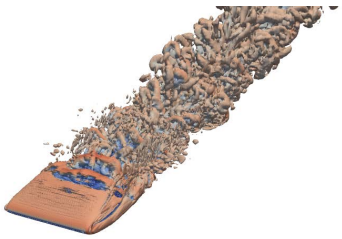

(s) 18°

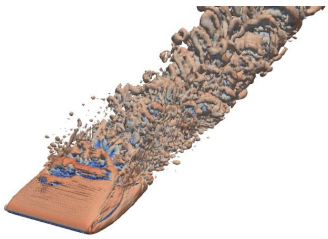

(t) 19°

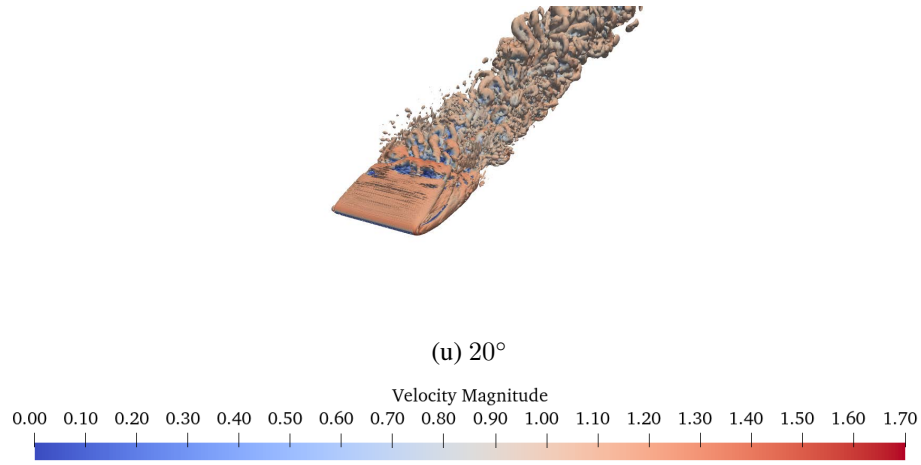

(u) 20°

Figure A.1. Q-criterion contours at each simulated angle of attack for a span 1 wing.

A.2 Span 2

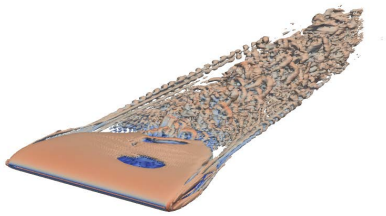

(a) 0°

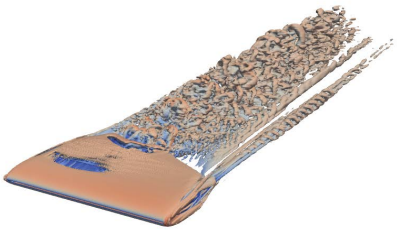

(b) 1°

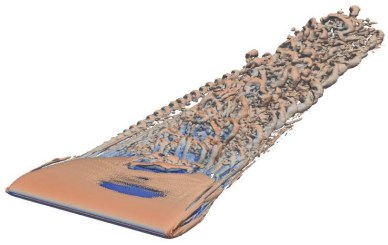

(c) 2°

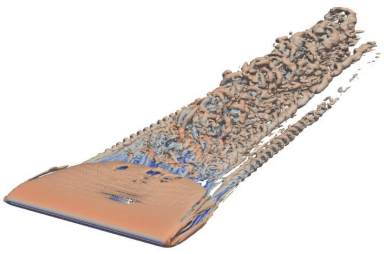

(d) 3°

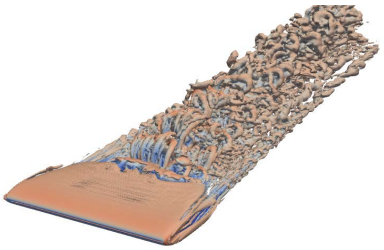

(e) 4°

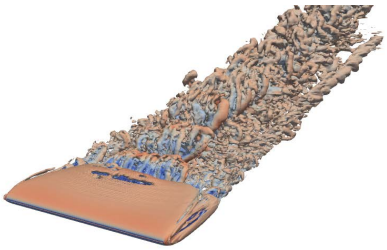

(f) 5°

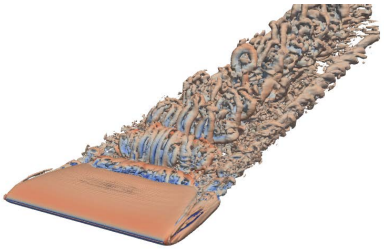

(g) 6°

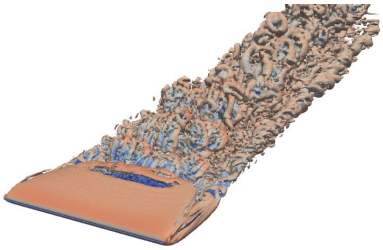

(h) 7°

(i) 8°

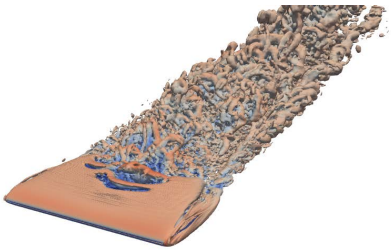

(j) 9°

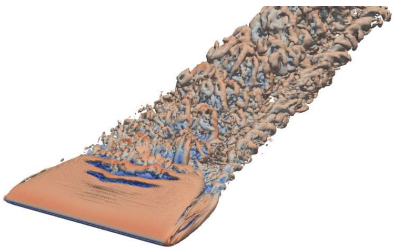

(k) 10°

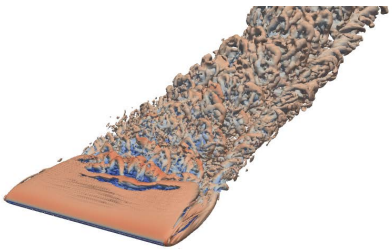

(l) 11°

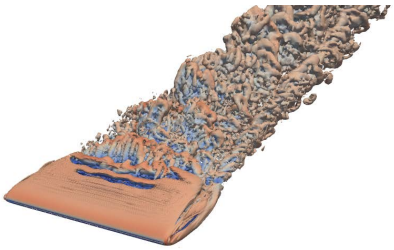

(m) 12°

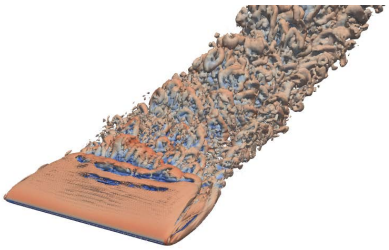

(n) 13°

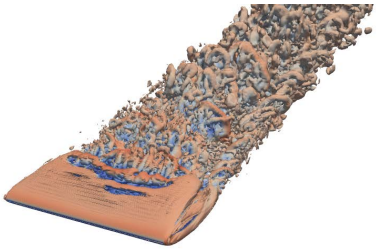

(o) 14°

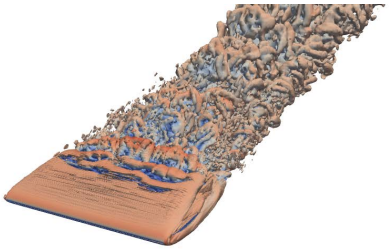

(p) 15°

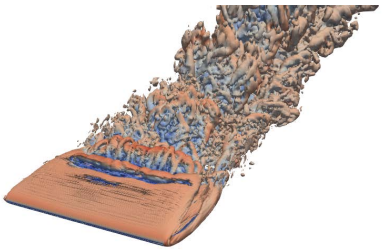

(q) 16°

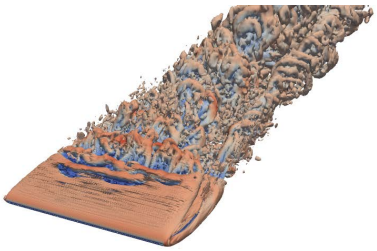

(r) 17°

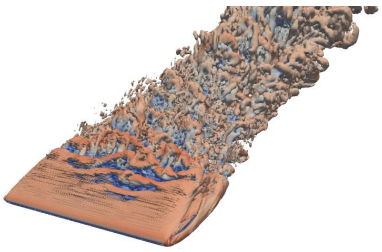

(s) 18°

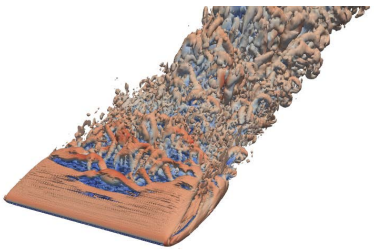

(t) 19°

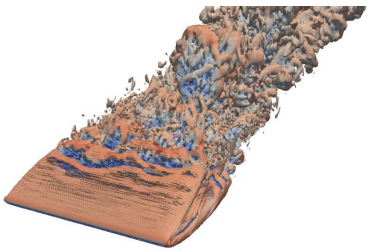

(u) 20°

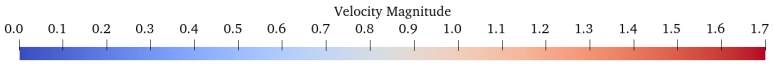

Figure A.2. Q-criterion contours at each simulated angle of attack for a span 2 wing.

A.3 Span 3

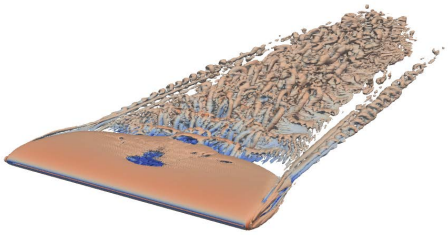

(a) 0°

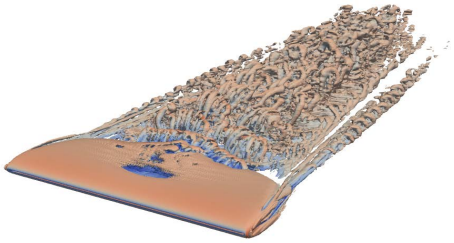

(b) 1°

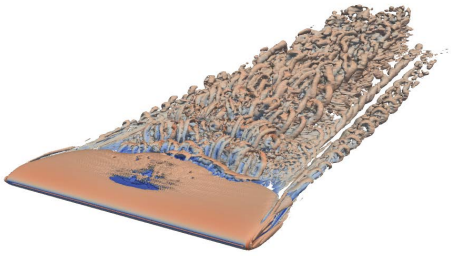

(c) 2°

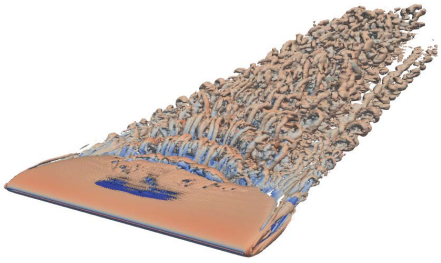

(d) 3°

(e) 4°

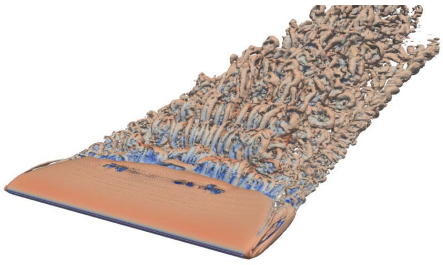

(f) 5°

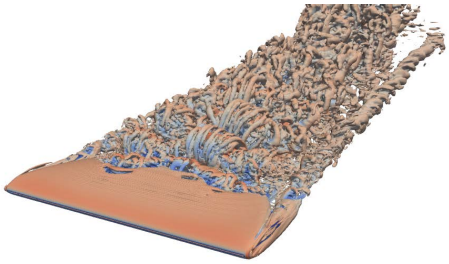

(g) 6°

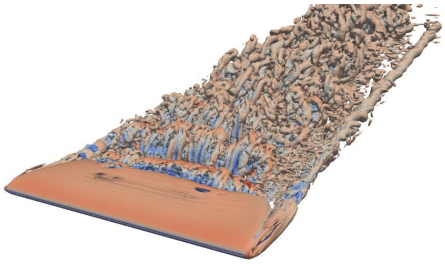

(h) 7°

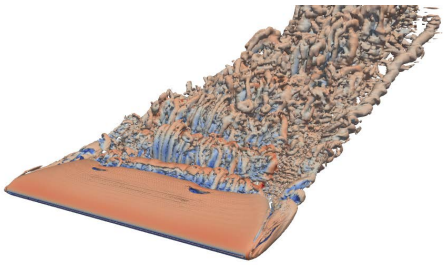

(i) 8°

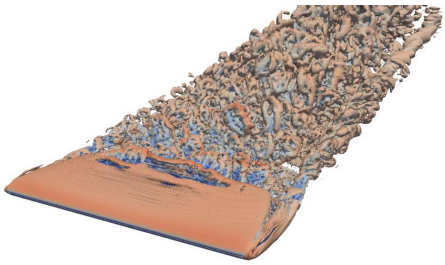

(j) 9°

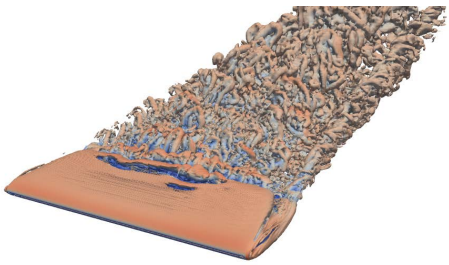

(k) 10°

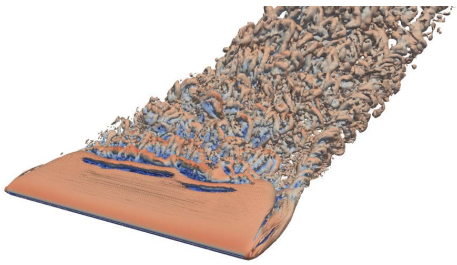

(l) 11°

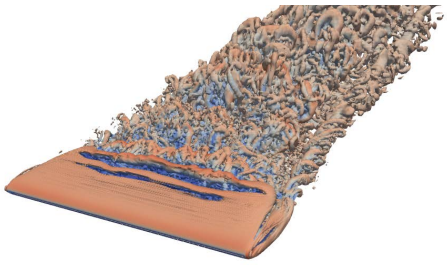

(m) 12°

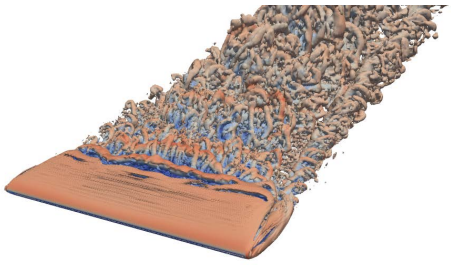

(n) 13°

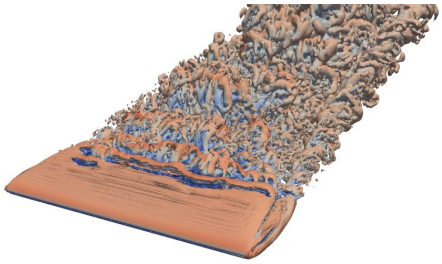

(o) 14°

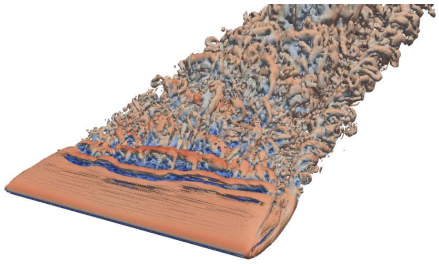

(p) 15°

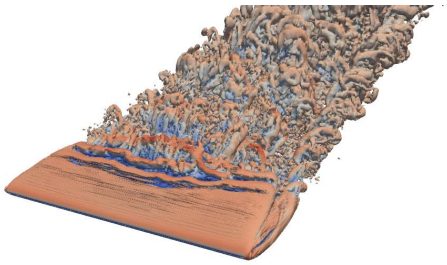

(q) 16°

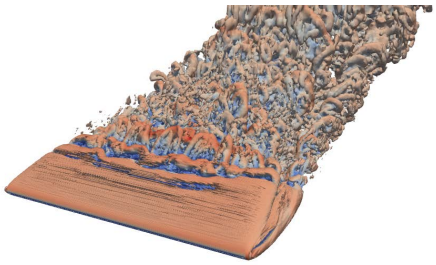

(r) 17°

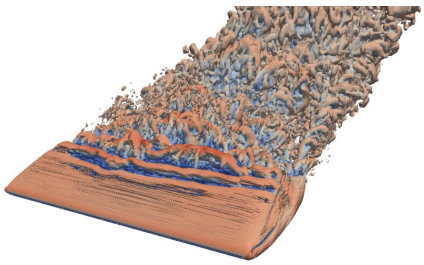

(s) 18°

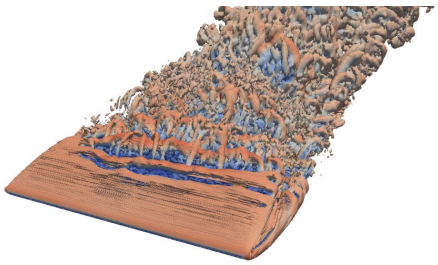

(t) 19°

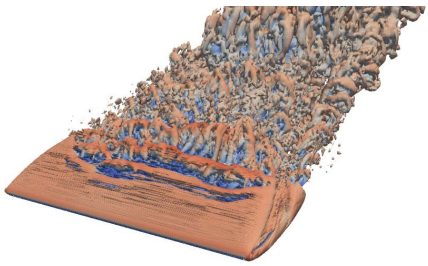

(u) 20°

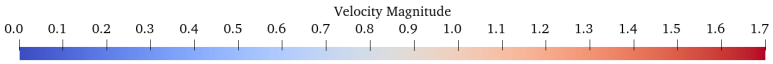

Figure A.3. Q-criterion contours at each simulated angle of attack for a span 3 wing.

A.4 Span 4

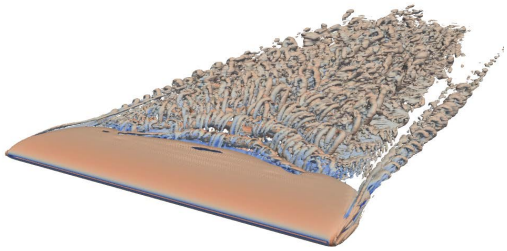

(a) 0°

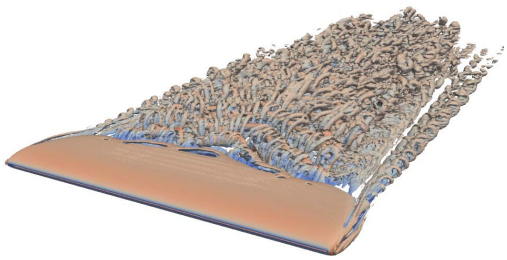

(b) 1°

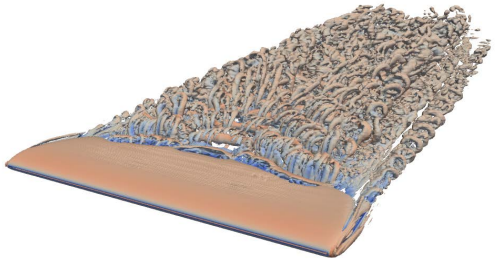

(c) 2°

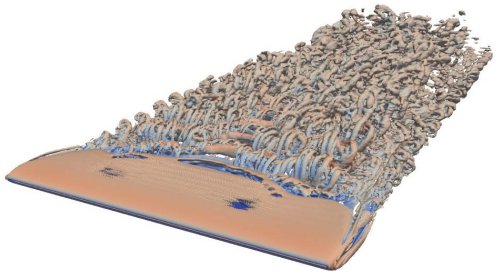

(d) 3°

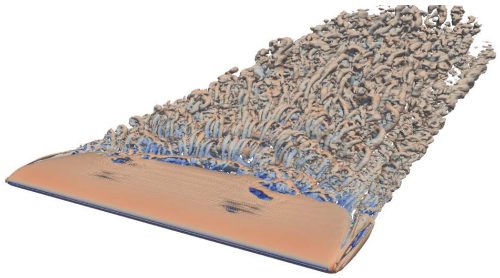

(e) 4°

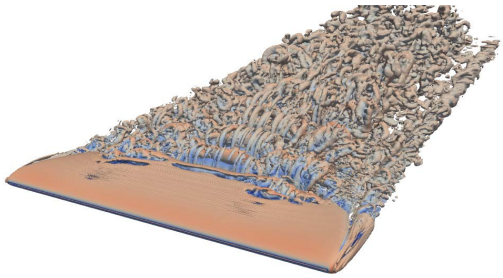

(f) 5°

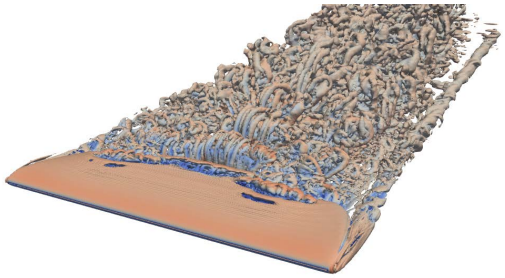

(g) 6°

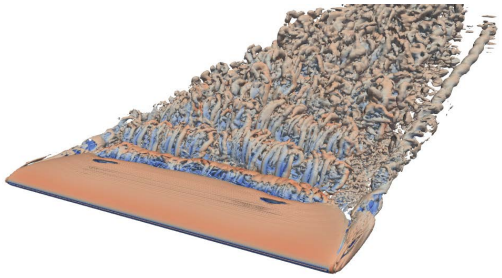

(h) 7°

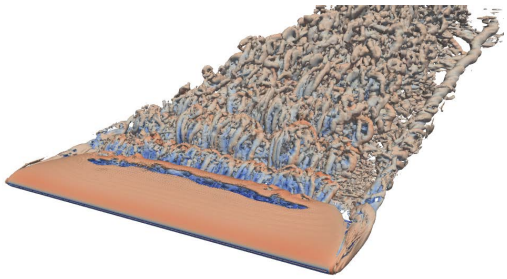

(i) 8°

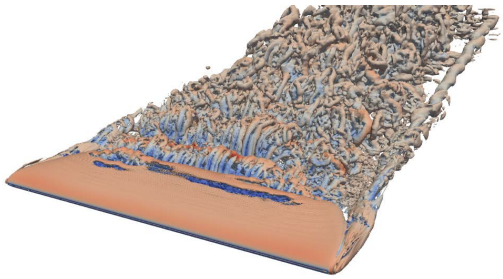

(j) 9°

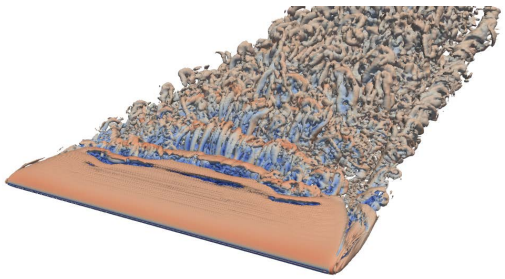

(k) 10°

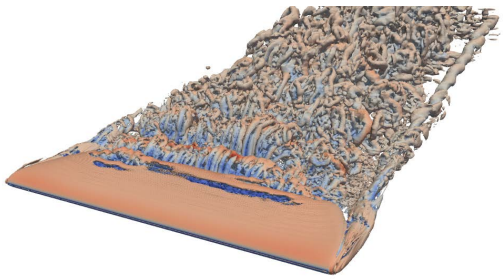

(l) 11°

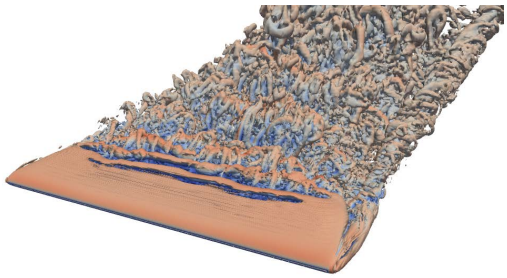

(m) 12°

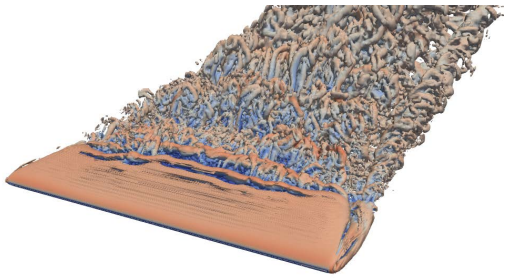

(n) 13°

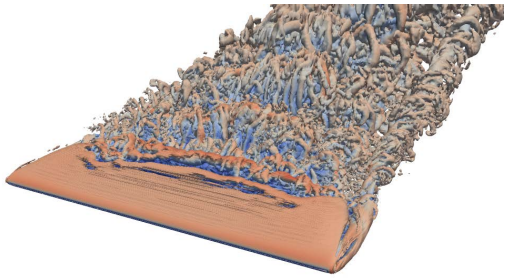

(o) 14°

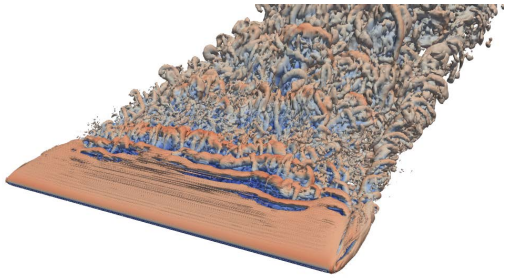

(p) 15°

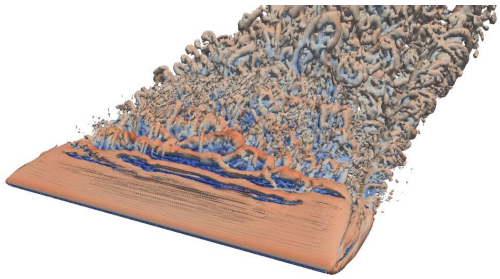

(q) 16°

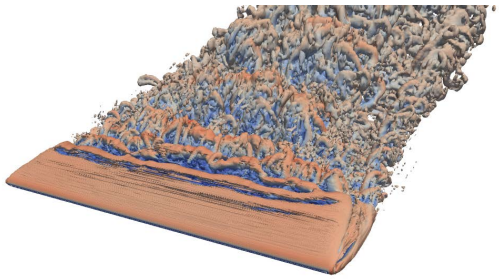

(r) 17°

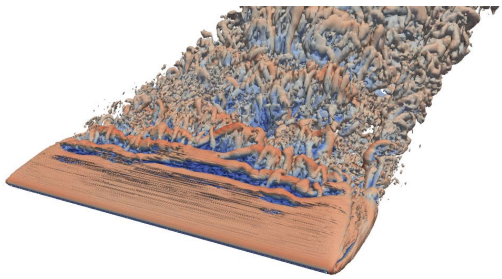

(s) 18°

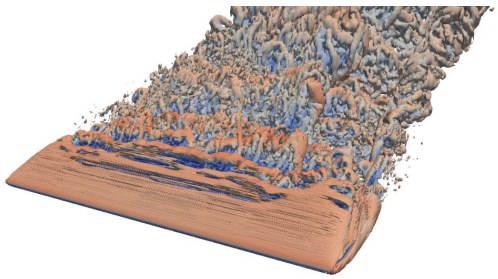

(t) 19°

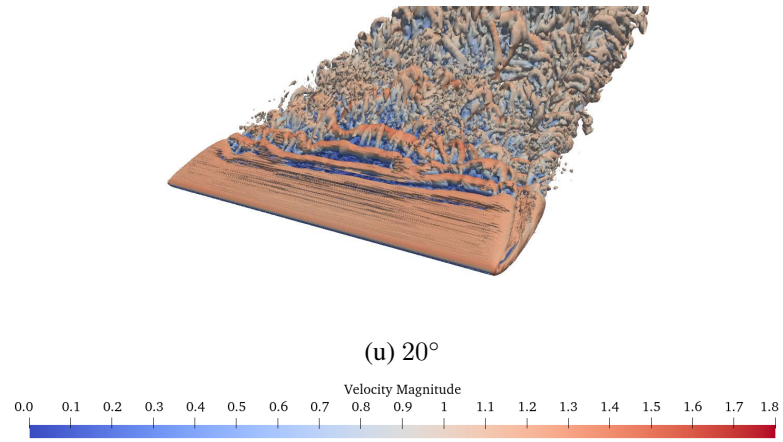

(u) 20°

Figure A.4. Q-criterion contours at each simulated angle of attack for a span 4 wing.

A.5 Periodic

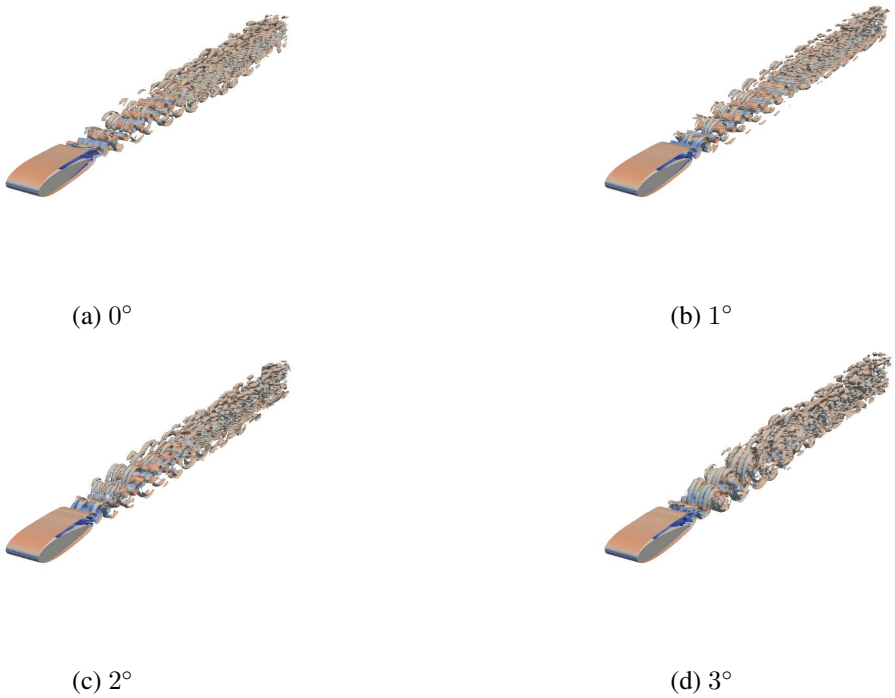

(a) 0°

(b) 1°

(c) 2°

(d) 3°

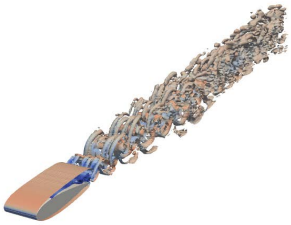

(e) 4°

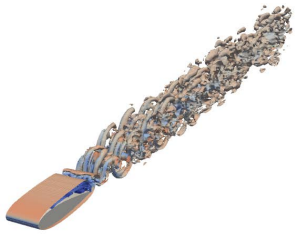

(f) 5°

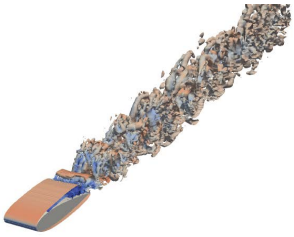

(g) 6°

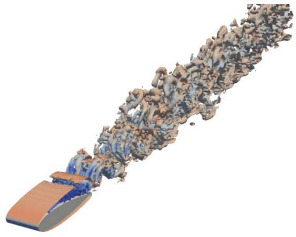

(h) 7°

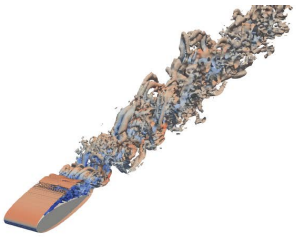

(i) 8°

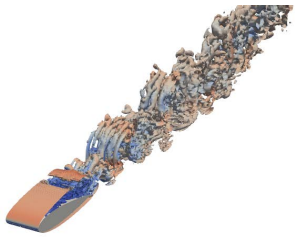

(j) 9°

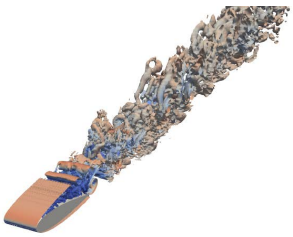

(k) 10°

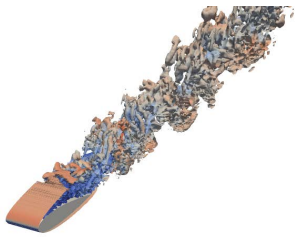

(l) 11°

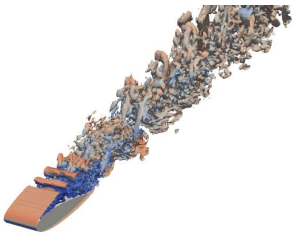

(m) 12°

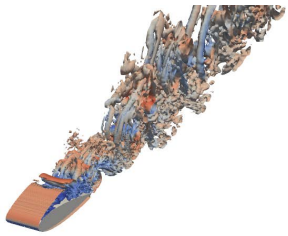

(n) 13°

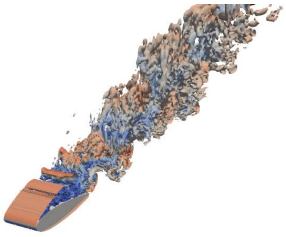

(o) 14°

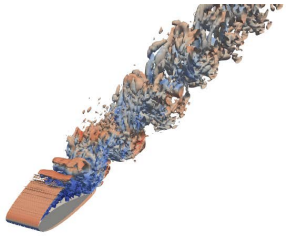

(p) 15°

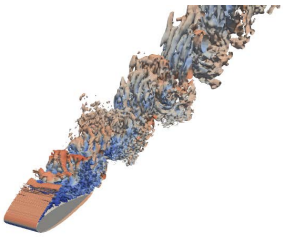

(q) 16°

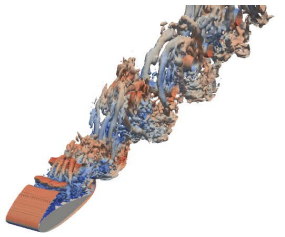

(r) 17°

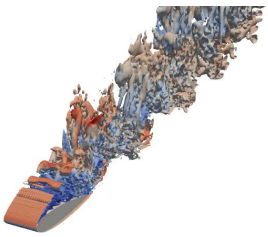

(s) 18°

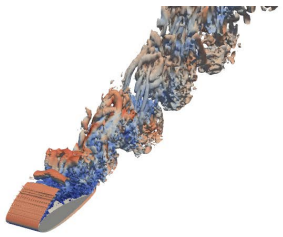

(t) 19°

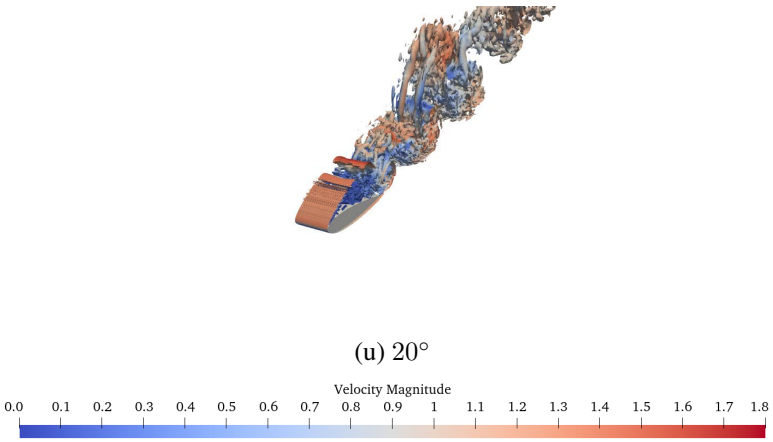

(u) 20°

Figure A.5. Q-criterion contours at each simulated angle of attack for a periodic wing.

Appendix B

Coefficient of Friction Plots - Lower Surface

B.1 Span 1

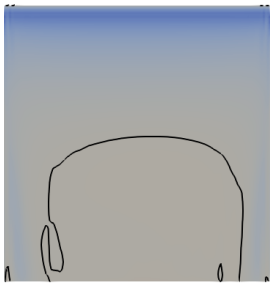

(a) 0°

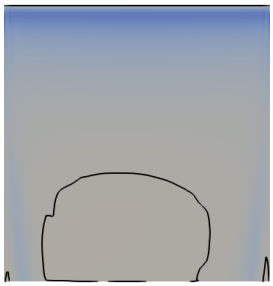

(b) 1°

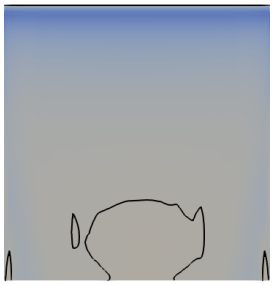

(c) 2°

(d) 3°

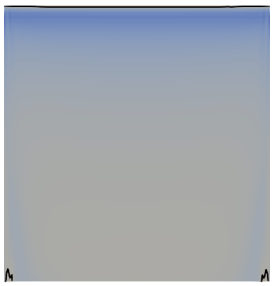

(e) 4°

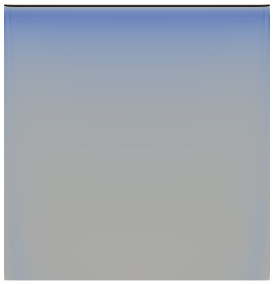

(f) 5°

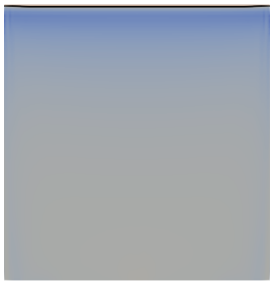

(g) 6°

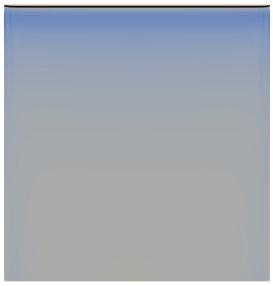

(h) 7°

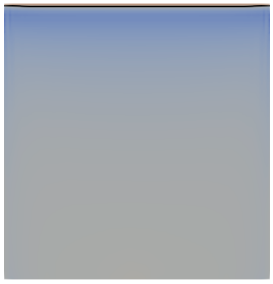

(i) 8°

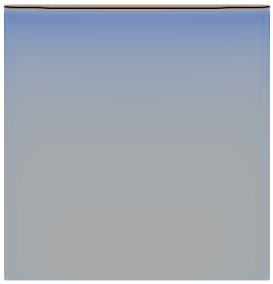

(j) 9°

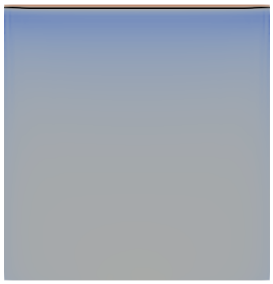

(k) 10°

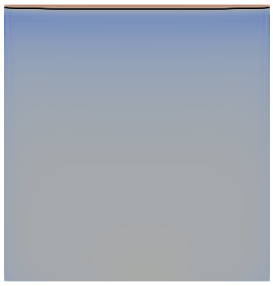

(l) 11°

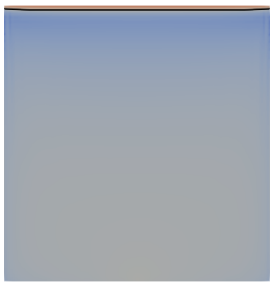

(m) 12°

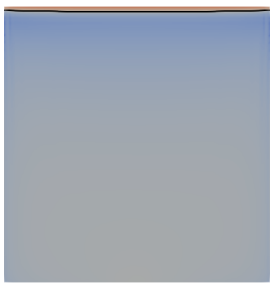

(n) 13°

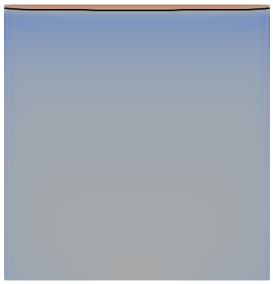

(o) 14°

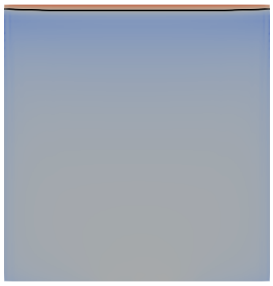

(p) 15°

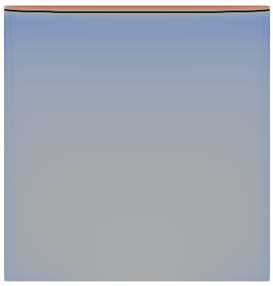

(q) 16°

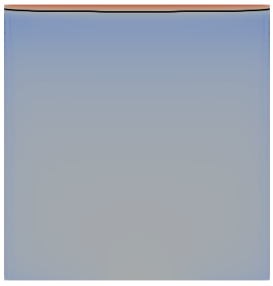

(r) 17°

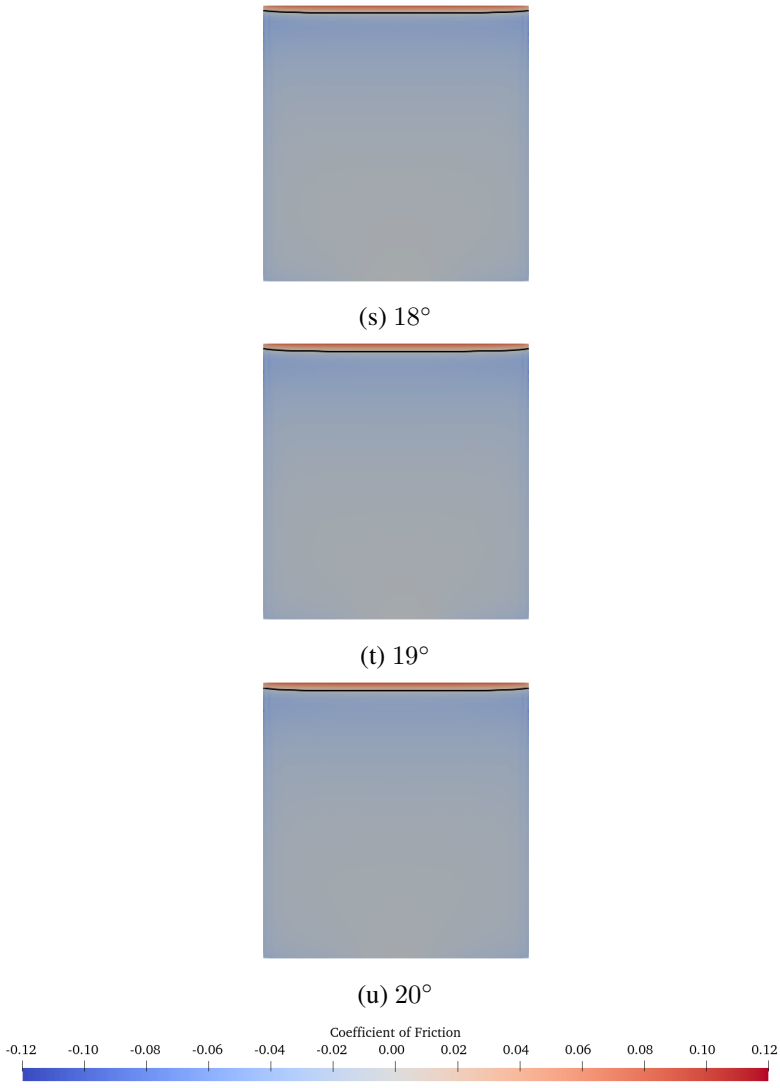

(s) 18°

(t) 19°

(u) 20°

Figure B.1. Coefficient of friction at each simulated angle of attack for a span 1 wing.

B.2 Span 2

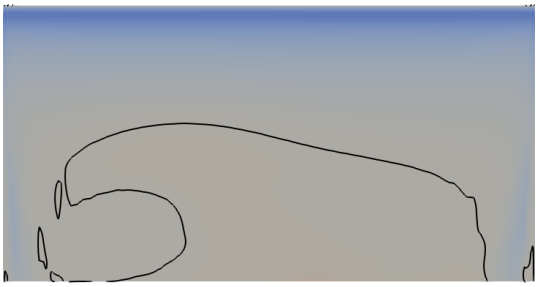

(a) 0°

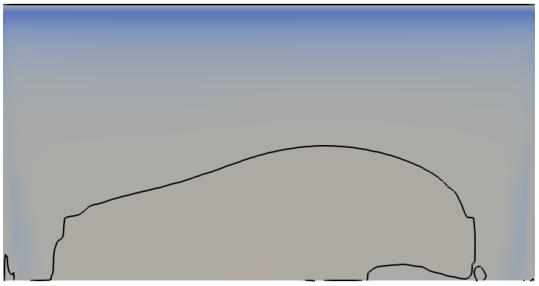

(b) 1°

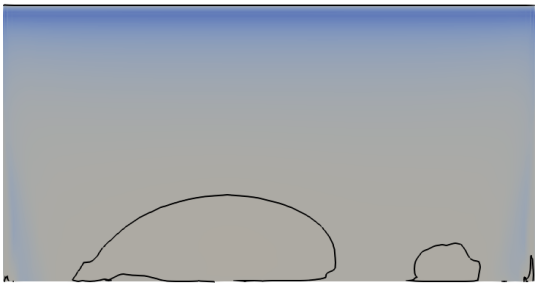

(c) 2°

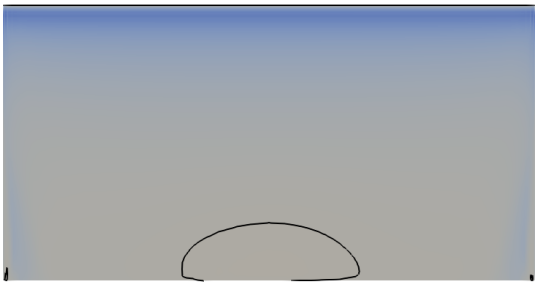

(d) 3°

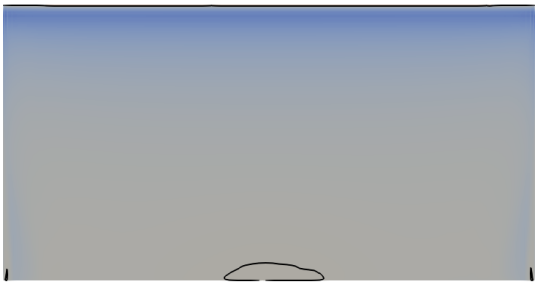

(e) 4°

(f) 5°

(g) 6°

(h) 7°

(i) 8°

(j) 9°

(k) 10°

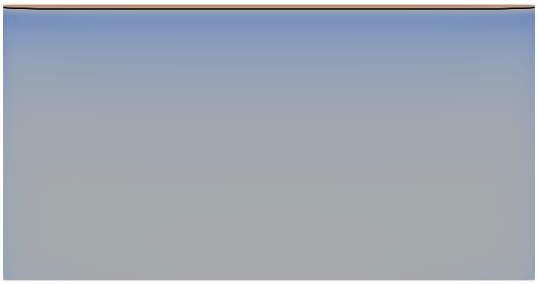

(l) 11°

(m) 12°

(n) 13°

(o) 14°

(p) 15°

(q) 16°

(r) 17°

(s) 18°

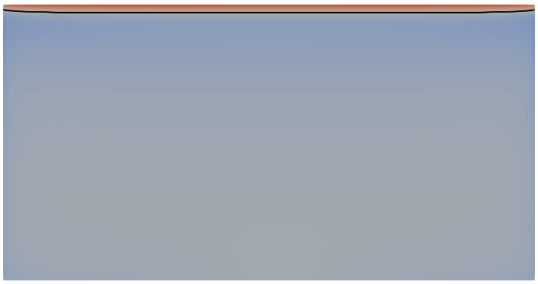

(t) 19°

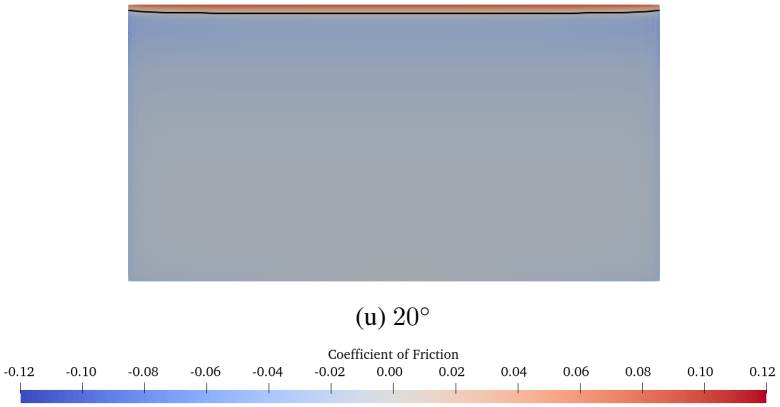

(u) 20°

Figure B.2. Coefficient of friction at each simulated angle of attack for a span 2 wing.

B.3 Span 3

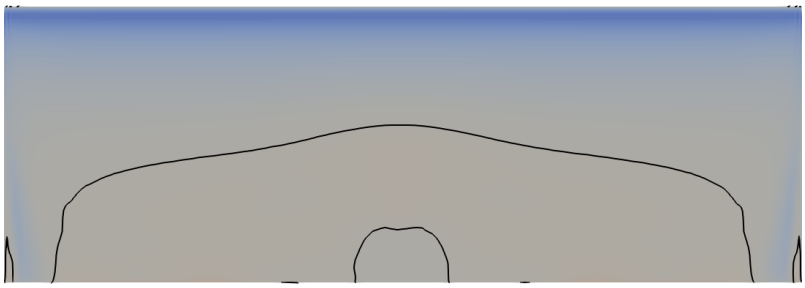

(a) 0°

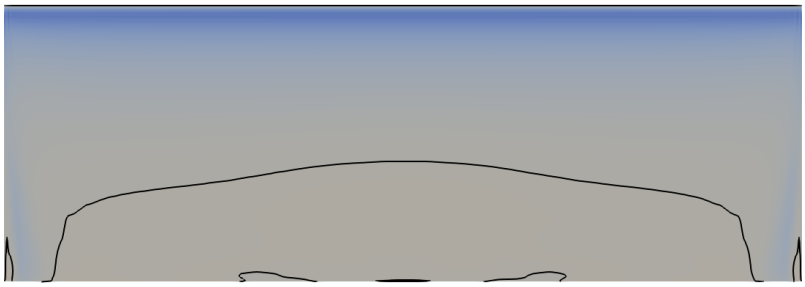

(b) 1°

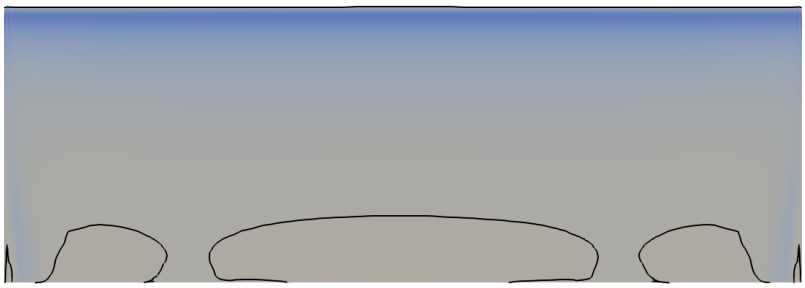

(c) 2°

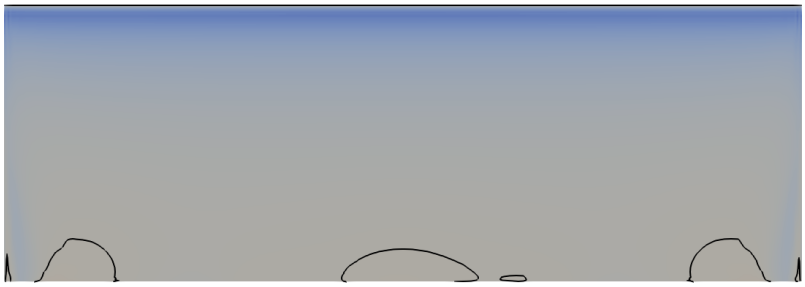

(d) 3°

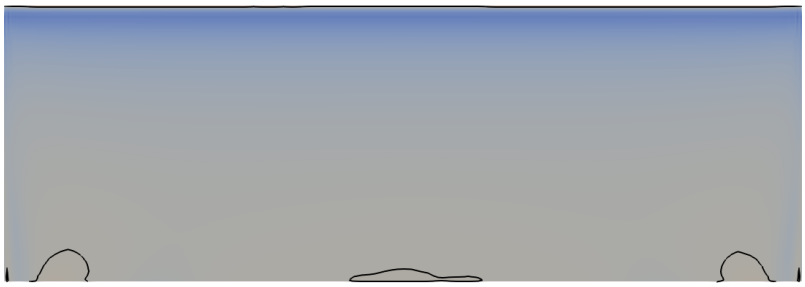

(e) 4°

(f) 5°

(g) 6°

(h) 7°

(i) 8°

(j) 9°

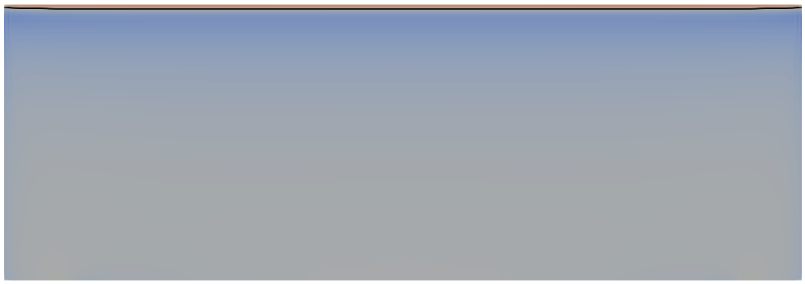

(k) 10°

(l) 11°

(m) 12°

(n) 13°

(o) 14°

(p) 15°

(q) 16°

(r) 17°

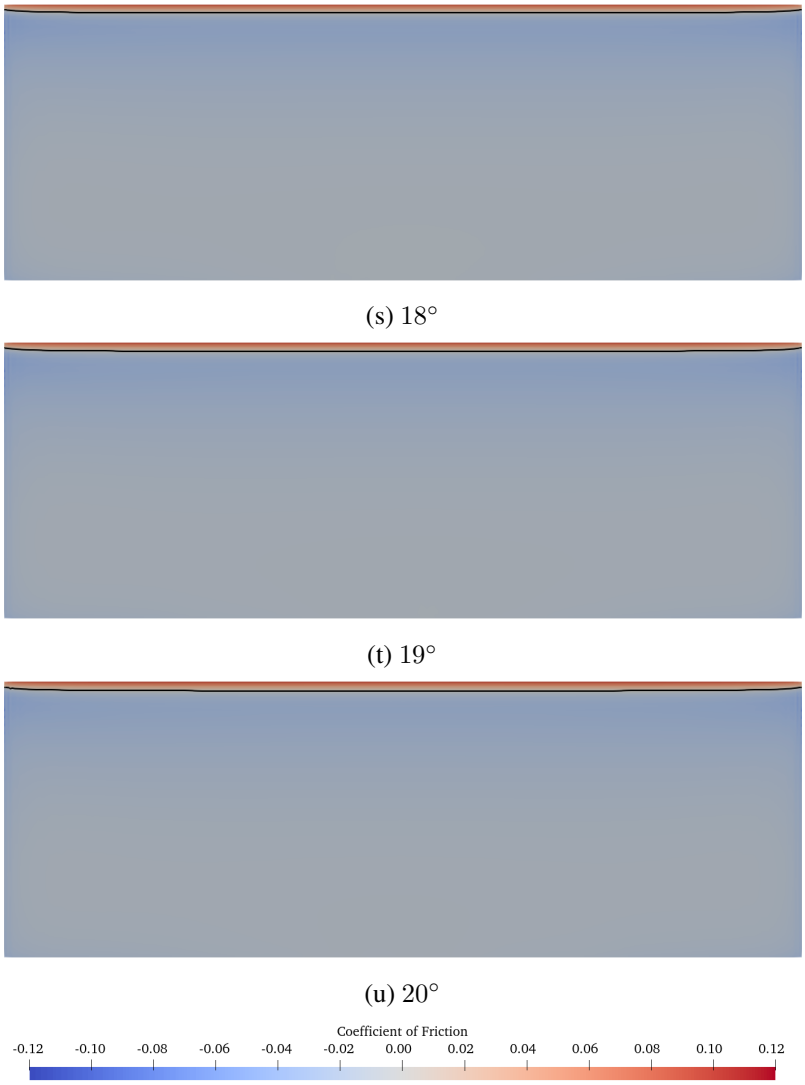

(s) 18°

(t) 19°

(u) 20°

Figure B.3. Coefficient of friction at each simulated angle of attack for a span 3 wing.

B.4 Span 4

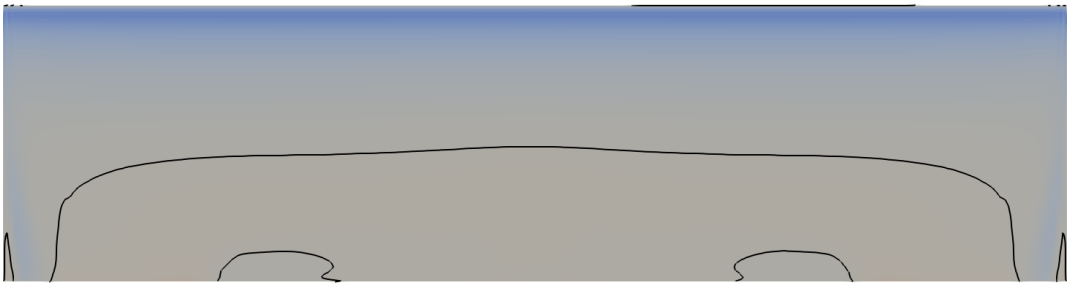

(a) 0°

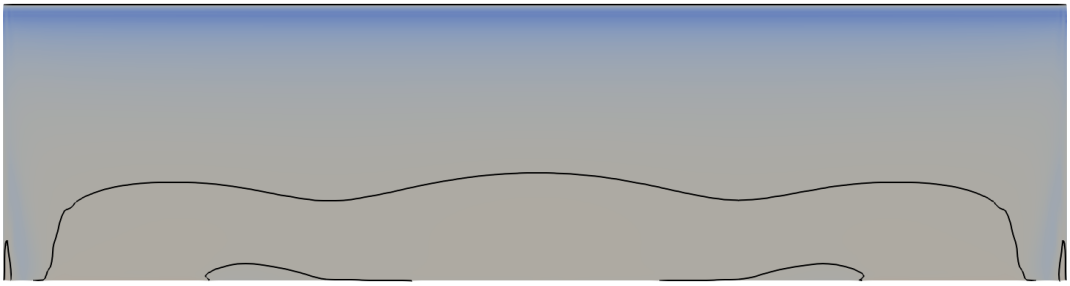

(b) 1°

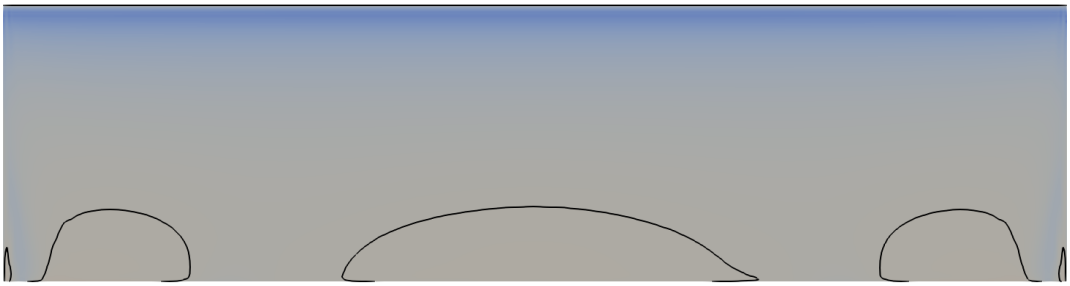

(c) 2°

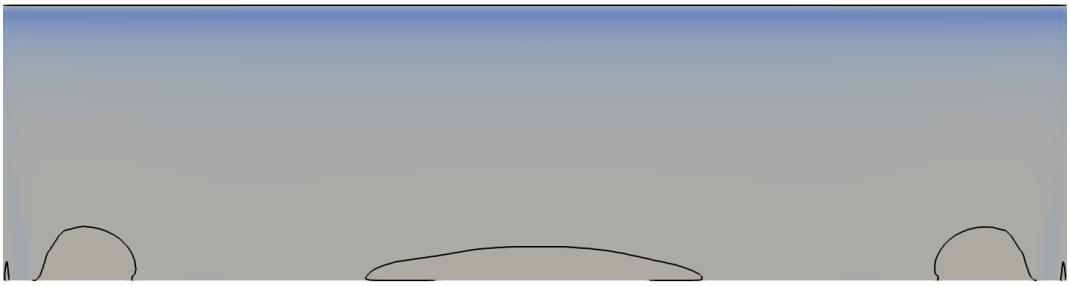

(d) 3°

(e) 4°

(f) 5°

(g) 6°

(h) 7°

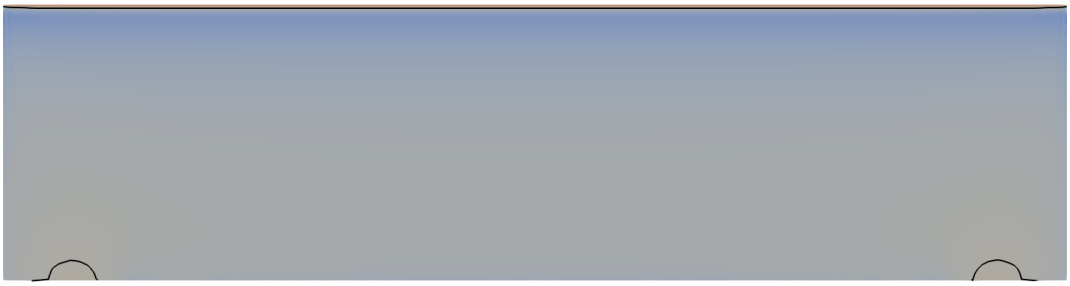

(i) 8°

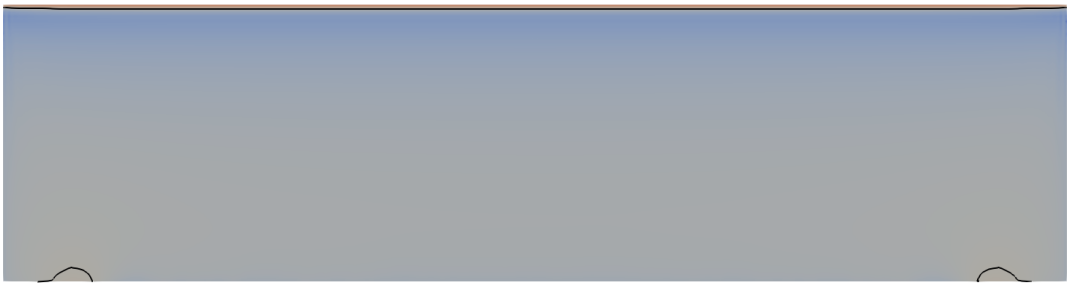

(j) 9°

(k) 10°

(l) 11°

(m) 12°

(n) 13°

(o) 14°

(p) 15°

(q) 16°

(r) 17°

(s) 18°

(t) 19°

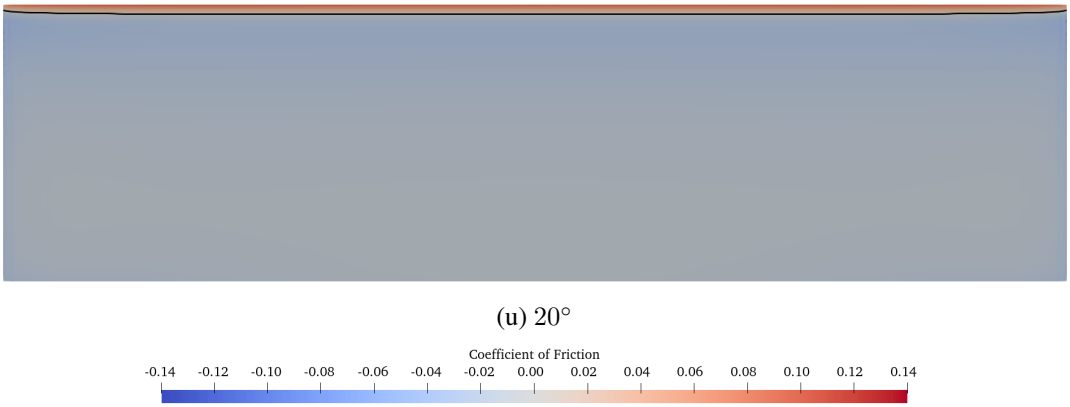

(u) 20°

Figure B.4. Coefficient of friction at each simulated angle of attack for a span 4 wing.

B.5 Periodic

(a) 0°

(b) 1°

(c) 2°

(d) 3°

(e) 4°

(f) 5°

(g) 6°

(h) 7°

(i) 8°

(j) 9°

(k) 10°

(l) 11°

(m) 12°

(n) 13°

(o) 14°

(p) 15°

(q) 16°

(r) 17°

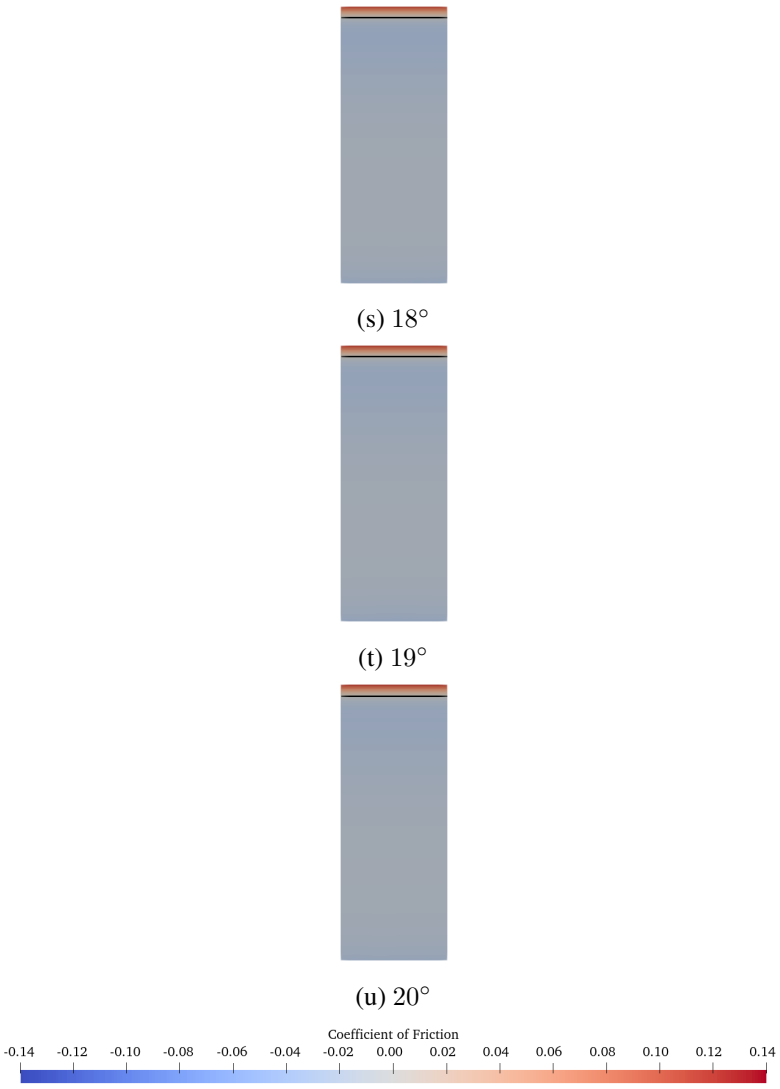

Figure B.5. Coefficient of friction at each simulated angle of attack for a periodic wing.

Appendix C

Coefficient of Friction Plots - Upper Surface

C.1 Span 1

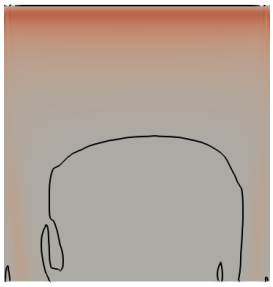

(a) 0°

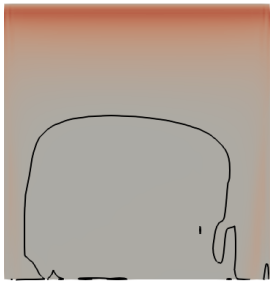

(b) 1°

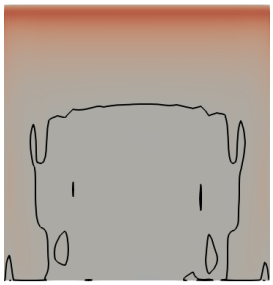

(c) 2°

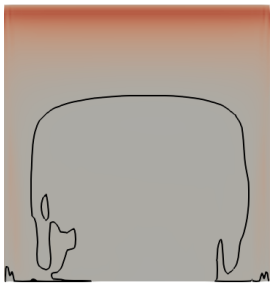

(d) 3°

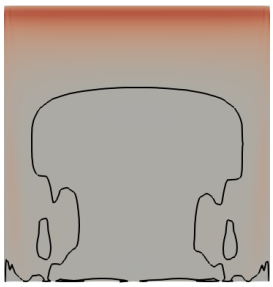

(e) 4°

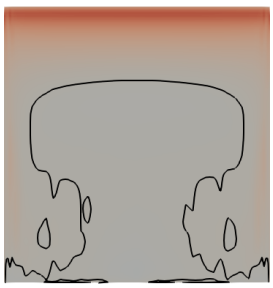

(f) 5°

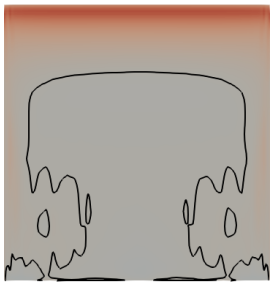

(g) 6°

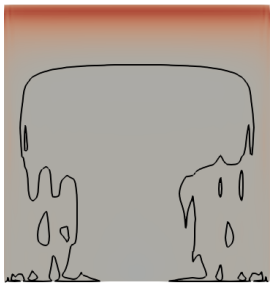

(h) 7°

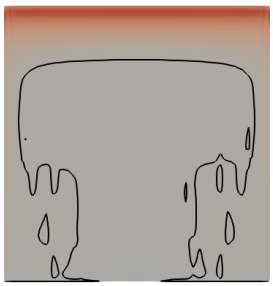

(i) 8°

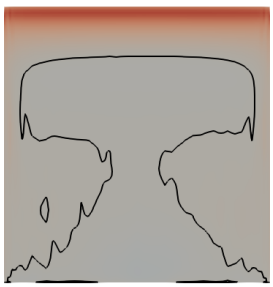

(j) 9°

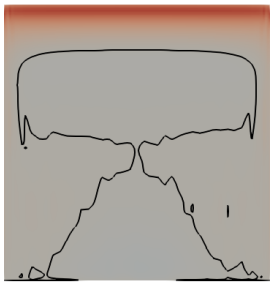

(k) 10°

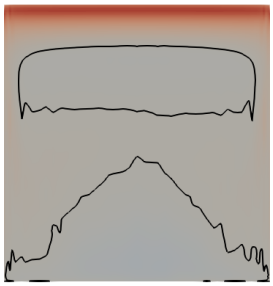

(l) 11°

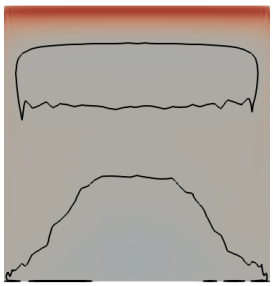

(m) 12°

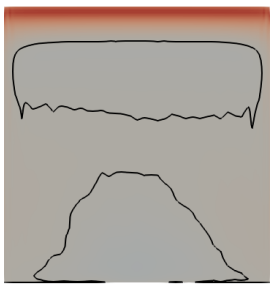

(n) 13°

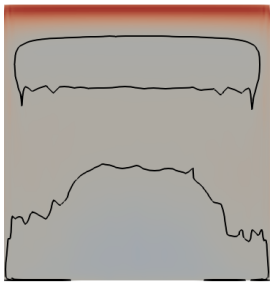

(o) 14°

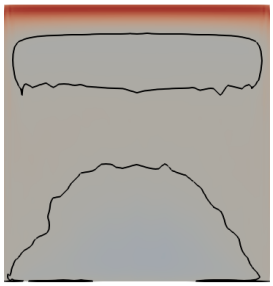

(p) 15°

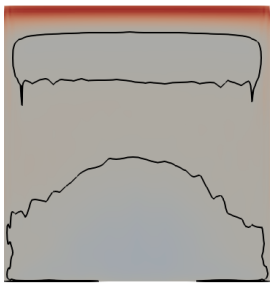

(q) 16°

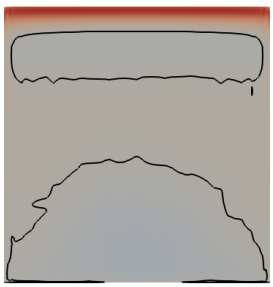

(r) 17°

(s) 18°

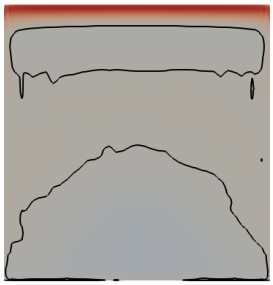

(t) 19°

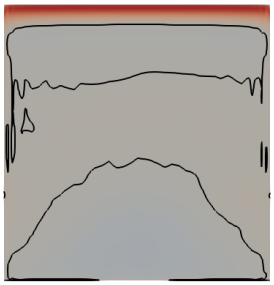

(u) 20°

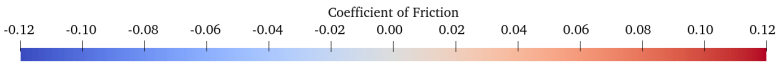

Figure C.1. Coefficient of friction at each simulated angle of attack for a span 1 wing.

C.2 Span 2

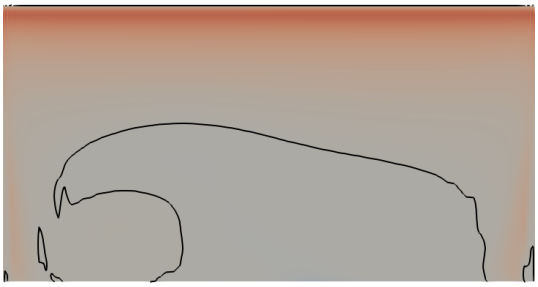

(a) 0°

(b) 1°

(c) 2°

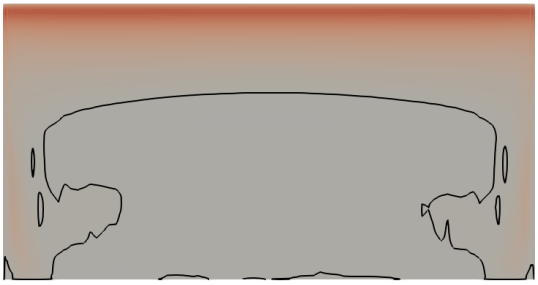

(d) 3°

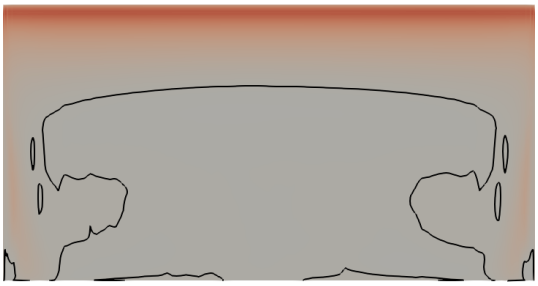

(e) 4°

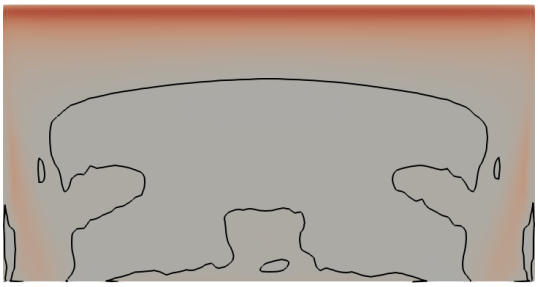

(f) 5°

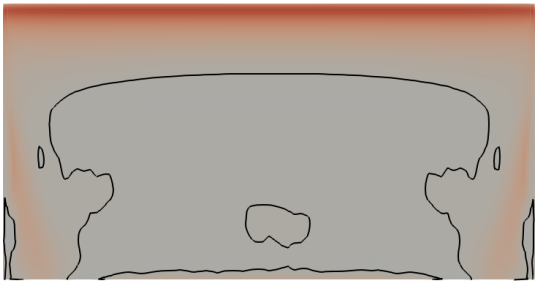

(g) 6°

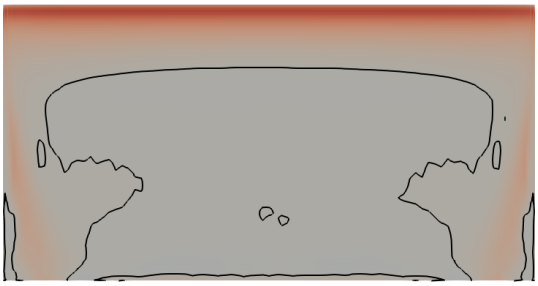

(h) 7°

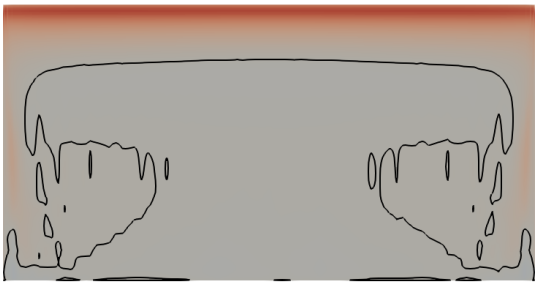

(i) 8°

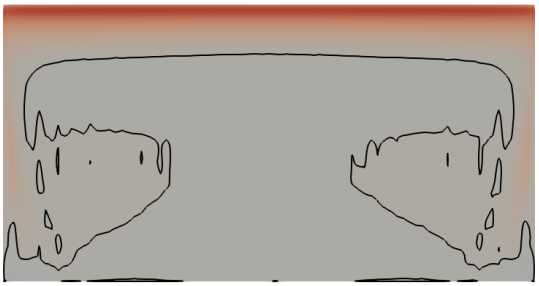

(j) 9°

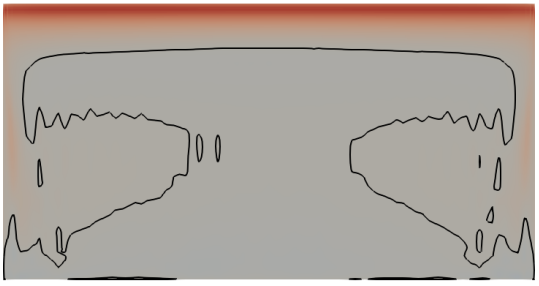

(k) 10°

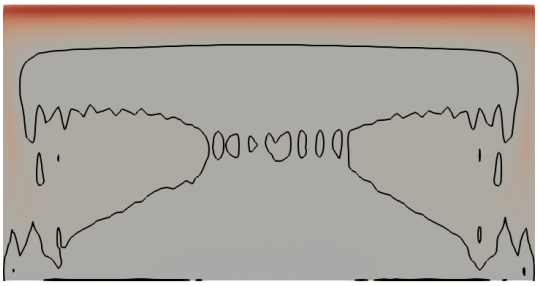

(l) 11°

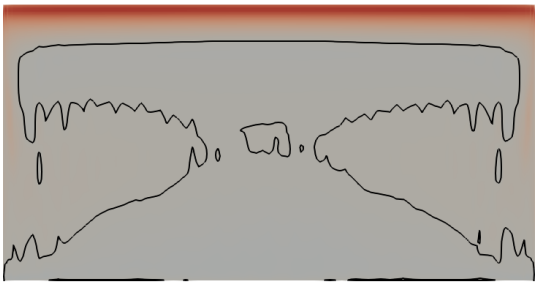

(m) 12°

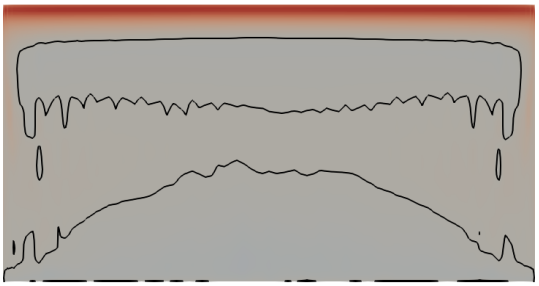

(n) 13°

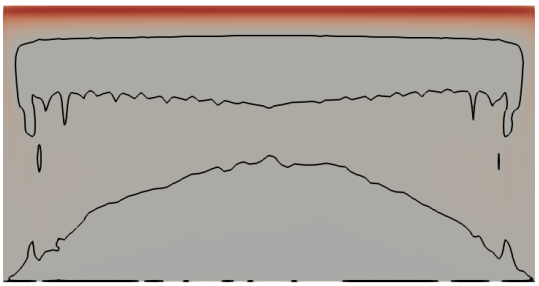

(o) 14°

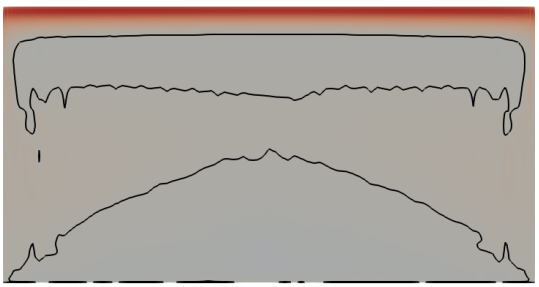

(p) 15°

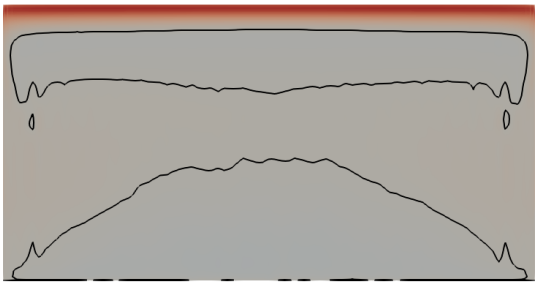

(q) 16°

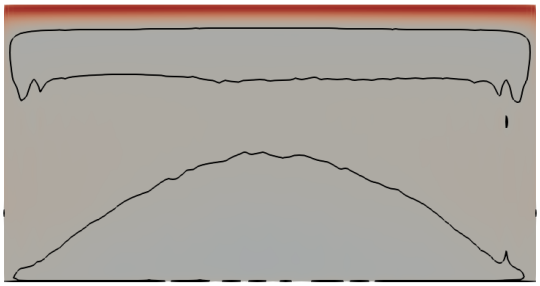

(r) 17°

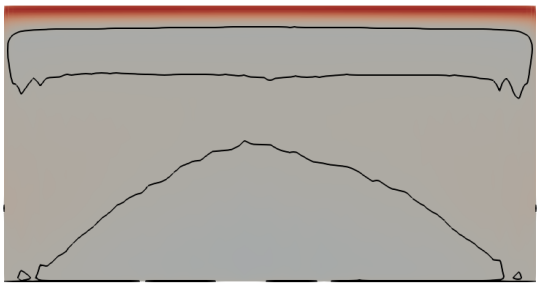

(s) 18°

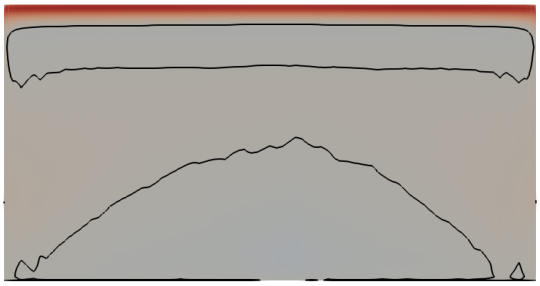

(t) 19°

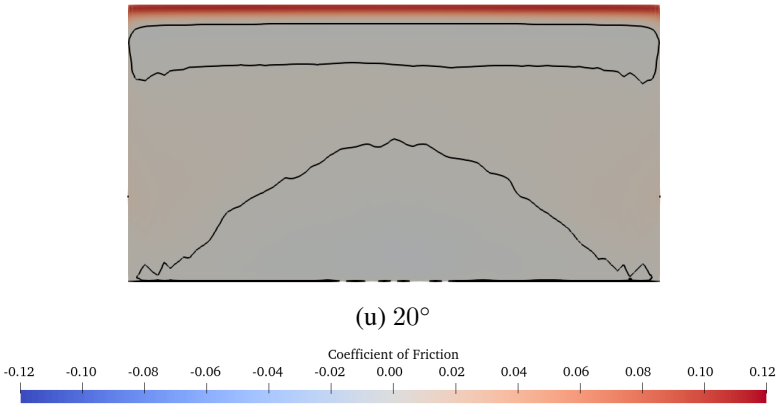

(u) 20°

Figure C.2. Coefficient of friction at each simulated angle of attack for a span 2 wing.

C.3 Span 3

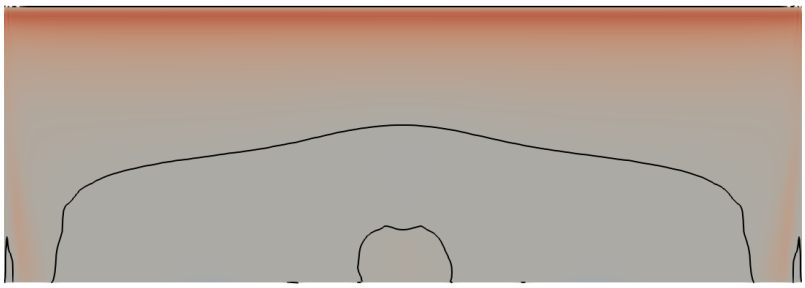

(a) 0°

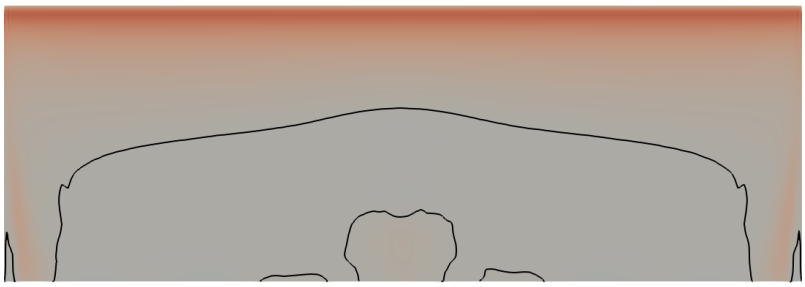

(b) 1°

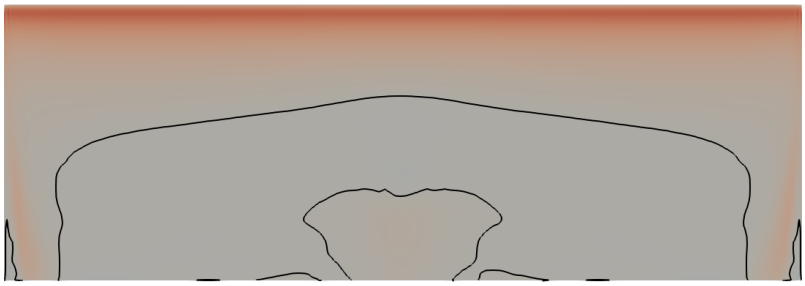

(c) 2°

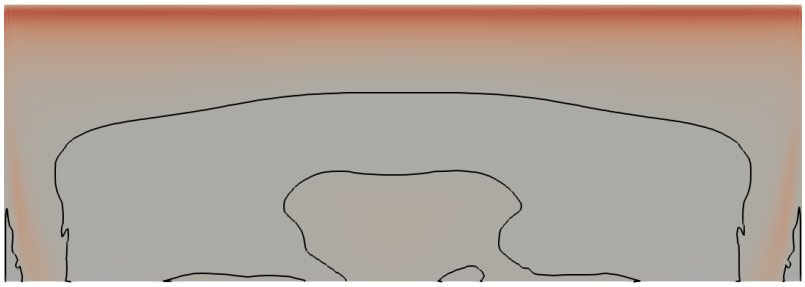

(d) 3°

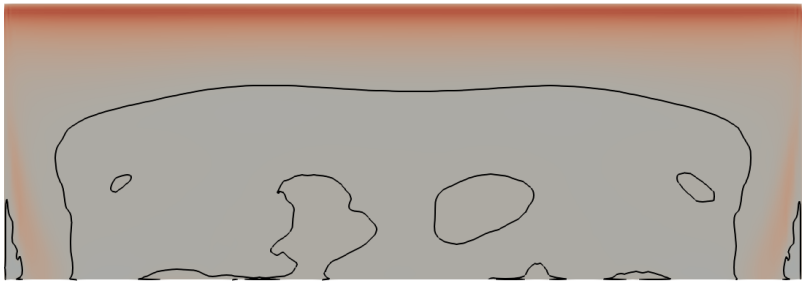

(e) 4°

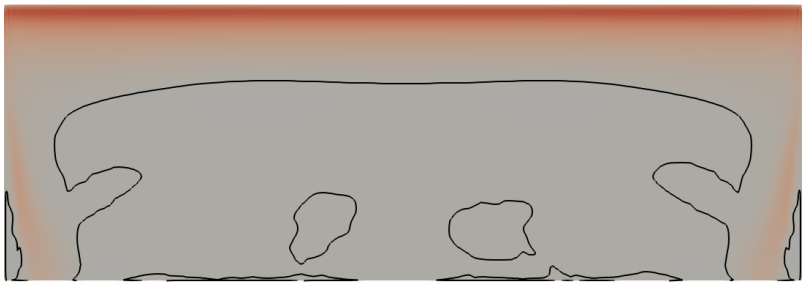

(f) 5°

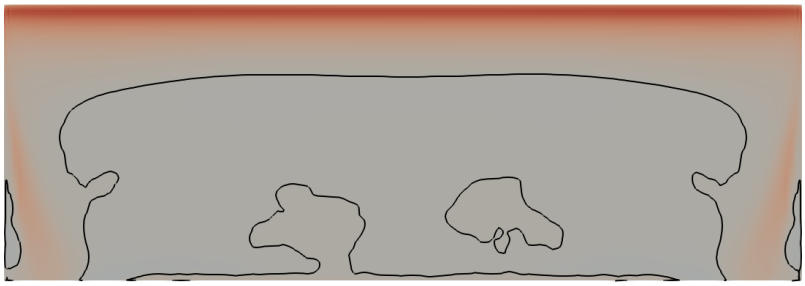

(g) 6°

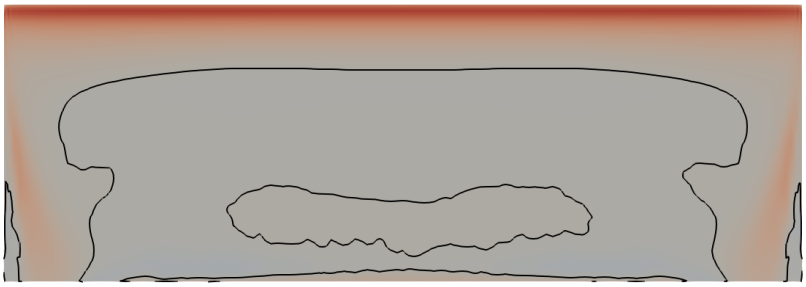

(h) 7°

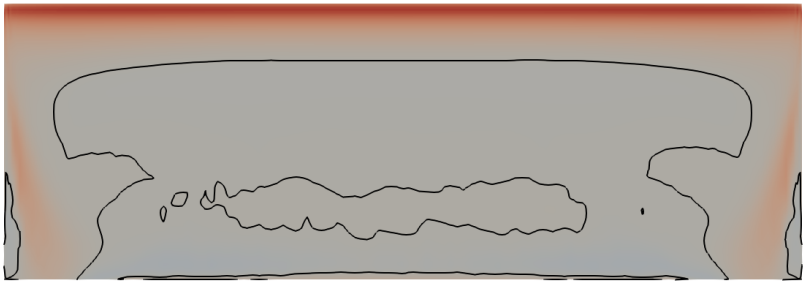

(i) 8°

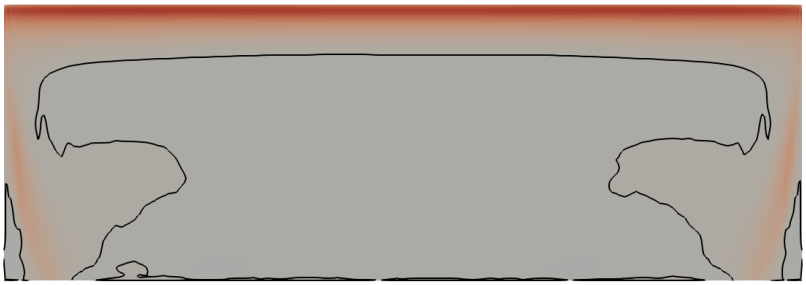

(j) 9°

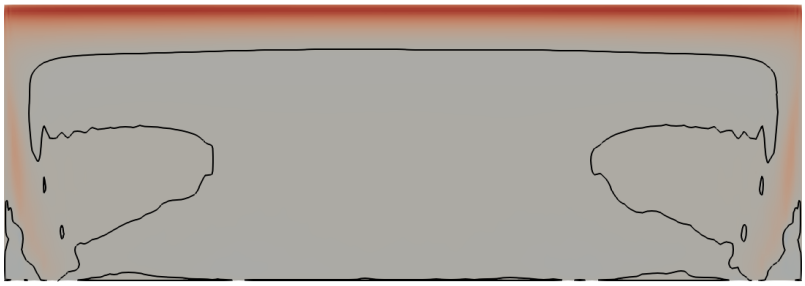

(k) 10°

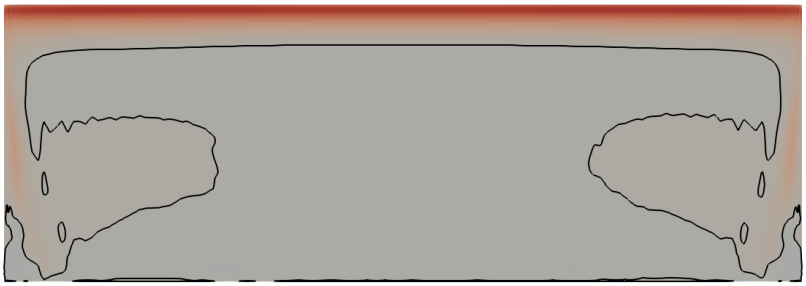

(l) 11°

(m) 12°

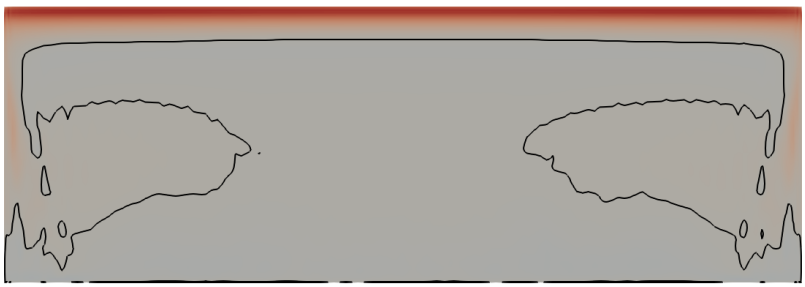

(n) 13°

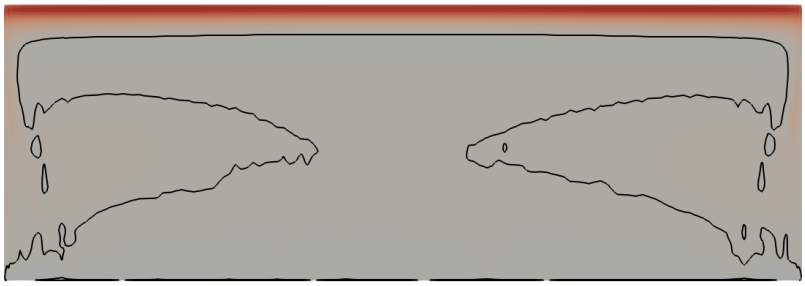

(o) 14°

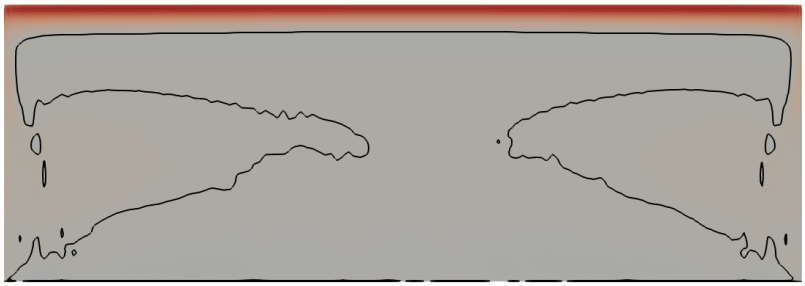

(p) 15°

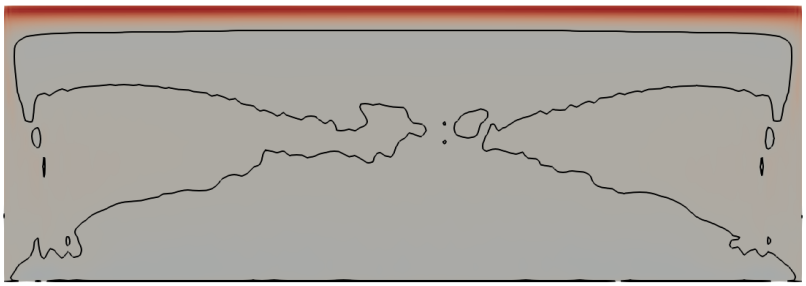

(q) 16°

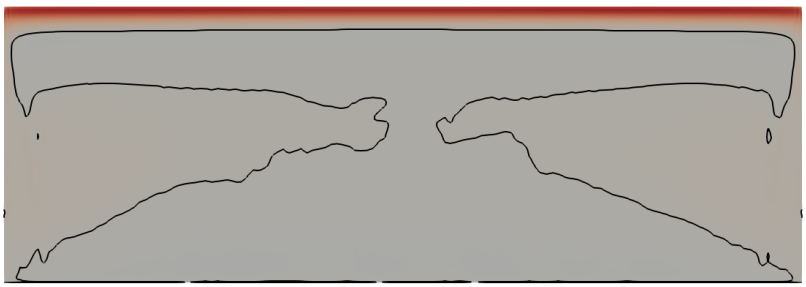

(r) 17°

(s) 18°

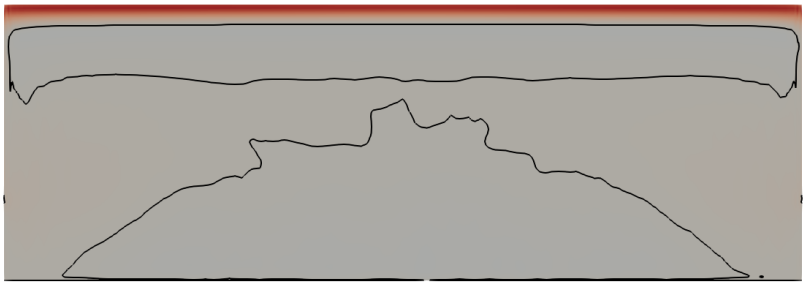

(t) 19°

(u) 20°

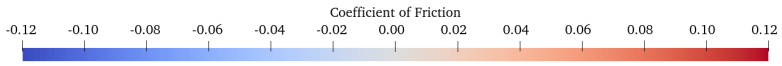

Figure C.3. Coefficient of friction at each simulated angle of attack for a span 3 wing.

C.4 Span 4

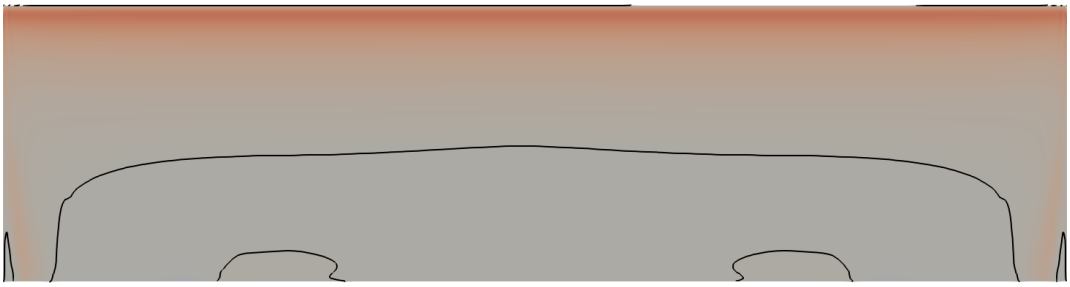

(a) 0°

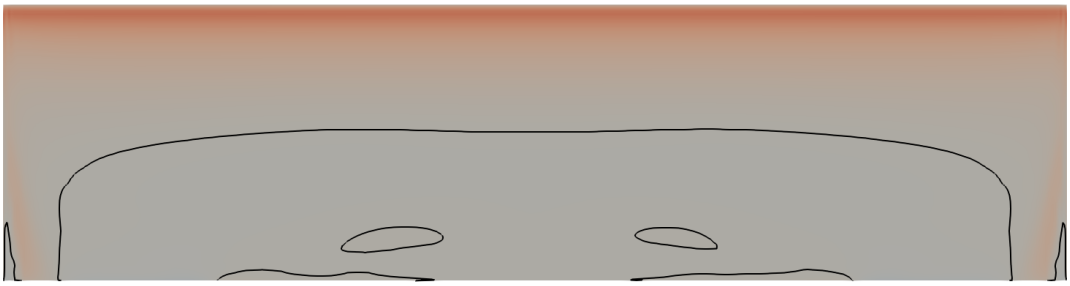

(b) 1°

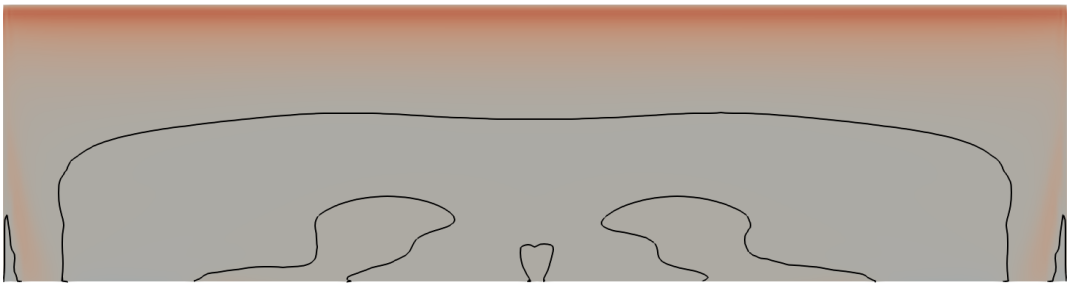

(c) 2°

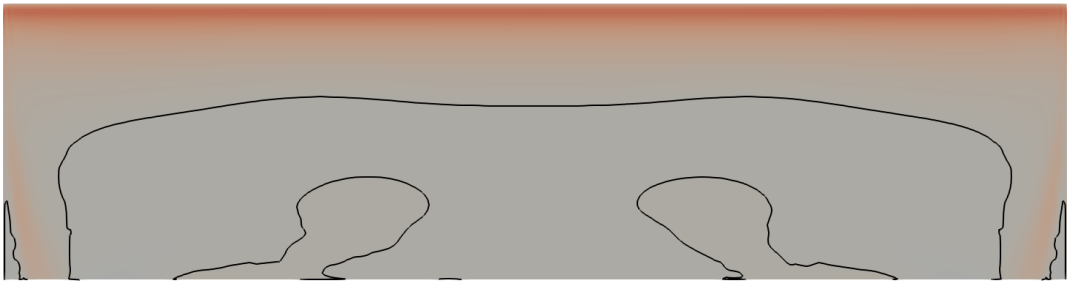

(d) 3°

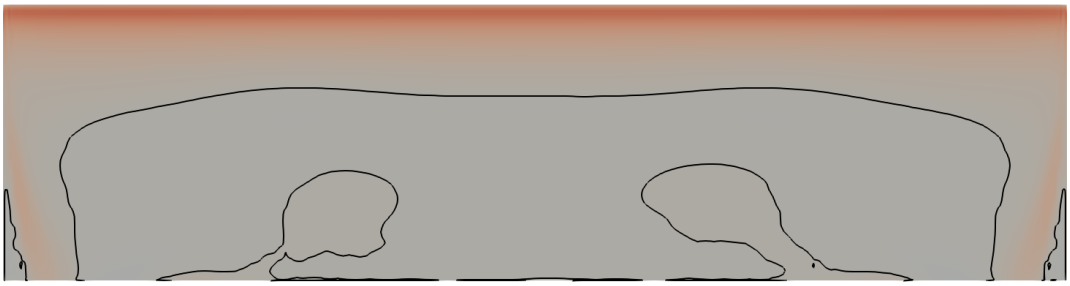

(e) 4°

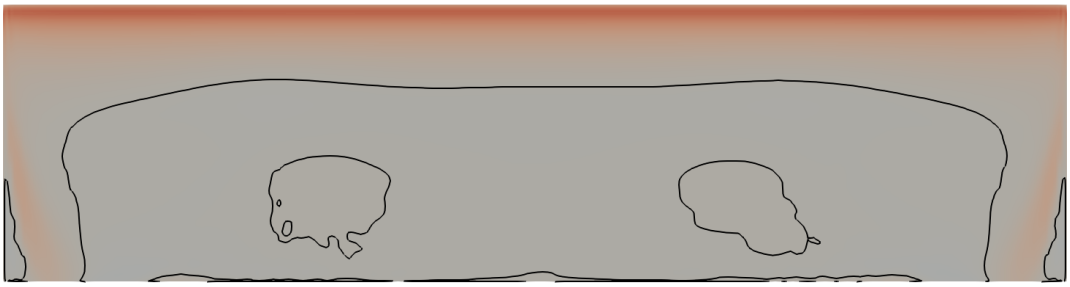

(f) 5°

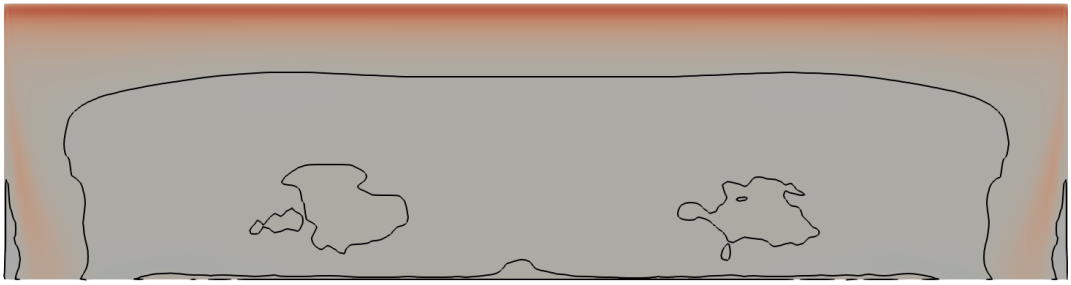

(g) 6°

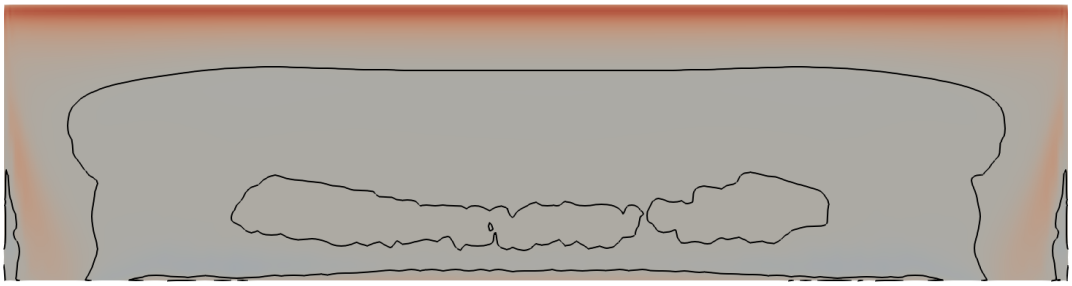

(h) 7°

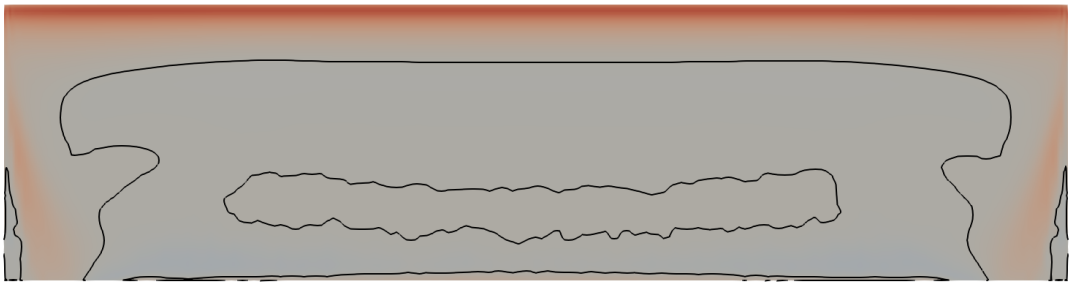

(i) 8°

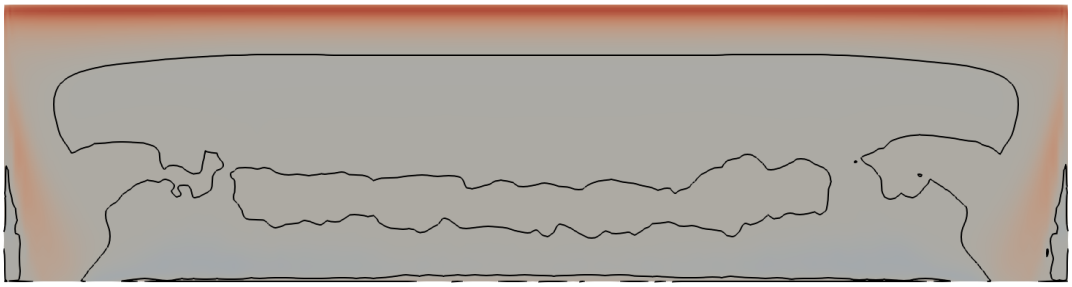

(j) 9°

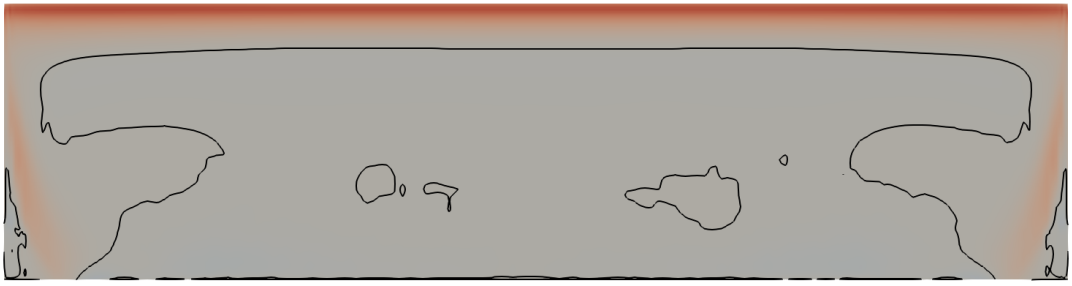

(k) 10°

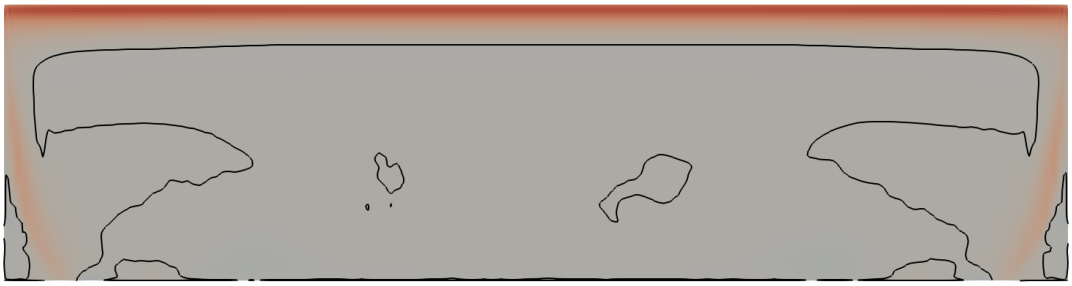

(l) 11°

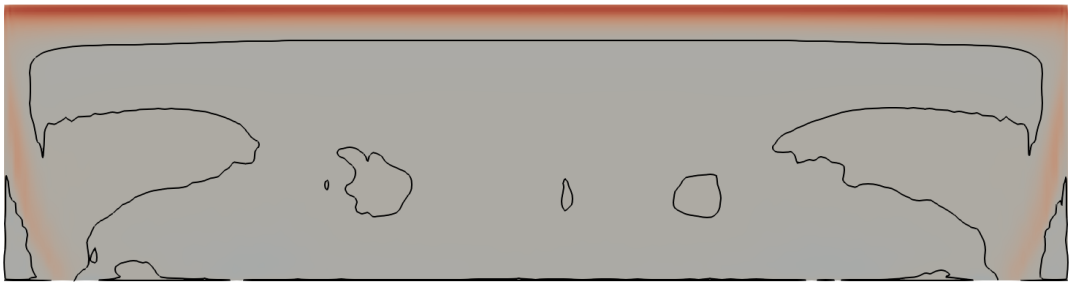

(m) 12°

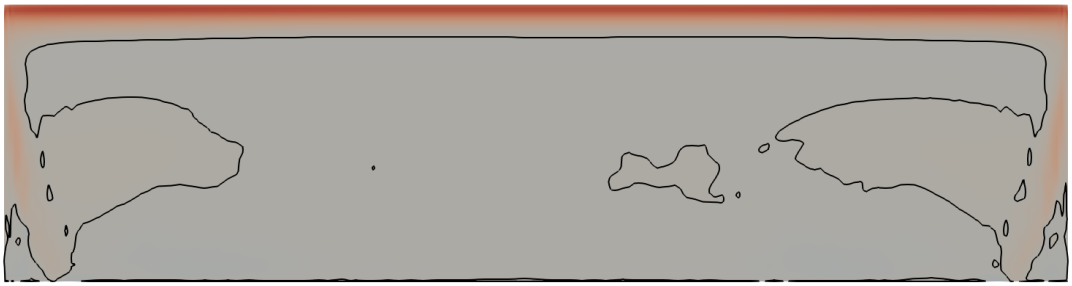

(n) 13°

(o) 14°

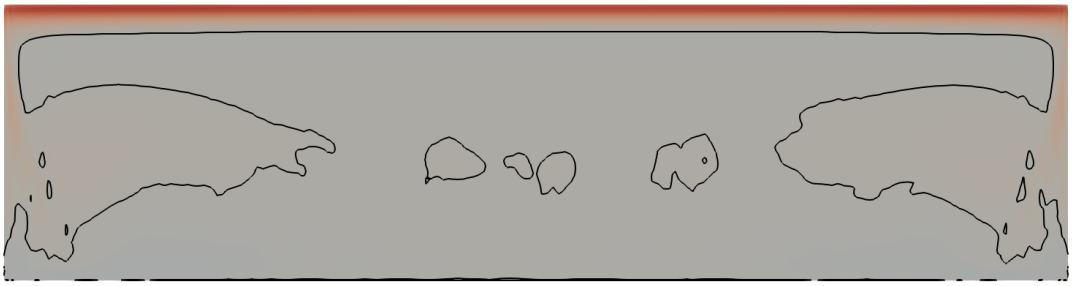

(p) 15°

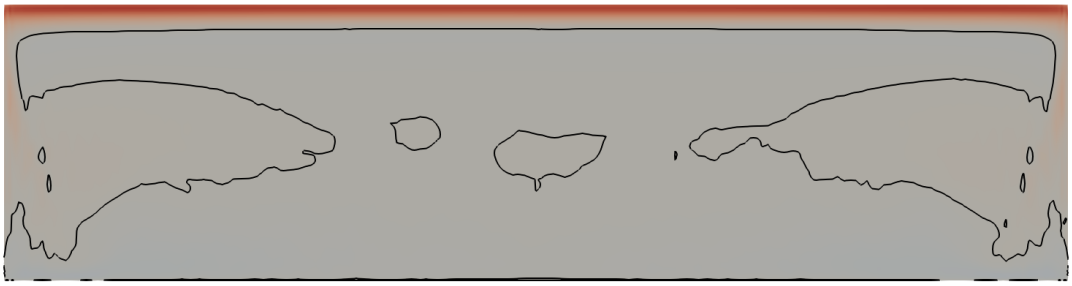

(q) 16°

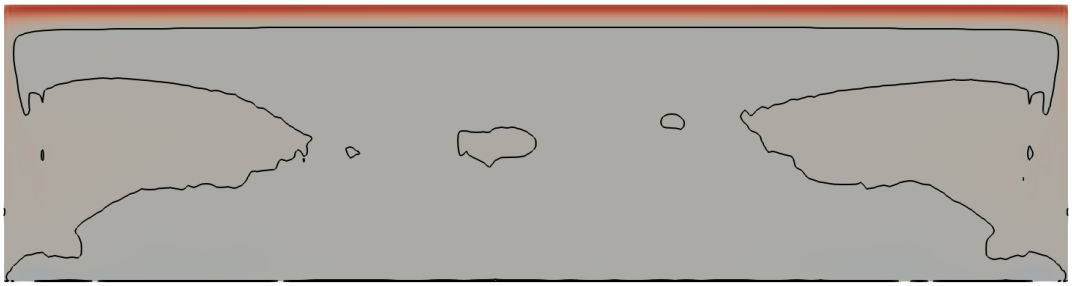

(r) 17°

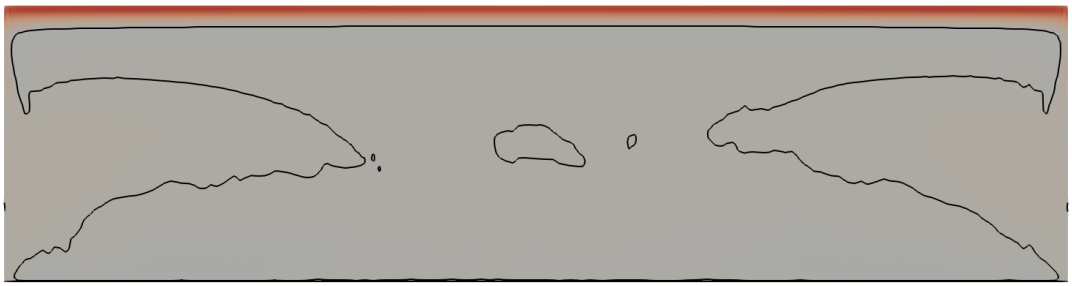

(s) 18°

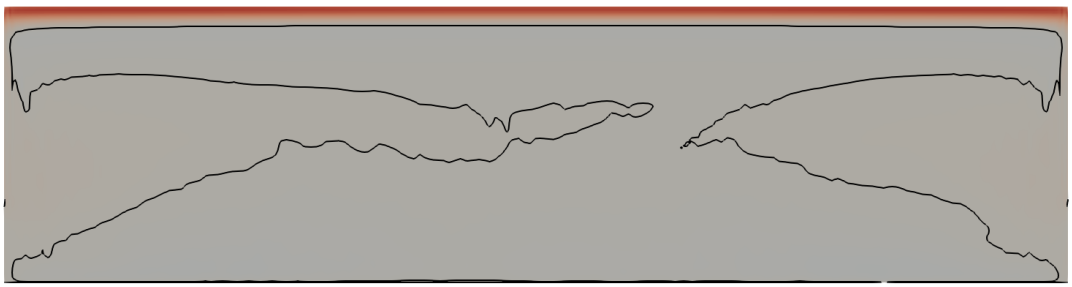

(t) 19°

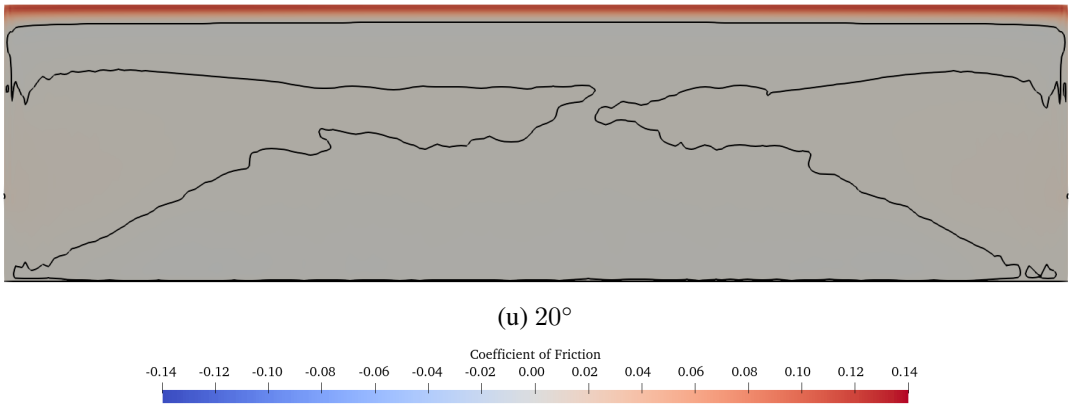

(u) 20°

Figure C.4. Coefficient of friction at each simulated angle of attack for a span 4 wing.

C.5 Periodic

(a) 0°

(b) 1°

(c) 2°

(d) 3°

(e) 4°

(f) 5°

(g) 6°

(h) 7°

(i) 8°

(j) 9°

(k) 10°

(l) 11°

(m) 12°

(n) 13°

(o) 14°

(p) 15°

(q) 16°

(r) 17°

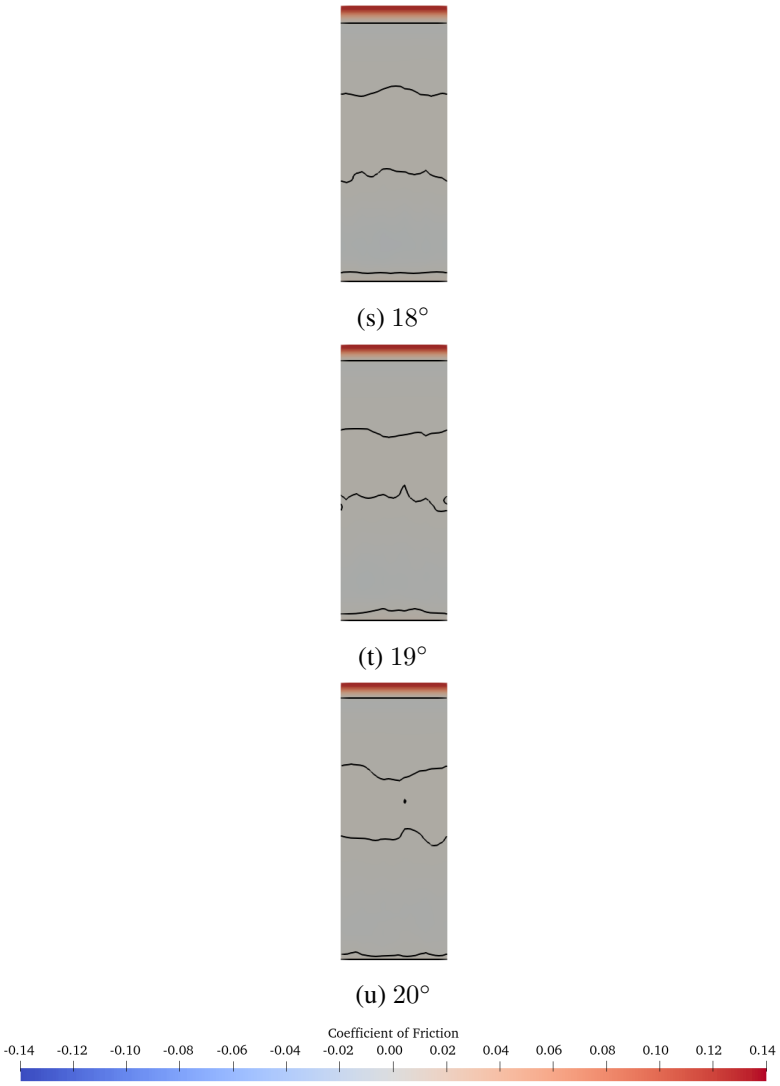

(s) 18°

(t) 19°

(u) 20°

Figure C.5. Coefficient of friction at each simulated angle of attack for a periodic wing.

Appendix D

Coefficient of Pressure Plots - Lower Surface

D.1 Span 1

(a) 0°

(b) 1°

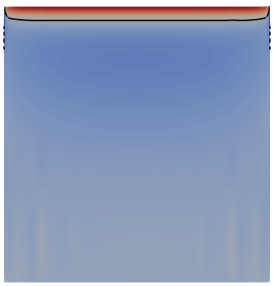

(c) 2°

(d) 3°

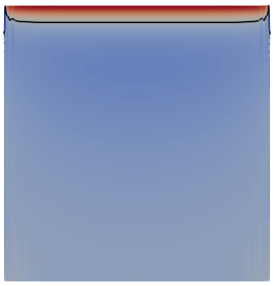

(e) 4°

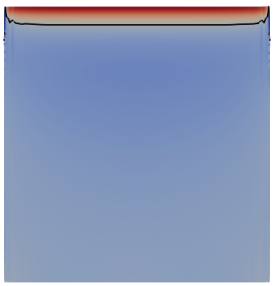

(f) 5°

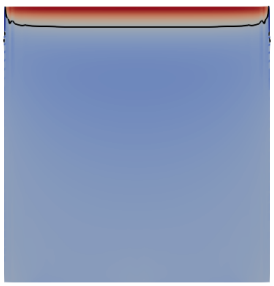

(g) 6°

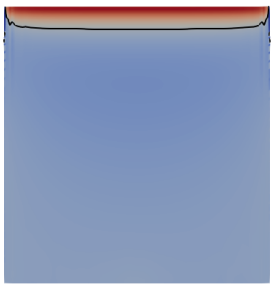

(h) 7°

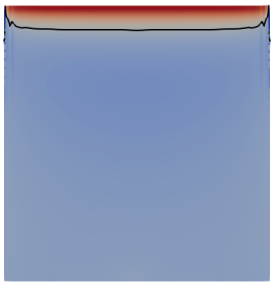

(i) 8°

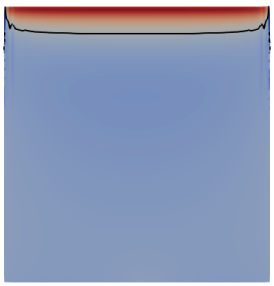

(j) 9°

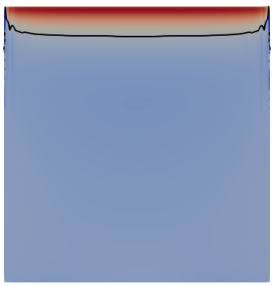

(k) 10°

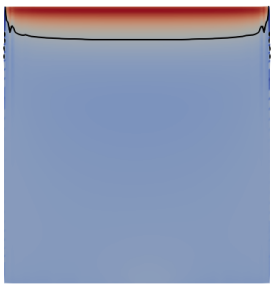

(l) 11°

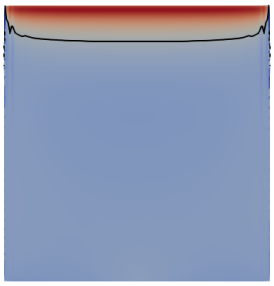

(m) 12°

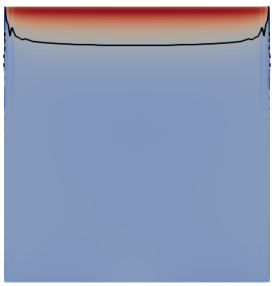

(n) 13°

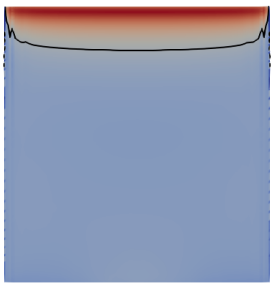

(o) 14°

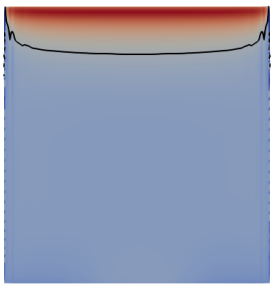

(p) 15°

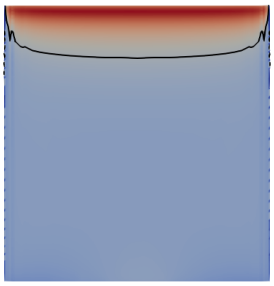

(q) 16°

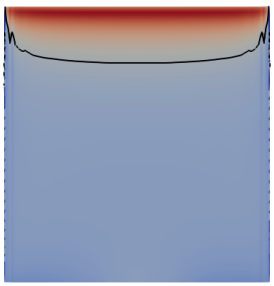

(r) 17°

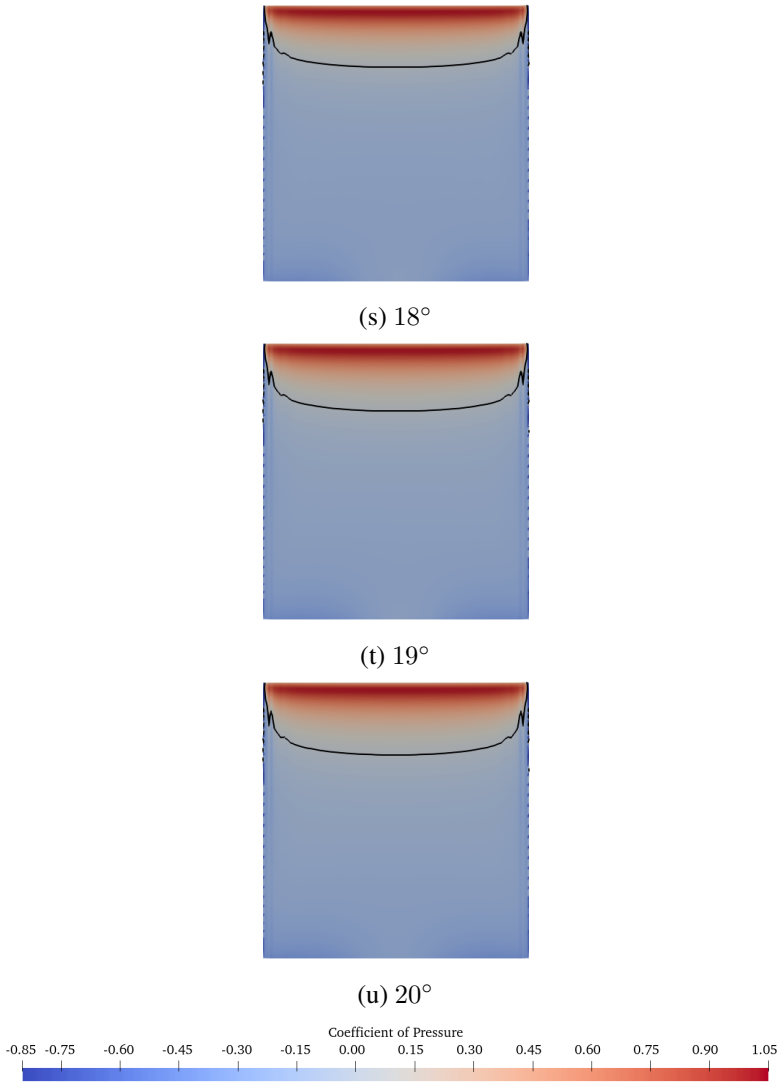

(s) 18°

(t) 19°

(u) 20°

Figure D.1. Coefficient of pressure at each simulated angle of attack for a span 1 wing.

D.2 Span 2

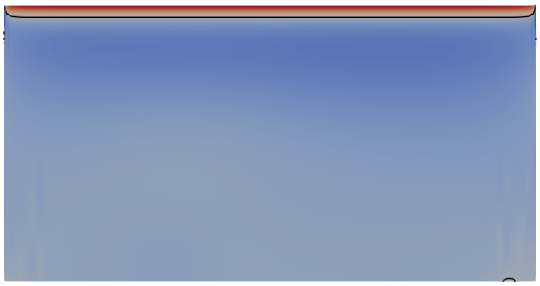

(a) 0°

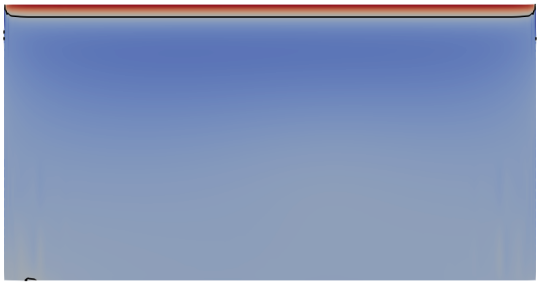

(b) 1°

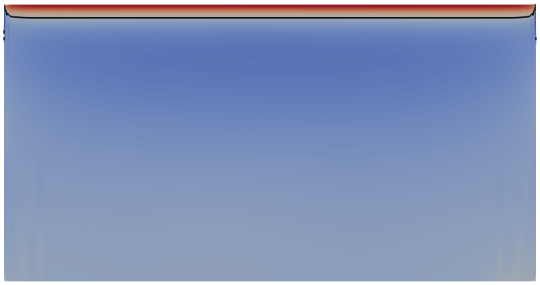

(c) 2°

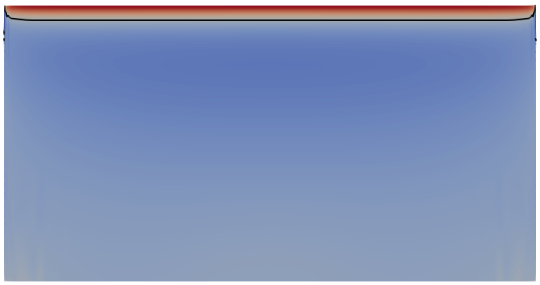

(d) 3°

(e) 4°

(f) 5°

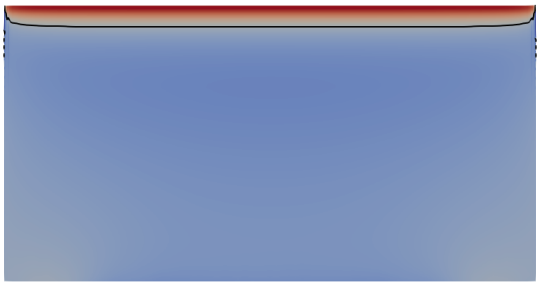

(g) 6°

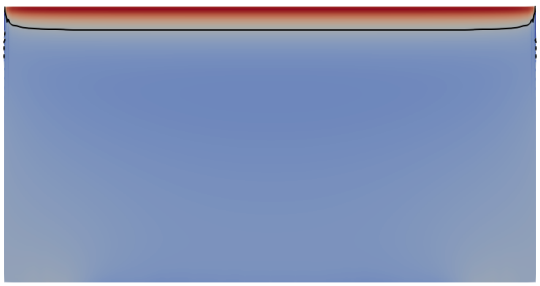

(h) 7°

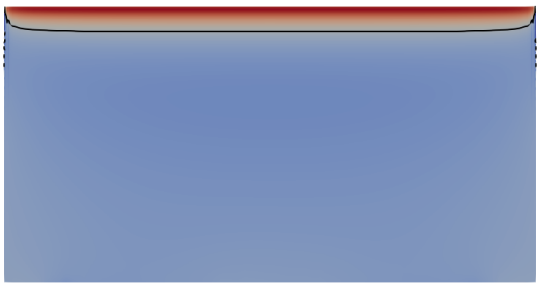

(i) 8°

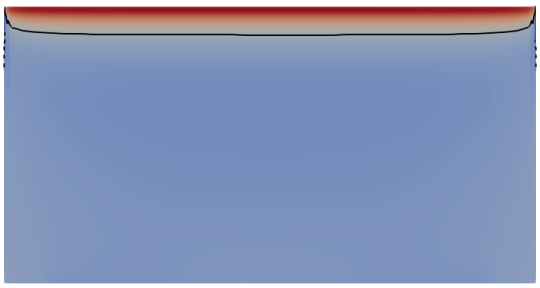

(j) 9°

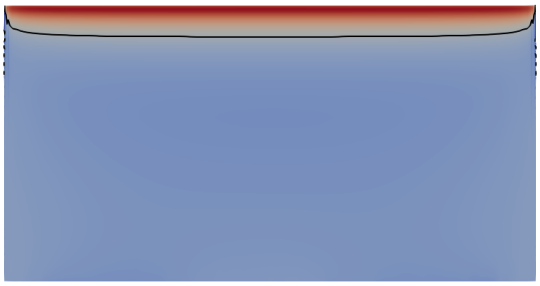

(k) 10°

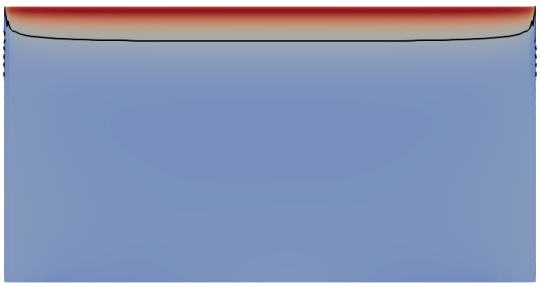

(l) 11°

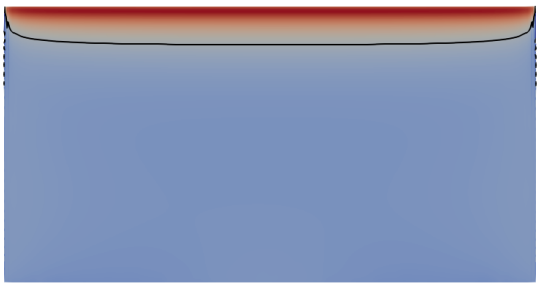

(m) 12°

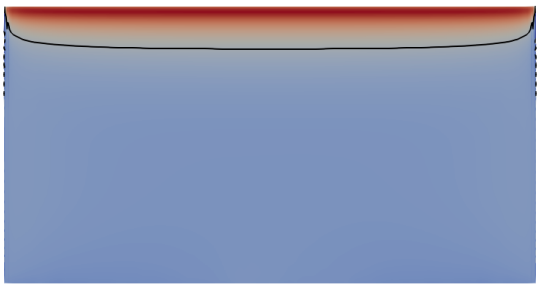

(n) 13°

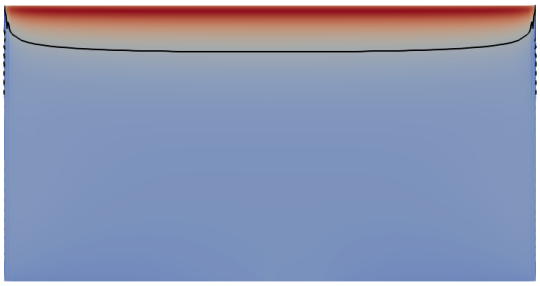

(o) 14°

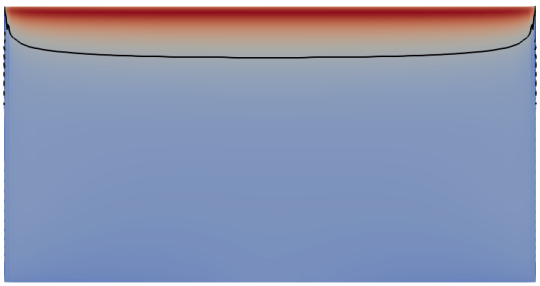

(p) 15°

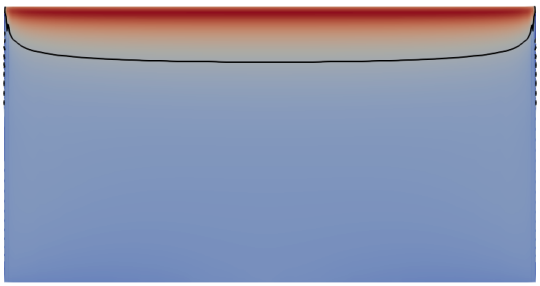

(q) 16°

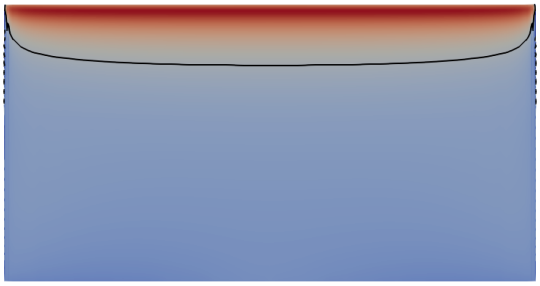

(r) 17°

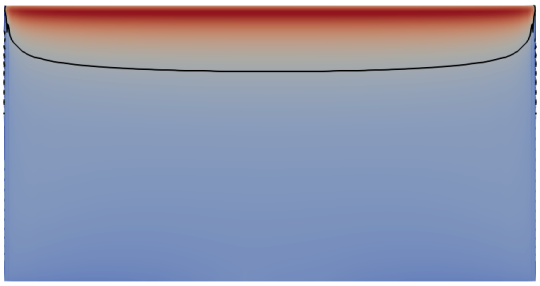

(s) 18°

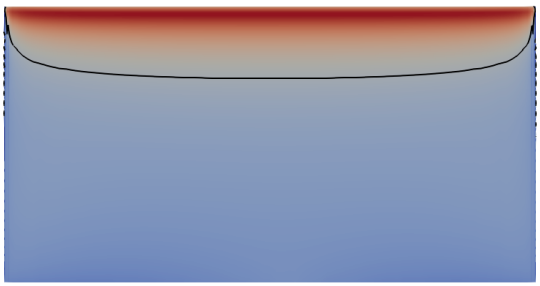

(t) 19°

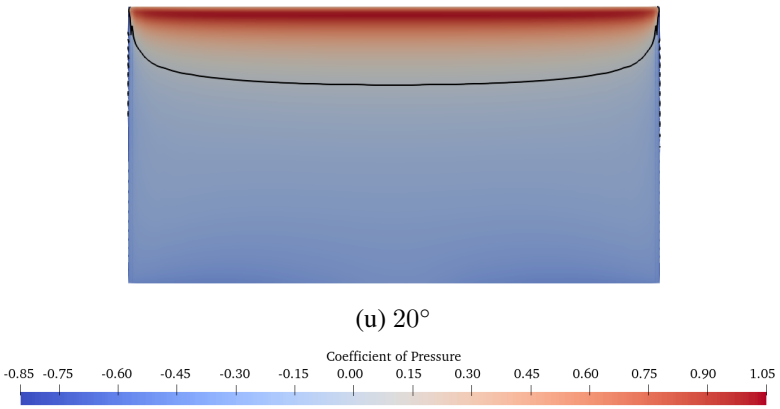

(u) 20°

Figure D.2. Coefficient of pressure at each simulated angle of attack for a span 2 wing.

D.3 Span 3

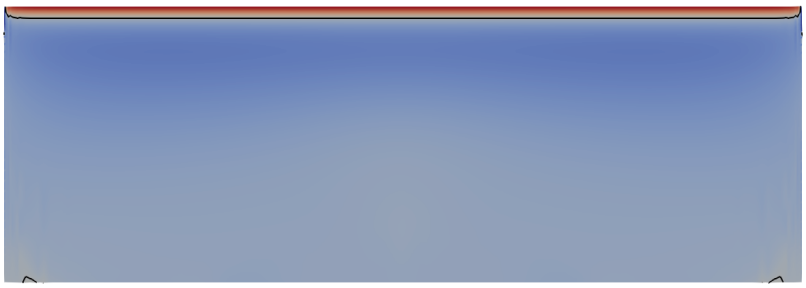

(a) 0°

(b) 1°

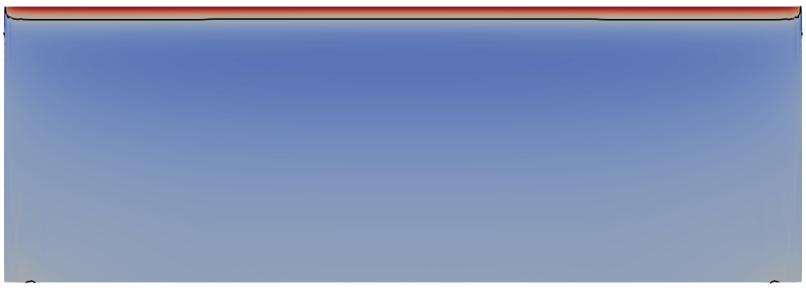

(c) 2°

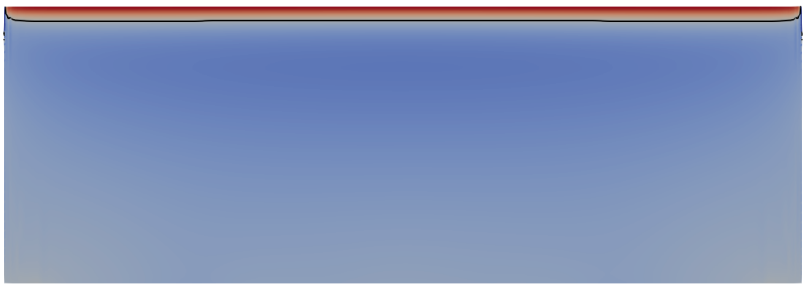

(d) 3°

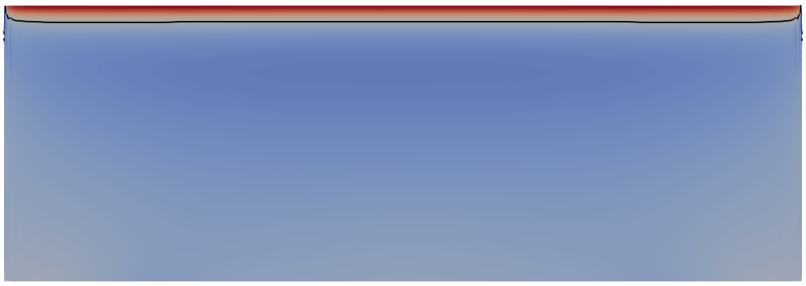

(e) 4°

(f) 5°

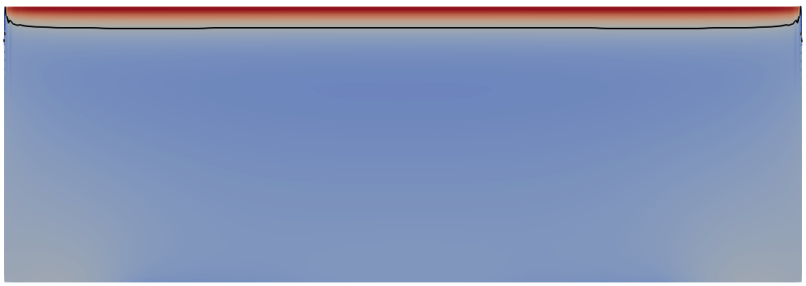

(g) 6°

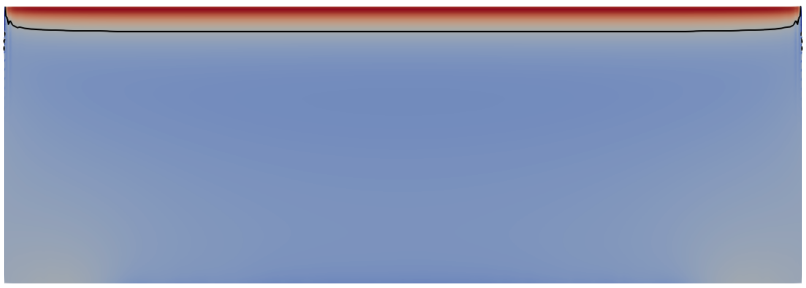

(h) 7°

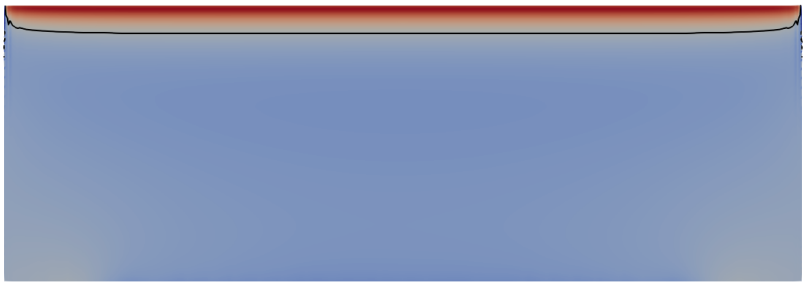

(i) 8°

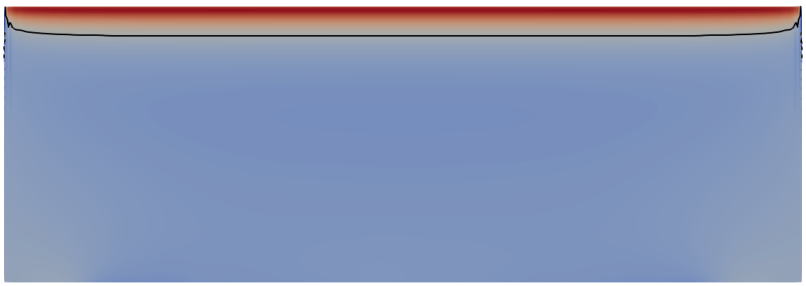

(j) 9°

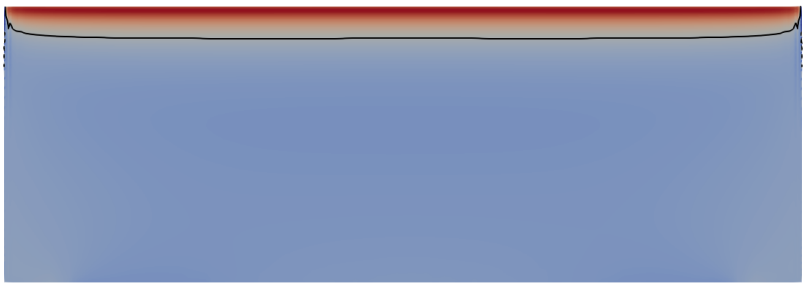

(k) 10°

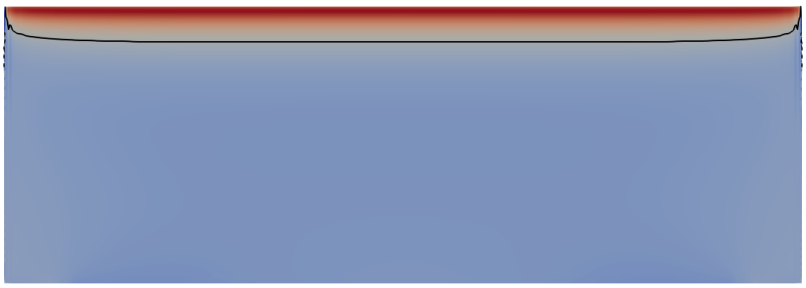

(l) 11°

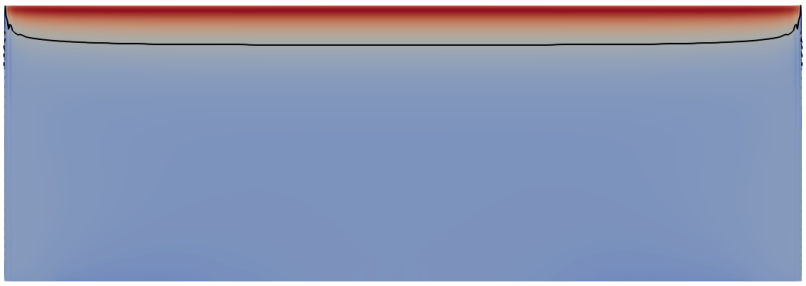

(m) 12°

(n) 13°

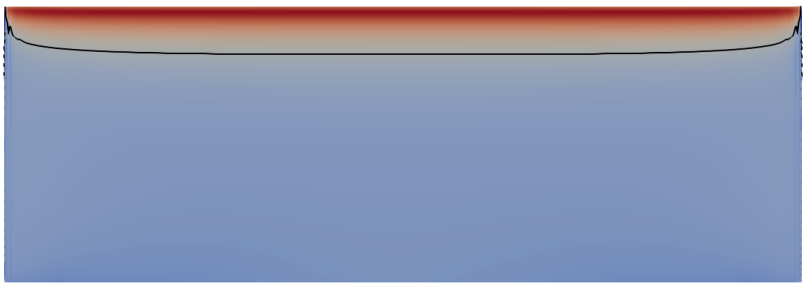

(o) 14°

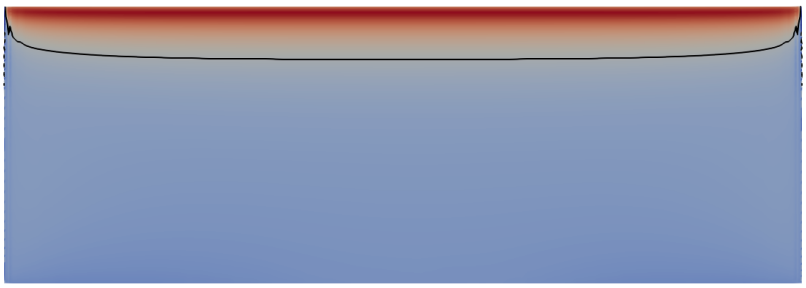

(p) 15°

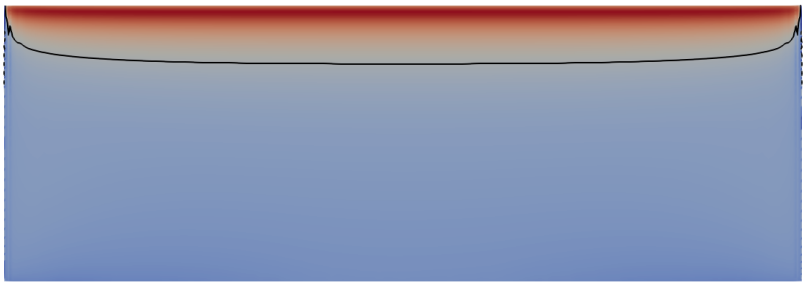

(q) 16°

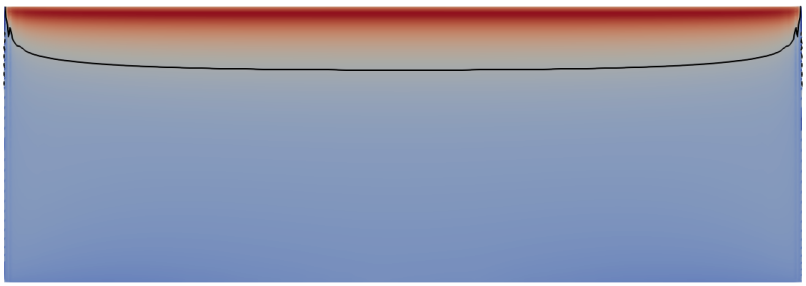

(r) 17°

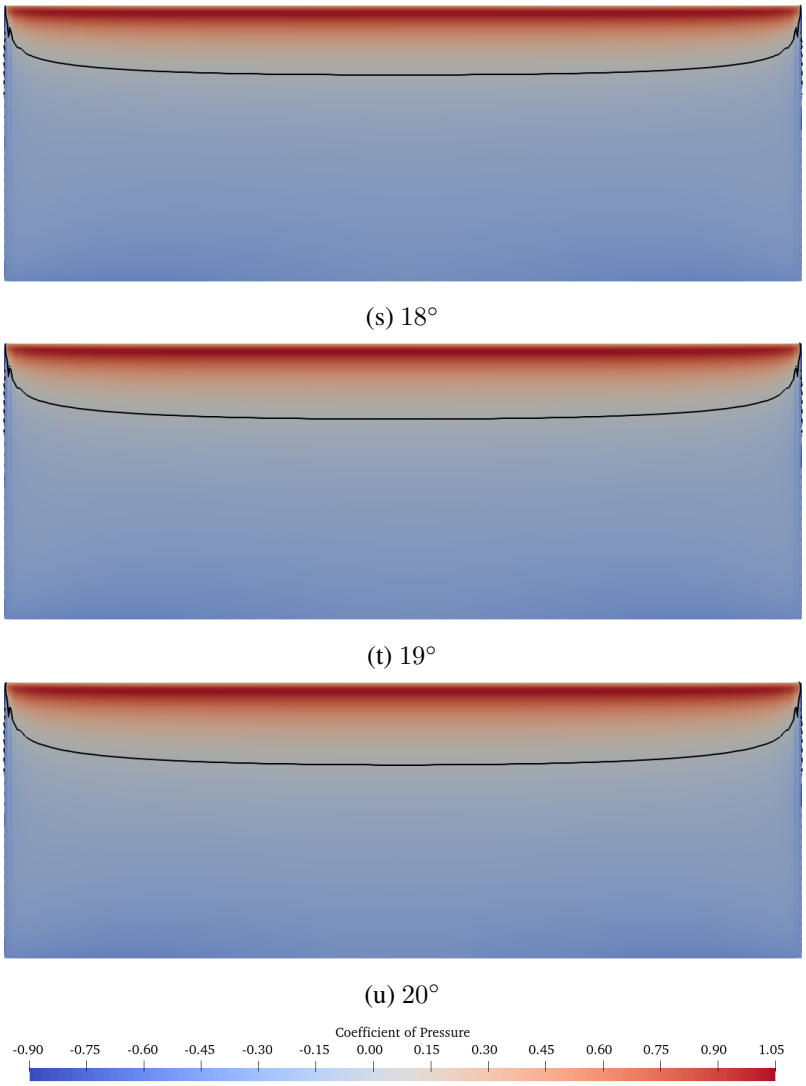

(s) 18°

(t) 19°

(u) 20°

Figure D.3. Coefficient of pressure at each simulated angle of attack for a span 3 wing.

D.4 Span 4

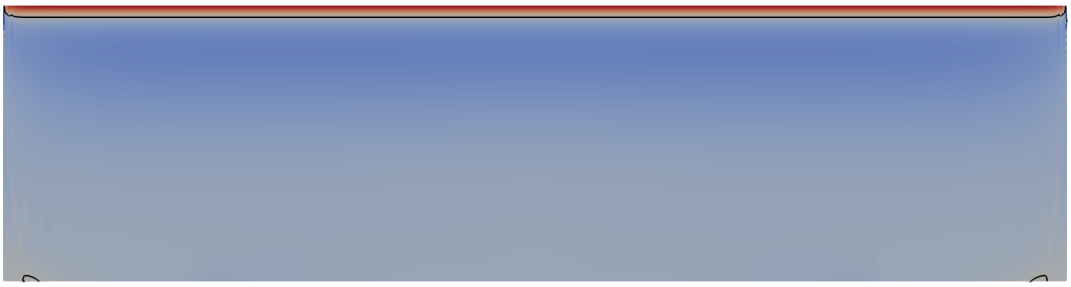

(a) 0°

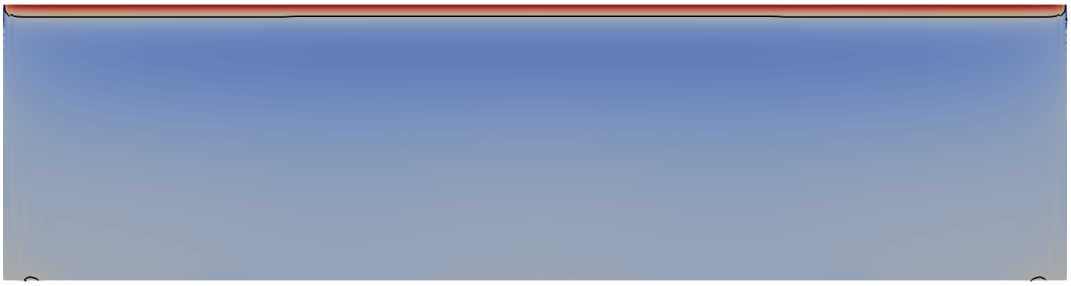

(b) 1°

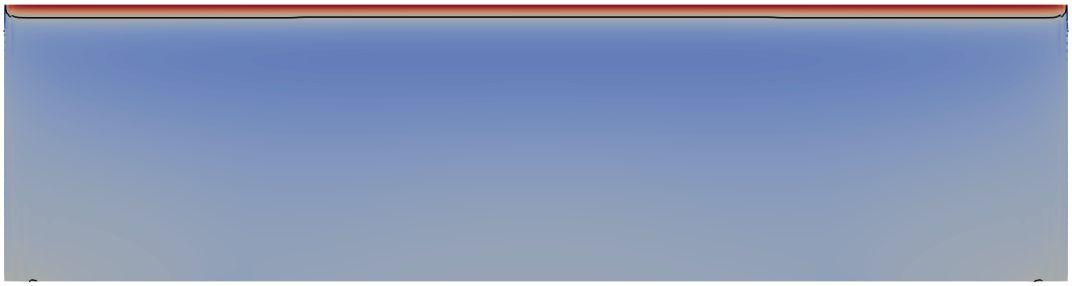

(c) 2°

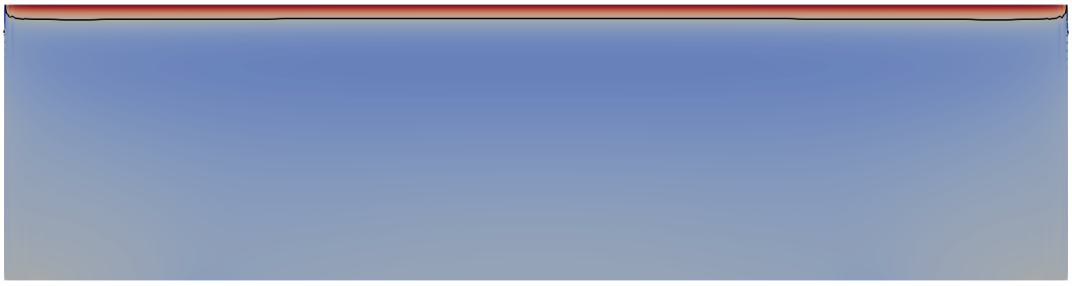

(d) 3°

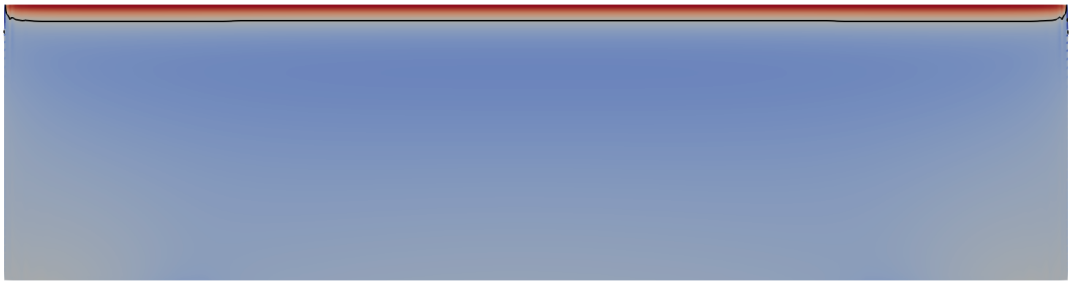

(e) 4°

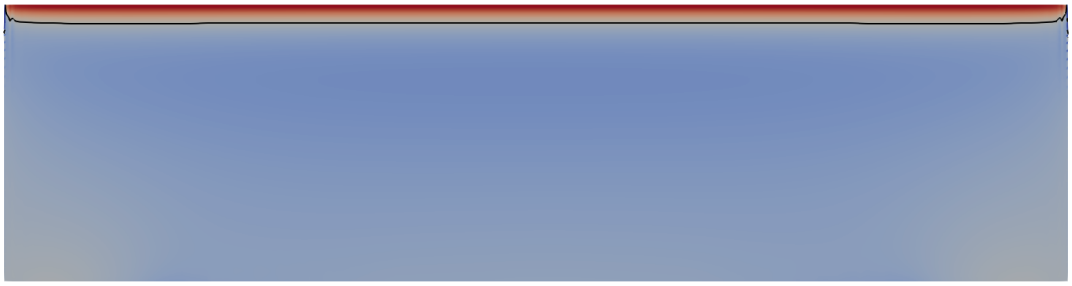

(f) 5°

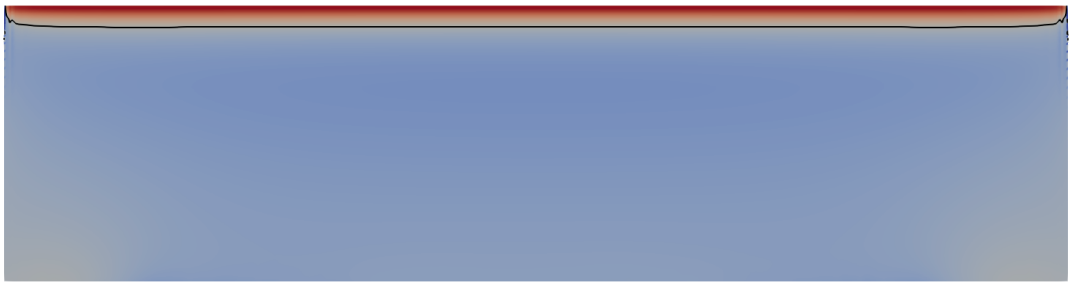

(g) 6°

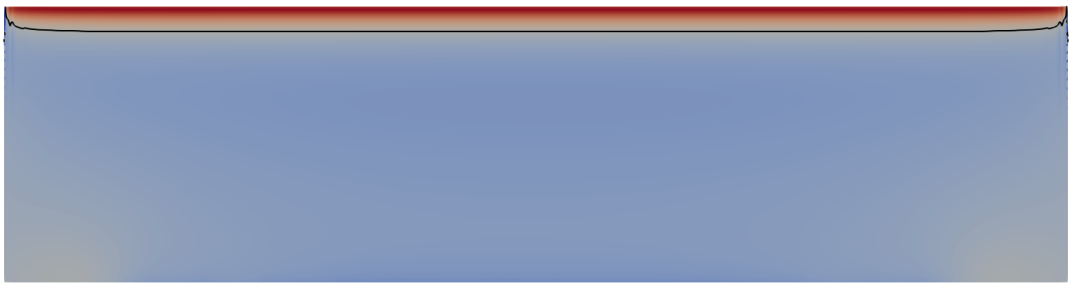

(h) 7°

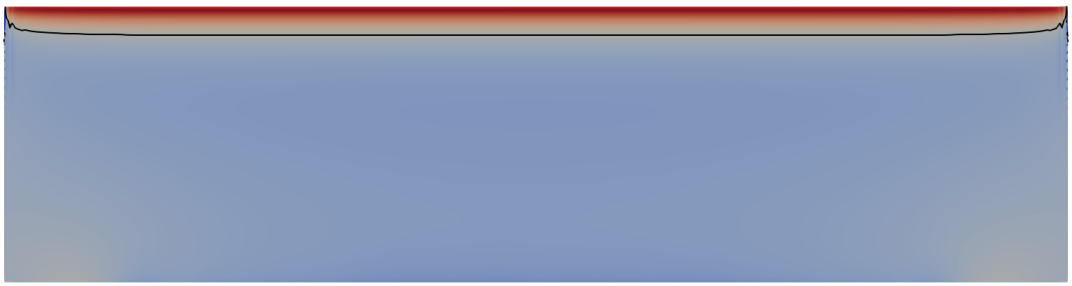

(i) 8°

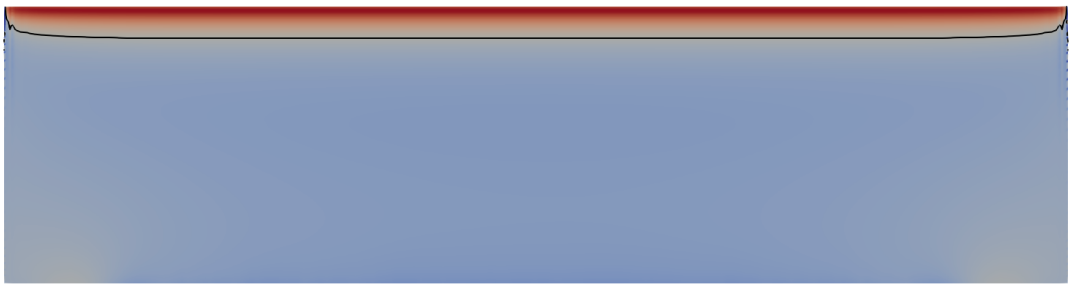

(j) 9°

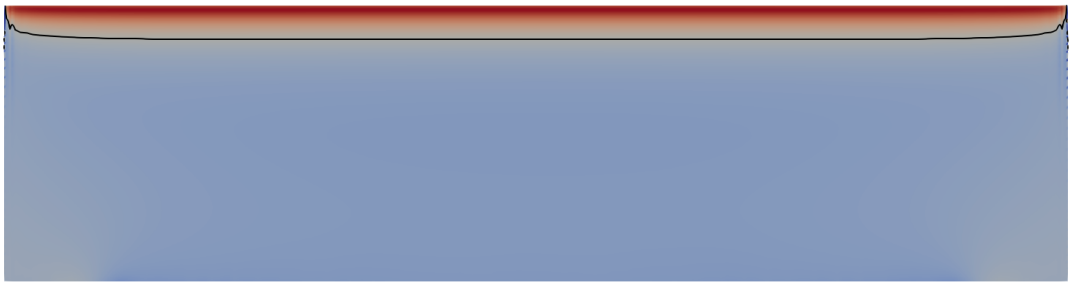

(k) 10°

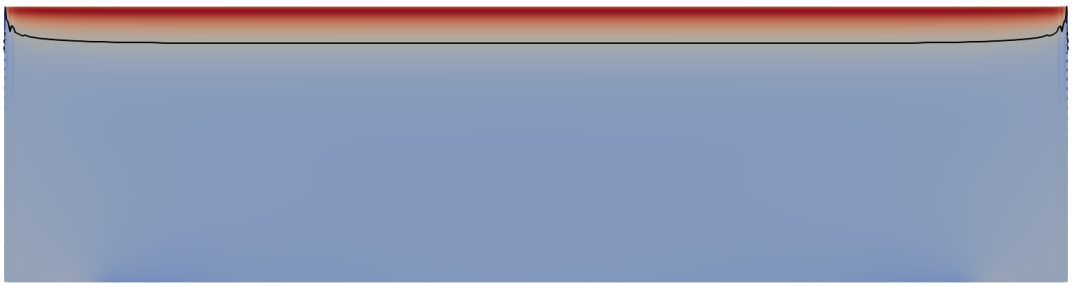

(l) 11°

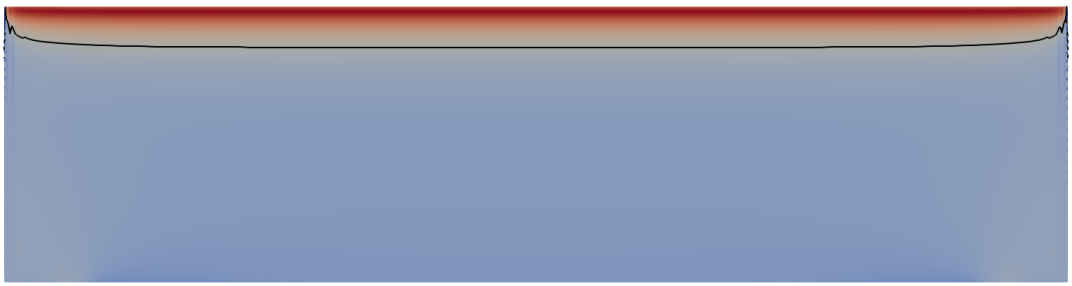

(m) 12°

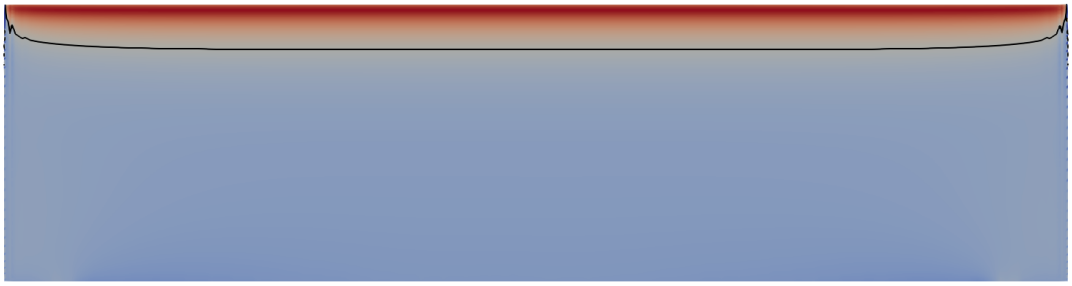

(n) 13°

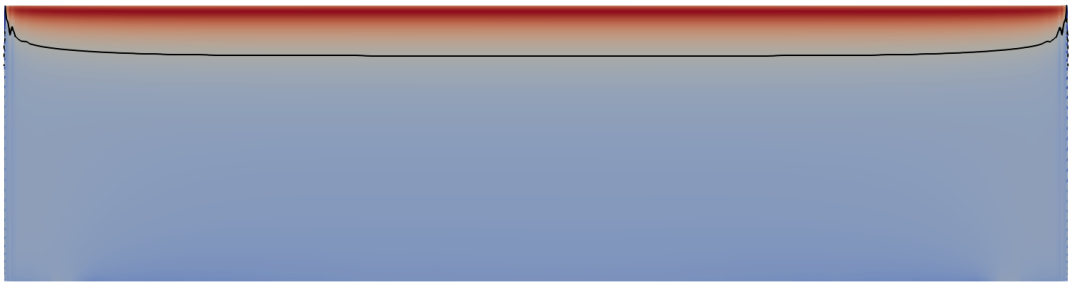

(o) 14°

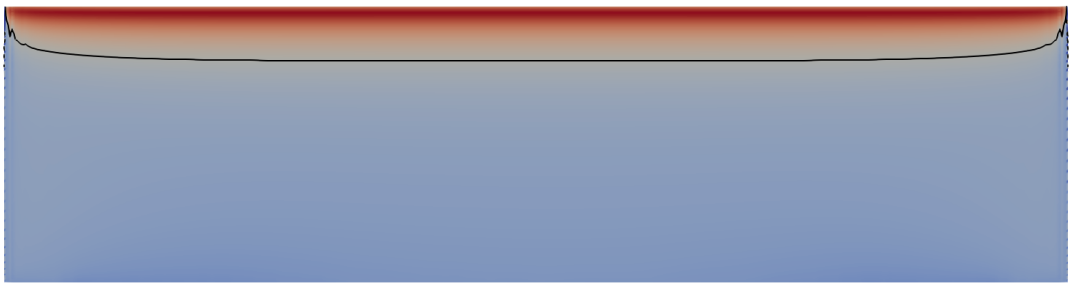

(p) 15°

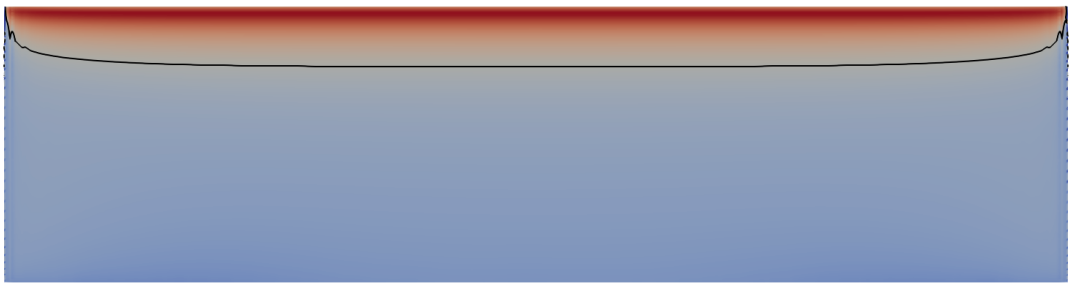

(q) 16°

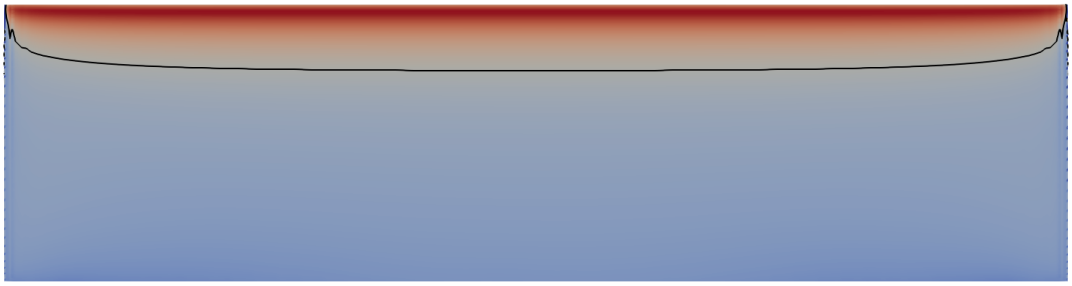

(r) 17°

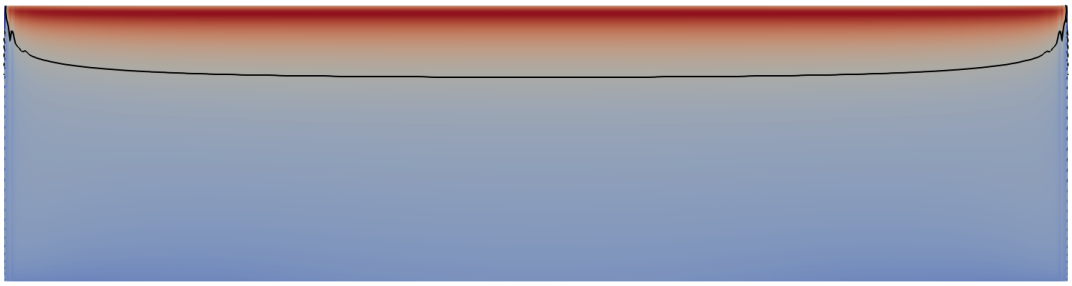

(s) 18°

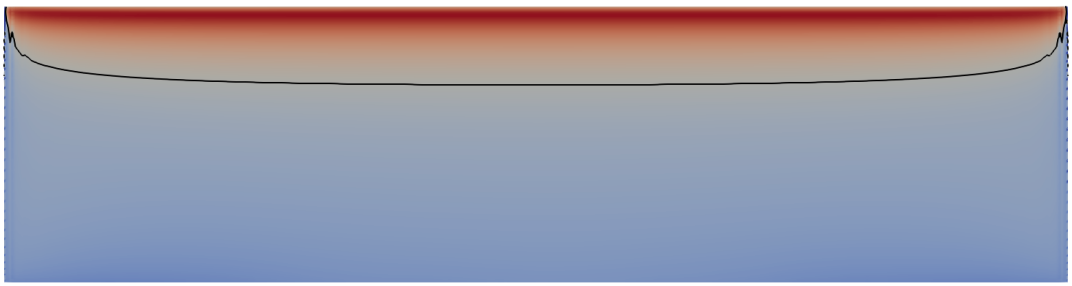

(t) 19°

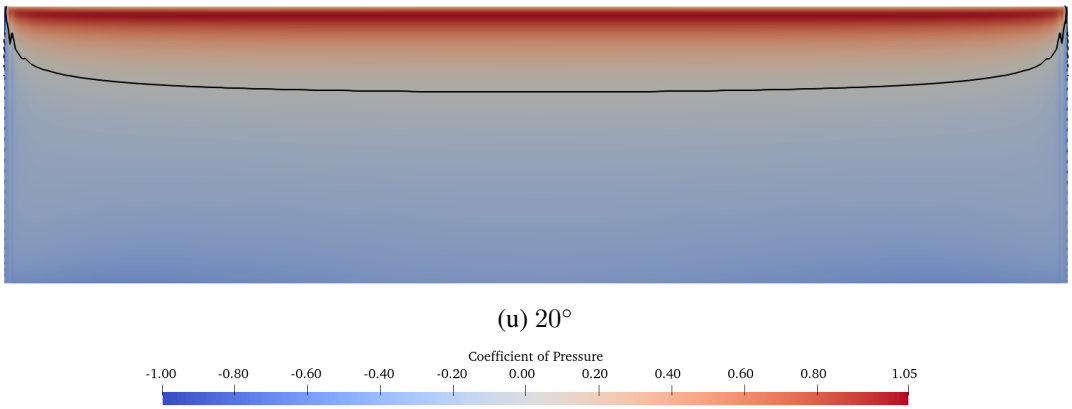

(u) 20°

Figure D.4. Coefficient of pressure at each simulated angle of attack for a span 4 wing.

D.5 Periodic

(a) 0°

(b) 1°

(c) 2°

(d) 3°

(e) 4°

(f) 5°

(g) 6°

(h) 7°

(i) 8°

(j) 9°

(k) 10°

(l) 11°

(m) 12°

(n) 13°

(o) 14°

(p) 15°

(q) 16°

(r) 17°

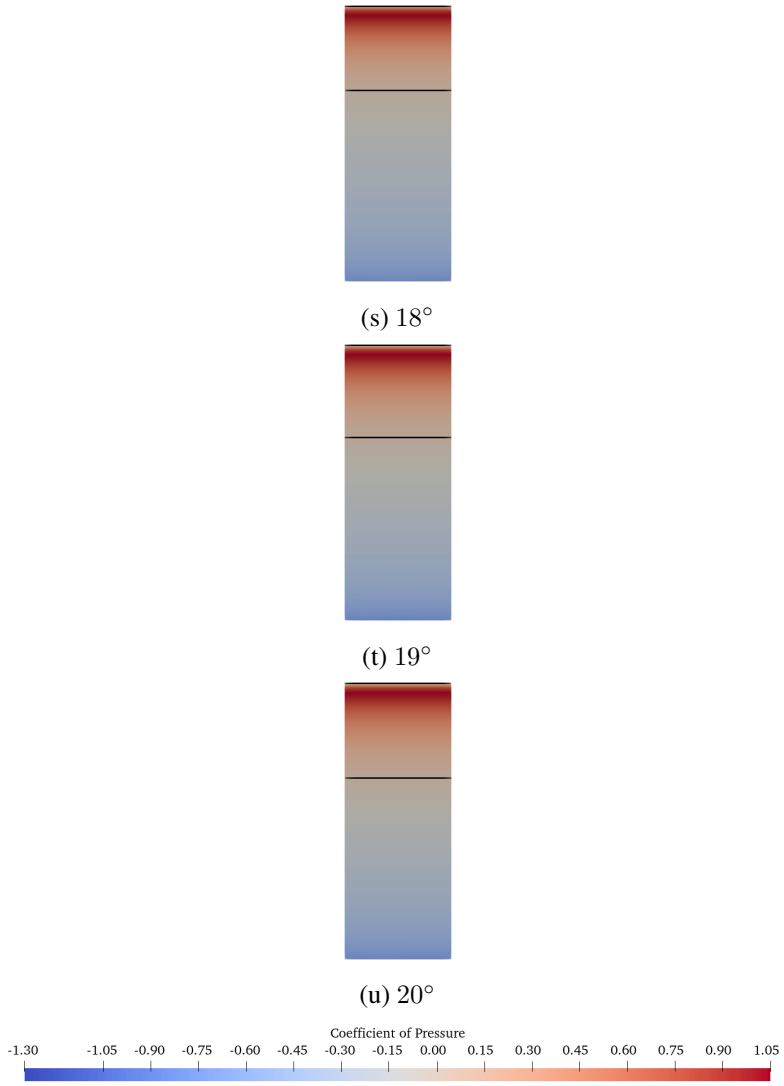

(s) 18°

(t) 19°

(u) 20°

Figure D.5. Coefficient of pressure at each simulated angle of attack for a periodic wing.

Appendix E

Coefficient of Pressure Plots - Upper Surface

E.1 Span 1

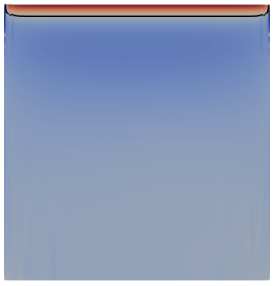

(a) 0°

(b) 1°

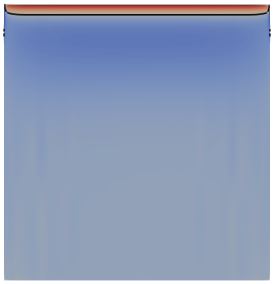

(c) 2°

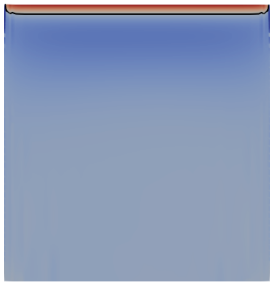

(d) 3°

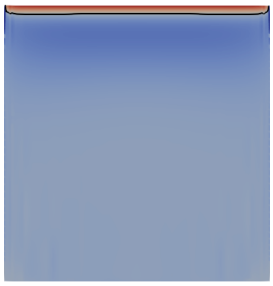

(e) 4°

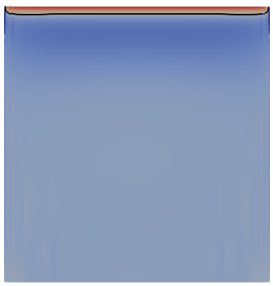

(f) 5°

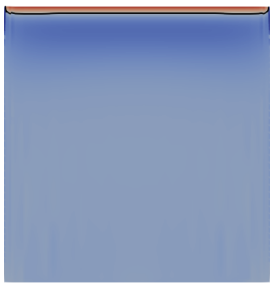

(g) 6°

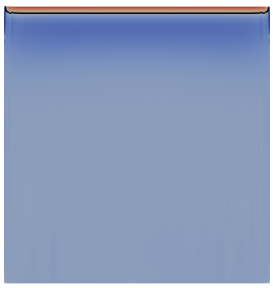

(h) 7°

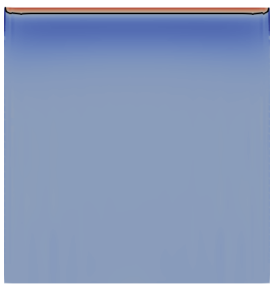

(i) 8°

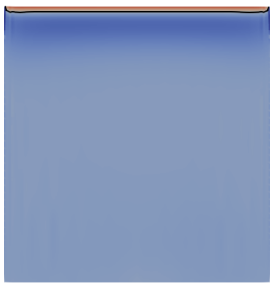

(j) 9°

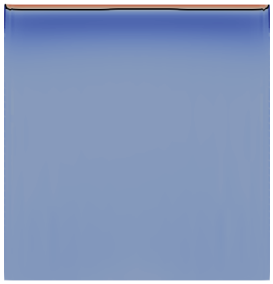

(k) 10°

(l) 11°

(m) 12°

(n) 13°

(o) 14°

(p) 15°

(q) 16°

(r) 17°

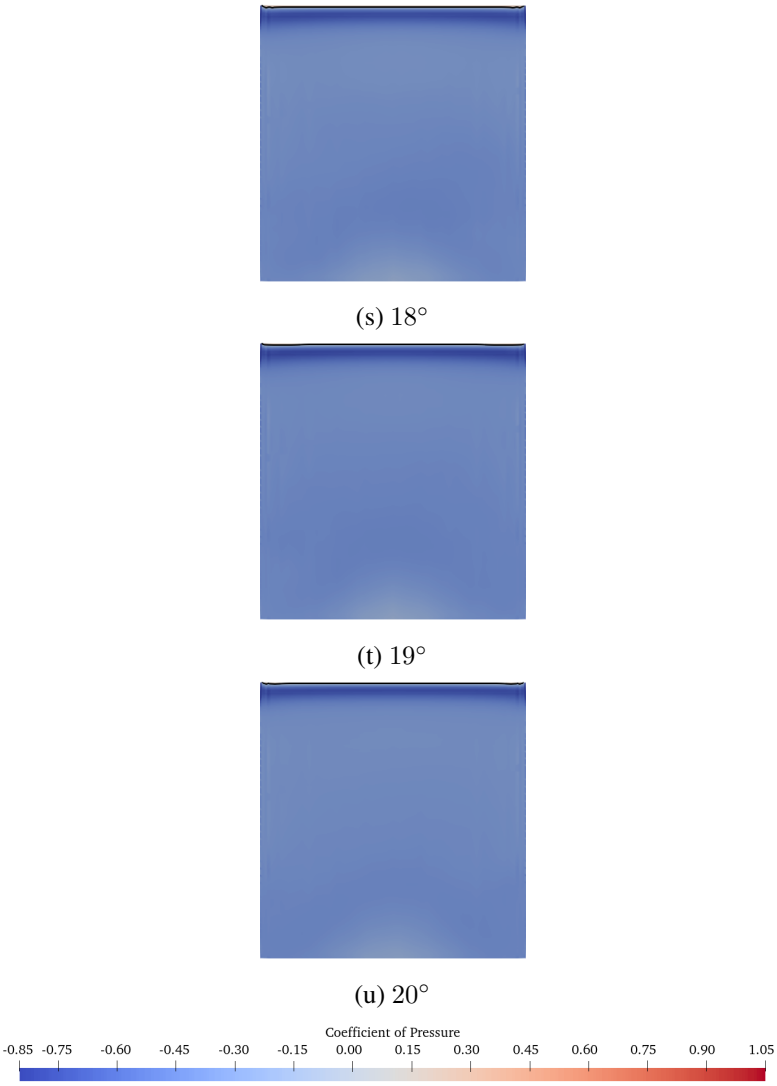

(s) 18°

(t) 19°

(u) 20°

Figure E.1. Coefficient of pressure at each simulated angle of attack for a span 1 wing.

E.2 Span 2

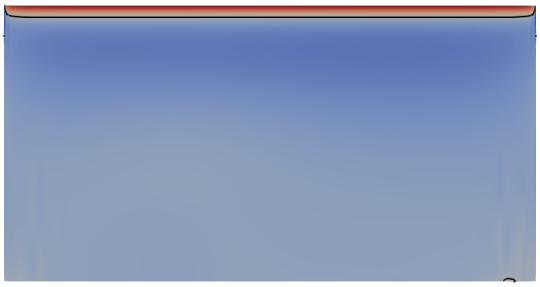

(a) 0°

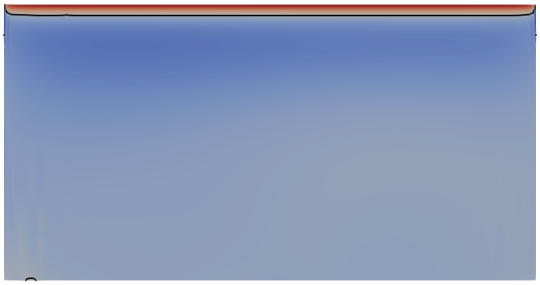

(b) 1°

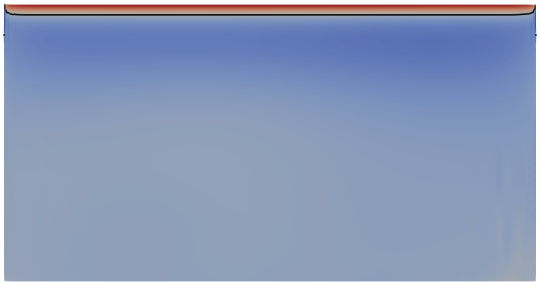

(c) 2°

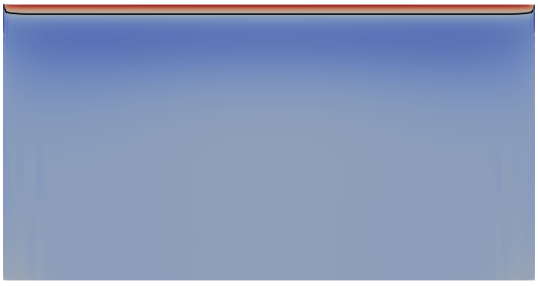

(d) 3°

(e) 4°

(f) 5°

(g) 6°

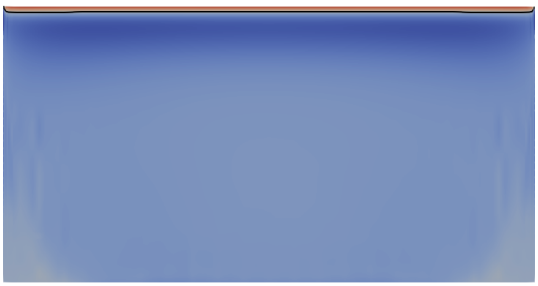

(h) 7°

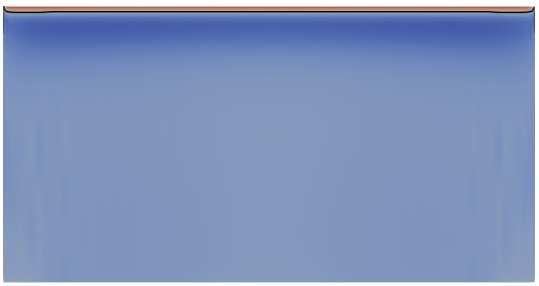

(i) 8°

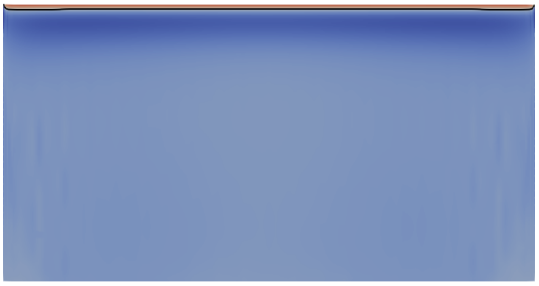

(j) 9°

(k) 10°

(l) 11°

(m) 12°

(n) 13°

(o) 14°

(p) 15°

(q) 16°

(r) 17°

(s) 18°

(t) 19°

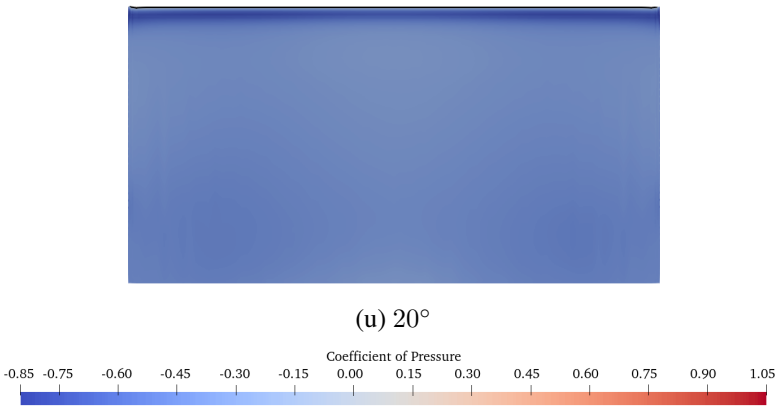

(u) 20°

Figure E.2. Coefficient of pressure at each simulated angle of attack for a span 2 wing.

E.3 Span 3

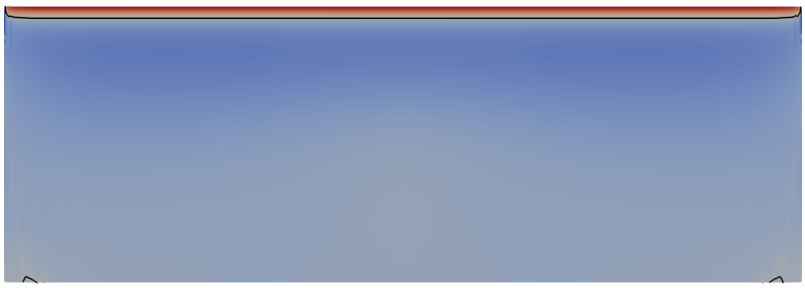

(a) 0°

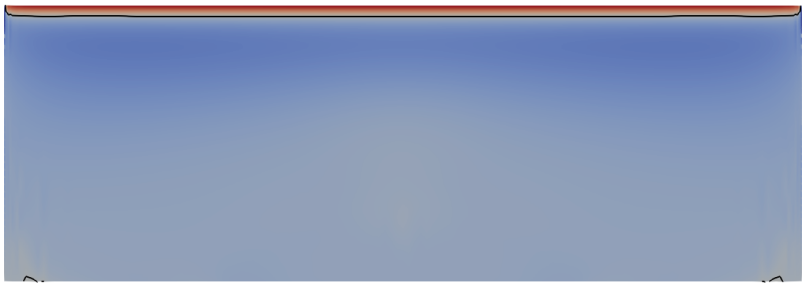

(b) 1°

(c) 2°

(d) 3°

(e) 4°

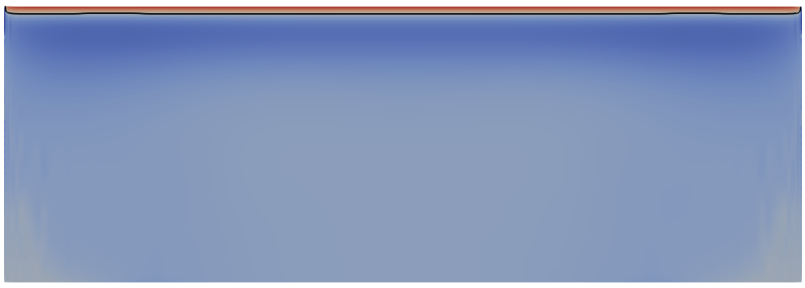

(f) 5°

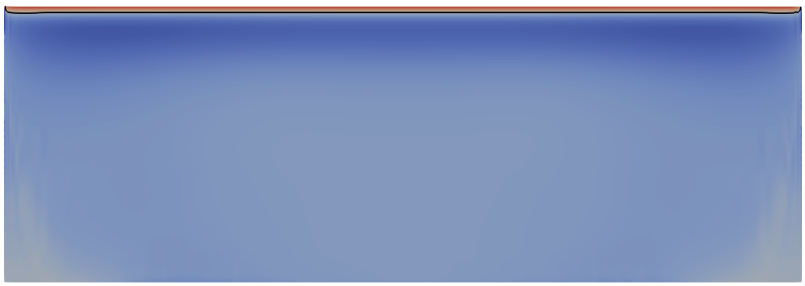

(g) 6°

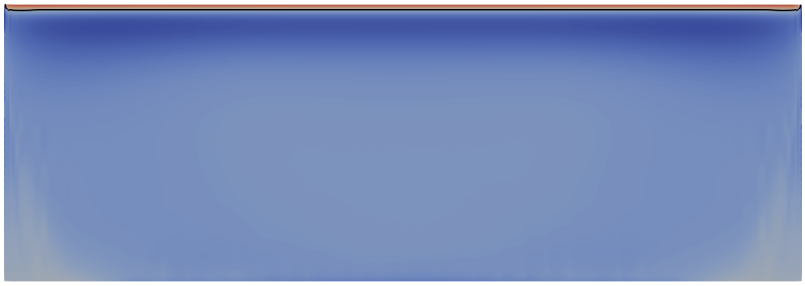

(h) 7°

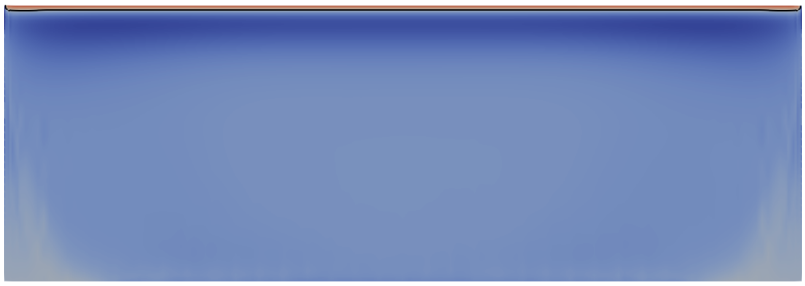

(i) 8°

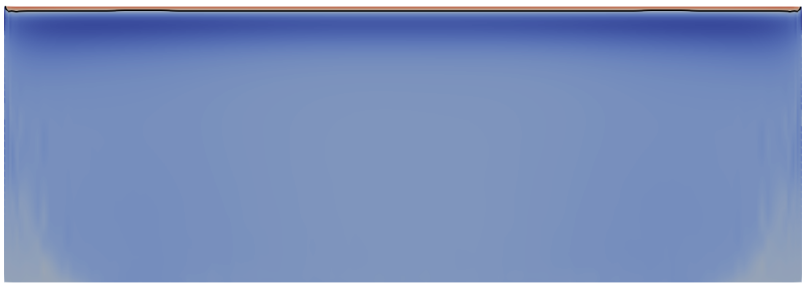

(j) 9°

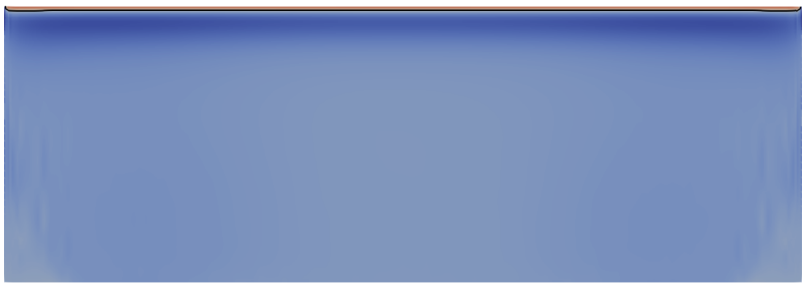

(k) 10°

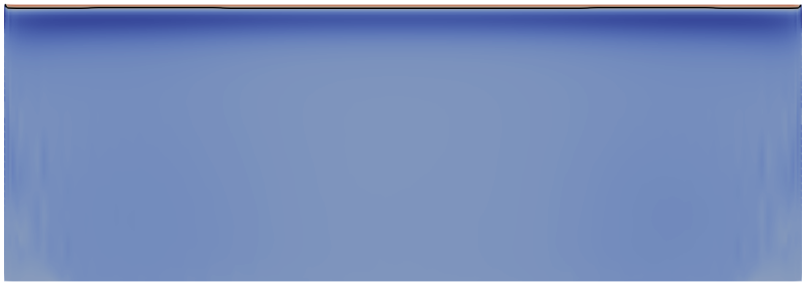

(l) 11°

(m) 12°

(n) 13°

(o) 14°

(p) 15°

(q) 16°

(r) 17°

(s) 18°

(t) 19°

(u) 20°

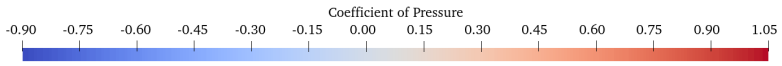

Figure E.3. Coefficient of pressure at each simulated angle of attack for a span 3 wing.

E.4 Span 4

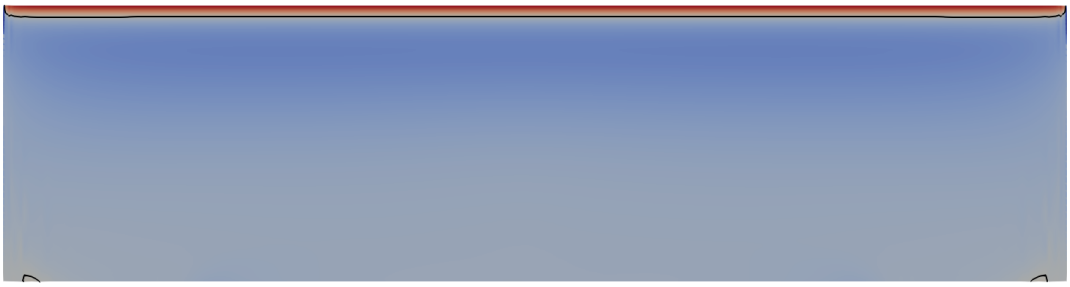

(a) 0°

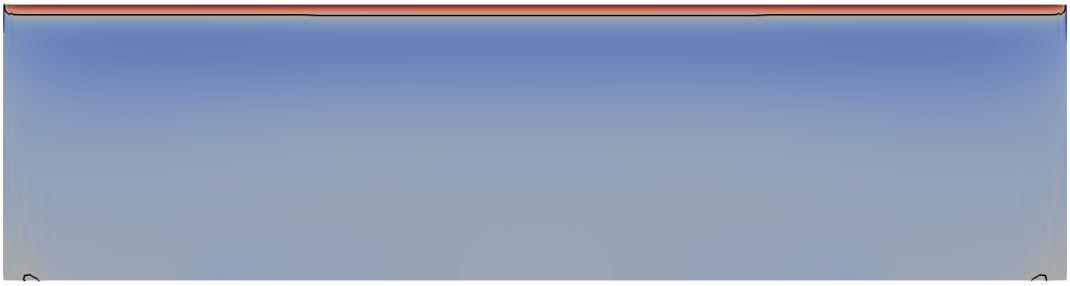

(b) 1°

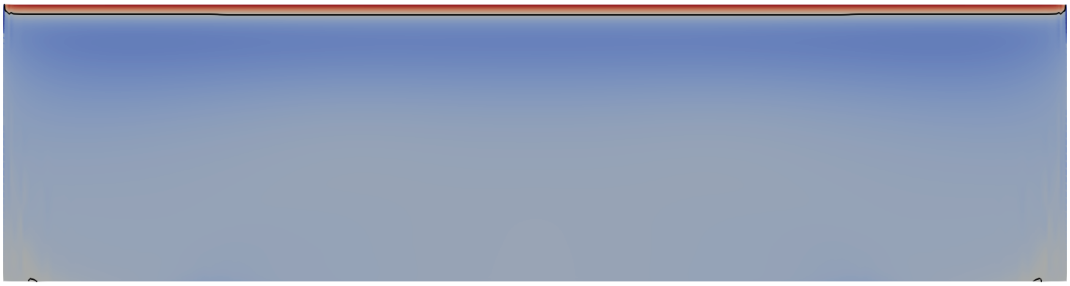

(c) 2°

(d) 3°

(e) 4°

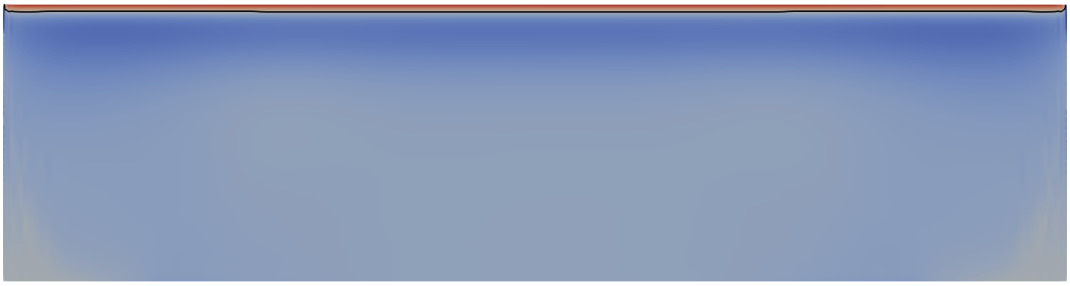

(f) 5°

(g) 6°

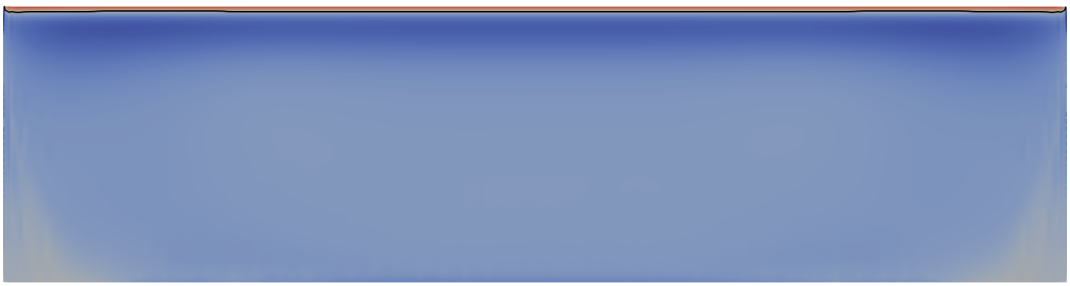

(h) 7°

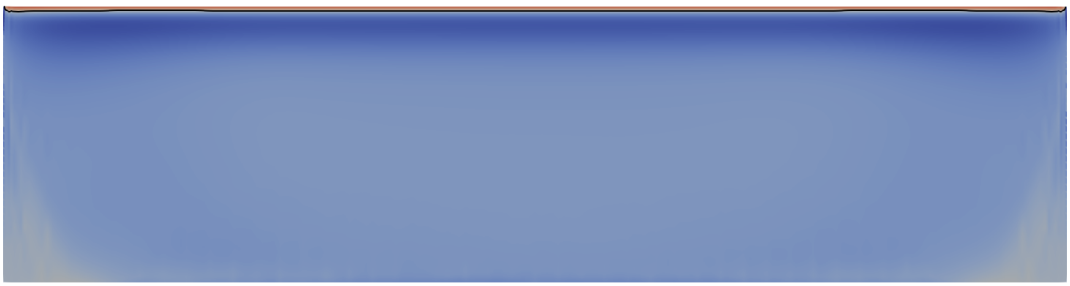

(i) 8°

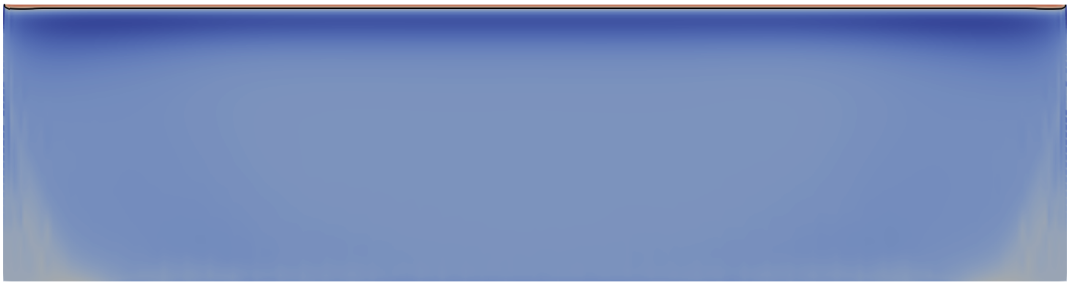

(j) 9°

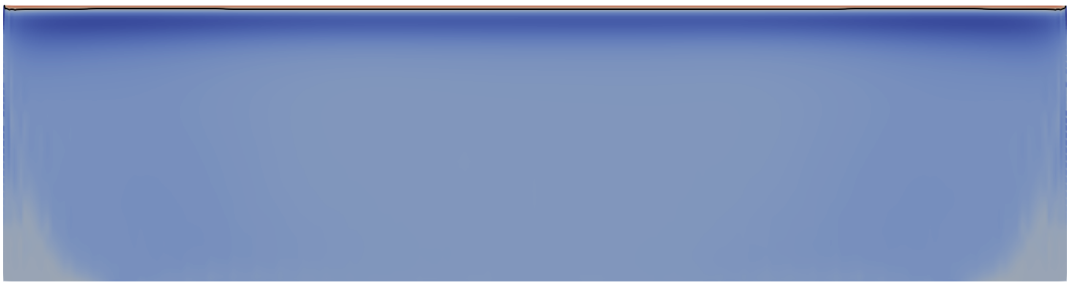

(k) 10°

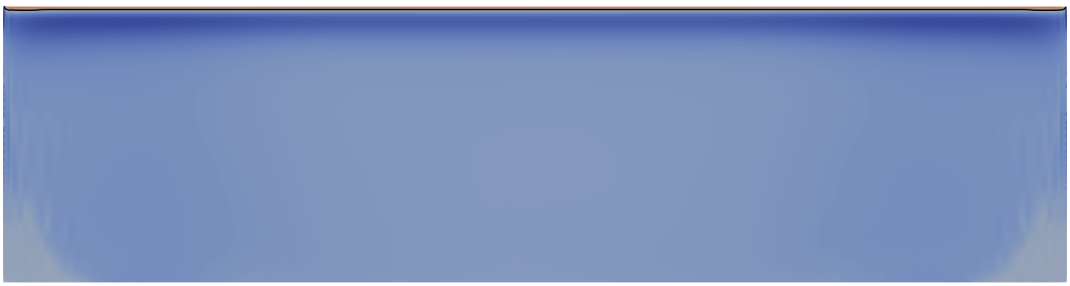

(l) 11°

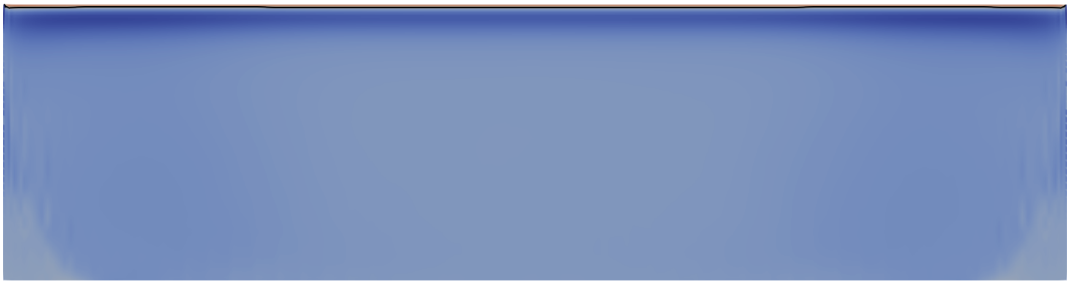

(m) 12°

(n) 13°

(o) 14°

(p) 15°

(q) 16°

(r) 17°

(s) 18°

(t) 19°

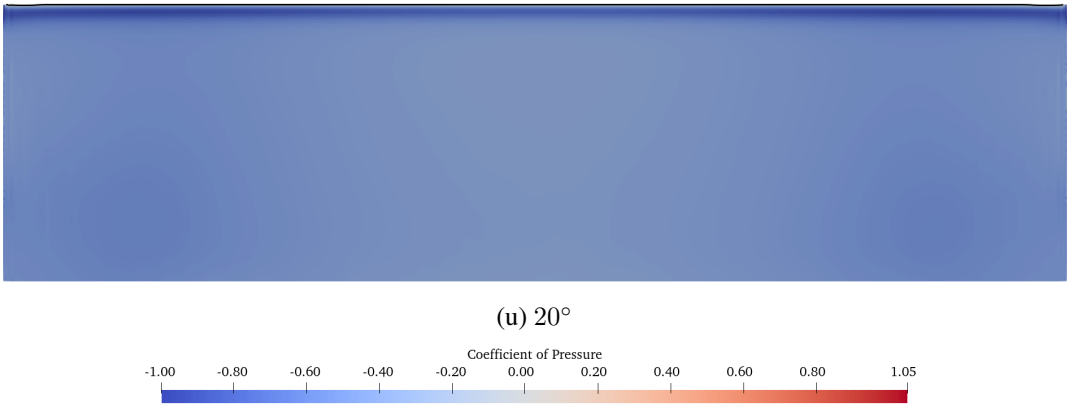

(u) 20°

Figure E.4. Coefficient of pressure at each simulated angle of attack for a span 4 wing.

E.5 Periodic

(a) 0°

(b) 1°

(c) 2°

(d) 3°

(e) 4°

(f) 5°

(g) 6°

(h) 7°

(i) 8°

(j) 9°

(k) 10°

(l) 11°

(m) 12°

(n) 13°

(o) 14°

(p) 15°

(q) 16°

(r) 17°

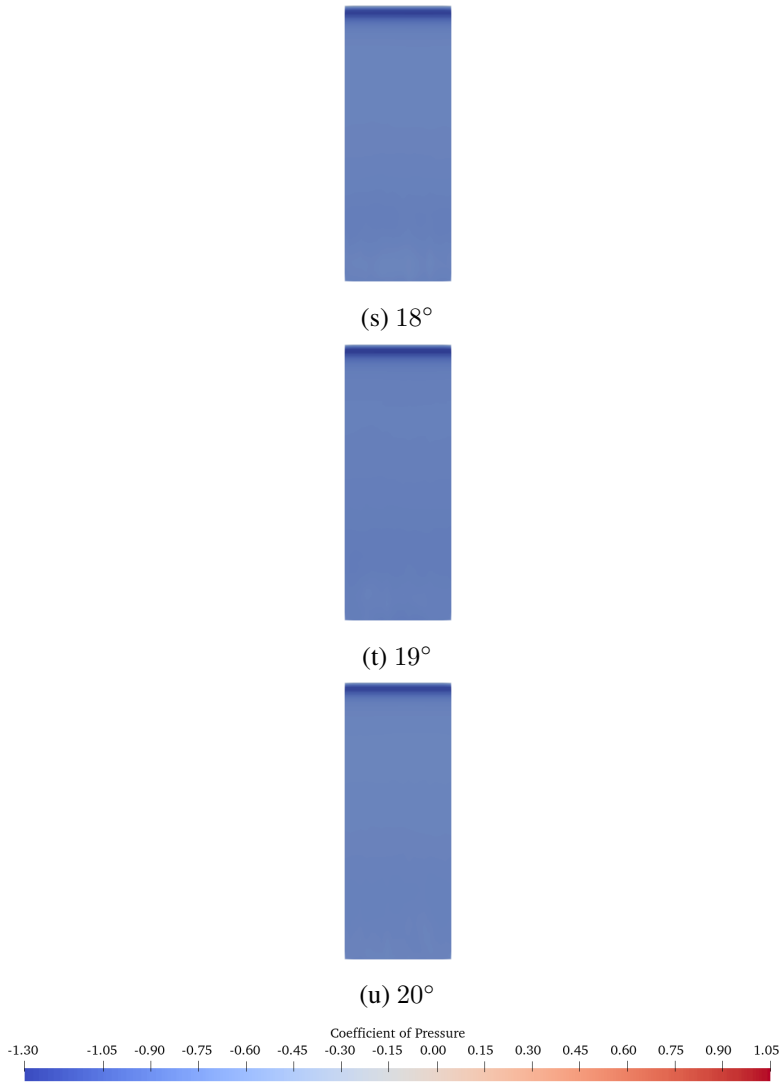

Figure E.5. Coefficient of pressure at each simulated angle of attack for a periodic wing.